

The Structural and Orbital Evolution of the Galilean Satellites

Constantine Thomas

BSc. (Hons.)

Submitted in partial fulfilment of the requirements for
the degree of Doctor of Philosophy

University of Lancaster

Department of Environmental Science

November, 2002

The Structural and Orbital Evolution of the Galilean Satellites

Constantine Thomas BSc. (Hons.)

**Submitted in partial fulfilment for the degree of
Doctor of Philosophy at the University of Lancaster,
November 2002.**

ABSTRACT

A synthesis of current data regarding the structural and orbital evolution of the Galilean satellites - Io, Europa, Ganymede, and Callisto - is presented and expanded here, using new insights from Galileo Orbiter data. New models of the internal structure of the Galilean satellites are presented that incorporate geological evidence, magnetic field and gravity data, and the most recent orbital evolution models.

I suggest that Io, Europa, and Ganymede entered the orbital resonances already fully differentiated into a metallic core, silicate mantle/crust, and ice/water shell structure. Io is partially molten today as a result of passage through a laplace-like orbital resonance in the past, and may suffer another episode of greater heating in the future. Tidal dissipation in Europa was insufficient to keep its interior molten so it cooled and solidified, but heating from the resonance was sufficient to keep part of the ice shell molten and maintain a water layer there. I propose that a combination of radiogenic, accretional and tidal heating (and greater size) allowed the metallic core of Ganymede to remain molten since the satellite's formation, and that it entered the orbital resonance with a deep water layer under a thick ice shell. Callisto has not been involved in any significant orbital resonances, and is partly differentiated with a rocky core, a deep ice/rock mantle increasing in density toward the core, and a water layer sandwiched between the surface ice I layer and an ice V ice shell below it. Radiogenic heating is sufficient to explain the water layer's presence in Callisto today.

ACKNOWLEDGEMENTS

Well, it's been a long haul - nearly eighty six months (!!) - but I finally made it to the end and I couldn't have done it without the help and support of a *lot* of people...

I would like to extend special thanks to my parents, Maria and George Thomas - without their emotional and financial support this work would have been impossible! Thank you for having faith in me and for letting me follow my dream. Special thanks also go to my supervisor Professor Lionel Wilson for his help, advice, support, and never-ending patience, and to Dr. Richard Ghail for his support over the years.

My sanity would have fallen apart long ago if it were not for all the friends who kept me going over the years and generally put me back together again when I needed it. Deep heartfelt bows of appreciation go to: Eric Anderson, DJ Babb, Dave & Jo Barrett, Paul Bowling, Sonia Calvari, Enzo Cataldo, Simon Emmins, Helen Flynn, Helen Gorman, Jez Green, Helena Greenwood, Jonathan 'Spike' Halls, Dave Hawksett, Björn Jónsson, Nicholas Kaplony, Doug Lowe, LuBBS, LURPS, Saskia Marshall, Karl Mitchell, Louise Norman, Jeya Palan, Jenny Petrycki, Elizabeth Phillips, the PyraMOO regulars, Michael Reed, Anders Sandberg, Eve & Rob Scott, Nicole Spaun, Nicola Thorley, Brandy Toft and the Bemidji Bunch, Jane Toothill, Tony Ward, and Chris Woodhead.

Thanks also to Tim Colvin at RAND Corporation for supplying me with accurate SPICE data for my image processing, James Head III for funding my trip to Brown University in 1997, everyone at USGS for all their help with ISIS, John Spencer, Carl Murray, Paul Helfenstein, Claudio Vita-Finzi and Tony Cook for scientific help and support, Voyagers 1 and 2 for changing my life in 1979 and setting me down this path, and the Galileo Orbiter for surviving as long as it did!

DEDICATION

This work is dedicated to all the pioneers, wherever you are.

“The meek shall inherit the Earth. The rest of us shall go to the stars.”

- Robert Heinlein.

I'll see you out there...

TABLE OF CONTENTS

Chapter 1	Introduction	1
 Chapter 2	 The surface geology of the Galilean satellites.	 5
2.1	The geology of Io.	7
2.2	The geology of Europa.	10
2.3	The geology of Ganymede.	15
2.4	The geology of Callisto.	20
2.5	Summary	24
 Chapter 3	 The magnetic fields of the Galilean satellites.	 25
3.1	The nature and origin of planetary magnetic fields.	25
3.2	Potential mechanisms of magnetic field generation in the Galilean satellites.	29
3.3	The observed magnetic fields of the Galilean satellites.	31
3.3.1	The magnetic field of Io.	31
3.3.2	The magnetic field of Europa.	33
3.3.2.1	Discussion	34
3.3.3	The magnetic field of Ganymede.	38
3.3.4	The magnetic field of Callisto.	39
3.4	Conclusion.	40
 Chapter 4	 The orbital dynamics of the Galilean satellites.	 41
4.1	The orbital evolution of natural satellites.	41
4.1.1	Orbital evolution in two-body systems.	41
4.1.2	Orbital evolution in multi-body systems.	48
4.1.3	Orbital terminology.	49
4.2	The mechanisms of orbital evolution.	52
4.2.1	The Q factor.	52
4.2.2	Rotational despinning of planets and satellites.	56
4.2.3	Tidal evolution equations.	58
4.2.3.1	Increase in orbital distance of satellites (general case).	58

4.2.3.2	Rotational despinning of satellites (general case).	60
4.2.3.3	Rotational despinning of planets due to satellites and sun (general case).	61
4.3	Orbital characteristics of the jovian system.	64
4.4	Application to Jupiter and the Galilean satellites.	68
4.4.1	The Q of Jupiter.	70
4.4.2	A lower bound for Q_J .	72
4.4.2.1	The initial orbital distance of Io.	72
4.4.2.2	Determining the Q of Jupiter.	75
4.4.2.3	The orbital evolution of the Galilean satellites.	82
4.4.3	Failures of the model.	93
4.5	The next step.	99
Chapter 5	The orbital and thermal evolution of Ganymede.	100
5.1	Tidal evolution into the Laplace resonance.	100
5.1.2	Discussion.	107
5.2	The orbital and thermal evolution of Ganymede.	112
5.2.1	Overview.	112
5.2.2	Global expansion due to ice melting.	120
5.2.2.2	Discussion.	121
5.2.2.3	Extrapolation.	125
Chapter 6	The interior structures of the Galilean satellites.	132
6.1	Introduction.	132
6.2	The ONIONSKIN moment of inertia model.	133
6.3	The internal structure of Io.	138
6.3.1	Published models.	138
6.3.2	Io ONIONSKIN Models.	141
6.4	The internal structure of Europa.	145
6.4.1	Published models.	145
6.4.2	Europa ONIONSKIN models.	147
6.5	The internal structure of Ganymede.	152
6.5.1	Published models.	152

6.5.2	Ganymede ONIONSKIN Model.	166
6.6	The internal structure of Callisto.	169
6.6.1	Published models.	169
6.6.2	Callisto ONIONSKIN Models.	170
6.7	The next stage.	176
Chapter 7	SATMOD: The next step in satellite modelling.	177
7.1	Introduction	177
7.2	Callisto SATMOD model	180
7.3	Discussion.	184
7.3.1	Initial results.	184
7.3.2	The temperature problem.	188
7.3.3	The salt problem.	192
7.4	A thermally realistic Callisto model?	196
7.4.2	A working model.	199
7.5	Conclusion.	207
Chapter 8	Conclusion	208
8.1	The structural and orbital evolution of Io.	208
8.2	The structural and orbital evolution of Europa.	210
8.3	The structural and orbital evolution of Ganymede.	214
8.4	The structural and orbital evolution of Callisto.	216
8.5	Future work.	219
	References.	222
Appendix 1	Bulk and orbital properties of the Galilean satellites.	233
Appendix 2	Other work: LPSC abstracts.	238
Appendix 3	Commensurability Charts.	254

LIST OF FIGURES

Figure 1.1	Diagram of the jovian system	1
Figure 2.1	Global view of Io with insets.	8
Figure 2.2	Eruption of Pele on Io.	9
Figure 2.3	The subjovian and trailing hemispheres of Europa.	12
Figure 2.4	Conamara Chaos, Europa.	13
Figure 2.5	Chaos, Ridges and Smooth Terrain on Europa.	14
Figure 2.6	The antijovian hemisphere of Ganymede.	17
Figure 2.7	Nicholson Regio, Ganymede.	19
Figure 2.8	Global view of Callisto.	21
Figure 2.9	Crater chain on Callisto.	23
Figure 4.1	Tidal bulge, frictionless material.	41
Figure 4.2	Planetary tides.	42
Figure 4.3	Diagram illustrating important orbital parameters.	50
Figure 4.4	Graph showing the value of calculated Q_J derived from assumed initial orbital distances of Io.	80
Figure 4.5	Orbital evolution of the Galilean satellites for $a_i = 2.5 R_J$.	84
Figure 4.6	Orbital evolution of the Galilean satellites for $a_i = 3.85 R_J$.	85
Figure 4.7	Orbital evolution of the Galilean satellites for $a_i = 5.0 R_J$.	86
Figure 5.1	The phase diagram of water ice.	114
Figure 5.2	Two profiles through a hypothetical Ganymedian satellite.	115
Figure 6.1	ONIONSKIN model flowchart.	135
Figure 6.2	Determining moment of inertia in ONIONSKIN.	136
Figure 6.3	The internal structure of Io.	144
Figure 6.4	The internal structure of Europa.	151
Figure 6.5	The internal structure of Ganymede.	168
Figure 6.6	The internal structure of Callisto.	174
Figure 6.7	Comparison of the internal structures of the Galilean satellites.	175

Figure 7.1	Distribution of Callisto SATMOD models.	183
Figure 7.2	Cutaway through Callisto SATMOD model.	185
Figure 7.3	Melting curves for ice I, ice III, and ice V	189
Figure 7.4	Temperature profile through SATMOD Callisto model	190
Figure 7.5	H ₂ O-MgSO ₄ temperature-composition diagram.	194
Figure 7.6	Temperature profile through ice V SATMOD Callisto model	201
Figure 7.7	Convective temperature profile through Callisto	205
Figure 7.8	Cutaway through final ice V SATMOD Callisto model	206

LIST OF TABLES

Table 4.1	Summary of orbital evolution end-points for satellites.	47
Table 4.2	Terms for orbital dynamics equations.	51
Table 4.3	Definitions of parameters used in orbital equations.	55
Table 4.4	Orbital parameters of the Galilean satellites.	64
Table 4.5	Estimates of Q_J and Q_i by various authors.	70
Table 4.6	Derived Q_J values for a range of initial Io orbital distances.	78
Table 4.7	a_i of Galilean satellites given Io $a_i = 2.5 R_J$, $Q_J = 1.15 \times 10^6$.	87
Table 4.8	a_i of Galilean satellites given Io $a_i = 3.85 R_J$, $Q_J = 1.22 \times 10^6$.	87
Table 4.9	a_i of Galilean satellites given Io $a_i = 5.0 R_J$, $Q_J = 1.73 \times 10^6$.	87
Table 4.10	Orbital evolution since formation (Io $a_i = 2.5 R_J$, $Q_J = 1.15 \times 10^6$).	89
Table 4.11	Orbital evolution since formation (Io $a_i = 3.85 R_J$, $Q_J = 1.22 \times 10^6$).	89
Table 4.12	Orbital evolution since formation (Io $a_i = 5.0 R_J$, $Q_J = 1.73 \times 10^6$).	89
Table 6.1	Io internal structure with Fe-FeS eutectic core (Anderson <i>et al.</i> , 1996a).	140
Table 6.2	Io internal structure with Fe core (Anderson <i>et al.</i> , 1996a).	140
Table 6.3	ONIONSKIN model of the internal structure of Io with an Fe-FeS eutectic core (density: 5150 kg m^{-3}).	142
Table 6.4	Io Fe-FeS core ONIONSKIN model results compared with target values for radius, mass, C/MR^2 , and density.	142
Table 6.5	ONIONSKIN model of the internal structure of Io with an Fe core (density: 8000 kg m^{-3}).	143
Table 6.6	Io Fe core ONIONSKIN model results compared with target values for radius, mass, C/MR^2 , and density.	143
Table 6.7	Europa internal structure according to Anderson <i>et al.</i> (1998b).	146
Table 6.8	ONIONSKIN model of the internal structure of Europa with an Fe-FeS core (density: 5150 kg m^{-3}).	150
Table 6.9	Europa Fe-FeS core ONIONSKIN model results compared with target values for radius, mass, C/MR^2 , and density.	150
Table 6.10	Ganymede Fe core model (Anderson <i>et al.</i> , 1996b).	154
Table 6.11	Ganymede Fe-FeS eutectic core model (Anderson <i>et al.</i> , 1996b).	155
Table 6.12	Ganymede Fe core models according to Schubert <i>et al.</i> (1996).	157
Table 6.13	Ganymede Fe-FeS core models according to Schubert <i>et al.</i> (1996).	157
Table 6.14	Heat flow parameters for Ganymede ($q = 0.010 \text{ W m}^{-2}$ at rock-ice	158

	interface) according to Schubert <i>et al.</i> (1996).	
Table 6.15	Heat flow of Ganymede (0.035 & 0.115 W m^{-2}) using Reynolds & Cassen (1979) heat flow models.	161
Table 6.16	Internal structure and corresponding heat flow of Ganymede with Earth-like radiogenics.	165
Table 6.17	Heat flow parameters for the Earth and Moon.	165
Table 6.18	ONIONSKIN model of the internal structure of Ganymede with a molten Fe-FeS outer core and solid Fe inner core.	167
Table 6.19	Ganymede Fe-FeS core ONIONSKIN model results compared with target values for radius, mass, C/MR^2 , and density.	167
Table 6.20	Callisto internal structure according to Anderson <i>et al.</i> (1998a).	169
Table 6.21	ONIONSKIN model of the internal structure of Callisto with a silicate core (density: 3500 kg m^{-3}).	171
Table 6.22	Callisto silicate core ONIONSKIN model results compared with target values for radius, mass, C/MR^2 , and density.	171
Table 7.1	Input SATMOD parameters to Callisto model.	181
Table 7.2	Callisto SATMOD output model.	184
Table 7.3	Parameters for ice melting curve equation.	189
Table 7.4	Ice V SATMOD parameters input.	199
Table 7.5	Ice V SATMOD Callisto output model.	200
Table 7.6	Conductive geothermal gradients through Callisto.	202
Table 7.7	Convective (realistic) geothermal gradients through Callisto.	203
Table A.1	Galilean satellite triaxial ellipsoid radii.	233
Table A.2	Bulk properties of the Galilean satellites and Jupiter.	233
Table A.3	Tidal and gravitational parameters of the Galilean satellites.	234
Table A.4	Some useful orbital and physical parameters of Jupiter and the Galilean satellites.	236
Table A.5	Known errors in the physical parameters of the Galilean satellites.	237
Table C.1	Chart showing commensurabilities for $R_i = 2.5 R_J$	254
Table C.2	Chart showing commensurabilities for $R_i = 3.85 R_J$	256
Table C.3	Chart showing commensurabilities for $R_i = 5 R_J$	258

Chapter 1 Introduction

The four major satellites of Jupiter - the largest planet in the Solar System, and fifth in order of distance from the sun - are known as the Galilean Satellites. The structural and orbital evolution of these satellites is a fascinating topic of study. The three innermost Galileans - Io, Europa, and Ganymede - are affected by tidal forces that have significantly altered their evolution. The outermost Galilean satellite - Callisto - lies beyond this tidal interplay but the Galileo mission has recently revealed it to hold many mysteries of its own that may help us to understand the evolution of large icy satellites in general. The jovian system is shown in Figure 1.1.

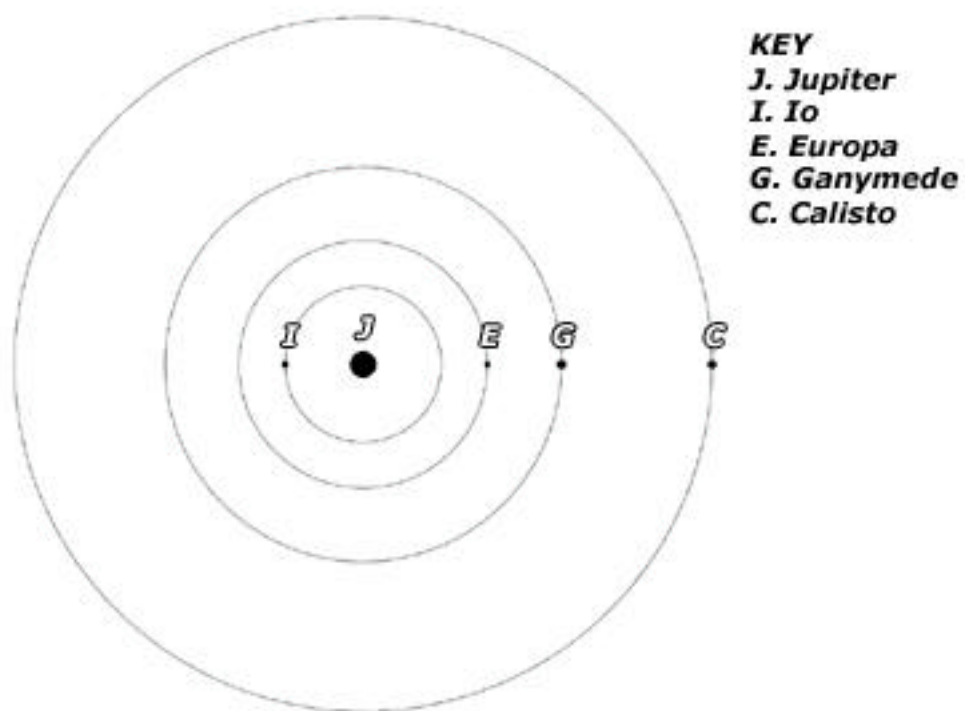


Figure 1.1: Diagram of the jovian system (orbits only to accurate scale)

The aim of this thesis is to bring together the most recent ideas on the orbital, thermal, and structural evolution of the Galilean satellites and expand on them given the most recent data from the Galileo spacecraft, in order to produce a coherent image of the current physical state of the Galilean satellites - in particular Ganymede and Callisto - and how they have evolved through time to reach that state. I focus more on the outer pair of Galileans because the Galileo mission has revealed that their evolution requires more scrutiny, and also because I find the geology and the mysteries held within their interiors more interesting than those of the inner pair!

Much interest has been focussed by the scientific community and the media on the surfaces of the inner pair of Galilean satellites, Io and Europa - the former because of its continuous spectacular volcanic activity, and the latter because of the possibilities of life in its oceans. A few authors have taken an interest in the interiors of Ganymede and Callisto and there is much work to do in understanding how these satellites have evolved and the reason why, given their broadly similar bulk properties (e.g. size and density), their surface geology and interiors are so different. In this thesis I critically review the earlier work and then expand on it in a number of areas.

I start in Chapter 2 by describing the geology of the Galileans - the surfaces of these satellites are varied and complex and provide many clues - some readily apparent, some not - as to what has been happening in the interiors of the bodies in question.

The magnetic fields of the Galileans are described in Chapter 3. The detection of magnetic fields around these satellites by Galileo was quite unexpected, and their presence and characteristics also provide important constraints on the satellites' internal structures.

The orbital evolution of the Galilean satellites is detailed in Chapter 4, based on a review of 'traditional' ideas - these ideas are examined and discussed and their limits tested and illustrated in a simple model.

Chapter 5 continues the discussion of orbital evolution and presents more recent ideas on the orbital evolution - focussing primarily on Ganymede - that greatly extend the 'traditional' scenario of Yoder and Peale (1981) discussed in the previous chapter.

Chapter 6 presents a preliminary model - ONIONSKIN - of the possible internal structures of the Galilean satellites constructed using gravity data from Galileo flybys. The interiors of the icy Galilean satellites are examined in particular detail, but the model can be applied in principle to any planetary body.

Chapter 7 presents SATMOD - a more accurate internal structure modelling program than those presented in the previous chapter, and applies this to Callisto.

Having produced internal structure models and discussed hypotheses for the orbital evolution of the Galilean satellites, I attempt to bring these ideas together in Chapter 8 in order to generate a consistent model for the satellites in which orbital and thermal evolution can produce the bodies we see today. A discussion of future work concludes the thesis, largely focussing on the need for a greater understanding of the processes involved in the orbital and thermal evolution of the satellites and of the world oceans hidden under the ice of the outer Galileans.

Chapter 2 The surface morphology of the Galilean satellites

The Voyager flybys in 1979 and the Galileo Orbiter between 1996 and 2003 have revealed a vast variety of surface morphologies on the Galilean satellites. It is clear that the surfaces have been - in some cases still are being - modified by a variety of tectonic, volcanic, and/or erosional processes.

The state of a planetary surface can provide important clues to the evolution of the interior of the body. A major constraint on any proposed scenarios regarding the orbital and thermal evolution of the Galilean satellites is their surface geology.

These bodies are not evolving in solitude, however: the inner three satellites have affected each other's evolution because of the interactions between their orbits around Jupiter. The current orbital configuration is known as the **Laplace resonance** and is unique in the Solar System. This resonance was first described by Laplace in 1829 but was more recently summarised by Goldreich (1965), and is explained in more detail in Chapter 4 of this thesis. These interactions result in tidal dissipation and heating in the bodies involved, which significantly affects their internal evolution and therefore their surface geology.

The surface appearance of the Galilean satellites is likely to be intimately coupled with their orbital evolution - internal heating is more likely to affect the surface morphology since the surfaces of the outer three Galileans are made of ices (Smith *et al.*, 1979), which have lower melting points than silicates. However, this is not certain - some or all of the features visible on the surface of a satellite may instead be

manifestations of processes independently occurring near the surface rather than caused by tidal dissipation (e.g. convective instability in a thick ice shell (McKinnon 1999)). However, it is likely that we can expect at least *some* expression of anomalous heating on the surfaces.

This chapter briefly summarises the range of surface morphologies of each satellite. It does not attempt to explain how specific features formed, however - it merely presents a general overview to help the reader understand the context in which the orbital and thermal evolution take place. The reader is encouraged to consult the papers referenced in this chapter if a more detailed examination of the surface morphologies is required.

2.1 The Geology of Io

Io is similar in size and bulk density to the Earth's Moon, but has an anomalously high (relative to any plausible radioactive source) heat flux ($1 - 3 \text{ W m}^{-2}$) (Nash *et al.*, 1986) and many active volcanoes on its silicate surface (Morabito *et al.*, 1979). Eruption temperatures are sometimes very high - up to 2000 K - implying the presence of ultrabasic silicate lavas (McEwen *et al.*, 1998). This activity is very energetic, with some eruptions sending umbrella-shaped plumes of material hundreds of kilometres above the surface! Furthermore, the volcanism must resurface large areas of the satellite very rapidly since no impact craters have been identified on its surface, implying that the surface is very young indeed. Io's surface is coloured in various shades of red, yellow, orange, brown and white, with black spots marking volcanic calderas tens of kilometres across. The colouration results from the many allotropes of sulphur, sulphur dioxide, and probably other sulphur compounds that contaminate the silicates erupted onto the surface (Nash *et al.*, 1986).

Figure 2.1 shows a global view of Io taken by the Galileo orbit in 1997, showing the general appearance of the satellite and some volcanic eruptions in progress. Figure 2.2 shows a Voyager 1 image of the active volcano Pele and illustrates the size of the eruption plume, visible over the limb of Io.

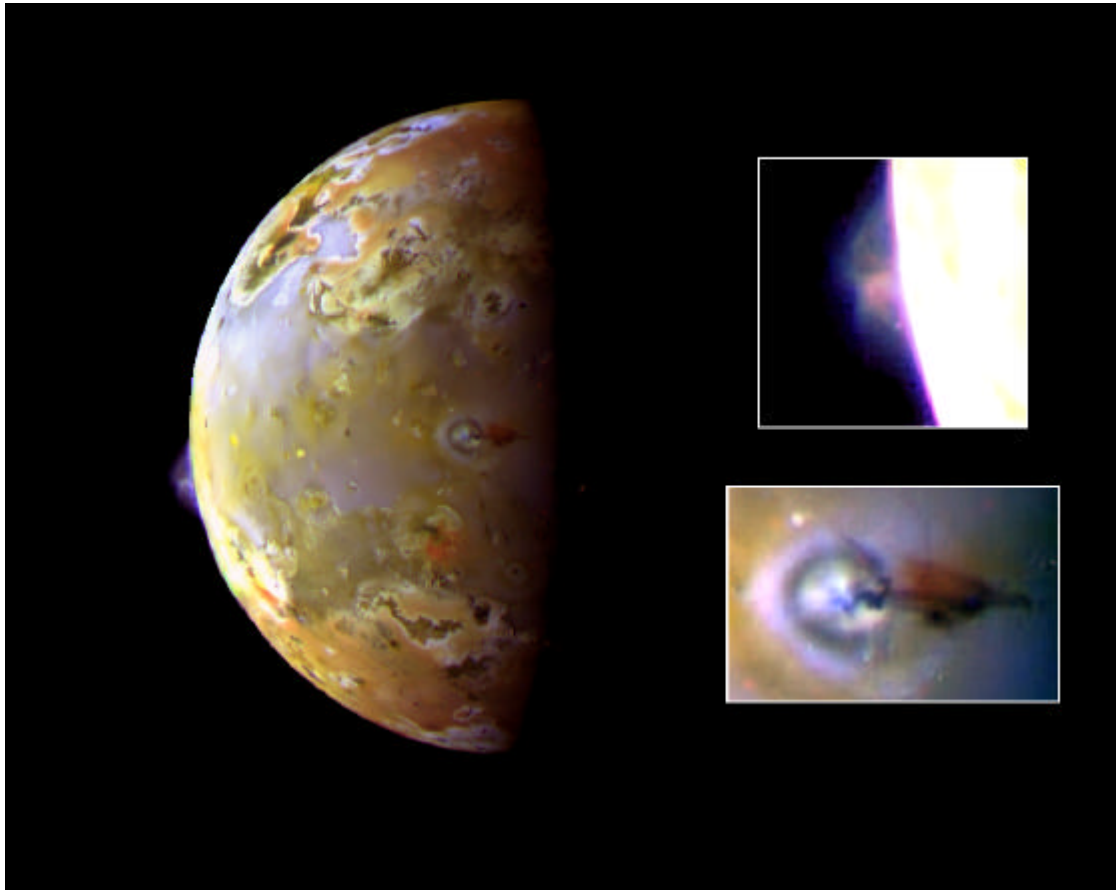


Figure 2.1: Global view of Io with insets. This colour image, acquired during Galileo's ninth orbit around Jupiter, shows two volcanic plumes on Io. One plume was captured on the bright limb or edge of the moon (see inset at upper right), erupting over a caldera named Pillan Patera. The plume seen by Galileo is 140 kilometres high. The second plume, seen near the terminator, erupts from a volcano known as Prometheus. The mushroom-shaped shadow of the 75 kilometre high airborne plume can be seen extending to the right of the eruption vent (see inset at lower right). The vent is near the centre of the bright and dark rings. Plumes on Io have a blue colour, so the plume shadow is reddish.

North is toward the top of the picture. This composite combines images taken with the green, violet and near infrared filters of the solid state imaging (CCD) system on the Galileo spacecraft. The images were obtained on June 28 1997, at a range of more than 600,000 kilometres. Image courtesy JPL/NASA.

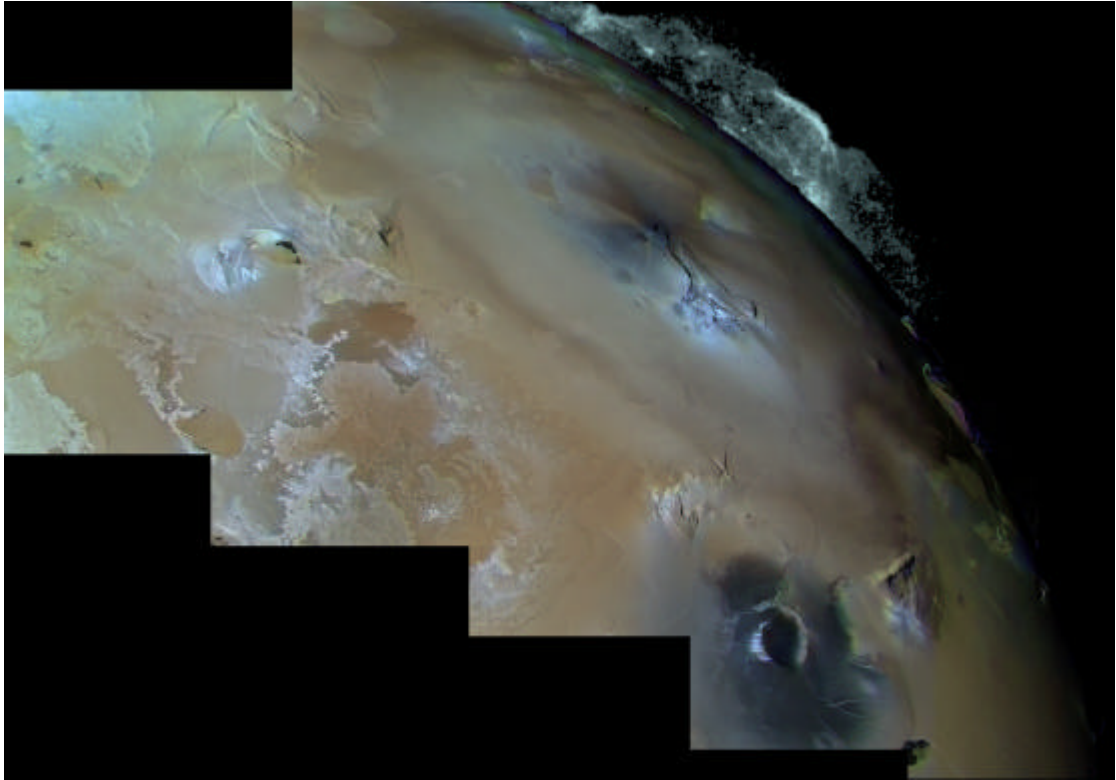


Figure 2.2: The eruption of Pele on Io. This eruption was observed by Voyager 1 in 1979. The umbrella-shaped volcanic plume has been enhanced for this image and can be seen over the edge of the limb - it rises 300 kilometres above the surface in an umbrella-like shape. The vent is a dark spot just north of the triangular-shaped plateau (right of centre). The hoof-shaped fallout deposit around Pele covers an area the size of Alaska. To the left, the surface is covered by colourful silicate lava flows rich in sulphur. North is to the top-left of the image. Image courtesy JPL/NASA.

2.2 The Geology of Europa

Although similar in size and bulk density to Io, Europa appears very different; its visible surface is composed largely of water ice rather than sulphurous silicates. Europa also has very few craters, again implying a young surface that has been recently active. Its surface is covered in a network of criss-crossing cracks and ridges that display a variety of morphologies. Some stretch for thousands of kilometres across the satellite (Smith *et al.*, 1979). In addition there are large brown and yellow patches tens to hundreds of kilometres across - Chaos terrain - that on closer examination are composed of blocks of ridged terrain separated by a hummocky ice matrix (Carr *et al.*, 1998). This matrix is usually what gives the terrain its dark appearance. The blocks or 'rafts' were apparently displaced and rotated from their original positions with in and around the edges of the Chaos (Spaun *et al.*, 1998).

Smaller (kilometre-scale) Chaos-like features also exist and can be found all over the satellite. These take the form of pits, spots, and domes ('*lenticulae*') that are usually brown or red in colour. Sometimes known as *micro-chaos*, lenticulae are irregularly-shaped pits, spots, and domes that punctuate the landscape. They can be up to 7 - 11 km across (Spaun *et al.*, 1999b), and usually form around larger chaos areas (Spaun *et al.*, 1999a). The depressions have broad floors, often containing hummocky, disrupted terrain - domes upwarp the existing terrain, and can contain hummocky terrain at their summits.

Figure 2.3 shows two Galileo global colour views of Europa, and Figures 2.4 and 2.5 illustrate examples of Europa's surface geology at high resolution.

The NIMS (Near Infrared Mapping Spectrometer) instrument (Carlson *et al.*, 1992), on the Galileo orbiter has shed some light on the nature of the red/yellow/brown material (Carlson *et al.*, 1996) - while the exact composition remains unclear, the observed spectra match those of hydrated magnesium and sodium salts, particularly those of magnesium sulphate and sodium carbonate (McCord *et al.*, 1998). An alternative possibility is that of sulphuric acid, or other radiolytic substances derived from decomposition of material by ionising radiation (Carlson *et al.*, 1999). Whatever the contaminants may be, they are concentrated in the Chaos regions, around lenticulae, and sometimes around the edges of the lineaments that cross the surface, and thus are likely to be endogenic in origin.

Figure 2.3 (next page): The subjovian and trailing hemispheres of Europa. On the left is a view of the subjovian hemisphere, and on the right is a view of the trailing hemisphere (this continues from the eastern limb of the subjovian view - the dark spot there is Callanish, also prominent in the west of the trailing hemisphere). The colour difference between the two hemispheres is real - the subjovian hemisphere appears to be more yellow than the trailing hemisphere. The subjovian hemisphere appears less distinct because the resolution of that image is approximately half that of the trailing hemisphere. The north pole is toward the top of the image. Image courtesy JPL/NASA.

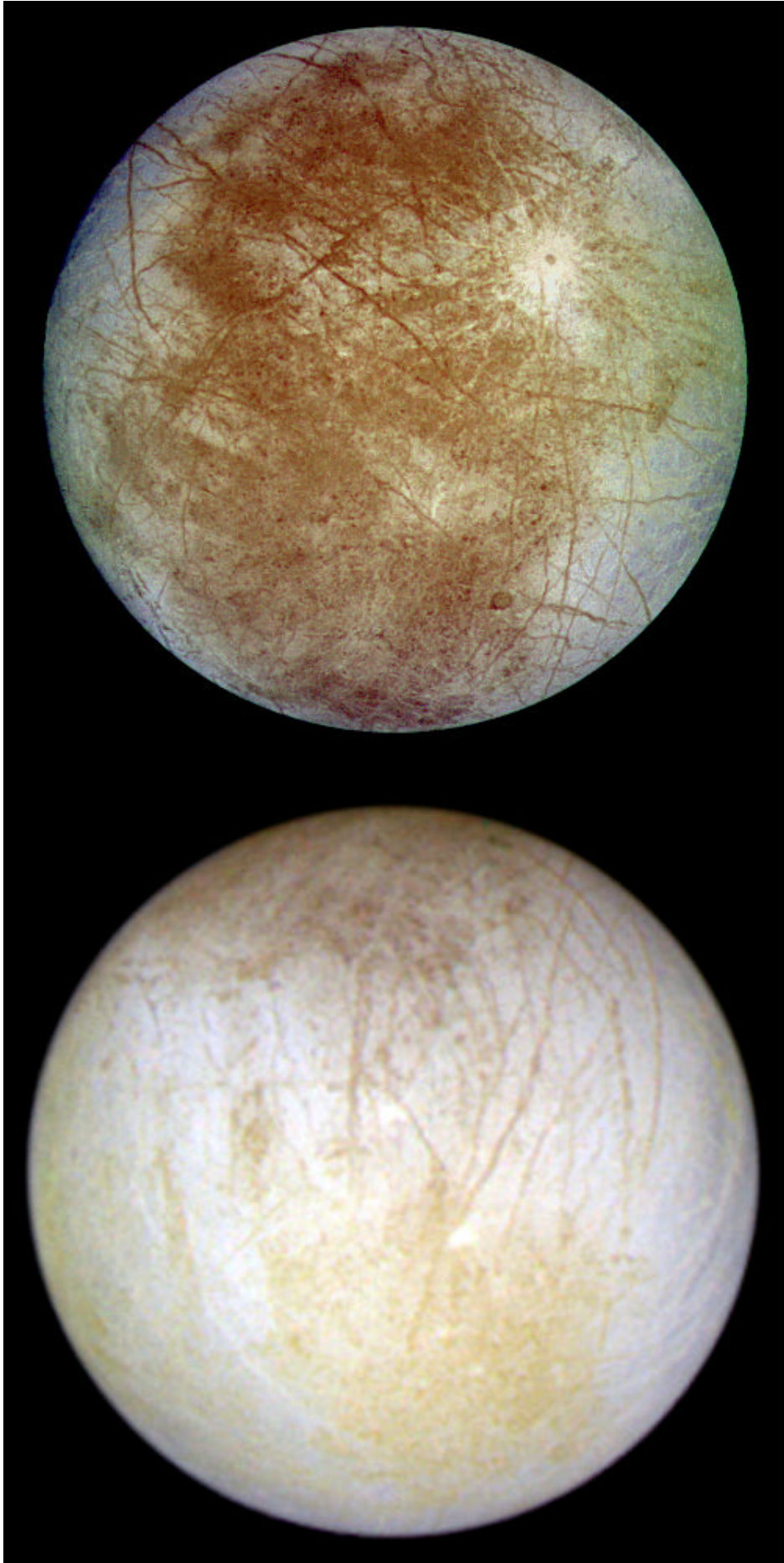


Figure 2.3: The subjovian and trailing hemispheres of Europa.

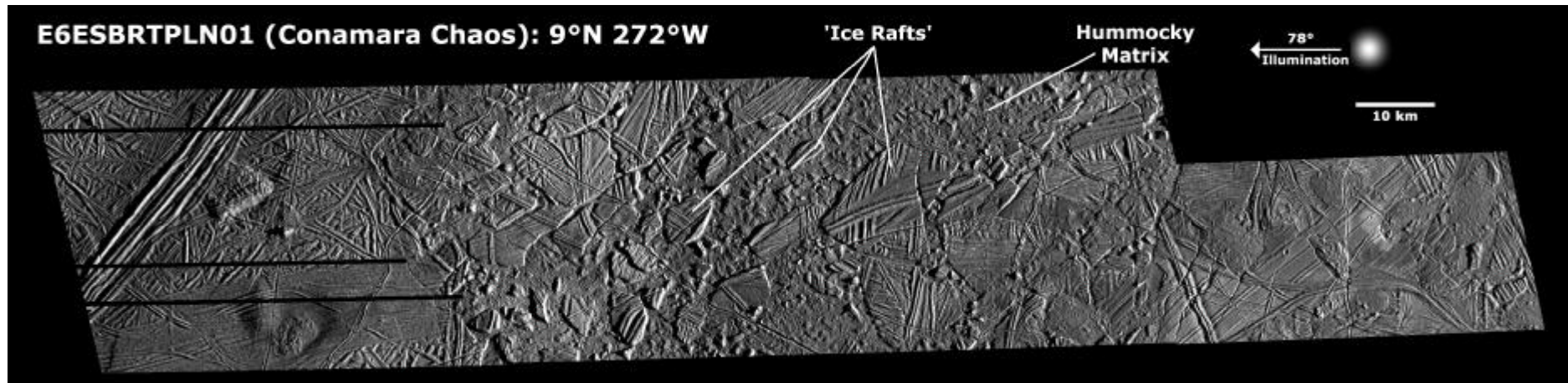


Figure 2.4: Conamara Chaos, Europa. This area of Europa is located at 9°N 272°W and was imaged at 53 m/pixel by the Galileo Orbiter in 1997. The sun is illuminating the image from the right (east) and is at an angle of 78° to the vertical - positive topography casts shadows to the left. This terrain appears to have been disrupted by activity from below. It consists of a large area of broken 'ice rafts' that have separated from the surrounding terrain and have been displaced away from the edge of the Chaos (Spaun *et al.*, 1998). The matrix between the rafts consists of hummocky icy terrain, and provides little clue as to the nature of the motion. Some suggest that Chaos Terrain forms as a result of warm ice diapirism penetrating the surface from the top of an ocean layer (e.g. Pappalardo *et al.*, 1998), while others, e.g. Greenberg *et al.* (1999), Thomson and Delaney (2001), suggest that this is an expression of oceanic material breaking through the icy crust of Europa. Image constructed by Constantine Thomas, using the USGS ISIS image processing system.

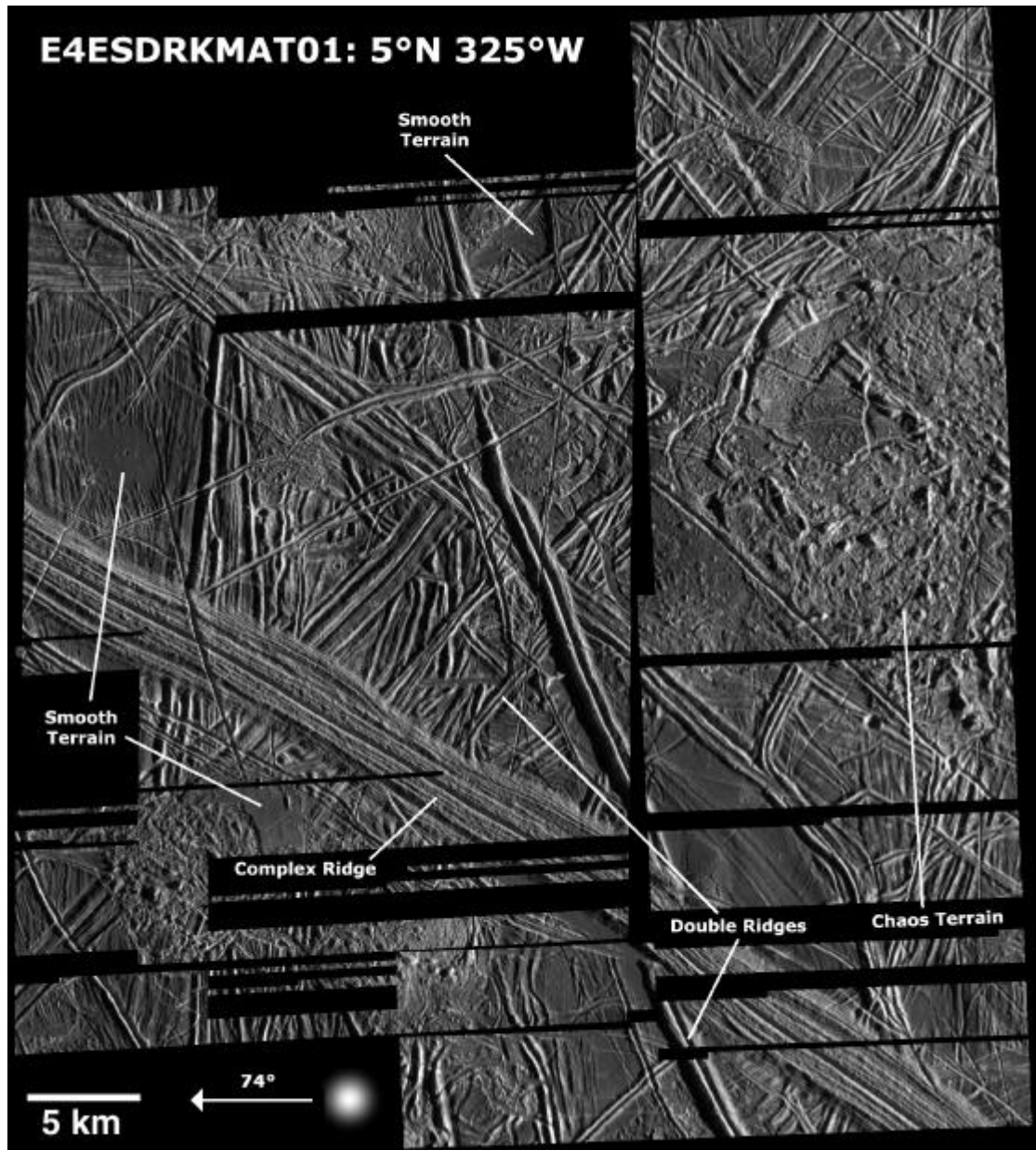


Figure 2.5: Chaos, Ridges, and Smooth Terrain on Europa. This area of Europa is located at 5°N 325°W and was imaged at 25 m/pixel by the Galileo Orbiter in 1996. The sun is illuminating the image from the right (east), at an angle of 74° to the vertical - positive topography casts shadows toward the left of the image. The area contains a variety of lineaments, ridges, and other tectonic features, and clearly illustrates the complexity of the small-scale surface geology of Europa. Several small Chaos regions are visible in the southwest and east of the area, and a small circular smooth area (the so-called ‘fishing pond’) is visible in the left of the image - this appears to be the result of cryovolcanic resurfacing (Thomas and Wilson, 2000 - see Appendix 2). Image constructed by Constantine Thomas, using the USGS ISIS image processing system.

2.3 The Geology of Ganymede

Ganymede is the largest satellite in the Solar System, approximately 700 km larger in radius than Io and Europa, and larger than the planet Mercury. Its bulk density is much less than that of the inner Galileans, indicating that its composition is nearer to a 50:50 mix of ice and silicates (McKinnon & Parmentier, 1986). Unlike the inner two Galilean satellites, however, impact craters are quite widespread on Ganymede's surface, but are more common in some terrain types than in others (Shoemaker *et al.*, 1982).

The surface of Ganymede is dark and light brown in colour, with whiter frost caps at the poles and bright white ejecta around some craters. The surface is divided into large polygonal blocks of dark, cratered 'Dark Terrain' separated by brighter swathes and bands of less cratered 'Bright Terrain' which has usually been tectonically modified to some extent (Parmentier *et al.*, 1982). Since the 'Dark Terrain' contains more craters, it must therefore be older than the 'Bright Terrain' (Strom *et al.*, 1981). Another indication of the greater age of the 'Dark Terrain' is the degraded appearance of some of the craters it contains, implying they have been eroded by micrometeorite impacts, mass wasting, or other processes for a longer period of time (Shoemaker *et al.*, 1982). A possible alternative erosion process unique to icy satellites is 'thermal segregation' (Spencer, 1987; Spencer *et al.*, 1998), where icy surface material sublimates as a result of local temperature variations and is re-deposited and concentrated in brighter, more reflective (and therefore cooler) regions on the surface. This acts to separate the surface material into brighter, colder, cleaner ice which is usually located on slopes

and topographic highs, and darker, warmer, dusty ‘lag’ deposits that are usually concentrated in topographic lows.

The ‘Bright Terrain’ usually contains sets of long ridges oriented in any direction (most are usually parallel to the sides of the lane) but some parts of it may be smooth in appearance. The origin of such features is clearly tectonic, given the linearity of the features. ‘Bright Terrain’ is always stratigraphically younger than the ‘Dark Terrain’ it cuts through - implying that it is the result of more recent tectonic activity - and sometimes individual belts or faults can be followed continuously for hundreds of kilometres. Galileo imaging revealed that there are several different morphologies of ‘Bright Terrain’, possibly implying different emplacement mechanisms. Recent stereo imaging using Galileo data (Schenk *et al.*, 2001) has indicated that smooth ‘Bright Terrain’ is generally found in topographically low terrain and may embay pre-existing terrain, implying a liquid origin for this material. Other types of ‘Bright Terrain’ appear to be tectonically disrupted ‘Dark Terrain’ (Head *et al.*, 1997) - while they do not appear to be made of physically different material, they appear brighter at low to medium resolutions because of the brighter, cleaner ice faces on the sub-pixel scale fault scarps. The difference between ‘Bright’ and ‘Dark’ Terrains therefore does not necessarily imply a difference in type of material.

Figure 2.6 shows a false-colour global view of the antiojovian hemisphere of Ganymede at 2 km/pixel resolution, as imaged by Voyager 2. Figure 2.7 shows a high resolution (150 m/pixel) greyscale Galileo mosaic of Nicholson Regio in the subjovian hemisphere, illustrating many different types of ‘Bright Terrain’.

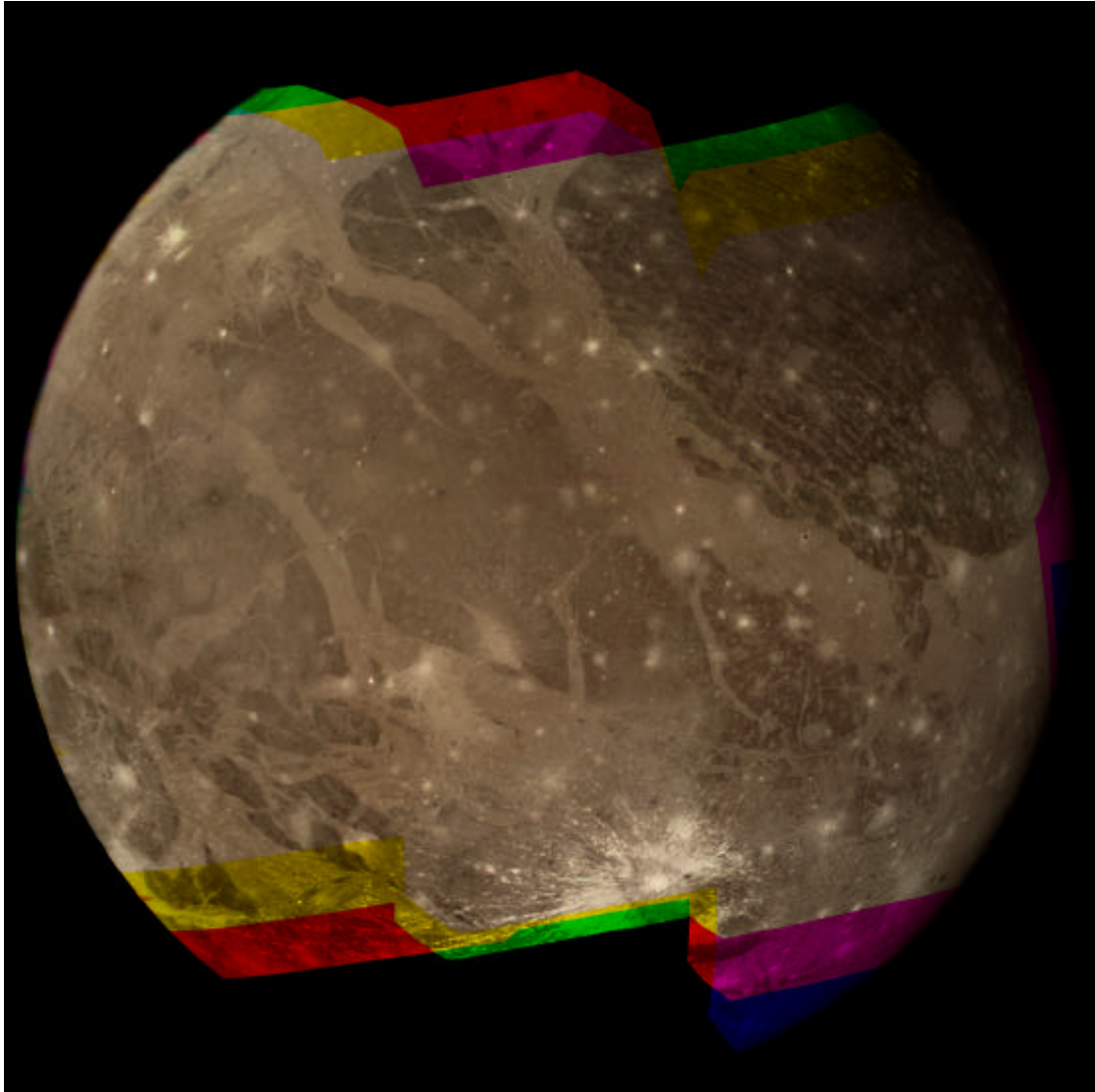


Figure 2.6: The antiojovian hemisphere of Ganymede. This is a false-colour (orange/blue/violet) global view of Ganymede at 2 km/pixel resolution, as imaged by Voyager 2. This is the side of Ganymede that always faces away from Jupiter; the antiojovian point at the centre of the hemisphere. Bands of 'Bright Terrain' are clearly visible, separating large areas of 'Dark Terrain'. North is toward the top of the image. The large area of Dark terrain in the north-east (top right) is Galileo Regio, and the large, bright crater in the southern hemisphere is Osiris. Image constructed by Constantine Thomas from Voyager 2 images, using the USGS ISIS image processing system and updated SPICE data supplied by Tim Colvin at RAND Corporation.

Figure 2.7 (next page): ‘Bright Terrain’ and ‘Dark Terrain’ in Nicholson Regio, Ganymede. This is a high resolution (150 m/pixel) greyscale mosaic of Nicholson Regio in the subjovian hemisphere. High resolution images from the seventh and 29th orbits of Galileo around Jupiter are overlaid onto a lower resolution Voyager 1 background image of the same area. This image illustrates many different types of ‘Bright Terrain’. The lane in the east of the Galileo coverage is Arbela Sulcus - this is topographically smoother than the other ‘Bright Terrain’ around it. Other lanes are more sinuous in appearance and appear to be belts of tectonised ‘Dark Terrain’. The ‘Dark Terrain’ itself also contains some irregular patches of higher albedo, of unknown origin. Image constructed by Constantine Thomas, using the USGS ISIS image processing system.

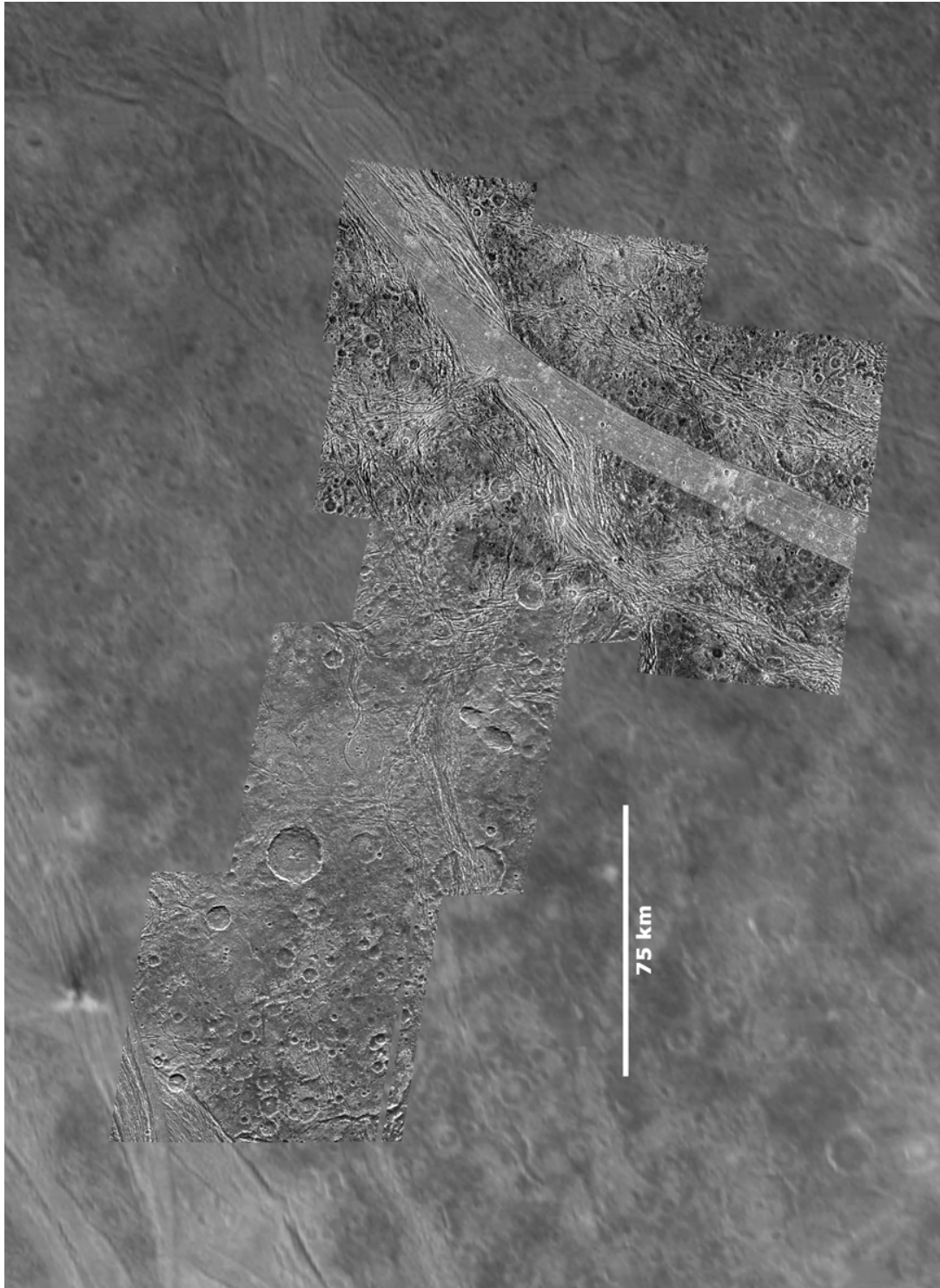


Figure 2.7: 'Bright Terrain' and 'Dark Terrain' in Nicholson Regio, Ganymede.

2.4 The Geology of Callisto

Callisto is slightly smaller than Ganymede and of similar bulk density. Unlike that of Ganymede, Callisto's surface is heavily cratered everywhere and there is little evidence for tectonic or cryovolcanic activity. Surface colouration ranges from light green-brown to dark brown, with white impact ejecta. Unlike Ganymede, Callisto has no brighter frost caps at the poles. The few large ringed features surrounded by scarps that break the monotony of the surface are interpreted to be relaxed impact basins (e.g. Valhalla and Asgard) (e.g. Melosh 1982, Schenk 1995). Galileo imaging revealed Callisto's surface in greater detail than was available from the Voyager missions, and revealed that smaller craters are not present in the quantity expected, implying that some process is destroying or covering them (Chapman *et al.*, 1997).

Galileo images reveal that much of the small-scale (10^2 metres scale and less) structure of the surface consists of dark, fine dusty material and bright, pointed triangular scarps that may be crater rims (Moore *et al.*, 1997). The nature of the process creating this dark 'dust' is uncertain, but it may be related to thermal segregation of ice (Spencer 1987).

Figure 2.8 shows a global colour mosaic of Callisto taken by Voyager 1 in 1979 - the inset shows a smaller global colour view of another hemisphere of Callisto taken by Galileo in May 2001. Figure 2.9 shows a high-resolution greyscale Galileo mosaic of an area of Callisto taken in 1996 - the image is of part of a chain of craters, and illustrates the dark dusty material that covers much of the surface.

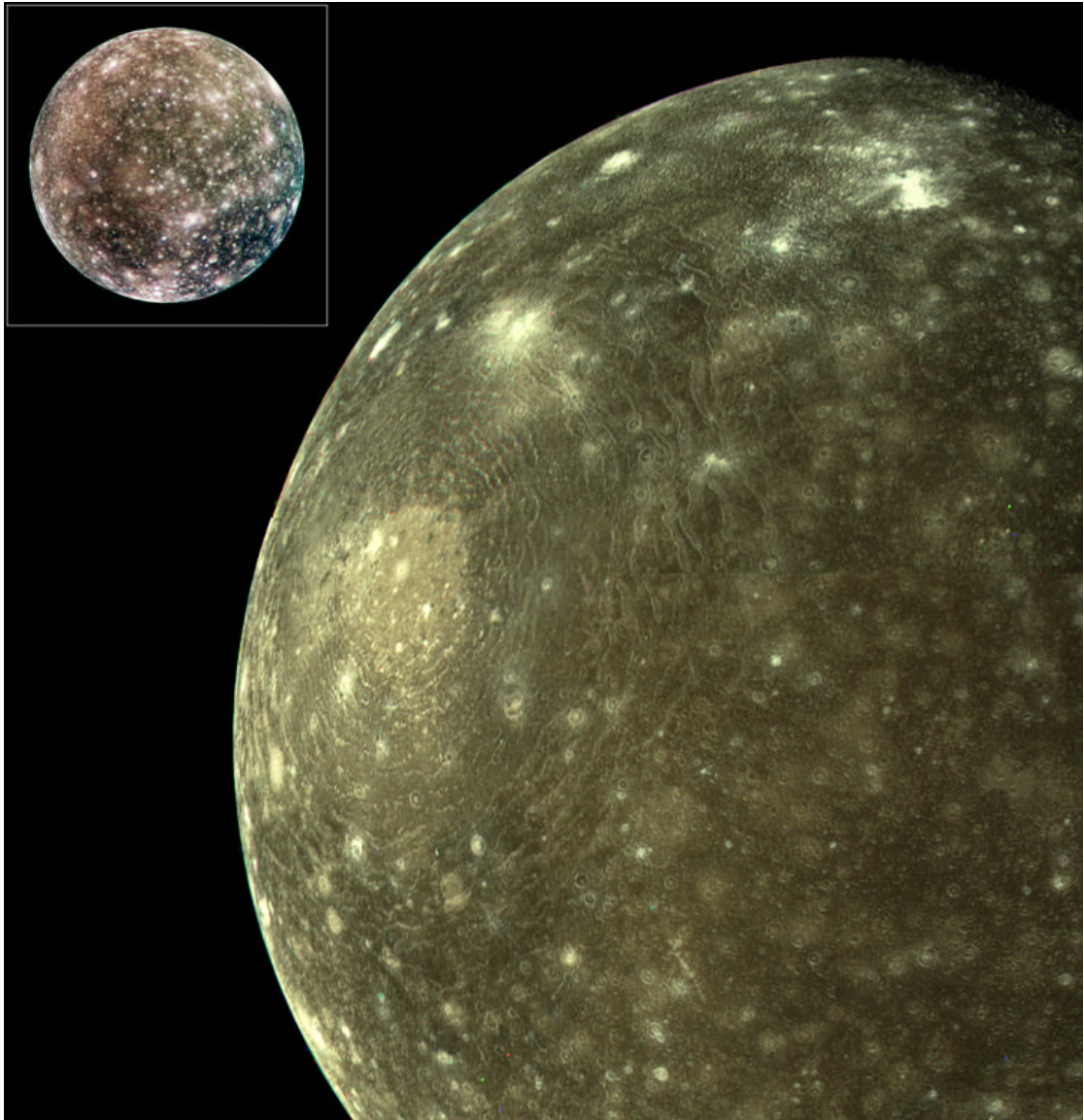


Figure 2.8: Global view of Callisto. This image shows a global (orange/blue/violet) false colour mosaic of Callisto taken by Voyager 1 in 1979 - the bright circular feature surrounded by scarps is the Valhalla impact basin. The inset shows a smaller global (true) colour view of another hemisphere of Callisto taken by Galileo in May 2001. The Galileo image shows that Callisto's surface is not a uniform colour - large regions are green, brown, and black in colour. The origin of the colour variation is unknown.

Figure 2.9 (next page): A crater chain on Callisto. This area of Callisto is located at 35°N 45°W and was imaged at 55 m/pixel by the Galileo Orbiter during its third orbit around Jupiter in 1996. The sun is illuminating the image from the left (west), at an angle of $\sim 74^\circ$ to the vertical. The image shows part of a chain of small craters near the Valhalla impact structure, and clearly shows the mantle of dark dusty material that covers much of the surface - note how this material is concentrated in topographic lows (e.g. the base of ridges). Image courtesy NASA/JPL.

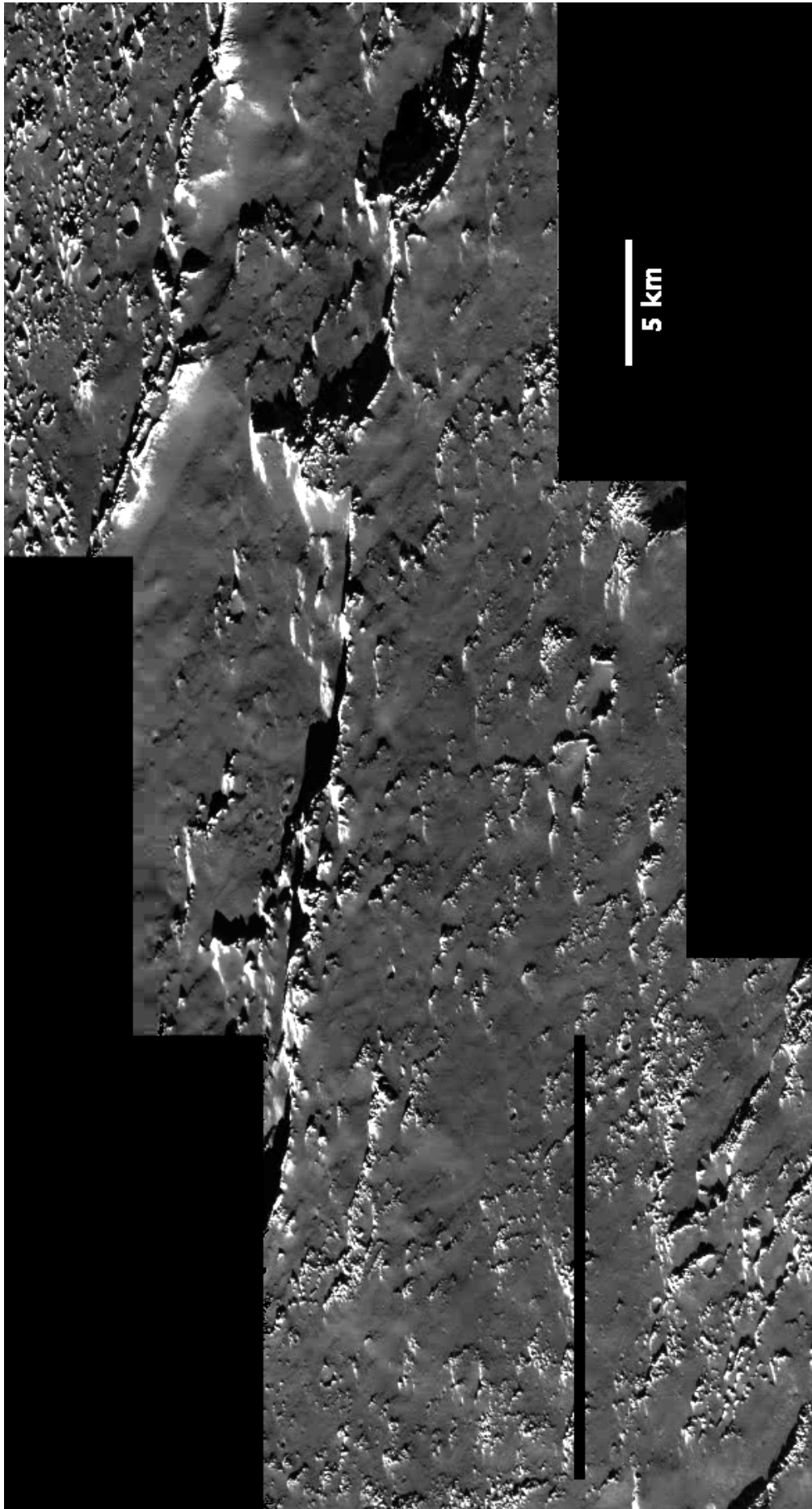


Figure 2.9: A crater chain on Callisto

2.5 Summary

A wide range of surface morphologies can be seen on the Galilean satellites - each body has its own unique features, many of which have no direct equivalent on the Earth. It is likely that at least some of the observed features can provide clues to the processes that have occurred in the interiors of the satellites, but clearly this is only one piece of the puzzle. In the next chapter, I discuss the magnetic fields of the satellites, and what insights can be gleaned regarding the internal structures of the Galilean satellites.

Chapter 3 The magnetic fields of the Galilean satellites

All the Galileans have been found to possess some form of magnetic field. The signatures of the fields detected by Galileo's magnetometer can be used to constrain the type of magnetic field generated in the satellite, which in turn can be used to infer the presence or absence of molten layers in the body. 'Internal dynamo' magnetic fields (such as that possessed by Earth) are those whose signatures can be modelled by dynamo convection in a circulating, molten, electrically conducting core (Stevenson, 1983). 'Induced' fields are those whose signatures indicate induction in an electrically conducting, near-surface layer by the powerful jovian magnetosphere (e.g. Sarson *et al.*, 1997).

In this chapter, I present a summary of current knowledge of the Galilean magnetospheres to provide context for later discussions. A more detailed examination of the subject can be found in the references cited here.

3.1 The nature and origin of planetary magnetic fields

(The issues discussed in this section refer heavily to the paper by Stevenson (1983) - I only give explicit references to other papers and to my own work here).

Magnetic fields can be generated in the interior of a body in several ways. Both internal dynamos and induced fields require the presence of a convecting, electrically conductive layer within the body. Dynamo fields (sometimes known as 'fixed dipoles') result from the magneto-hydrodynamic conversion of the mechanical energy

of convection (in an electrically conducting fluid) into electro-magnetic energy. Dynamo convection is either thermally or compositionally driven, and the magnetic field that results is self-sustaining so long as the magnetic Reynolds number (Re_m) exceeds a critical value of ~ 10 , where $Re_m = UL/\eta$ and U is a representative convective velocity, L is a representative length scale, and η is the magnetic diffusivity (defined as a measure of the tendency of a magnetic field to diffuse through a conducting medium at rest). Since the convective velocity and length scales are strongly related to the heat flow within a body, if they have been previously determined they can be used to estimate the size and type of the magnetic field created (Schubert *et al.*, 1996).

Dynamo generation in a planetary core initially occurs as a result of thermal convection. The heat generated through planetary accretion and radioactive decay manifests as a heat flux, which can be transported to the surface via convection and/or conduction, depending on the level of flux, as follows. If the heat flux from the planetary core (F_c) is greater than the conductive adiabatic cooling rate of the planetary interior ($F_{cond,ad}$), then the excess heat flow ($F_c - F_{cond,ad}$) will be transported convectively. Thus, core convection will occur in the core fluid when $F_c > F_{cond,ad}$. If the heat flux from the core is less than heat flux that can be transported by adiabatic conduction ($F_c < F_{cond,ad}$), then convection cannot occur since large-scale motions of fluid in the core are not possible in these conditions. Mantle convection also constrains the core heat flux, since the core cannot cool faster than the mantle.

Above a critical convective velocity (Schubert *et al.*, 1996), a magnetic field is generated as a direct result of the rapid motion of the electrically conducting fluid, which in turn creates a current which also drives the dynamo. In a purely thermally-driven system - such as that found in a hot, recently formed planet - this critical convective velocity can be related to the heat flux F_d (the total heat flux required to generate enough convection to drive a dynamo). If F_d is sufficiently greater than $F_{\text{cond,ad}}$ (i.e., if $F_d - F_{\text{cond,ad}}$ reaches a critical value), then a dynamo will be generated.

In a system where only heat flow is important, there are thus three possible ‘regimes’ under which the planetary interior can develop - which path the planet follows depends on its heat flux. The parameters used below are $F_{\text{cond,ad}}$, F_c , F_d (all defined above) and F (the actual heat flux of the planet):

1. If $F < F_{\text{cond,ad}}$, the heat flux is conductive, and there is insufficient energy to drive convection (thus no dynamo is present).
2. If $F_{\text{cond,ad}} < F < F_d$, the temperature profile is adiabatic, and convection can occur. This means that there is both conductive heat flow (through $F_{\text{cond,ad}}$) and convective heat flow ($F - F_{\text{cond,ad}}$). However, since $F_d - F_{\text{cond,ad}}$ is not large enough, no dynamo is generated (even though convection is present).
3. If $F > F_d$, convection occurs as described above, but $(F - F_{\text{cond,ad}})$ now exceeds $(F_d - F_{\text{cond,ad}})$, allowing the creation of a dynamo.

The difference between \mathbf{F}_d and $\mathbf{F}_{\text{cond,ad}}$ is known to be much smaller than $\mathbf{F}_{\text{cond,ad}}$ itself, so it is unlikely that Regime (2) would occur in a planet. Knowing this, it is most probable that any given world will initially satisfy either Regime (1) or (3) - i.e. there will either be no core convection at all, or there will be convection *and* a dynamo.

Compositional convection occurs when a solid inner core starts to crystallise from the molten outer core. This process usually begins at some point after the core heat flux has decreased to sufficiently low levels that thermal convection can either no longer be maintained at all, or the magnetic Reynolds number Re_m is less than the critical value required to maintain a dynamo. Compositional convection drives the dynamo until the core completely solidifies, at which point the magnetic field collapses. Thereafter, any magnetic field the body possesses will be a remanent one, preserved in solid magnetic minerals within the body at temperatures below their Curie points (Stevenson, 1983).

Induced fields are generated by the convective motions of an electrically conducting fluid that is affected by an imposed (usually external) magnetic field - note that the fluid must already be convecting for this to take place. This process is known as **magneto-convection** (Sarson et al., 1999) Magnetic fields generated in this manner are generally similar to or weaker in strength than the field inducing them at that location (Khurana *et al.*, 1998) - conversely, dynamo fields may be much stronger than the ambient field. Induced fields require no critical value for Re_m , so the scales of motion are not important in these situations. However, internal convection by itself is generally not sufficient to create a magnetic field - thus if the external field is removed, the induced field ceases to exist. The key difference between induced and

dynamo fields is that the former require an external field to exist and are similar in strength to it, whereas the latter do not and can be much stronger (Schubert *et al.*, 1998).

Finally, remanent magnetic fields may exist (Crary and Bagenal, 1998). These preserve magnetic fields that existed in the past in magnetic minerals that have cooled through their Curie temperature. While such minerals may be present in small quantities in the silicate crusts of the Galileans, any remanent magnetism is not likely to contribute significantly to detected global magnetic fields since such fields are usually very weak (c.f. Mars and the Moon). In the icy Galileans, the magnetised material would also be buried under hundreds of kilometres of ice which would significantly mask the signature (Kivelson *et al.*, 1999).

3.2 Potential mechanisms of magnetic field generation in the Galilean satellites

Given the above discussion, there are a number of processes that might generate magnetic fields in the Galilean satellites:

- 1) Dynamo action in a convecting metallic core. Convection can be thermal or compositional in nature. In the thermal case, the convection arises because the heat flux from the core is greater than the adiabatic cooling rate of the planetary interior. If the opposite is true, convection cannot be initiated or sustained in the core by thermal means alone. Additionally, if the mantle is kept warmer than the core (e.g. by tidal heating) then core convection will not occur. The details of this process are discussed in Section 3.1.

- 2) Magneto-convection in a convecting metallic core. The field is induced in the core by Jupiter's magnetic field. This might occur if the thermal regime is such that core convection is occurring, but at a rate below the critical Re_m required to generate an intrinsic dynamo and in the absence of compositional convection.
- 3) Magneto-convection in a convecting, electrically conducting layer near the surface. The most likely candidate for such material is water containing electrolytic salts, i.e., a brine. (e.g. Kivelson *et al.*, 1999)
- 4) Dynamo action in a convecting, electrically conducting layer near the surface.
- 5) Remanent magnetism in ferromagnetic material. The material must be below its Curie temperature for the remanent field to survive, and is therefore likely to be located near the surface, unless the deep interior is cool enough to preserve an ancient field. (e.g. Cray and Bagenal, 1998).

Of these processes, option (4) is physically unlikely because the nature of suitable near-surface layers (usually composed of briny water) makes it extremely difficult to spontaneously generate a magnetic field through internal convection processes alone. Such processes could generate a magnetic field through dynamo action if the layer were composed of molten metal, or some exotic superconductor; another possibility would be a high temperature, thermally convecting subsurface salty water layer, circulating vigorously enough to start a dynamo. The layer would have to be convecting so vigorously that the convection goes above the critical Raleigh number and generates an intrinsic field all on its own, without induction from the external

field. Such materials and situations are completely unrealistic in the context of an icy satellite.

The other options are physically plausible. While remanent magnetism (option #5) is possible, it is unlikely to be important in icy satellites given that the surface layers are not composed of magnetic material and any such material would be buried beneath a thick ice crust (e.g. Ganymede and Callisto) that would mask the magnetic signature. However, it could be plausible in the case of Io or Europa - Io does have a rocky surface that could potentially preserve an ancient magnetic field, and a remanent field could potentially be detected at or above the surface of Europa if the ice layer over the silicate interior is thin enough to allow it.

3.3 The observed magnetic fields of the Galilean satellites

3.3.1 The magnetic field of Io

Magnetic perturbations were detected in Io's vicinity during the extremely close flyby at Jupiter Orbit Insertion (JOI) in 1995, but the origin of these disturbances was unclear - high energy plasma and ion pickup near the satellite can produce magnetic perturbations, and these processes are particularly active around Io. As a result, the presence of any magnetic field originating from Io was very ambiguous. Assuming that a field did exist, Kivelson *et al.* (1996a) suggested that an intrinsic dipole model could fit the observations once the plasma effects were removed, but noted that the detected strength of the ionian magnetic field is similar to that of the ambient jovian field. This raises the possibility that the putative ionian field may actually be induced

by the jovian magnetosphere. Kivelson *et al.* also noted that their derived dipole moment is an overestimate, primarily because plasma effects and induction may add significantly to an existing intrinsic ionian dipole. Schubert *et al.* (1996) point out that tidal heating within Io may prevent an intrinsic dynamo from working, but this depends on where the tidal dissipation is occurring. Mantle heating would reduce the core heat flux which may prevent the convection currents from forming within it that could sustain a dynamo. Therefore it could be more likely for an ionian field to be generated by magneto-convection in a molten core, or at most by a weak dynamo within it.

The situation remained unclear until August 2001, when more accurate magnetometer data were collected during the I31 flyby. Analysis of these data now indicates that Io either has an extremely weak magnetic field or - more likely - does not have one at all (Kivelson *et al.*, 2001a, 2001b). The implication here is that Io almost certainly has a molten iron core given the vast amount of tidal dissipation it is suffering, but that stable thermal convection cells cannot form there - perhaps because the mantle is being heated more than the core - and thus no internal dynamo can be created. The magnetic perturbations detected during previous flybys are more likely to have resulted from the previously mentioned plasma and ion pickup phenomena found near Io

3.3.2 The magnetic field of Europa

For Europa, the magnetometer measurements up to orbit E14 (the 14th orbit of Galileo around Jupiter, which targeted Europa) cannot distinguish between an induced field and an intrinsic dynamo field model. While an intrinsic dynamo can be modelled, it requires considerable modification to fit the observations. As a result, Kivelson *et al.* (1999) favour an induced field model since it works well with no modification (differences between the model and reality can be closely correlated with the effects of plasma/ion pickup near Europa) and also since a fixed dipole (i.e. intrinsic dynamo field) for Europa would have to be tilted at 135° to its spin axis to produce the measured results. Two other bodies in the solar system possess a large magnetic dipole tilt angle - Uranus and Neptune - but these arise because the fields are generated in a poorly conducting icy shell around their cores (Connerney, 1993). Another important consideration is that the presence of an ambient magnetic field - that of Jupiter - provides a preferred direction for any magnetic field generated in a satellite within it, as does the satellite's spin vector (Schubert *et al.*, 1996), which also makes it more likely that the european magnetic field is one that is induced by the jovian field in a near-surface conducting layer within the satellite.

3.3.2.1 Discussion

I am intrigued by the fact that Europa lacks a magnetic signature unambiguously typical of a core dynamo, since models derived from Galileo gravity data (Anderson *et al.*, 1998b) suggest that Europa has differentiated into a metallic core (possibly up to half the satellite's radius in size) surrounded by a silicate mantle and ice/water (these models are discussed in Chapter 6). Magnetic field models (Khurana *et al.*, 1998) suggest that Europa's magnetic field originates near the surface, most likely by induction in a layer of electrolyte-rich water. They rule out induction in a metallic core since the signature produced would be much smaller than that observed. However, if there is induction occurring in a near-surface conducting layer and there is also a metallic core, then it becomes necessary to explain why no intrinsic magnetic signature is being picked up from the core.

One possibility is that a weak field *is* being induced in the core, but it is being swamped by the signature of the induced field produced near the surface. Alternatively, conditions in the core may be such that a magnetic field cannot be created by any means at all - either because the core has frozen solid, or it is molten but not convecting, or it is molten but convecting at rates below the critical Re_m . However, if the outer parts of the core are molten, a field should still be induced by magneto-convection since this does not require any critical convection velocities and the Jovian magnetic field is strong enough around Europa to initiate the process. Furthermore, compositional convection is unlikely to be occurring in Europa, otherwise an internal dynamo would be evident. Therefore the 'molten and convecting core' option can be ruled out. This leaves four options:

a) A core is present and is molten and not convecting at all *and is stable against convection*. This is usually only possible if the satellite's thermal regime is intermediate between thermal and compositional convection (similar to Venus - Stevenson, 1983). Tidal heating in the mantle or core might prevent convection from occurring within the core and thus prevent magneto-convection from taking place.

One possible variation on this theme is that the core itself *could* still be molten if it was composed of low-melting point material such as iron sulphide (FeS) - which coincidentally is not ferromagnetic and thus cannot support a magnetic field (even if thermal or compositional convection was occurring). This variation would not require an external heat source today - the core could be cooling from formation or (more likely) an earlier episode of tidal dissipation. The core would also be at a lower temperature than one containing Fe, since FeS has a lower melting point. However, it is unclear that a molten 'cool' core could exist inside Europa - the chemistry of Europa's interior is largely unknown.

b) A core is not present at all and Europa is only partly differentiated. Anderson *et al.* (1998b) do not hold this possibility to be likely, since a model of Europa that lacks a metallic core would require that Europa's interior is enriched in metallic phases relative to Io. They reject this hypothesis because of Europa's greater distance from Jupiter than Io - the proportion of metallic components in the protojovian nebula would decrease with distance from the primary, so some very unusual formation mechanism would be required to concentrate metals more at Europa's orbit than at Io's.

c) The core is actually molten, and is also convecting enough to generate an intrinsic dynamo field. However, the generated field is not strong enough to be detected over the field generated by magneto-convection in a water layer near the surface.

d) A core is present, but it has solidified completely. This has the implication that surface geological activity is caused entirely by the presence of the implied near-surface saltwater ocean layer (which can only exist as a result of tidal heating) and/or solid-state convection in the ice.

The magnetic data indicate that Europa possesses an induced magnetic field generated by convection currents in a near-surface electrolyte-rich convecting water layer. Option (b) has already been discounted for cosmochemical reasons. Gravity data indicate that Europa has differentiated to produce a metallic core, but the magnetic signature of an internal dynamo field would be quite distinctive. The lack of such a signature therefore implies that conditions in the core are unsuitable for dynamo action - this rules out option (c). Therefore, out of the options presented above, only (a) and (d) seem likely.

This results in two very different scenarios describing the interior structure of Europa. Option (a) suggests that the satellite is fully differentiated, with either a molten, non-magnetic core or one that is not convecting because an anomalous (tidal?) heat source is still keeping the mantle warmer than the core. The heat from within the mantle would melt the ice above the silicate crust, thus creating a near-surface water layer in which a magnetic field can be induced.

Alternatively, if option (d) holds, Europa fully differentiated (possibly not long after its formation) and its core then cooled solid. Comparatively recent tidal dissipation was not sufficient to melt the core again, but was sufficient to melt some of the ice near the surface and create the saltwater layer in which the magnetic field is induced.

It is difficult to choose between these two options, because there are insufficient data to make the decision. While it is not clear that the silicate body of Europa is completely ‘geologically dead’ as a result of a frozen core, it is more likely to be so if that is the case - therefore it is quite probable that the observed surface geology of Europa may be exclusively the result of tidal heating and flexing within the ice/water shell above the silicate surface. On the other hand, a molten core increases the possibility of volcanic, tectonic and hydrothermal activity on the silicate seafloor, an option that is attractive to those who propose indigenous euroman life around such thermal hotspots on the seafloor. More work needs to be done to assess the likelihood of either of these options.

3.3.3 The magnetic field of Ganymede

The magnetic field detected at Ganymede has the signature of a strong internal dynamo generated in a convecting, molten iron core (Schubert *et al.*, 1998, Kivelson *et al.*, 1996b). Given the existence of a molten core, it seemed possible that Ganymede may also have a salt-water layer near the surface in which magneto-convection could occur and contribute to the existing magnetic field. The existence of the ocean-generated component was confirmed by closer examination of the magnetometer data (Kivelson *et al.*, 2001a, 2001b, 2002). The strength of the dipole moment is calculated to be $719 \text{ nT} \pm 2 \text{ nT}$, tilted by $176^\circ \pm 1^\circ$ from Ganymede's spin axis (Kivelson *et al.*, 2002) - the field is a combination of a permanent dipole and an induced component. Ganymede is the only solid body in the Solar System known to possess an internally generated dynamo field other than the Earth. It is not clear whether the core convection is thermal or compositional in nature, and Kivelson *et al.* (2002) suggest that it may even be possible that Ganymede's internal field is generated by magnetoconvection in its metallic core (Option 2 in Section 3.2 of this thesis).

Given that Ganymede is not currently affected by a tremendous external heat source (e.g. tidal heating), I suggest that it is more likely that an inner core is in the process of solidifying and therefore that the currents are compositional. The core could remain molten today if it contained a significant amount of iron sulphide (though not 100% FeS, since it would not be able to form a magnetic field at all). The larger size of Ganymede also results in less efficient heat loss than in a smaller body - this would allow its interior to stay molten for longer than Europa even if it contained the same amount of radioactive material.

3.3.4 The magnetic field of Callisto

During the C3 and C9 Callisto fly-bys, Galileo detected magnetic perturbations near Callisto. Since Callisto lies outside the parts of the jovian magnetic field containing energetic plasma that could confuse magnetometer readings, the perturbations near the satellite could be easily recognised as being the result of induction by the jovian field, and indeed closely fit the induced dipole models of Kivelson *et al.* (1999). The magnetic perturbations indicate that a field could be generated in Callisto within a liquid water layer beneath its surface - this came as a surprise since there are no endogenic features on Callisto's surface that would indicate the presence of an ocean today, and Callisto was not previously expected to remain warm enough internally to allow such an ocean to exist. As a result, our assumptions about Callisto's interior require a great deal of alteration to explain the observations, but it remains clear that the only mechanism to explain the field is induction in a briny ocean layer at least 100 km below the surface (Khurana *et al.*, 1998). No internal dynamo field was detected at Callisto - internal structure models indicate that Callisto has no metallic core in which to generate such fields (Anderson *et al.*, 1998a, 2001).

3.4 Conclusion

Galileo magnetometer data for Europa, Ganymede and Callisto all require magneto-convection within salty ocean layers of appreciable thickness within a few hundred kilometres of the icy surface to explain the presence of the magnetic fields detected (Khurana *et al.*, 1998). The presence of a saltwater layer on Callisto came as a great surprise, but a possible explanation by Ruiz (2001) suggests that it exists because the rheology of the ice shell above it prevents convective heat transport through the shell and heat conduction has not been sufficient to allow all of the ocean to freeze. Magnetometer data for Ganymede indicate that it possesses an internally generated permanent dipole as well as that induced in a near-surface saltwater layer. Data indicate that Io does not possess any significant magnetic field.

Chapter 4 The Orbital Dynamics of the Galilean Satellites

4.1 The orbital evolution of natural satellites

4.1.1 Orbital evolution in two-body systems

A complete review of general orbital dynamics processes is beyond the scope of this thesis - the summary presented in this section is based on the reviews of the subject written by Burns (1977, 1986), except where otherwise specified.

A system containing one planet and one (less massive) satellite - and no external influences - is a classic example of a two-body system. The gravitational field of one body distorts the shape of the other, creating equatorial bulges in both that would ideally be symmetric about the line of centres connecting the planet and satellite if they were made from material that could respond instantly to the stresses. This situation is shown in Figure 4.1.

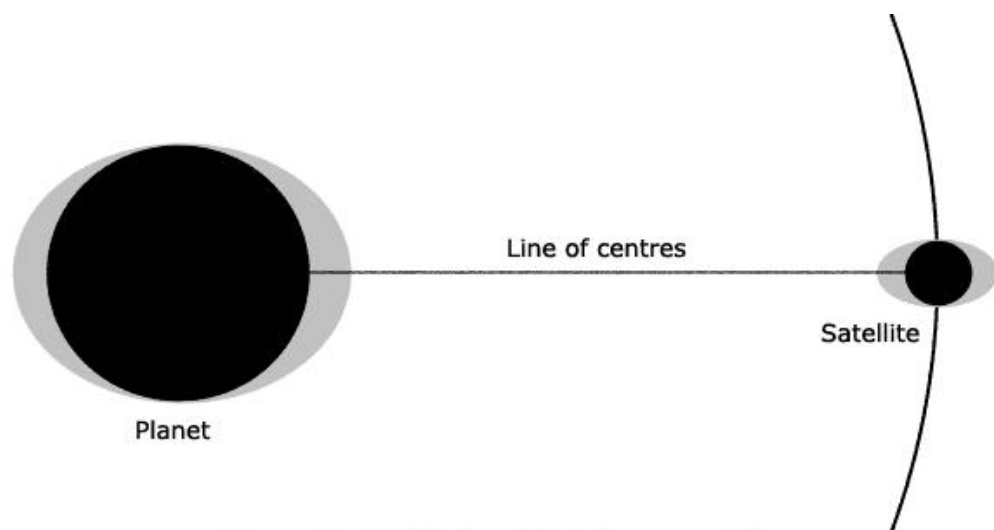


Figure 4.1: Tidal bulge, frictionless material

In real systems, energy is lost in straining the material that comprises the bodies, and this delays the response to the stress. As a result, the bulges will become misaligned relative to the body causing them if the rotational angular velocity of the planet (Ω) differs from the orbital angular velocity (n - also known as *mean motion*) of the satellite. If the planet rotates faster than the satellite orbits around it ($\Omega > n$) then the bulge raised on the planet leads ahead of the satellite. If the opposite is true ($\Omega < n$), then the bulge raised on the planet lags behind the satellite. Only when the two are equal ($\Omega = n$) - when synchronous orbit is achieved - will the bulges remain aligned. This is shown graphically in Figure 4.2.

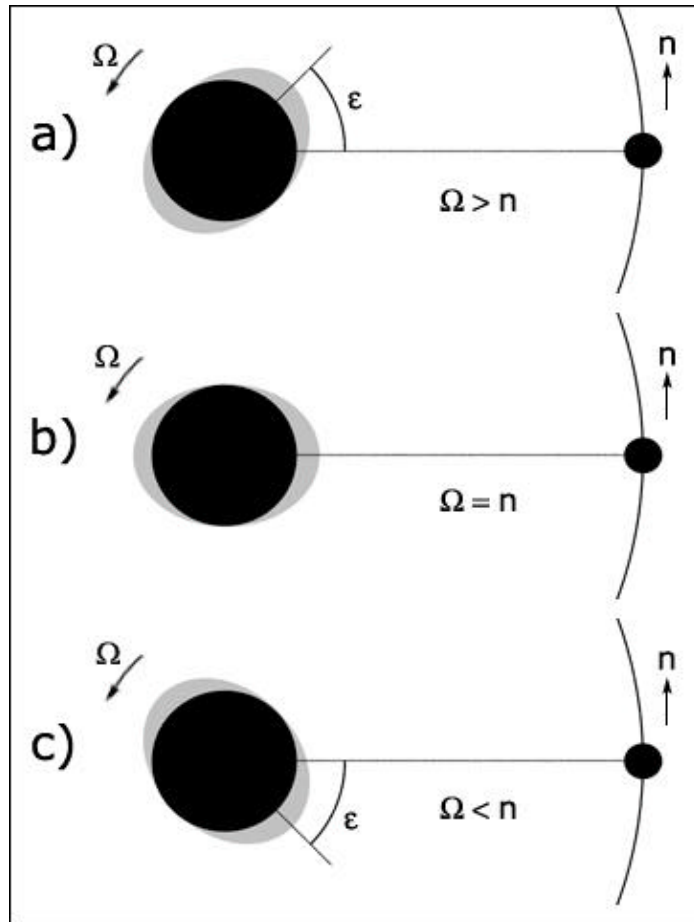


Figure 4.2: Planetary Tides (satellite tides not shown). (a) if the planet rotates faster than the satellite orbits ($\Omega > n$), the tidal bulge leads the satellite by the lag angle ϵ , expanding the satellite orbit and slowing planetary rotation. (b) if the planetary rotation period is the same as the satellite orbital period ($\Omega = n$) or the planet is made from material that can respond instantly to the stresses, the bulge remains symmetrical around the line of centres. No tidal dissipation occurs. (c) if the planet rotates more slowly than the satellite orbits ($\Omega < n$), the tidal bulge lags behind the satellite by the lag angle ϵ , reducing the satellite orbital distance and increasing planetary rotation.

This ‘tidal lag’ can have a number of possible effects, depending on the configuration of the system. Whether the bulge leads or lags, a torque is produced on the planet by the misaligned bulge. If ($W > n$), the planet’s rotation is slowed by this torque - the energy taken out of the rotation is partly dissipated as frictional heating in the planet (“tidal dissipation”). However, because angular momentum must be conserved in the system, the orbital momentum of the satellite is increased when the planet’s rotation is slowed and the satellite is pulled forward in its orbit, moving away from the planet in the process. This increases the longest radius of the satellite’s elliptical orbit (the *semi-major axis* (a)).

The ($W > n$) configuration is by far the most common in the Solar System - and is certainly true for the Galileans, which all take longer than Jupiter’s 9.9 hours rotational period to orbit the planet; as a result, the following discussion assumes that ($W > n$). It should be noted that this applies to both the planet and the satellite - if the satellite rotates around its axis, the rotation will be rapidly slowed down until its rotational period is the same as its orbital period. This process is known as “tidal despinning”, and is completed more rapidly for satellites than planets because the former are less massive than the body they orbit.

Since this process is occurring on both the planet and the satellite, the orbital distance between the two increases rapidly if both have non-synchronous rotation periods. When the satellite rotation becomes synchronous, the planetary rotation slows down less rapidly, pushing the satellite outwards, and the satellite rotation slows ‘in synch’ with the orbital period, thus maintaining the synchronous rotation. Thus, tidal dissipation occurs in the satellite as well as in the planet, and is again often greater in the satellite because it is less massive than its primary.

We have not yet considered the eccentricity and inclination of the satellite orbit. All astronomical orbits are non-circular to some extent, even if only by a very small amount. Since the semi-major axis of the orbit is increased by the transfer of angular momentum from planetary rotation to the satellite orbit, and orbital theory dictates that the pericentre distance (determined by $a(1-e)$) must remain constant, the eccentricity must increase as this process occurs.

This is not the whole story, however - another process is at work that complicates the situation. Since the orbit is eccentric, tidal forces are strongest when a satellite is closest to the primary (at the pericentre of the orbit) and weakest when it is furthest from the primary (at the apocentre). The eccentricity of the orbit generated two types of tide within the satellite - 'radial tides' and 'librational tides'. Radial tides occur as the distance between the two bodies changes over the course of the orbit - when the satellite is closest to the planet, the tidal bulge is larger than when it is furthest from the planet. The continual flexing that results dissipates more energy in the body of satellite. Librational tides also occur because the satellite's orbital angular velocity changes over the eccentric orbit according to Kepler's laws of motion - the velocity is greatest at pericentre and smallest at apocentre. While a synchronously-locked satellite's tidal bulge generally points toward the planet during its orbit, the inelasticity of the satellite prevents the bulge from responding instantly to the changing velocities near pericentre and apocentre. This causes the bulge to sometimes lag behind or lead ahead of the planet-satellite line over the course of an orbit, causing more dissipation within the body of the satellite as the bulge rocks back and forth. While the orbital angular momentum does not change as a result of this dissipation, the eccentricity of the orbit is reduced, thus circularising the orbit. This

reduction is greater than the increase caused by the planetary tides described earlier, so the satellite orbit will circularise with time.

The inclination of a satellite orbit relative to the planetary rotational equator also evolves over time. The primary's rotation carries the tidal bulge out of the satellite's orbital plane, producing a torque that acts to align the planet's equator with the satellite's orbit. As a result, inclination decreases with time.

The above summary applies only to a satellite that has an orbital period longer than the rotation period of its primary, and that is also rotating in the same (prograde) direction as the planet (we shall return to this latter point soon) - this is the case for all prograde satellites that orbit beyond the synchronous orbit where ($\mathbf{W} = n$). If the satellite's orbital period is shorter than the primary's rotational period and the satellite is in a prograde orbit, the evolution is exactly opposite to that described above - this would be the case for a prograde satellite orbiting within the synchronous orbit.

Some satellites (most famously Phobos around Mars, and Triton around Neptune) orbit their primary in the opposite (retrograde) direction to the majority. In these cases, the evolution is the reverse of what one would expect for a prograde satellite. Retrograde satellites will evolve toward the synchronous orbit ($\mathbf{W} = n$), whether they start within or beyond it - however, this state is not necessarily stable. Prograde satellites forming outside the radius where $\mathbf{W} = n$ will evolve outward toward a synchronous state where the rotational period of the satellite, the increased orbital period of the satellite, and the extended rotational period of the planet are all the same (this is known as “total tidal

despinning”, or “sync-locking”). Prograde satellites forming within the synchronous orbit ($W = n$) will spiral toward the planet, eventually either hitting it or breaking up.

Eventually, one of three end goals to orbital evolution will occur: either (1) the planetary rotational period and satellite orbital period will converge, or (2) the satellite escapes the planet’s gravitational sphere of influence and becomes a solar-orbiting body, or (3) the satellite impacts onto the planetary surface/is broken up by tides. The outcome depends on the relative masses of the bodies involved, and it should be noted that it is entirely possible that none of these results will occur within the complete lifespan of the solar system.

However, if tides from outside the planet-satellite system are involved (usually tides caused by the sun on the planet), there may still be one final act to play. Although the planet-satellite system reaches its equilibrium as describe in option (1) above, the solar tides still act to slow down the planet’s rotation. This will eventually cause the synchronous orbit to move further outward from the planet. Once this happens, the satellite’s orbit will start evolving as it should within the synchronous orbit - by approaching the planet, and speeding up the planetary rotation until it impacts on the surface or breaks up around it because of tidal stresses. However, the timescale for this may be much longer than the age of the planetary system.

The orbital and rotational evolution of prograde and retrograde satellites is summarised in Table 4.1.

Table 4.1: Summary of orbital evolution end-points for satellites

<u>PROGRADE SATELLITES</u>	
Satellite orbits beyond synchronous orbit ($W > n$)	Planet Rotation slows down (W decreases) Orbital Period slows down (n decreases) Orbital distance (a) increases Eccentricity decreases Inclination decreases ORBIT TENDS TO OUTER SYNCHRONOUS STATE
Satellite orbits within synchronous orbit ($W < n$)	Planet rotation speeds up (W increases) Orbital period speeds up (n increases) Orbital distance (a) decreases Eccentricity increases if within 2/3 synchronous orbit Inclination increases if within 1/2 of synchronous orbit distance ORBIT DECAYS TO PLANET SURFACE
<u>RETROGRADE SATELLITES</u>	
Satellite orbits beyond synchronous orbit ($W > n$)	Planet Rotation speeds up (W increases) Orbital Period speeds up (n increases) Orbital distance (a) decreases Eccentricity decreases Inclination decreases ORBIT TENDS TO INNER SYNCHRONOUS ORBIT
Satellite orbits within synchronous orbit ($W < n$)	Planet rotation speeds up (W decreases) Orbital period speeds up (n decreases) Orbital distance (a) increases Eccentricity increases if within 2/3 synchronous orbit Inclination increases if within 1/2 of synchronous orbit ORBIT TENDS TO INNER SYNCHRONOUS ORBIT

Note that the eccentricity and inclination of retrograde satellites evolve in the same way as the prograde equivalent, since these are dependent on the tidal dissipation within the satellite, not the planet.

4.1.2 Orbital evolution in multi-body systems

While this evolution generally applies to all systems, there are complications when multiple satellites are considered. The most important consequence is the formation of **orbit-orbit resonances**, which arise because the orbits of the satellites can be gravitationally perturbed by each other as well as by the primary planet. A resonance generally occurs when the periodic behaviour of a dynamical system is matched by some periodic driving force (Greenberg 1977). Orbit-orbit resonances occur when small-integer ratios (commensurabilities) between the orbital periods of satellites in the same system are reached due to the different rates of orbital evolution of the satellites. Resonances are usually referred to by these ratios - therefore a 3:1 resonance occurs when an inner satellite completes three orbits in the same period of time as an outer satellite completes one orbit. These resonances enhance mutual perturbations, and are stable if the enhanced perturbations maintain commensurability against outside disruptive influences (e.g. tidal dissipation) - thus they are a natural end result of orbital evolution in a multi-satellite system. Orbit-orbit resonances can affect the *mean motion* of the satellites (their orbital velocity), as well as the orientation, inclination, and eccentricity of their orbits. Specifically, orbital resonances can force an orbit to become more eccentric than it should be if the orbit was not resonant. As a result, two eccentricity values are derived - one is *forced eccentricity* that the orbit has as a result of the perturbations, and the other is the *free eccentricity* that the orbit should have if it was completely unperturbed.

It should be noted that there is another variety of resonance known as a **spin-orbit resonance**, which links the satellite's rotational period to its orbital period. The most common spin-orbit resonance is that of synchronous rotation, which is a 1:1 spin-orbit resonance. (e.g. Goldreich 1966; Goldreich & Peale, 1966).

To summarise: orbital evolution is an important factor in the satellite's physical evolution because it results in tidal dissipation within the satellite's interior. The variation in distance from the primary (and hence in tidal effect) of a satellite due to its orbital eccentricity during each orbit results in the gravitational 'flexing' of the satellite's body, which generates friction in the interior which serves to dissipate the tidal energy. The heat generated by this cyclical process can have significant effects on the physical state of the satellite's interior, particularly if it contains large amounts of ice and other volatiles. Changes in the satellite's interior can in turn affect the orbital evolution since the material properties of the interior affect the way in which tidal dissipation is distributed therein - so the process is actually a complicated interplay of factors.

4.1.3 Orbital Terminology

A variety of terms and parameters are used in orbital dynamics, and it would be useful to summarise them before proceeding - these are shown in Table 4.2. Where possible, these parameters are illustrated in Figure 4.3.

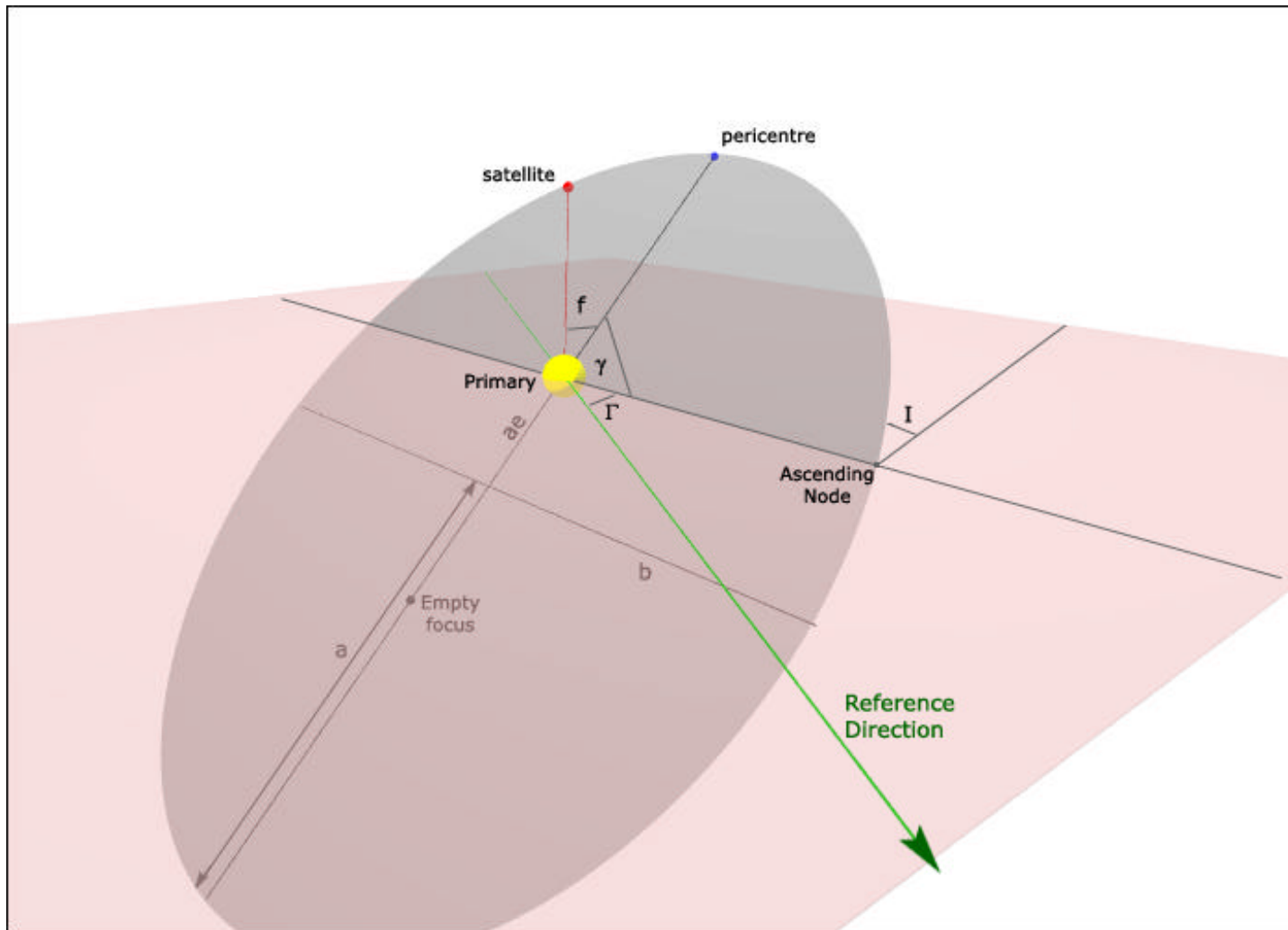


Figure 4.3: Diagram illustrating important orbit parameters shown in Table 4.2.

Table 4.2: Terms for Orbital Dynamics equations

Parameter	Calculation	Definition	Explanation
n	$2\pi/T$	mean motion	Average orbital velocity of satellite ($^{\circ} \text{ day}^{-1}$ or rad s^{-1})
a		semi-major axis	radius of longest ellipse axis measured from centre of orbit.
v ($^{\circ}$)	$\omega + \Gamma$	Longitude of pericentre	Angle between pericentre of orbit and arbitrary reference direction.
G ($^{\circ}$)	$\varpi - \gamma$	Longitude of the Ascending Node	Angle between reference line within reference plane and line where orbital plane intersects reference plane [line of nodes].
g ($^{\circ}$)	$\varpi - \Gamma$	Argument of pericentre	Angle [within orbital plane] between line of nodes and pericentre of orbit.
f ($^{\circ}$)		True anomaly	Angle between current satellite position in orbit and pericentre of orbit.
e			Orbital Eccentricity
I ($^{\circ}$)			Orbital Inclination
M	$n(t - \tau)$	Mean anomaly	[($t - \tau$) = time past pericentre passage]. M is an angle, but has no simple geometric interpretation.
l	$M + \varpi$	Mean longitude	(no simple geometric interpretation).

4.2 The mechanisms of orbital evolution

4.2.1 The Q factor

One of the most important factors in determining the rate of tidal dissipation - and thus of orbital evolution - is Q , the **Tidal Dissipation Factor**. Essentially, Q represents the amount of total rotational and orbital energy lost within the system by dissipation, most commonly via frictional heating. In the case of orbital dynamics, the Q values for primaries and satellites may both be important in influencing the evolution of the system.

Goldreich and Soter (1966) (G&S, 1966) were among the first to investigate Q in the context of planetary systems. The effective Tidal Dissipation Function ($1/Q$) is related to the lag angle (ϵ , shown in Figure 4.2) of the tidal bulge on the planet.

The exact relation is given by:

$$\frac{1}{Q} = \frac{1}{2\pi E_o} \oint \left(-\frac{dE}{dt} \right) dt \quad (\text{G\&S, 1966}) \quad (4.1)$$

where E_o is the maximum energy stored in the tidal distortion and the integral over $-dE/dT$ (the rate of dissipation) is the energy lost during one complete cycle.

Thus effectively:

$$\frac{1}{Q} \propto \frac{\text{The energy lost over a complete cycle}}{\text{The maximum energy stored in the tidal distortion}} \quad (4.2)$$

$1/Q$ approximates to unity if the amount of energy lost by dissipation during one orbit approaches the total energy in the tidal distortion, but is small ($\ll 1$) if the amount of energy lost during one orbit is small compared to the total energy in the distortion. The values of Q for terrestrial planets are of the order of 10^1 to 10^2 , but are much greater (between 10^4 and 10^6) for the gas giants (e.g. Goldreich and Soter, 1966). Thinking in terms of Q itself rather than $1/Q$: **Q is small ($< 10^2$) if a lot of energy is being dissipated in the system per cycle, and large ($\gg 10^6$) if little energy is being dissipated in the system per cycle.**

The general relationship between Q and e is given by Goldreich and Soter (1966):

$$\frac{1}{Q} = \tan 2e \approx \sin 2e \approx 2e \quad \text{if } Q \text{ is large (which it generally is).} \quad (4.3)$$

The lag angle is therefore roughly inversely proportional to Q , and is small if Q is large (and vice versa). Thus the lag angle is smaller in systems where little tidal energy is being dissipated (i.e. where Q is large, as for gas giants like Jupiter).

Q' is a quantity that appears in many tidal equations, and is derived through the net effective torque (N) on a body. N_1 is the torque due to tides raised on a planet by a satellite, N_2 is the torque due to tides raised on a planet by the Sun, and N_3 is the torque due to tides raised on a satellite by a planet. Q' is a function of Q for a planet or satellite, and is useful in many tidal equations - however, it is calculated in a different manner for planets (Q_p) and satellites (Q_s). The derivations given on pg. 378 of Goldreich and Soter (1966) give results of:

$$Q'_p = Q_p \left(1 + \frac{19m}{2gRr} \right) \quad (4.4)$$

and:

$$Q'_s = Q_s \left(1 + \frac{38p r^4 m}{3Gm^2} \right) \quad (4.5)$$

It should be noted that the general form of the terms in brackets here are identical - equation (4.5) merely expands p and g from (4.4). These equations can be further simplified and generalised as:

$$Q' = Q \cdot (1 + \tilde{m}) \quad \text{where} \quad \tilde{m} = \left(\frac{19m}{2gRr} \right) = \left(\frac{38p r^4 m}{3Gm^2} \right) \quad (4.6)$$

\tilde{m} is the *effective rigidity* of the body (Murray and Dermott, 1999). This parameter is dimensionless, and represents the ratio of the elastic and gravitational forcing acting on the body.

Table 4.3 defines the variables used hereafter.

Table 4.3: Definitions of parameters used in orbital equations

Quantity	Planet (p)	Satellite (s)	Units
Mass	M	m	kg
Radius	R	r	m
Orbital Semimajor Axis	A	a	m
Axial Angular Velocity	W	w	rad s ⁻¹
Tidal Dissipation	Q_p	Q_s	dimensionless
Mean Motion		n	rad s ⁻¹ or ° day ⁻¹
Effective Rigidity	\tilde{m}_p	\tilde{m}_s	dimensionless

Rigidity	m	N m ⁻²
Density	r	kg m ⁻³
Gravitational Constant	G (6.672559 x 10 ⁻¹¹)	N m ² kg ⁻²
Time	t	s
Moment of Inertia factor	α (2/5 for an undifferentiated body, ~ 1/3 for a body with core).	dimensionless
Tidal Torque	N	kg m ² s ⁻²

We can now derive several very useful functions.

4.2.2 Rotational despinning of planets and satellites

The moment of inertia through the spin axis of a rotating sphere is given by:

$$I_p = \mathbf{a}MR^2 \quad (\text{G\&S, 1966}) \quad (4.7)$$

where the moment of inertia factor \mathbf{a} is a factor that is determined by the planet's internal structure. \mathbf{a} is equal to 2/5 (0.4) for a homogeneous sphere with a uniform density distribution, whereas a more centrally-condensed body with a dense core has a lower value. I shall still explicitly state \mathbf{a} in the equations that follow rather than substitute values, for the sake of generality.

The rotational despinning of the planet (the rate at which the rotational angular velocity decreases) due to tides raised by the satellite is given by N_1/I_p where N is the tidal torque described at the end of Section 4.2.1:

$$-\frac{d\Omega_1}{dt} = \frac{N_1}{I_p} = \frac{9}{4} \frac{GR^3 m^2}{\mathbf{a}MQ'_p a^6} \quad (\text{G\&S, 1966}) \quad (4.8)$$

whereas rotational despinning due to tides raised by the Sun is given by N_2/I_p :

$$-\frac{d\Omega_2}{dt} = \frac{N_2}{I_p} = \frac{9}{4} \frac{GM_{sol}^2 R^3}{\mathbf{a}MQ'_p A^6} \quad (\text{G\&S, 1966}) \quad (4.9)$$

where M_{sol} is the mass of the Sun (1.9891×10^{30} kg). These solar tides are only really important for the innermost worlds, however - indeed, the Earth is being spun down much more by lunar tides than solar tides. Nevertheless, the rate of rotational despinning caused by both a satellite and the sun on a planet can now be calculated using equations (4.8) and (4.9). This can be integrated over the history of the system to calculate the total rotational despinning of the planet (see Section 4.2.3.3).

For satellites, the general moment of inertia equation still holds (c.f. Equation 4.7), so:

$$I_s = \mathbf{a}mr^2 \quad (\text{G\&S, 1966}) \quad (4.10)$$

The rate of rotational despinning of a satellite due to tides raised on it by a planet is given by N_3/I_s :

$$-\frac{d\mathbf{w}}{dt} = \frac{N_3}{I_s} = \frac{9}{4}GM^2 \frac{r^3}{\mathbf{a}mQ'_sa^6} \quad (\text{G\&S, 1966}) \quad (4.11)$$

(IMPORTANT NOTE: The coefficient is given as 45/8 in Goldreich and Soter (1966) - this is because they assume $\mathbf{a} = 2/5$ (that of a homogeneous sphere) and multiply this out by the 9/4 coefficient. Thus, they have not explicitly included the factor \mathbf{a} in the denominator on the right-hand side, whereas I have done so).

4.2.3 Tidal Evolution Equations

We are now in a position to be able to calculate the evolution of the semi-major axis a (and thus the satellite's orbital period), the satellite's rotation period, and the planet's rotation period through time. When the satellite rotation period is the same as its orbital period, synchronous rotation has been reached, and the rotation rate slows down as the orbital period increases, as described in section 4.1. These equations will prove very useful generally.

4.2.3.1 Increase in orbital distance of satellites (general case)

The tidal bulge raised on the planet serves to decrease the mean motion of the satellite, pushing it outwards into an orbit with a greater radius and longer period. It should be noted that Q for solid-body appears to be independent of tidal frequency but may be amplitude-dependent (G&S, 1966) for large strains - the implication is that Q remains constant as the orbital distance changes, though other processes (discussed in Chapter 5) may act change it for planetary bodies.

The equation for the orbital evolution is:

$$\frac{da}{dt} = \frac{9}{2} \left(\frac{G}{M} \right)^{1/2} \frac{R^5}{Q'_p} \frac{m}{a^{11/2}} \quad \text{where } Q'_p = Q_p (1 + \tilde{m}_p) \quad (4.12)$$

(G&S, 1966) which can be re-written as:

$$\frac{da}{dt} = \frac{\Xi}{a^{11/2}} \quad \text{where} \quad \Xi = \frac{9}{2} \left(\frac{G}{M} \right)^{1/2} \frac{R^5 m}{Q'_p} \quad (4.13)$$

It should be noted that X has no physical significance itself - it is merely a convenient substitute for the non-variable terms in the equation.

Integrating between limits of the current orbital distance (a) and the initial orbital distance (a_i), this becomes:

$$\Xi t = \frac{2}{13} \left(a^{13/2} - a_i^{13/2} \right) \quad (4.14)$$

where t is the timespan over which evolution occurs.

This can be rephrased as:

$$a = \left(\frac{13}{2} \Xi t + a_i^{13/2} \right)^{2/13} \quad \text{and, more usefully,} \quad (4.15)$$

$$a_i = \left(a^{13/2} - \frac{13}{2} \Xi t \right)^{2/13} \quad (4.16)$$

Equation (4.16) can be used to calculate the orbital evolution of a satellite over a given timespan t if the orbital distance a at that time is known.

4.2.3.2 Rotational despinning of satellites (general case)

Recall equations (4.11) and (4.5):

$$-\frac{d\mathbf{w}}{dt} = \frac{9}{4} GM^2 \frac{r^3}{amQ'_s a^6} \quad \text{where } Q'_s = Q_s (1 + \tilde{\mathbf{m}}_s)$$

Again, we can rephrase this as a constant (\mathbf{Y}) multiplied by a factor of a , so that:

$$-\frac{d\mathbf{w}}{dt} = \frac{\Psi}{a^6} \quad \text{where for convenience} \quad \Psi = \frac{9}{4} GM^2 \frac{r^3}{amQ'_s} \quad (4.17)$$

Again, the terms included in \mathbf{Y} are assumed to be constant. Since this has to be integrated with respect to a , we need to include the constant \mathbf{X} from equation (4.13). We replace a_i with a using equation (4.16), simplify, then integrate, and arrive at:

$$\begin{aligned} \Delta \mathbf{w} &= \frac{2\Psi}{\Xi} \left[\left(\frac{13}{2} \Xi t + (a_i^{13/2}) \right)^{1/13} - a_i^{1/2} \right] \\ \Delta \mathbf{w} &= \frac{2\Psi}{\Xi} \left[\left(\frac{13}{2} \Xi t + a^{13/2} - \frac{13}{2} \Xi t \right)^{1/13} - \left[a^{13/2} - \frac{13}{2} \Xi t \right]^{1/13} \right] \\ \mathbb{P} \quad \Delta \mathbf{w} &= \frac{2\Psi}{\Xi} \left[a^{1/2} - \left(a^{13/2} - \frac{13}{2} \Xi t \right)^{1/13} \right] \end{aligned} \quad (4.18)$$

where \mathbf{Dw} is the total rotational despinning of the satellite over time interval t .

Note that we can simplify so that:

$$\frac{2\Psi}{\Xi} = \frac{(GM^5)^{1/2} r^3 Q'_p}{a R^5 m^2 Q'_s} \quad (4.19)$$

4.2.3.3 Rotational despinning of planet due to satellites and sun (general case)

Substituting equation (4.15) into (4.8):

$$-\frac{d\Omega_1}{dt} = \frac{N_1}{I_p} = \frac{9}{4} \frac{GR^3 m^2}{a M Q'_p a^6} \quad \text{and} \quad a = \left(\frac{13}{2} \Xi t + a_i^{13/2} \right)^{2/13}$$

$$\Rightarrow -\frac{d\Omega_1}{dt} = 9GR^3 m^2 / \left(4a M Q'_p \left(\left(\frac{13}{2} \Xi t + a_i^{13/2} \right)^{12/13} \right) \right)$$

Re-arrange so that:

$$-\frac{4a M Q'_p}{9GR^3 m^2} d\Omega_1 = dt / \left(\frac{13}{2} \Xi t + a_i^{13/2} \right)^{12/13}$$

Integrating between $t = 0$ to $t = t_{final}$, so W_l goes from $W_{l,initial}$ to $W_{l,final}$ yields:

$$[\Omega_{1,initial} - \Omega_{1,final}] = \frac{9GR^3 m^2}{4a M Q'_p} \frac{2}{\Xi} \left(\frac{13}{2} \Xi t + a_i^{13/2} \right)^{1/13} - a_i^{1/2} \quad (4.20)$$

Substituting:

$$\frac{9GR^3m^2}{4aMQ'_p} \frac{2}{\Xi} = \left(\frac{G}{M}\right)^{1/2} \frac{m}{R^2a} \left(\frac{13}{2}\Xi t + a_i^{13/2}\right)^{1/13} = a^{1/2}$$

$$a_i^{1/2} = \left(a^{13/2} - \frac{13}{2}\Xi t\right)^{1/13}$$

$$\Rightarrow [\Omega_{1,initial} - \Omega_{1,final}] = \left(\frac{G}{M}\right)^{1/2} \frac{m}{R^2a} \left[a^{1/2} - \left(a^{13/2} - \frac{13}{2}\Xi t\right)^{1/13} \right] \quad (4.21)$$

$$\Rightarrow \Omega_{1,initial} = \Omega_{1,final} + \left\{ \left(\frac{G}{M}\right)^{1/2} \frac{m}{R^2a} \left[a^{1/2} - \left(a^{13/2} - \frac{13}{2}\Xi t\right)^{1/13} \right] \right\} \quad (4.22)$$

This allows us to determine the initial rotation period P_i of a planet with a single satellite:

$$\Omega_{1,initial} = \frac{2\pi}{P_i} \quad (\text{Murray and Dermott, 1999}) \quad (4.23)$$

Solar tides also slow down a planet's rotation. Recall equation (4.9):

$$-\frac{d\Omega_2}{dt} = \frac{9}{4} \frac{GM_{sol}^2 R^3}{aMQ'_p A^6}$$

We can assume that none of these parameters are changing, so all we need to do to find out the total despinning caused by solar tides over time t is to multiply the RHS by t :

$$-\Delta\Omega_2 = \frac{9}{4} \frac{GM_{sol}^2 R^3 t}{aMQ_p' A^6} \quad (4.24)$$

From this, we can see that:

$$\Omega_{initial} = \Omega_t - \Delta\Omega_2 \quad (4.25)$$

We can then use equation (4.23) to determine the initial rotation period from $\Omega_{initial}$.

Note that if a planet has a satellite and is affected by solar tides - or has more than one satellite - it becomes much more difficult to determine the initial rotation rate of the planet, since it is being slowed by both the solar and satellite tide at the same time.

However, for distant worlds the solar tides will be small unless the star is extremely massive - the effect on Jupiter's rotation is almost undetectable and thus can be ignored. Assuming an initial arbitrarily-selected rotation period of 10 hours for the Earth, its rotation period would have slowed down to 14 hours after 4.6 Ga (however, the presence of fluid oceans and atmosphere on the Earth also contributes to tidal braking, as of course does the tide from the Moon). It is interesting to note that if it was solely under the influence of solar tides, the Earth would be tide-locked to the Sun today if its initial rotation period had been longer than 35.2 hours.

4.3 Orbital characteristics of the jovian system

Table 4.4 summarises the orbital parameters of the Galilean satellites:

Table 4.4: Orbital parameters of the Galilean satellites

	a (m)	e	I (°)	P (days)	n (° day⁻¹)
Io	0.4217 x 10 ⁹	0.0041 (0.00001)	0.03	1.769	203.489
Europa	0.6710 x 10 ⁹	0.0101 (0.0001)	0.46	3.551	101.375
Ganymede	1.070 x 10 ⁹	0.0006 (0.0015)	0.18	7.155	50.317
Callisto	1.883 x 10 ⁹	0.007	0.25	16.689	21.571

a = semimajor axis (m); **e** = free (forced in **bold**) eccentricity (Malhotra, 1991); **i** = orbital inclination w.r.t. Jupiter equator (Hartmann, 1993); **P** = satellite orbital period; **n** = orbital mean motion (° day⁻¹) (Murray & Dermott, 1999). 1 day = 24 hours.

The orbits of the Galilean satellites evolve with time as described in Section 4.1.1, but the situation here is complicated by orbital resonances. There are in fact three such resonances acting in the Jovian system - Io and Europa are locked in a 2:1 orbit-orbit resonance, Europa and Ganymede are also locked into a 2:1 orbit-orbit resonance, and all three are locked in a complex 4:2:1 relationship called the **Laplace Resonance**, described later in this section.

These resonances can be expressed more precisely as:

$$\lambda_1 - 2\lambda_2 + \varpi_1 = 0^\circ \quad \lambda_1 - 2\lambda_2 + \varpi_2 = 180^\circ \quad \lambda_2 - 2\lambda_3 + \varpi_2 = 0^\circ \quad (4.26)$$

$$n_1 - 2n_2 + \frac{d\mathbf{v}_1}{dt} = 0 \quad n_1 - 2n_2 + \frac{d\mathbf{v}_2}{dt} = 0 \quad n_2 - 2n_3 + \frac{d\mathbf{v}_2}{dt} = 0 \quad (4.27)$$

(Murray and Dermott, 1999) where the subscripts 1, 2, or 3 refer to Io, Europa and Ganymede respectively in this and subsequent equations, and the terms are explained in Table 4.2. It should be noted that Equations (4.26) librate around those angles.

All three inner Galileans are also locked in the unique **Laplace Resonance** - a stable 4:2:1 resonance between Io, Europa and Ganymede.

The Laplace relation states that:

$$\Phi_L = \lambda_1 - 3\lambda_2 + 2\lambda_3 = 180^\circ \quad (4.28)$$

and

$$n_1 - 3n_2 + 2n_3 = 0 \quad (4.29)$$

where Φ_L is the resonant argument, λ_n is the mean longitude of the body defined in Table 4.2 (Murray and Dermott, 1999)

For every one orbit that Ganymede completes around Jupiter, Europa completes two, and Io completes four (since $n_3 = 2n_2 = 4n_1$). The resonant argument $\Phi_L = 180^\circ$ implies that there can never be a triple conjunction of Io, Europa, and Ganymede - when two satellites and Jupiter are aligned in a straight line, the other satellite is always at least 60° away. These resonances have several other implications for the orbital dynamics of the Io-Europa-Ganymede system. Showman and Malhotra (1997a) have summarised these very concisely, as quoted below:

“The mean motion ratios within the Io-Europa and Europa-Ganymede pairs is not exactly 2:1. [This means that] the conjunctions between Io and Europa drift at a mean angular velocity of $[\mathbf{d}_1] = 2n_2 - n_1$, while the conjunctions between Europa and Ganymede drift at a rate of $[\mathbf{d}_2] = 2n_3 - n_2$ [...]. The Io-Europa conjunction is locked to Io’s perijove and also to Europa’s apojove, and the Europa-Ganymede conjunction occurs when Europa is near perijove [...]. The Europa-Ganymede conjunction is not locked to either apse of Ganymede’s orbit [...].

The Laplace resonance is a 1:1 commensurability between the rates of motion of the Io-Europa and Europa-Ganymede conjunctions (as opposed to the 2:1 commensurabilities between the satellites’ mean motions): The Io-Europa conjunction drifts at the same rate as the Europa-Ganymede conjunction, so $[\mathbf{d}_1/\mathbf{d}_2] = 1$. Currently we have $[\mathbf{d}_1] = [\mathbf{d}_2] = -0.74^\circ \text{ day}^{-1}$. This is an extremely small value compared with the satellites’ mean motions [...].”

The most important practical consequence of the Laplace Resonance is that the inner three Galilean satellites have been affected by significant heating caused by tidal dissipation as energy and angular momentum have been transferred from Io to Europa to Ganymede. This is fully described in Yoder and Peale (1981) and extended by Gomes (1998).

Yoder and Peale (1981) show that the tidal dissipation rate in Io is a key controlling mechanism for the orbital evolution of the Galilean Satellites involved in the resonances, and can also be used to determine bounds for the Q value (the tidal dissipation function) of Jupiter. This can also be used to determine the rate of orbital evolution of Io and the other Galileans involved in the resonances, within limits.

In the following sections, I shall attempt to determine how the orbits of the Galilean satellites evolved over the history of the Solar System. I calculate a realistic value for the Q of Jupiter, determine a realistic initial orbital distance of Io, and determine the evolution of the orbits of the Galileans.

4.4 Application to Jupiter and the Galilean satellites

Q'_p can be simplified for the Gas Giant planets, since $I_9 m \ll 2g r R$ - they have very little or no rigidity - this means that the $(1 + \tilde{m})$ term in equation (4.4) approaches 1 for Gas Giants, so Q'_p approaches Q_p . Note that Q'_s cannot be simplified like this however, since the satellites do have significant rigidity.

Hence:

$$Q'_p \Rightarrow Q_p \qquad Q'_s = Q_s (1 + \tilde{m}_s)$$

Recall from equation (4.13) and (4.17) that:

$$\Xi = \frac{9}{2} \left(\frac{G}{M} \right)^{1/2} \frac{R^5 m}{Q'_p} \qquad \Psi = \frac{9}{4} G M^2 \frac{r^3}{a m Q'_s}$$

Substituting Q'_p and Q'_s into the X and Y equations:

$$\Xi = \frac{9}{2} \left(\frac{G}{M} \right)^{1/2} \frac{R^5 m}{Q_p} \tag{4.30}$$

and

$$\Psi = \frac{9}{4} G M^2 \frac{r^3}{a m Q_s (1 + \tilde{m}_s)} \tag{4.31}$$

Recalling equation (4.16):

$$a_i = \left(a^{13/2} - \frac{13}{2} \Xi t \right)^{2/13}$$

and expanding \mathbf{X} out in full:

$$a^{13/2} - a_i^{13/2} = \frac{\frac{117}{4} (G/M)^{1/2} R^5 m t}{Q_p}$$

which implies:

$$Q_p = \frac{\frac{117}{4} (G/M)^{1/2} R^5 m t}{\left(a^{13/2} - a_i^{13/2} \right)} \quad (4.32)$$

or:

$$a_i^{13/2} = a^{13/2} - \frac{\frac{117}{4} (G/M)^{1/2} R^5 m t}{Q_p} \quad (4.33)$$

Equation (4.32) allows us to determine Q_p for Jupiter. Note that this is a simplification where we assume that \mathbf{m}_p (the rigidity of the planet) is very small and so $Q'_p \approx Q_p$ - thus it can only be applied with confidence to Jupiter and Saturn.

Equation (4.24) - equivalent to Equation (4.16) - is very useful, since it allows us to determine the initial orbital distance (a_i) of a satellite from Jupiter given its current orbital distance (a) at any time over the history of the solar system (t).

4.4.1 The Q of Jupiter

I begin by reviewing various estimates of the Q of Jupiter (and of Io) in Table 4.5:

Table 4.5: Estimates of Q_J and Q_i by various authors.

Paper	Q_J	Q_i
Goldreich & Soter (1966)	$1 \times 10^5 < Q_J \ll 1 \times 10^6$	-
Yoder (1979)	$2 \times 10^5 < Q_J \ll 2 \times 10^6$	$12 < Q_i \ll 120$
Yoder & Peale (1981)	$6 \times 10^4 < Q_J \ll 2 \times 10^6$	$12 < Q_i \ll 120$
Tittlemore (1990)	$< 1.4 \times 10^4$ *	-
Malhotra (1991)	$\sim 5 \times 10^5$	-

*: Tittlemore's Q_J appears to be questionable, according to Malhotra.

The consensus for Q_J seems to be that it lies between 10^5 and 10^6 . Tittlemore (1990) also estimated the values of Q for Europa and Ganymede and determined them to be $10 < Q_e \ll 500$ and $10 < Q_g \ll 200$ respectively - so the Q values of the satellites appear to lie between 10^1 and 10^2 .

However, there is an important *caveat* here: The value of Q depends on what dissipation process is used to calculate it - tidal dissipation yields one value, convection currents in the interior yield another (very large) value, interaction of Jupiter's electrical flux tube with Io yet another. The rigidity of the solid core of Jupiter may also play a significant role, or the highly compressed inner layers of the planet may have a rigidity of their own (Dermott, 1979), so this generalisation might not apply. For further discussion, the reader is referred to Section 7 of Yoder and Peale (1981). For this purpose, I shall be considering only the tidal dissipation Q since it is the only mechanism that has been explored in any detail.

It should also be noted that Malhotra (1991) adopts a ‘plausible’ value for Q_J of $\sim 5 \times 10^5$ - this was justified by Showman and Malhotra (1997a) based on work done by other authors in determining the Q of Uranus and Neptune. The values these authors derived for Uranus and Neptune were $Q_U < 3.9 \times 10^5$ and $Q_N < 3 \times 10^5$ respectively. However, it is important to realise that Uranus and Neptune have different internal structures and bulk composition from Jupiter and Saturn. Compositionally, Uranus and Neptune consist of a comparatively thin H_2/He atmosphere overlying an ice-rich (water/ammonia/methane) mantle and a relatively large rocky core. Jupiter and Saturn, on the other hand, consist of a deep H_2/He atmosphere, overlying liquid and liquid metallic Hydrogen and Helium layers, and possibly a small rocky core (Connerney, 1993). It is therefore perhaps not entirely sensible to assume that the Q of Jupiter or Saturn will be the same order of magnitude as the Q of Uranus or Neptune. I will therefore assume here that a ‘plausible’ value of the Q of Jupiter is of the order 10^6 rather than 10^5 - within the upper range of the values that Yoder and Peale (1981) have derived.

It is also interesting to note that Q values for Callisto have not been calculated or bounded by any authors, presumably because it has never been involved in tidal interactions. Given that it is a small solid body however, it is likely that its Q value is of the order of 100 like that of the other satellites. If it was never involved in a resonance in its history, then it may be instructive to calculate da/dt for Callisto, since it fits within my simplified scenario for orbital evolution. However, there is a significant problem with this approach, which I shall discuss in Section 4.4.3.

The orbital and physical parameters for Jupiter and the Galilean satellites that I use in subsequent calculations are listed in Table A.4 in Appendix 1.

4.4.2 A lower bound for Q_J

4.4.2.1 The initial orbital distance of Io

We can use equation (4.32) to set a lower limit for the value of Q_p for Jupiter, but first we need to determine the initial orbital distance for a satellite. We can only use Io for this, since it is the innermost spherical satellite of Jupiter and there are very definite limits to its orbital evolution, explained here.

When Jupiter formed from the protosolar nebula 4.6 billion years ago, it was larger and hotter than it is today (Pollack and Reynolds, 1974). This explains why the inner Galilean satellites are predominantly rocky (density $\sim 3500 \text{ kg m}^{-3}$) whereas the outer ones are predominantly icy (density $\sim 2000 \text{ kg m}^{-3}$) - the temperature nearer Jupiter prevented ices from condensing out of the protojovian nebula while the satellites were forming. Pollack and Reynolds (1974) suggest that the Galilean satellites formed within 5 million years. The early Jupiter collapsed from 14 times its current radius (around the orbit of Ganymede) to 1.5 times its current radius after approximately a million years - 10^5 years after its formation, it had collapsed to within the current orbital distance of Io. Thus it is likely that the Galileans started to form around a million years after Jupiter formed, and completed the process five million years later. During this period, Jupiter contracted from $\sim 1.5 R_J$ ($1 R_J$ = Jupiter's current radius) to $\sim 1.2 R_J$.

Jupiter was larger than it is today while the Galilean satellites were forming, so its rotation period would have been slower (due to conservation of angular momentum while it was contracting). Furthermore, since Jupiter is much more massive than its satellites,

tidal despinning probably has not drastically slowed down its rotation since it formed (see equation (4.22)).

Assuming that the degree of central condensation and the mass of Jupiter does not change (i.e. only the radius is changing) we see that:

$$\frac{2}{5}MR_1^2\Omega_1 = \frac{2}{5}MR_2^2\Omega_2 \quad (4.34)$$

where the subscripts ₁ and ₂ denote parameters for the early Jupiter and the current Jupiter respectively. Therefore:

$$\frac{R_1^2}{R_2^2} = \frac{\Omega_2}{\Omega_1} \Rightarrow \Omega_1 = \frac{\Omega_2 R_2^2}{R_1^2} \quad (4.35)$$

Inserting values: $R_1 = 107097000$ m, $R_2 = 71398000$ m, $\Omega_2 = 1.7587 \times 10^{-4}$ rad s⁻¹.

Thus $\Omega_1 = 7.8162 \times 10^{-5}$ rad s⁻¹. This translates to a rotational period of 22.33 hours for the proto-jupiter, when its radius was 1.5 R_J .

I shall now use this initial rotation period and larger radius to set an inner limit to Io's initial orbital distance - Io cannot have formed within the synchronous orbit, since it would still be within it today assuming it had not spiralled into Jupiter by now (see section 4.1).

The synchronous orbit of the 1.5 R_J proto-jupiter will be at a distance of:

$$a_s = \left(\frac{GM}{\Omega^2} \right)^{1/3} \quad (4.36)$$

For $W = 7.8162 \times 10^{-5} \text{ rad s}^{-1}$, $M = 1.89861 \times 10^{27} \text{ kg}$, $G = 6.672559 \times 10^{-11} \text{ N m}^2 \text{ kg}^{-2}$, the ‘proto-synchronous orbit’ a_s is **2.747 x 10⁸ m**, or 2.565 proto-Jupiter radii. This is equivalent to **3.848 current Jupiter radii**, and thus sets a minimum orbital distance for Io. If the proto-jupiter had the same rotational period as it does today, this radius would be at $1.6 \times 10^8 \text{ m}$, or 2.241 current R_J.

The value of 3.85 current R_J represents a lower limit to the initial orbital distance of Io, and provides a firm constraint on how much Io’s semimajor axis has evolved over the history of the solar system.

Another constraint on the initial orbital distance for Io the *Roche Limit* for a satellite (d_R , expressed in planetary radii), given by:

$$d_R \approx 3 \left(\frac{r_P}{r_S} \right)^{1/3} \quad (\text{Murray and Dermott, 1999}) \quad (4.37)$$

This is the limit within which an accreting proto-satellite would be unable to form around a planet because of tidal forces - a ring system would be more likely instead. Using Io's density (3548 kg m^{-3}), $d_R \sim 2.2 R_J$ - this is the minimum possible distance at which Io (in its present form) could have accreted around Jupiter. We know from Pollack and Reynolds (1974) that the particles that would have formed Io contained little volatile material so the particle density would probably have been at least 2500 kg m^{-3} . Assuming this density sets d_R to be just over $2.4 R_J$. However, we can see that the Roche Limit for particles with the same density as Jupiter - i.e. those consisting entirely of volatile (non-silicate) material - is at $3 R_J$, which is still well within the 'proto-synchronous orbit' at $3.848 R_J$. Thus, determination of the Roche Limit cannot additionally constrain the lower limit of Io's initial orbital distance. I therefore assume that the minimum possible orbital distance for Io is at $3.85 R_J$.

4.4.2.2 Determining the Q of Jupiter

I shall now attempt to define a lower limit for the possible value of Q_J . This can be calculated using equation (4.32):

$$Q_p = \frac{\frac{117}{4} (G/M)^{1/2} R^5 m t}{\left(a^{13/2} - a_i^{13/2} \right)}$$

where t is the time elapsed since formation (and $a = a_i$ at formation)

In Equation (4.32), t is assumed to be the age of the Solar System (4.6 billion years, or 1.45×10^{17} s), a of Io is 4.216×10^8 m (5.905 R_J , or 421,600 km) and a_i for Io is 2.749×10^8 m (3.85 R_J , or 274,882 km).

Using equation (4.32), I find that when $a_i = 3.85 R_J$, $Q_J = 1218080.828$, or $\sim 1.22 \times 10^6$.

Therefore: **$Q_J > 1.22 \times 10^6$**

This is well within the acceptable range of Q_J shown in Table 4.5. It is interesting to note that this is well above the value adopted by Malhotra (1991) shown in Table 4.5 and also adopted by Showman and Malhotra (1997a) and Showman *et al.* (1997b). In fact, given that the only unknown in equation (4.32) is a_i - which is set to the smallest possible value it can realistically be (3.85 Jupiter radius) in order to calculate the minimum possible value of Q_J - it appears to be *impossible* for Q_J to be less than 1.0×10^6 .

Lower values of Q_J can be derived by setting the time of evolution to less than 4.6 Ga (2.0 Ga yields a value for Q_J of $\sim 5.2 \times 10^5$) - but this would make no realistic sense, as it implies that the Jovian system formed 2 Ga ago and there is no evidence to support this hypothesis.

Although it is highly unlikely (if not impossible) that Io formed closer to Jupiter, I shall calculate Q_J for values of $a_i < 3.85 R_J$ in order to show more clearly how different initial orbital distances of Io affect the calculated value of Q_J . While setting $a_i = 1 R_J$ would be somewhat nonsensical, it at least sets an *absolute* lowest bound to what the value of Q_J can be. However, the corresponding value of Q_J is still greater than 1×10^6 , even using this extremely unrealistic assumption. Again, it appears that values for $Q_J < 1 \times 10^6$ are not valid.

Q_J can be greater than 1.22×10^6 if Io formed further beyond the ‘proto-synchronous orbit’ at $a_i = 3.85 R_J$. It would therefore be instructive to calculate Q_J given a range of possible initial Ionian orbital distances, up to the limit of its current orbital distance.

To illustrate this range, I calculate values of Q_J for r_i values that range from $1 R_J$ to $5.0 R_J$. Table 4.6 shows the range of derived Q_J values given different values of a_i . In all cases, the time of evolution was 4.6 billion years (1.4517×10^{17} s), which is the assumed age of the Solar System.

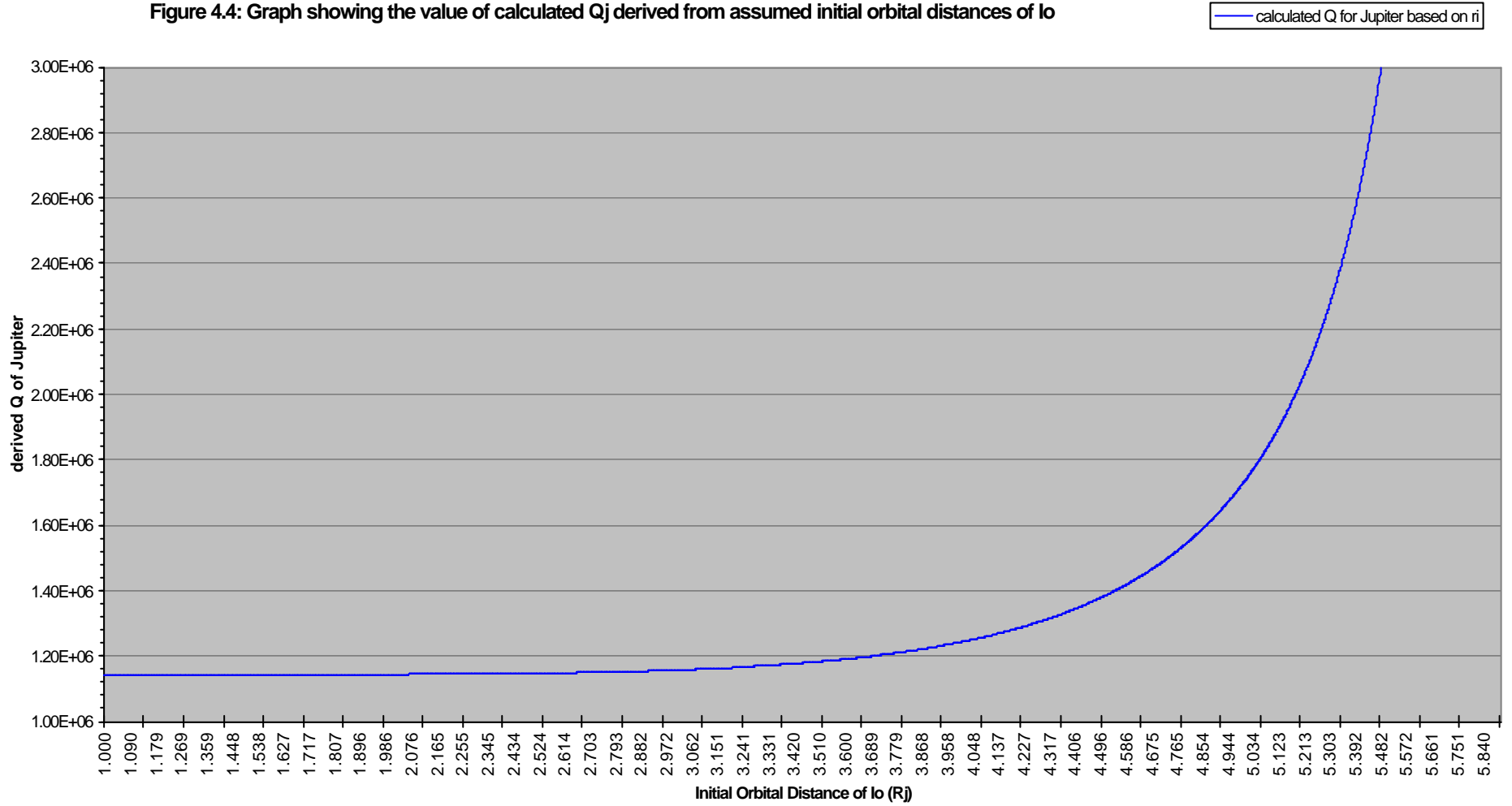
Table 4.6: Derived Q_J values for a range of initial Io orbital distances.

Initial Io orbital distance in m (a_i)	a_i in Jupiter Radii (R_J)	Derived Q of Jupiter (Q_J)
7.1398×10^7	1.000	1.1426×10^6
1.6000×10^8	2.241	1.1447×10^6
1.7850×10^8	2.500	1.1469×10^6
2.1419×10^8	3.000	1.1568×10^6
2.4989×10^8	3.500	1.1820×10^6
2.7488×10^8	3.850	1.2181×10^6
2.8559×10^8	4.000	1.2412×10^6
3.2129×10^8	4.500	1.3780×10^6
3.5699×10^8	5.000	1.7280×10^6
4.2125×10^8	5.900	1.7215×10^8

These figures (and intermediate values) are plotted graphically in Figure 4.4. The figures shown in Table 4.6 as bold text require further explanation: 2.241 R_J is the current synchronous orbit of Jupiter, and thus represents the *absolute* lowest physically possible value for Io's initial orbital distance. The 3.850 R_J value is just above the proto-synchronous orbit of Jupiter at 3.848 R_J that would have been likely during the formation of the Galilean satellites, and thus represents the most realistic lowest bound for Io's initial orbit. The 5.900 R_J value is located just within Io's current orbital distance, and represents the value of Q_J if Io's orbital distance has increased only very slightly (by only 431.8 km) over 4.6 billion years. The value for Q_J associated with this last a_i is very high, and implies that very little dissipation is occurring in the system.

Figure 4.4 shows that Q_J increases as the assumed initial orbital distance of Io is set nearer its current distance, and increases to infinity as a_i approaches the current distance. This is to be expected - if Io's orbit has not expanded significantly over 4.6 Ga, Q_J would have to be very large and there would be little energy dissipation within Jupiter. Q_J is only larger than 2×10^6 at values of $a_i > 5.185 R_J$, and increases very rapidly for higher values of a_i - this value of Q_J is the upper bound derived by Yoder and Peale (1981). If this upper bound of Q_J is valid then the radius associated with it represents the uppermost realistic limit to Io's initial orbital distance.

Figure 4.4: Graph showing the value of calculated Q_j derived from assumed initial orbital distances of Io



It is important to remember that Q_J itself is assumed to remain constant with time.

The different values of Q_J shown in Table 4.6 are calculated assuming different values of a_i for Io - the table indicates that “if Io is assumed to form at [Column 2] R_J , the value of Q_J is found to be [Column 3]”. The calculated value of Q_J can then be used in all subsequent orbital calculations, along with the assumption that Io formed at the associated a_i .

Taking a realistic range of a_i for Io is between 3.85 and 5 R_J , we see that:

$$\begin{aligned} 1.2181 \times 10^6 < Q_J < 1.7280 \times 10^6 \\ (a_i = 3.85 R_J) \qquad \qquad (a_i = 5 R_J) \end{aligned}$$

These values lie well within the ranges defined by Yoder (1979) and Yoder and Peale (1981). It should be noted that the derived value of Q_J increases slowly from 1.1426×10^6 (at $a_i = 71398$ km) to 2×10^6 (at $a_i \sim 370200$ km) then rapidly increases asymptotically as the initial orbital distance of Io is set even closer to its present-day radius (theoretically, Q_J becomes infinite if Io has not moved at all).

4.4.2.3 The orbital evolution of the Galilean satellites

I can now take these initial orbital distances and show graphically how the orbital distance of Io (and the other satellites) varies over the history of the solar system. I shall assume that the system is 4.6×10^9 years old (i.e. that orbital evolution begins as the system is forming).

The orbital evolution is determined as follows:

$$(1) \quad Q_J = \frac{\frac{117}{4}(G/M)^{1/2} R^5 m t}{\left(a^{13/2} - a_i^{13/2}\right)} \quad [4.32]$$

is first used to determine the value of Q_J for an assumed r_i of Io.

$$(2) \quad a_i^{13/2} = a^{13/2} - \frac{\frac{117}{4}(G/M)^{1/2} R^5 m t}{Q_J} \quad [4.33]$$

is then used to determine a_i for Europa, Ganymede and Callisto, using their current values of a and the value of Q_J determined from step (1).

$$(3) \quad a^{13/2} = a_i^{13/2} + \frac{\frac{117}{4}(G/M)^{1/2} R^5 m t}{Q_J} \quad (4.38)$$

The evolution of each satellite's orbital distance can then be determined by calculating the current a at a given time t . In this case, I calculated a at 100 million year (3.15576×10^{15} s) intervals, from $t = 0$ (the formation of the Solar System) to $t = 4.6 \times 10^9$ years (the current age of the Solar System).

The results are shown graphically in **Figure 4.5**, **Figure 4.6**, and **Figure 4.7**. These graphs illustrate the effect of different values of Q_J (and therefore also of associated values of Io's a_i) on the evolution of the semimajor axes of the Galilean satellites over the lifetime of the Solar System. **Figure 4.5** shows the evolution for $a_i = 2.5 R_J$ (178495 km) where Q_J is 1.15×10^6 . **Figure 4.6** shows the evolution for $a_i = 3.85 R_J$ (356990 km - Io's proto-synchronous orbit) where Q_J is 1.22×10^6 . **Figure 4.7** shows the evolution for $a_i = 5.0 R_J$ (356990 km) where Q_J is 1.73×10^6 .

**Figure 4.5: Orbital Evolution of the Galilean satellites
for $a_i = 2.5 \text{ RJ}$ and $QJ = 1.15 \times 10^6$**

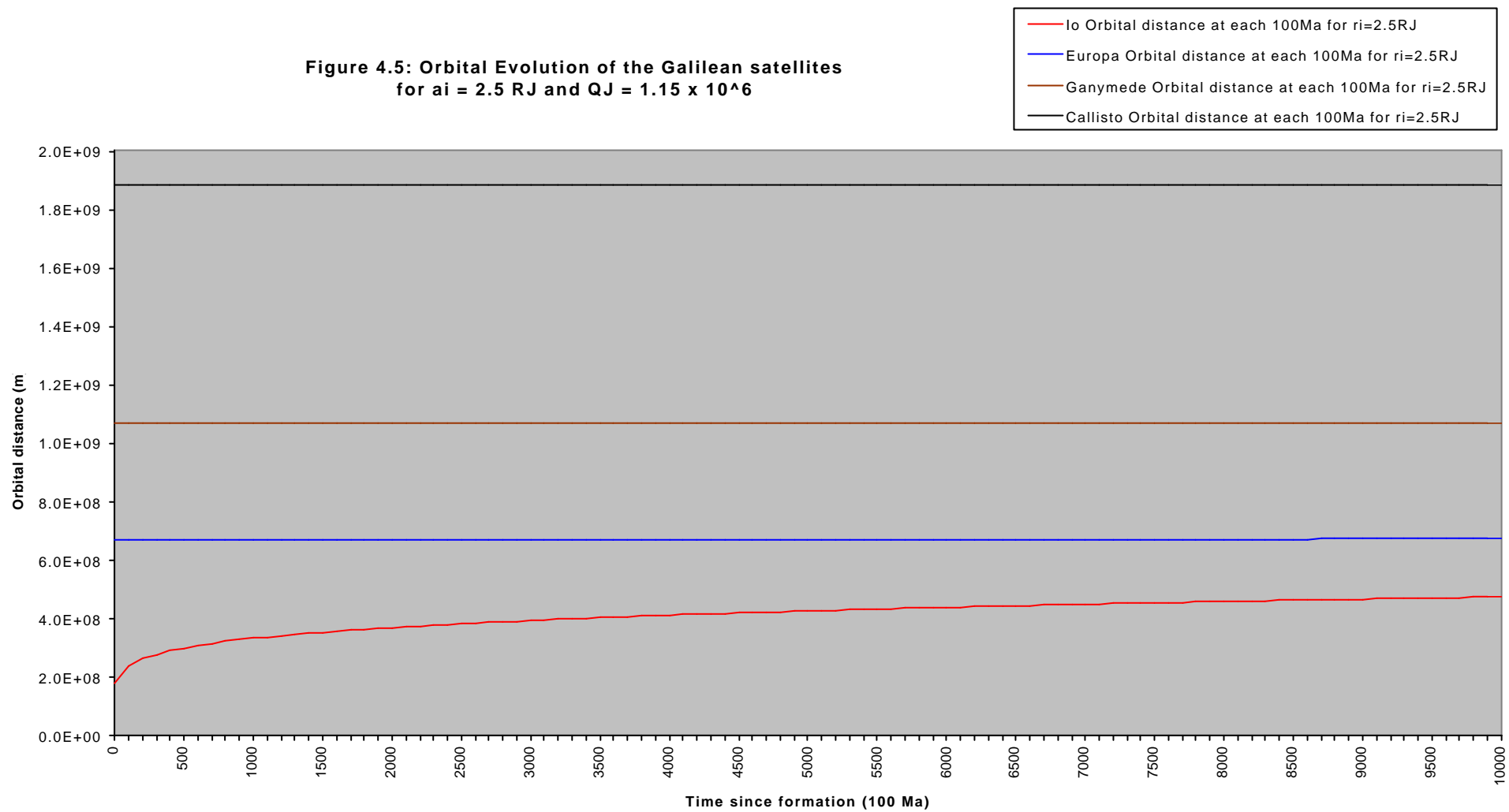


**Figure 4.6: Orbital Evolution of the Galilean satellites
for $a_i = 3.85 \text{ RJ}$ and $QJ = 1.22 \times 10^6$**

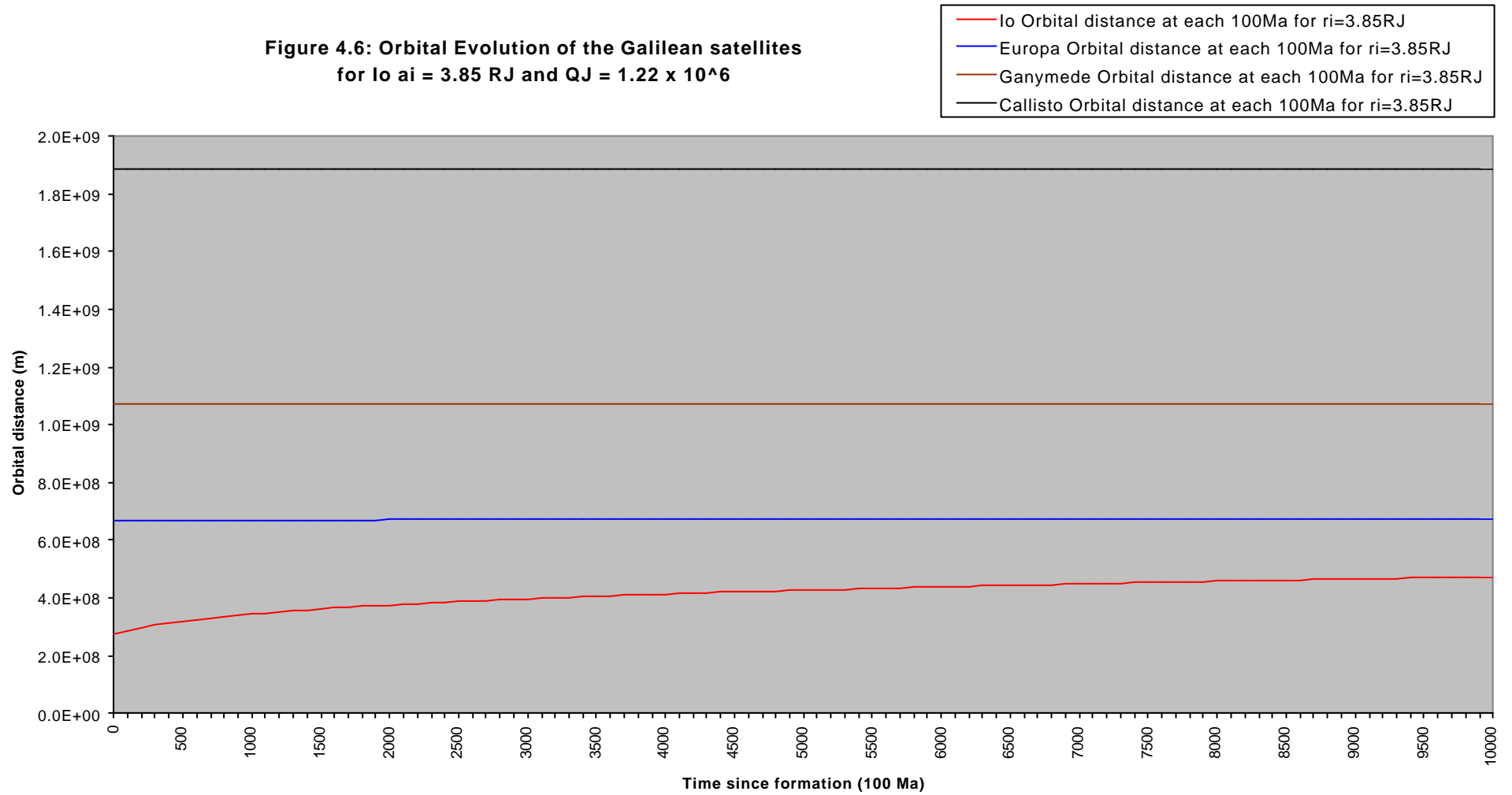
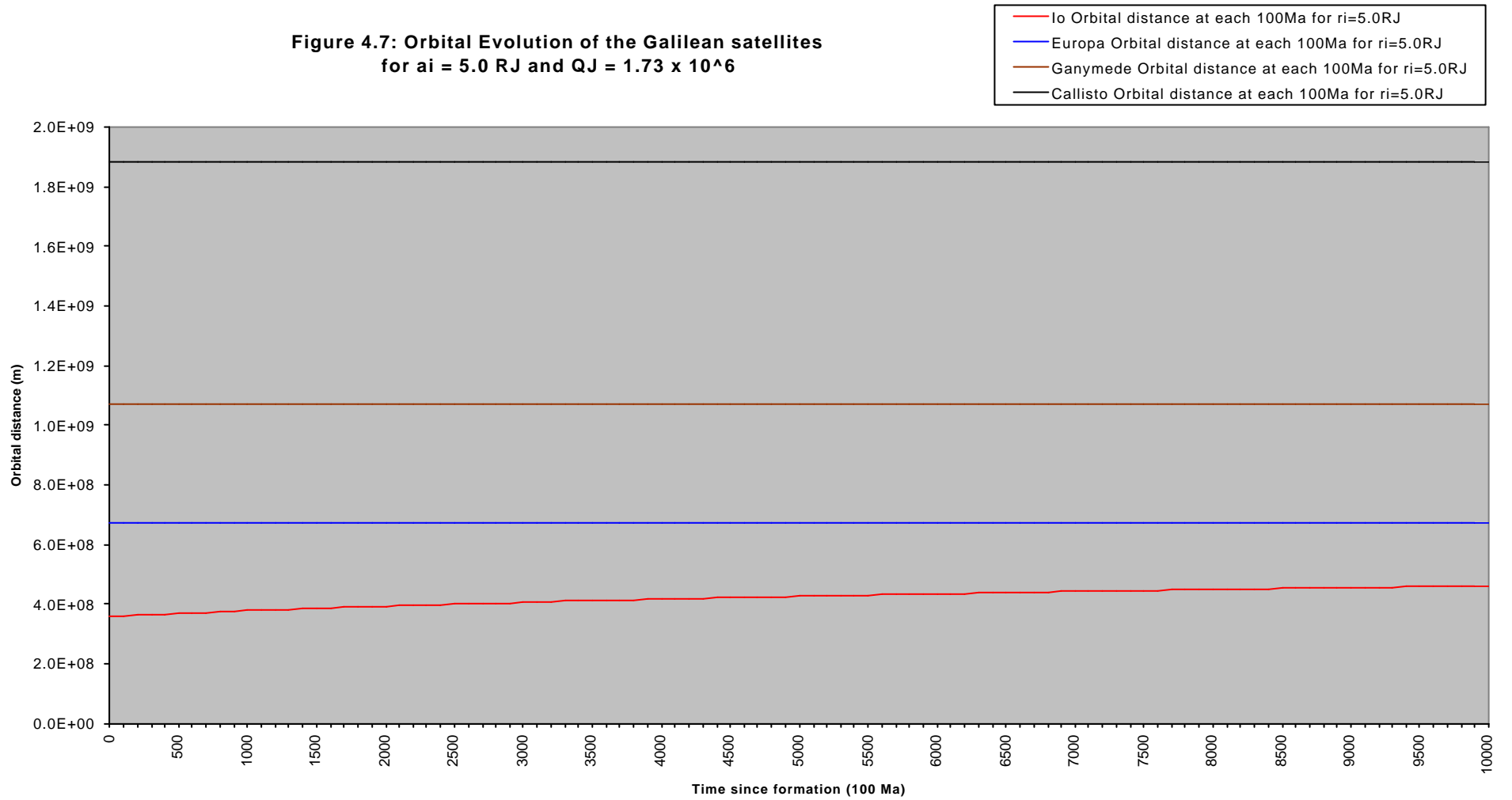


**Figure 4.7: Orbital Evolution of the Galilean satellites
for $a_i = 5.0 \text{ RJ}$ and $Q_J = 1.73 \times 10^6$**



These graphs show that whereas the value of Q_J significantly affects the rate of Io's orbital evolution (red line), the semimajor axes of the other Galilean satellites are barely affected at all, even over 4.6 Ga. The initial orbital distances for the Galilean satellites, given values of Q_J appropriate to the initial distance of Io, are shown in Tables 4.7, 4.8 and 4.9:

Table 4.7: a_i of Galilean satellites given Io $a_i = 2.5 R_J$, $Q_J = 1.15 \times 10^6$

	Io	Europa	Ganymede	Callisto
current a (km)	421680	670990	1070300	1882600
initial a_i (km)	178495	668263	1069696	1882591
Da (km)	243185	2729.27	639.87	20.78

Table 4.8: a_i of Galilean satellites given Io $a_i = 3.85 R_J$, $Q_J = 1.22 \times 10^6$

	Io	Europa	Ganymede	Callisto
current a (km)	421680	670990	1070300	1882600
initial a_i (km)	274882.3	668421.9	1069697.6	1882580.4
Da (km)	146797.7	2568.1	602.4	19.6

Table 4.9: a_i of Galilean satellites given Io $a_i = 5.0 R_J$, $Q_J = 1.73 \times 10^6$

	Io	Europa	Ganymede	Callisto
current a (km)	421680	670990	1070300	1882600
initial a_i (km)	356990	669185.3	1069875.5	1882586.2
Da (km)	64690	1804.7	424.5	13.8

These tables clearly illustrate that irrespective of Io's a_i , the distance over which Europa's orbit expands over 4.6 billion years is $\sim 10^3$ km. Da for Ganymede is $\sim 10^2$ km, and Da for Callisto is $\sim 10^1$ km.

Now that I have mapped out the evolution of the system for two extreme values of Q_J ($1.15 - 1.73 \times 10^6$) and a more likely intermediate value of 1.22×10^6 ($a_i = 3.85 R_J$), it is possible to search for commensurabilities within the system. This should enable us to determine when the satellites entered the orbit-orbit resonances that they currently occupy.

Recall from Section 4.1.2 that orbit-orbit resonances occur when the ratio of the orbital periods is a small integer. The ‘strongest’ orbit-orbit ratio is the 2:1. ‘Weaker’ resonances (e.g. 5:1, 10:1, 7:3) are conversely easier to break out of (Murray and Dermott, 1999). Since the gravitational interaction between the two bodies is reinforced most often, systems usually ‘lock’ into 2:1 resonances. Although tidal evolution is still occurring to push the orbits of each satellite out at different rates, it is not possible for this evolution to ‘break’ such a strong resonance - instead the pair evolve outwards at the same rate, maintaining the 2:1 lock. Conversely, tidal evolution can overcome the weaker resonant locks, allowing the system to pass through the resonance and continue evolving towards 2:1.

The commensurabilities for the systems shown in Figures 4.5 - 4.7 are tabulated in Appendix 3. This allows us to determine when the satellites could have passed through commensurabilities in the early history of the system - the possible histories of the system are summarised in Tables 4.10, 4.11 and 4.12:

Table 4.10: Orbital evolution since formation (Io $a_i = 2.5 R_J$, $Q_J = 1.15 \times 10^6$)

0 - 4600 Ma	Callisto and Ganymede in 7:3 resonance
0 - 4600 Ma	Europa and Ganymede in 2:1 resonance (locked).
100-700 Ma	Io and Ganymede pass through 5:1 resonance.
200 - 400 Ma	Io and Europa pass through 5:2 resonance.
1900 - 4400 Ma	Io and Callisto pass through 10:1 resonance.
4300 - 4600 Ma	Io and Ganymede in 4:1 resonance.
4400 - 4600 Ma	Io and Europa in 2:1 resonance (locked).

Table 4.11: Orbital evolution since formation (Io $a_i = 3.85 R_J$, $Q_J = 1.22 \times 10^6$)

0 - 4600 Ma	Callisto and Ganymede in 7:3 resonance
500 Ma	Io and Europa pass through 3:1 resonance
1100 - 4600 Ma	Europa and Ganymede in 2:1 resonance (locked).
1500 - 1800 Ma	Io and Ganymede pass through 5:1 resonance
2700 - 4400 Ma	Io and Callisto pass through 10:1 resonance
4400 - 4600 Ma	Io and Ganymede in 4:1 resonance.
4450 - 4600 Ma	Io and Europa in 2:1 resonance (locked)

Table 4.12: Orbital evolution since formation (Io $a_i = 5.0 R_J$, $Q_J = 1.73 \times 10^6$)

0 - 4600 Ma	Callisto and Ganymede in 7:3 resonance
750 Ma	Io and Europa pass through 3:1 resonance
1300 - 4600 Ma	Europa and Ganymede in 2:1 resonance (locked)
1700 - 2000 Ma	Io and Ganymede pass through 5:1 resonance
2800 - 4500 Ma	Io and Callisto pass through 10:1 resonance
4400 - 4600 Ma	Io and Ganymede in 4:1 resonance
4500 - 4600 Ma	Io and Europa in 2:1 resonance (locked).

It should be noted that resonances do not have to be *exact* in order to affect other satellites - the present values for the orbital periods are not in exact 2:1 ratios, as shown in the top row of the tables in Appendix 3. I assume that a resonance occurs when the ratio is ± 0.005 (e.g. a 5:1 resonance occurs when the ratio of orbital periods is between 0.195 and 0.205).

There are several interesting features to note in these scenarios. In all three scenarios, Io enters some ‘weak’ resonances early in the history of the system. Since Io’s orbital evolution is quite rapid - particularly for lower values of Q_J - I assume that these resonances are passed through quickly, and are not permanent. Obviously these resonances cannot be permanent, since Io is in a 2:1 resonance with Europa today. These weak resonances will have some effect on the orbital evolution rate (also affecting eccentricity, inclination and other orbital parameters) that is not quantified here. Goldreich (1965) shows that (stable) mean motion commensurabilities between pairs of satellites will act to redistribute angular momentum from their primary’s spin between their orbits in such a way that the orbits evolve to maintain the commensurability. Thus, the orbit of a satellite involved in an orbital resonance evolves more slowly than it did when it was evolving independently before reaching the commensurability.

Another interesting result is that in all scenarios Callisto and Ganymede formed in a 7:3 resonance, and remain there for the lifetime of the solar system. This is not particularly surprising given what I have shown in Figures 4.5 - 4.7 - the orbital evolution rates are very small in the outer Galileans, irrespective of which Q_J values are used for Jupiter. However, it is interesting that these values **are** commensurate, even if the resonance is weak. It is possible that gas drag and other similar effects unique to the protojovian

nebula environment conspired to put these satellites in the 7:3 resonance as they were forming - or alternatively this is just a coincidence. It is also interesting to note that no other authors have described this resonance, despite it being much more exact than the other resonances. Also of note are the 5:1 and the 10:1 resonances with Ganymede and Callisto respectively that Io passes through between 1500 and 2000 Ma after formation. These have also not been investigated by other authors.

The key feature that all of these scenarios share is that Io enters a 4:1 resonance with Ganymede at 4350 ± 50 Ma and enters a 2:1 resonance with Europa at 4350 ± 50 Ma. In addition, Europa and Ganymede either form in a 2:1 resonance (if Q_I is low) or rapidly evolve into it (if Q_I is high).

My results imply that the current 4:2:1 resonance between Io, Europa and Ganymede is quite young - only two hundred million years at most. It also paints a very different picture of the evolution of the system to that described by Yoder and Peale (1981), who describe a sequence of events in which Io's orbit increases more rapidly than Europa's and Ganymede's because of their distance from Jupiter. As Io moves outwards, it is first captured into the 2:1 resonance with Europa, and then the pair evolve outward together (more slowly, because of the resonance) until Europa reaches the 2:1 lock with Ganymede. In their scenario, Ganymede is the last body to enter the resonance, and Io has been in resonance the longest.

My scenarios indicate the reverse - that Ganymede is the oldest body in the resonance, and Io is the newest. First, Europa entered a 2:1 resonance with Ganymede - either as it formed or within 1.5 billion years after formation (if Q_I is high). This would probably

cause heating in both satellites, affecting their surface geology - this heating could be responsible for the formation of Bright Terrain on Ganymede, which has been dated at between 1 and 3 billion years old (Zahnle *et al.*, 1998). This 2:1 system settled, as Io continued to evolve outward from Jupiter. Nearly 3 billion years later, Io entered a 4:1 resonance with Ganymede, and slipped into the 2:1 lock with Europa very soon afterwards, creating the 4:2:1 system we see today. Note that since Europa and Ganymede would be in their 2:1 resonance at the time, it is likely that Io entered the resonances with them slightly earlier than indicated here. Thus, the Laplace Resonance appears to be recent.

This could explain why Io is still so active today - Io may even have been rapidly transformed from an inert Moon-like body into the volcanic body it is today by dissipation caused by a rapid increase in the eccentricity of its orbit as a result of entry into the 2:1 resonance.

If the older Europa:Ganymede resonance did not significantly affect the surface and interior of Europa, then the heating from the Io:Europa resonance (and the Laplace resonance involving all three bodies) could at least have melted the surface and destroyed any ancient terrain. Ganymede would remain largely unchanged by the new resonance.

4.4.3 Failures of the model

There are, however, several problems that may cause my models of orbital evolution to deviate significantly from reality. The most important is that I neglect to account for mutual perturbations between the satellites. Even when they are not in resonance, the gravitational interaction between the satellites do affect their orbits as they travel around Jupiter. Second, I am only considering the semi-major axis evolution here - in reality, the eccentricity, inclination, and other orbital parameters such as argument of perihelion are also affected by these perturbations and resonances. Passage through resonances is not necessarily as simple as I have assumed here - depending on exactly how the satellites approach resonance, the resulting interactions may be stable, unstable, or chaotic (Murray and Dermott, 1999). Some of these complications are discussed more fully - with specific reference to Ganymede's orbital evolution - in my analysis of Showman and Malhotra's (1997) papers presented in Chapter 5.

Another potential problem is that it is impossible to determine the amount of time a satellite spends in an orbital resonance. If the lower-order early resonances that Io passes through are real, we cannot account for the time Io spends in them or passing through them. Recall that the orbital evolution rate of both satellites involved slows down compared to their evolution when independent of each other. This means that we lose a degree of certainty as to exactly when Io enters subsequent resonances.

The early 3:1 Io:Europa resonance that occurs between 500 and 1000 Ma after formation for higher values of Q_J is somewhat more difficult to break, since it is a higher order resonance than a 5:1 or 10:1. It is obvious that the pair must have escaped from this resonance (if they did pass through it) since they are in a 2:1 lock today. Again, it is likely that the resonance was very short lived because of Io's rapid outward evolution (Europa's orbit was almost the same as it is today even during this early period). This may also have slightly delayed Europa's entry into the subsequent Europa:Ganymede 2:1 resonance \sim 600 Ma later. It is interesting to note that it is very difficult to identify any changes in the interiors of Io and Europa that would have occurred as a result of tidal dissipation during the 3:1 resonance - the heating from the 2:1 resonance has probably overwhelmed anything that could be specifically tied down to the earlier resonances.

In the case of the basic model described here, I use equation (4.32) to calculate Q_J based on Io's current orbital distance a and an assumed a_i . However, since Io has been involved in orbital resonances, the current a is actually smaller than it should be if Io's orbit evolved independently of the influence of the other satellites over 4.6 Ga. However, this is not as significant a problem as it may appear to be. In order to be *locked* into a resonance, the commensurability ratio between the two satellites must remain the same, and not increase gradually over time. Figures 4.5 - 4.7 show that the outward orbital evolution of Io is still rapid during the first 2 billion years of its orbital evolution, and that it is rapid for all realistic values of Q_J . For the early low-order resonances it is likely (as described previously) that the orbital radius of Io increases too rapidly to allow the commensurability to stabilise and thus cause an actual resonance lock.

To be fully realistic, I should use a larger value for the current a of Io than the existing value in equation (4.32) to take into account the slower orbital evolution while in the resonance - this larger value represents the value of a reached if Io's orbital evolution had been unimpeded by resonances. Unfortunately, there is no method by which this distance could be calculated. One could guess a value, and assume an initial starting distance as before and thus be able to calculate Q_J . However, there would then be no means to determine the current a , the larger a , or the a_i of any of the other Galilean satellites since the only term known for equation (4.32) would be the new value of Q_J (the initial orbital position of the other satellites is not constrained as it is for Io). This would therefore be a significant problem. However, Io has entered the 2:1 and 4:1 resonances with Europa and Ganymede comparatively recently, which means it is likely that the outward evolution of Io has not been sufficiently retarded by these resonances to significantly modify the value of Q_J calculated here. Thus, it is likely that the values of Q_J calculated here for the various assumed Ionian a_i values are valid.

One possible alternative approach mentioned in Section 4.4.1 would be to use Callisto's orbit to determine Q_J . The original rationale to do this was that Callisto did not appear to have been involved in a resonance - however, we have seen that Callisto was and still is in a 7:3 resonance with Ganymede. Furthermore, the range of possible a_i values for Callisto is much less well constrained than that for Io. If we were to place Callisto's a_i at Ganymede's orbit (1070300 km from Jupiter) we would find that the calculated Q_J is ~ 80 . This value is far too low compared to those accepted for Gas Giants (though it is more appropriate for terrestrial planets like the Earth), and results in unreasonably rapid orbital evolution rates. Even if Callisto's a_i is set at 1880000 km from Jupiter (2600 km within its present orbital distance), Q_J is $\sim 1 \times 10^4$ - far too low to be realistic. We only find

reasonable values of $Q_J > 1 \times 10^6$ when Callisto's a_i is set at 1882580 km - only 20 km short of its current orbital distance. This distance corresponds to the values shown on Tables 4.8 - 4.10, and indicates that the Q of Jupiter must indeed be $\sim 1 \times 10^6$.

Yoder and Peale (1981) propose a sequence of key events that describes the orbital evolution of the Galilean satellites - I examine this here with added notes on the behaviour of Q_J . I summarise their version of events in *italics*, with my subsequent comments (based specifically on my model in which Io forms at 3.85 R_J) written in normal text.

1) All four satellites form 4.6 Ga ago at their initial orbital distances, far from any commensurabilities, and commence their orbital evolution. Their evolution is independent and based solely on tides raised on and by Jupiter, based on the value of Q_J which is $\sim 10^6$. The initial free eccentricity of Io's orbit is almost completely damped within 10^7 years due to its proximity to Jupiter. (Y&P, 1981)

My model is similar to this assessment, with one major difference - the Galileans do not start far from any commensurabilities - Ganymede and Callisto must start in a 7:3 resonance that they remain in today, and Europa and Ganymede start near the 2:1 resonance. Io starts at 3.85 R_J , and begins to move rapidly away from Jupiter.

2) Io's orbit evolves outwards faster than that of Europa, until it reaches a 2:1 mean motion commensurability with Europa. Resonant interactions between the two increase Io's forced eccentricity as the commensurability is approached, causing a significant increase in tidal dissipation and heating within Io. The forced eccentricity continues to increase until it reaches a critical value (~ 0.0026) and entry into the resonance is completed. Thereafter, the orbits of the two satellites evolve together so that the commensurability is maintained - Io moves outwards more slowly in the resonance than it did before the resonance. (Y&P, 1981)

Here my models deviate significantly from that of Yoder and Peale (1981), since the first 2:1 resonance in the system occurs between Europa and Ganymede. The events of this stage are likely to apply to Europa when it enters the 2:1 resonance with Ganymede in my model (in an appropriately modified form that takes into account whatever the critical value should be for Europa). It is probable that something similar may occur when Io enters the early 3:1 resonance with Europa, but that resonance is ultimately doomed to be short-lived because of Io's much more rapid outward evolution from Jupiter. Still, there could be some significant variations in the eccentricity of Io's and Europa's orbit over the period of a few million years during the passage through/capture into these resonances, which could result in significant heating.

3) Since Europa's orbit is still evolving faster than that of Ganymede, Europa approaches and enters the 2:1 mean motion commensurability with Ganymede. However, since Europa is already in a 2:1 resonance with Io, a three-body 4:2:1 resonance forms and Io must work harder to transfer angular momentum from Europa's orbit to Ganymede's. Io's eccentricity increases to ~ 0.0042 and still more tidal heating occurs in the satellite, probably causing the volcanic activity and heat output observed on Io today. A steady state is then reached and the system evolves in unison, with the orbits of the three satellites evolving to maintain the commensurabilities.

Again, my models are very different to the Y&P (1981) model. The most recent stage of the system's evolution in my model is that Io enters the 4:1 and 2:1 resonances with Ganymede and Europa respectively. The orbital eccentricity of Io will increase as a result of entry into the 4:1 resonance with Ganymede, but this will not prevent it from entering the 2:1 resonance with Europa afterwards. If this is to be the cause of Io's volcanism, the eccentricity of Io must be pumped to high values to cause massive tidal heating within that satellite. Europa would also have to be subject to significant tidal dissipation as the effects of the new resonance with Io are restricted by its existing resonance with Ganymede. This must be sufficient to at least melt the icy surface of Europa, in order to create the young surface we see today. Ganymede meanwhile is likely to have some increased dissipation, but not enough to significantly affect its ice surface.

Once these resonances are entered, a steady state is reached and the system evolves in unison as described by Yoder and Peale (1981).

4.5 The next step

My model has produced some interesting results, despite containing some omissions and failings, and provides useful insights and clarifications into the orbital evolution of the Galilean satellites.

I have shown here that a realistic initial orbit distance for Io is most likely to be at the synchronous orbit for a Jupiter at the time the satellites were forming, which lies at 3.85 Jupiter Radii (2.747×10^8 m). This leads to the calculation of $Q_J = 1.22 \times 10^6$, which is well within the range of values calculated by other authors.

I have also presented a number of possible scenarios for the orbital evolution of the Galilean Satellites based on a range of realistic values for Q_J that range between 1.15×10^6 and 1.72×10^6 . In all cases, Io's orbit is found to evolve outwards rapidly while the orbits of Europa, Ganymede, and Callisto change very little over the age of the solar system. Europa and Ganymede are found to enter and remain in a 2:1 resonance early in solar system history, while Io enters the current 2:1 orbital resonance with Europa and 4:1 resonance with Ganymede very recently - only ~ 150 Ma ago.

My models are not entirely realistic since they do not account for interactions between the satellites as they evolve. Showman and Malhotra (1997a) and Showman *et al.* (1997b) have expanded significantly on the work of Malhotra (1991) and have proposed a more complicated and realistic scenario for the orbital evolution of the Galilean satellites. In the next chapter I shall examine their model, which relates primarily to the orbital and thermal evolution of Ganymede, while keeping in mind the insights gained in this chapter.

Chapter 5 The orbital and thermal evolution of Ganymede

In the previous chapter I discussed the Yoder and Peale (1981) model of the orbital evolution of the Galilean satellites and derived my own - simplified - simulation of their evolution. However, that simulation did not account for the effects of passing through resonances or of mutual non-resonant perturbations between the satellites. I also did not consider the effects of the evolution of other orbital parameters such as eccentricity, and orientation of the orbit in space.

In this chapter I expand the discussion to cover more recent work by Malhotra (1991), Showman and Malhotra (1997a) and Showman *et al.* (1997b), which presents a more realistic model than that of Yoder and Peale and myself. Since they also focus on the physical effect of this orbital evolution on Ganymede, I shall also take this opportunity to discuss some of the implications of their model for that satellite's evolution.

5.1 Tidal evolution into the Laplace resonance

Showman and Malhotra (1997a) and Showman *et al.* (1997b) have recently provided a very detailed model of the internal evolution of Ganymede that takes into account the highly differentiated nature of the satellite and the presence of a dense core and magnetic field, and most importantly the orbital evolution of the Galilean satellites as modelled by Malhotra (1991). While much of the actual orbital dynamics is rather complex, the results of initial simulations of the Jovian system that lead to the Laplace resonance seen today can be summarised here.

Malhotra (1991) shows that the Yoder and Peale (1981) model contains numerous approximations that masked some important dynamics in the orbital evolution. She performs a more detailed analysis that removes these approximations and examines the resonant interactions of all three satellites involved in the Laplace resonance simultaneously.

Malhotra proposes the existence of Laplace-*like* resonances - LLRs - based on the ratios of the mean motions of satellites within each dynamical pair. She defines the following terms:

$$\mathbf{z}_1 = 2n_2 - n_1 \qquad \mathbf{z}_2 = 2n_3 - n_2 \qquad (5.1)$$

These in turn define the following parameters:

$$\mathbf{u} = \frac{\mathbf{z}_1}{\mathbf{z}_2} \qquad \mathbf{z}_L = \mathbf{z}_1 - \mathbf{z}_2 \qquad (5.2)$$

Here, n is the satellite's mean motion, and the subscripts 1, 2 and 3 represent Io, Europa, and Ganymede respectively. Note that the symbols \mathbf{r} (rho) and \mathbf{w} (omega) were used in the Malhotra's paper, but I have changed them here to \mathbf{u} (upsilon) and \mathbf{z} (zeta) respectively to avoid confusion with the symbols used in Chapter 4. The current Laplace resonance is represented by $\mathbf{z}_1 \sim \mathbf{z}_2$, so $\mathbf{u} = 1$ and $\mathbf{z}_L = 0$. Malhotra finds that before entry into the present three-body resonance, all three satellites would have passed through other $\mathbf{z}_1:\mathbf{z}_2$ commensurabilities - the LLRs - where $\mathbf{z}_1/\mathbf{z}_2 = j/(j+1)$ or $(j+1)/j$ [$j = 1, 2, 3 \dots$].

Passage through these commensurabilities excites the orbital eccentricities of one or more of the satellites and thus provide a significant source of tidal dissipation. Two particular LLRs - $u = 3/2$ and $u = 2$ - have very high (≥ 0.9) probabilities of capture, so long as they are approached from below (with z_1/z_2 increasing with time). Capture into these LLRs appears impossible if they are approached from above but, in the one case of this that was examined, the satellites pass through the LLR from above without capture, then reverse and approach the LLR from below and *do* get captured into it.

Passage through these resonances could have served to pump up Ganymede's forced eccentricity to quite high levels (~ 0.07) and provided much tidal heating. However, a mechanism is required by which the satellites can escape the LLR and progress to the current ($z_1/z_2 = 1$) Laplace resonance. This mechanism hinges on the ratio Q^*/Q^*_J , where $Q^* = Q/k_2$, the ratio of a given body's Q (defined in Chapter 4) to its k_2 *Love Number*).

Love numbers are coefficients first defined by A. E. H. Love (1929). h_2 is a parameter relating the rigidity of the planet to the height of the vertical tide raised, and k_2 is related to the additional potential produced by the redistribution of mass caused by the deforming tidal potential. They are defined by:

$$k_2 = \frac{(3/2)}{1 + \tilde{m}} \quad (\text{Murray and Dermott, 1999}) \quad (5.3)$$

$$h_2 = \frac{(5/2)}{1 + \tilde{m}} \quad (\text{Murray and Dermott, 1999}) \quad (5.4)$$

Recall from Chapter 4 that:

$$Q' = Q(1 + \tilde{m}) \quad \text{where:} \quad \tilde{m} = \left(\frac{19m}{2gr} \right) = \left(\frac{38p r^4 m}{3Gm^2} \right) \quad [4.6]$$

From Equation (5.3) we can see that:

$$Q^* = \frac{Q}{k_2} = \frac{Q(1 + \tilde{m})}{(3/2)} = \frac{2}{3} [Q(1 + \tilde{m})] = \frac{2}{3} Q' \quad (5.5)$$

The Q of Jupiter is taken by Malhotra (1991) to be $Q_J \sim 5 \times 10^5$ - somewhat lower than the value I calculated in Chapter 4 - and Q_1 refers to Io, Q_2 to Europa, and Q_3 to Ganymede.

If Q_i^*/Q_J^* is constant, it is not possible to escape from the LLRs and there cannot be paths to the Laplace Resonance. However, by varying Q_1^*/Q_J^* and Q_2^*/Q_J^* , Showman and Malhotra (1997a) found that the LLRs could be disrupted and the satellites could continue to evolve to their current configuration. There are potentially four quantities that could change - Q_1^* , Q_2^* , Q_3^* , and Q_J^* (remember also that $Q_i^* = Q/k_2$). It is unlikely that there are any processes that can change the value of Q_J over the lifespan of the solar system - so the alternative (that they suggest) is to change either the Q or the k_2 values of the satellites. This can be achieved by melting (or freezing) the interiors of the satellites, which would change the satellite's bulk rigidity m and k_2 Love number and might also affect Q_s directly. This freezing or melting may also have a visible effect on the satellite surfaces.

Showman and Malhotra (1997a) took an initial value for Q^*_{1}/Q^*_{J} , (and fixed the Q^*_{2}/Q^*_{J} and Q^*_{3}/Q^*_{J} values) and increased this to a new value $(Q^*_{1}/Q^*_{J})_0$ at a given time t_0 - set to various values between $3300Q_J$ and $13300Q_J$ years - and ran their orbital evolution model.

For $\mathbf{z}_1/\mathbf{z}_2 = 3/2$, they found that the LLR was always disrupted by taking an initial value of 4×10^{-4} for Q^*_{1}/Q^*_{J} and increasing this to a new value of 1.3×10^{-3} at t_0 . In most cases, the system destabilised and entered a true Laplace Resonance ($\mathbf{z}_1/\mathbf{z}_2 = 1$), but it entered another LLR where $\mathbf{z}_1/\mathbf{z}_2 = 2$ when the time of disruption was later - although it should be noted that the path taken after disruption at *any* time is not predictable, so all that can be inferred from this is that it is much more likely for the system to enter a Laplace resonance than an LLR with $\mathbf{z}_1/\mathbf{z}_2 = 2$.

Increasing Q^*_{1}/Q^*_{J} to values in the range $4 \times 10^{-4} < Q^*_{1}/Q^*_{J} < 1 \times 10^{-3}$ did not disrupt the LLR at all. There was also a delay of $\sim 10^3 Q_J$ years after t_0 before disruption of the LLR actually occurred, which increased if Q^*_{3}/Q^*_{J} was decreased in otherwise identical runs. The LLR was more stable with smaller values of Q^*_{3}/Q^*_{J} , though if $(Q^*_{1}/Q^*_{J})_0$ was set at a larger value then the LLR was disrupted almost instantly at the low Q^*_{3}/Q^*_{J} values.

Showman and Malhotra (1997a) repeated these runs for $\mathbf{z}_1/\mathbf{z}_2 = 2$ and found that this LLR was generally more stable than the LLR with $\mathbf{u} = 3/2$. A larger value of $(Q^*_{I}/Q^*_{J})_0 \sim 1.9 \times 10^{-3}$ was required to disrupt this LLR from the same initial Q^*_{I}/Q^*_{J} as in the previous runs. **It should be noted that, in both cases, decreasing Q^*_{2}/Q^*_{J} by a factor of ~ 100 also disrupted the LLR.** The most likely way in which this can occur is to melt or partially melt Europa - this is discussed later.

They showed that are three main sources of instability when Q^*_{I}/Q^*_{J} is increased:

1) The resonance is unstable when the eccentricity of Io, e_I , exceeds a critical value. This occurs when Q^*_{I}/Q^*_{J} is increased to the large value of 10^{-2} while within the Laplace Resonance. When this occurs, the eccentricity of Io increases rapidly to 0.012, and the resonance is subsequently disrupted. This was predicted by Yoder and Peale (1981). For the LLRs this upper e_I limit is smaller, so they are more easily disrupted if Q^*_{I}/Q^*_{J} is increased to large values.

2) LLRs tend to occur when \mathbf{z}_1 and \mathbf{z}_2 are both small. However, if these values get *too* small, the satellites exit the LLR, go through a period of chaotic evolution, and eventually reach the Laplace resonance which tends to dominate the phase space where \mathbf{z}_1 and \mathbf{z}_2 tend to 0.

3) If Q^*_I/Q^*_J is increased by a factor of greater than ~ 2.6 after Io's eccentricity has reached equilibrium, the tidal term in the pendulum-like equation for $z_1/z_2 = 2$ changes sign. This causes the tidal torque to change direction slowly, which in turn causes the libration amplitude to increase until the resonance librations are disrupted. This factor is different for the other LLRs.

Exactly which of these sources of instability is the most important when Q^*_I/Q^*_J is increased depends on the state of the system. However, it is clear that a sufficiently large increase in Q^*_I/Q^*_J during the course of the evolution is certain to disrupt the system.

Recall that the orbital evolution runs of Showman and Malhotra begin with Q^*_I/Q^*_J at a particular value, which is then increased to $(Q^*_I/Q^*_J)_0$ at time t_0 . During the successful capture runs, the orbital evolution generally proceeded as follows (specifics depend on the parameters of the model):

Initially, z_1/z_2 decreases as the orbits of Io and Europa evolve, until it reaches a resonant value ($3/2$, 2 , or another value) and enters an LLR. It remains there until t_0 , when it is disrupted and (usually) enters the Laplace resonance. During the LLR, Io's eccentricity increases gradually, Europa's forced eccentricity is increased greatly during the LLR and fluctuates over a range of large values, and Ganymede's forced eccentricity increases gradually to ~ 50 times greater than its pre-LLR value where it remains until the LLR is disrupted.

When Q^*_I/Q^*_J is increased to $(Q^*_I/Q^*_J)_0$, the system begins to destabilise. Io's eccentricity continues to increase towards the new equilibrium value for the new $(Q^*_I/Q^*_J)_0$, while on average z_1/z_2 stays around the resonant value. During this period Ganymede's large eccentricity is maintained at a large value, although it does not continue its previous increase caused by its presence in the LLR. This is because the LLR remains temporarily in place given the new $(Q^*_I/Q^*_J)_0$, but there is no longer the same secular transfer of orbital energy and angular momentum to Ganymede from Io and Europa. Eventually however, the 3/2 or 2 LLR becomes unstable when Io's mean forced eccentricity approaches 0.005. After this, a short ($10^3 Q_J$ years) period of chaotic large-amplitude fluctuations in all dynamical variables follows which culminates in the satellites entering the Laplace resonance. The Laplace resonance cannot maintain Ganymede's high forced eccentricity, so e_3 plummets rapidly. It appears likely in this case that the parameters of the system conspire in such a way that all three causes of instability described previously occur simultaneously.

5.1.2 Discussion

There are however (at this stage) some problems with this model - first, the authors have used a simple step-function for the time variation of Q^*_I/Q^*_J , meaning that they suddenly increase it at a specific point in time, rather than gradually increasing it over a longer period. They suggest that using a more realistic increase may be able to explain the other discrepancy in their calculations - that the observed free eccentricity of Ganymede (0.0015) is still about two times larger than the value they calculate (Ganymede's free eccentricity is not pumped by the current Laplace resonance, but it could be pumped by earlier resonances and LLRs). This discrepancy cannot

be explained by a large impactor such as the one that formed the Gilgamesh basin on Ganymede either - the mass of the impactor even in the most ideal situation has to be $\sim 10^2 - 10^3$ times larger than that producing Gilgamesh in order to produce the increase in Ganymede's eccentricity. However, exploratory runs with a gradual (billion-year) increase from Q^*_I/Q^*_J to $(Q^*_I/Q^*_J)_0$ result in more stable LLRs (though they can still be disrupted), and allow the free eccentricity of Ganymede to increase further within the resonance before disruption can occur. A slow change up to $(Q^*_I/Q^*_J)_0 = 10^{-3}$ leads to a free eccentricity of 0.001 in the runs where disruption does not occur, and a larger free eccentricity may be possible if Q^*_I/Q^*_J becomes even larger before disruption. It therefore looks likely that this is not a problem. However, it is not clear to me at this time whether such a gradual increase in Q^*_I/Q^*_J would be able to continue for the required length of time - the increase would have to occur faster than the system could stabilise, and continue until it is forced to stop when Q^*_I/Q^*_J reaches $(Q^*_I/Q^*_J)_0$.

A gradual change in Q/k_2 to increase Q^*_I/Q^*_J is certainly not ruled out over the course of the LLR (as described in the previous paragraph), but it is not clear whether the sudden, discrete change at the end of the LLR as used in most of the Showman and Malhotra models is possible. If Q/k_2 was not allowed to change until some critical level of dissipation occurred (e.g. something that results in a runaway melting of the interior), then such a discrete increase may actually be possible. The feedback between the orbital evolution and Q^* makes it difficult to determine the effects of one on the other.

Showman and Malhotra (1997a) suggest that there are two main methods by which the LLR could be disrupted - by increasing Q^*_{I}/Q^*_{J} by a factor of up to ~ 5 , or decreasing Q^*_{2}/Q^*_{J} by two orders of magnitude. Recall that both terms Q and k_2 are dependent on bulk rigidity. Since $k_2 \sim 1$ for a mostly molten interior and $k_2 \sim 0.02$ for a mostly solid interior, melting the interior would increase k_2 whereas solidifying it would decrease it (assuming Q remained unchanged). However, the value of Q is smaller for less rigid bodies and larger for more rigid bodies - melting the interior of a body would decrease Q , whereas freezing the interior would increase Q . These two effects combine constructively so that melting the interior of a satellite always decreases Q^* , while solidifying the interior always increases Q^* . A warm, molten satellite therefore has a smaller value of Q^*_i than a cold, rigid one.

Increasing Q^*_{I}/Q^*_{J} would require an increase in Q^*_{I} or a decrease in Q_J - conversely, decreasing Q^*_{2}/Q^*_{J} would require a decrease in Q^*_{2} or an increase in Q_J . Since it is not likely for Q_J to change with time, that process can effectively be ruled out. The only options remaining are therefore to increase Q^*_{I} or decrease Q^*_{2} - by freezing Io or melting Europa. The implication is that Io was either hotter during the LLR and somehow cooled enough towards the end of the LLR to disrupt it and force the system into the Laplace resonance, or that Europa suffered significant tidal heating at that point.

An increase in Q^*_{I}/Q^*_{J} requires that Io cools and solidifies to some degree at the end of the LLR. Given that Q^*_{I}/Q^*_{J} only has to increase by a factor of 2 to 5 for the LLR to be disrupted, it may not take much cooling to induce disruption of the LLR. However, Io's eccentricity increases gradually over the duration of the LLR (Showman and Malhotra,

1997a), so it is likely that *more* of Io's interior was molten towards the end of the LLR as a result of the slowly increasing tidal dissipation, thus decreasing Q^*_I . A resolution to this problem is possible, however - if enough of the interior were to melt, convection would become a more effective heat transfer process and would cool the satellite more rapidly. Cooling and solidification of the interior would result in an increase in the magnitude of Q^*_I , allowing the orbital eccentricity to increase and more dissipation to occur - the variation becomes cyclical. Showman and Malhotra (1997a) found that the LLR became less stable when Q^*_I reached high values in this cycle, and suggest that after a few of these cycles it becomes so unstable that the LLR is disrupted and the system is forced into the Laplace resonance.

Ojakangas and Stevenson (1987) discuss a similar mechanism that allows Q^*_I to vary cyclically with time. They also propose that the eccentricity of Io's orbit is linked to the state of its interior. When Io is hot and at least partially molten, energy is drawn out of the orbit and eccentricity decreases. Volcanism and convection then remove heat while the eccentricity decreases, and so Q^*_I increases as Io cools. The energy can then be removed convectively faster than it is being generated by tidal dissipation so the satellite cools further. However, the increasing Q^*_I causes the eccentricity to increase, which increases dissipation and heating, until the heat generation surpasses the convective heat loss rate and a thermal runaway results and the cycle repeats.

However, the Ojakangas and Stevenson (1987) model takes place entirely within the Laplace resonance. - Showman and Malhotra (1997a) use the possible variability of Q^*_I to break the system out of the LLR and into the Laplace resonance. The latter model does not preclude the continuation of the oscillations in Q^*_I within the Laplace resonance so the two models are compatible. The implication is that Io is presently cooling after its passage through the LLR (or possibly a subsequent Q^*_I oscillation within the Laplace resonance) but remains sufficiently molten for its surface to remain volcanically active. In the future it may cool sufficiently for its eccentricity to increase again and runaway melting to occur - but it will do so while remaining within the Laplace resonance, and will not enter another LLR in the process.

However, this is only part of the story. Showman *et al.* go on to elaborate specifically on what happens within Ganymede during passage through the LLRs in their second (1997b) paper. There, they attempt to model these changes, so this is the first place to look for the solution to the problem.

5.2 The orbital and thermal evolution of Ganymede

5.2.1 Overview

Showman *et al.* (1997b) raise some intriguing possibilities that show just how complex the Jovian System could be, which are summarised in this section and discussed in the next. They show that differentiation of Ganymede (described in more detail in Chapter 6 of this thesis) into a silicate/metal core and ice mantle/crust must have happened *early* in the satellite's history. Significantly, the differentiation must have occurred *before* the formation of 'Dark Terrain' (DT) - i.e. 'Dark Terrain' is not the original, primordial surface of Ganymede, though it is must obviously still be a very ancient one (they place DT formation at 3.5 - 4.0 Ga). The logic behind this is that this ancient differentiation would have re-arranged material within Ganymede such that denser material was near the centre and the less dense material was nearer the surface - any primordial surface terrain would have been destroyed in this redistribution of material. Since the DT is still recognisable today, it must have been the *consequence* of this differentiation, not the predecessor. This also implies that the material comprising the Dark Terrain must have a density similar to that of clean ice if the satellite has differentiated. All this being the case, global differentiation and DT formation are ancient events and can not be related to passage through orbital resonances.

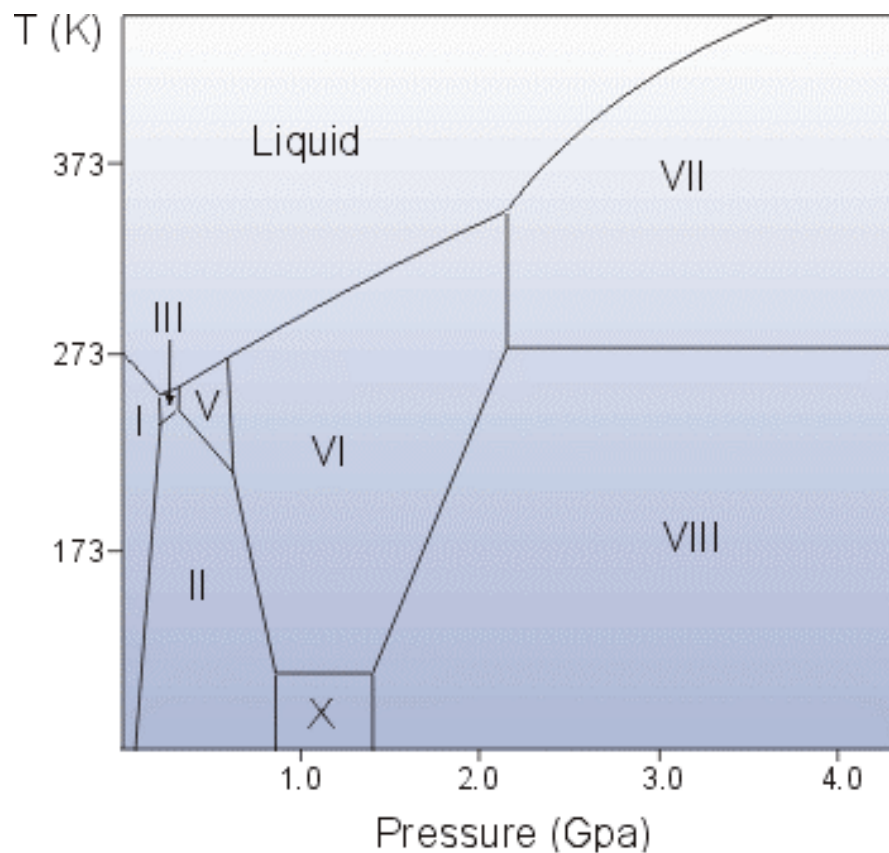
The authors caution that in most cases there is generally not enough tidal heating to increase the upper icy mantle activity enough to lead to resurfacing - the scenarios presented in Showman and Malhotra (1997a) are optimum scenarios. The most dramatic increase in tidal heating rate

occurs when Q_I is rather small (near its time-averaged lower limit of 3×10^4) and the system passes through the $\nu = 2$ LLR, which is the most powerful of the eccentricity-pumping LLRs and is the one that is used in all the models shown hereafter. However, Q_I is unknown and as described in the previous chapter is likely to be at least an order of magnitude larger than the lower limit 3×10^4 - if this is the case, the heating rate will be smaller - also, if the system passes through the $3/2$ or $1/2$ LLR then the heating rate is decreased further. In other words, it is likely that tidal heating as a result of passage through the LLR is insufficient to significantly affect the internal structure and surface of Ganymede. This makes no assumptions about the state of Ganymede's interior during the Laplace-like resonance, however

I have shown in Section 5.1 that the state of a satellite's interior and its orbital evolution (and the tidal dissipation it suffers) are intimately coupled. If the Q/k_2 value of a satellite were to decrease rapidly, the power dissipated through short time intervals would increase dramatically, and this can overwhelm the radiogenic heating. One way to decrease Q^* (i.e. Q/k_2) is by changing the bulk rigidity μ (and internal structure and temperature) of the satellite - e.g. by melting/freezing. The increase in the eccentricity that results from being within the LLR is quite likely to be sufficient to cause increased dissipation and slight warming in the interior of a frozen satellite with a high Q^* . This would then decrease Q^* slightly, which would increase the dissipation further and decrease the eccentricity more (though Q^* must decrease faster than e^2 for this to work), thus accelerating the warming and decreasing Q^* further, and so on. A positive feedback results, in which the satellite undergoes massive 'runaway' heating and e plummets over a very short time interval (Showman *et al.*, 1997b).

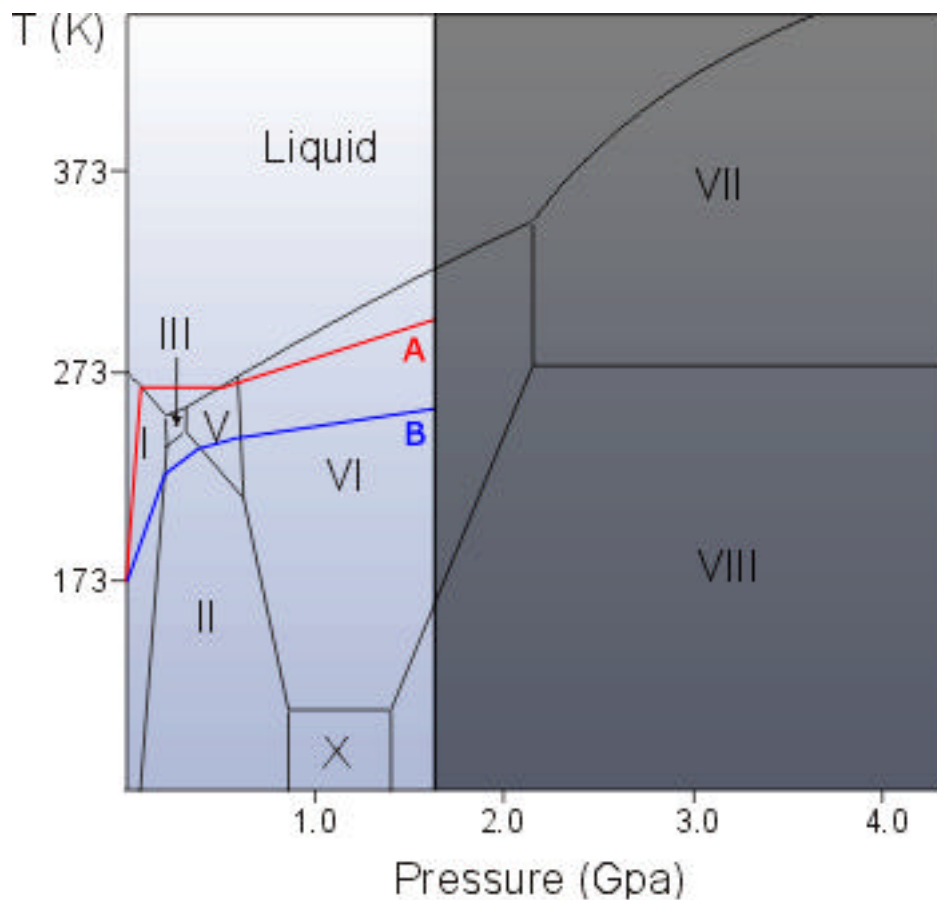
Of course, most of the satellites are not composed solely of high-melting point silicate material - a large amount of water ice is present on Europa, Ganymede, and Callisto. Water is a strange substance, with at least 12 different solid phases that form as certain pressure and temperature thresholds are passed. These are referred to by roman numerals (e.g. Ice I, Ice III, Ice VII), and have different crystallographic and physical properties. Ice I - the phase that we are familiar with in ambient conditions on Earth - is unusual in that it is one of the few solid phases that is less dense than the liquid phase of the substance - however, all the other phases are denser than pure water. The phase diagram of Ice is shown in Figure 5.1, and the properties of the various forms of ice are listed in Fortes (1999).

Figure 5.1: The phase diagram of water ice.



As the label implies, “high pressure ices” (Ice II - X) will form under pressure - at the sort of pressure found in a satellite’s interior. Therefore, there is a progression of ice phases from the surface of a satellite to its deep interior. However, the temperature also determines what phase of ice is present at a given depth - if the temperature gradient through the satellite is high enough, there may even be liquid water present. Figure 5.2 shows two temperature/pressure profiles through a hypothetical Ganymedian satellite, and the shells of ice that result. Neither of these temperature profiles are intended to be realistic; they are merely used to illustrate the relation between temperature and ice phase.

Figure 5.2: Two profiles through a hypothetical Ganymedian satellite



Profile A (in red) results in a thin Ice I shell, overlying a deeper liquid water layer (the pressure can be used to determine the thickness of each shell). At the bottom of this ‘ocean’ lies a thin layer of Ice V, and a very thick layer of Ice VI down to the silicate interior (marked as the shaded region on the right of the diagram). Note that the temperature profile flattens while in the water layer - the temperature throughout the liquid layer is assumed to be the same because of convection. **Profile B** (in blue) produces a thick Ice I shell at the surface, overlying a thinner layer of Ice II, then Ice V, and a very thick ice VI layer above the silicate shell - no liquid ocean is present in this profile.

The results of running various models of orbital evolution with different parameters can be summarised into three types, all of which are largely controlled by the initial temperature of Ganymede before entry into the LLR that is modelled.

- 1) ‘Warm’ Ganymede. This is the typical result when Ganymede’s interior is warm (271 K), which is sufficient for a liquid water layer to exist before entry into the LLR, sandwiched between ice I on the surface and ice V and VI below, above a large rocky core (Showman *et al.* use a rocky core rather than a metallic core for their models). This water layer cannot exist unless the internal temperature is greater than 251 K, the ice I-III-liquid triple point. Melting would start here because the ice I-III boundary has the lowest melting point of the ice phase boundaries. Melting would consume the ice III, then the ice I and V layers, and eventually result in a thin ice I crust overlying a thick (hundreds of km) water layer with an ice VI layer below, overlying the rocky core (this is most similar to Profile A in Figure 5.2).

In such cases Q/k_2 remains low because of the existence of the large water layer (which lowers the effective rigidity of the satellite, and therefore also reduces k_2), and the eccentricity is never pumped up high enough (it only reaches 0.0002) to cause a ‘thermal runaway’. Instead, the temperature stabilises at around 260 K after 1.5 Ga and remains there until the LLR is disrupted at 2.6 Ga (an arbitrary time used in all the runs) by increasing Q^*_I/Q^*_J . After this, Ganymede’s eccentricity stabilises at 0.001 (roughly its current value), and the internal temperature decreases monotonically (latent heat of the water layer delays this a while) for a duration of ~ 1 Ga when it decreases to less than 251 K and the water layer freezes.

- 2) ‘Cold’ Ganymede. If the interior temperature is too small (170 K), the interior is frozen and Q/k_2 is large (since the effective rigidity of the satellite is high), so the tidal dissipation is also small. Although the eccentricity increases significantly to 0.02, the resulting dissipation is insufficient to significantly change the internal temperature during the resonance. By the time the LLR is disrupted at 2.6 Ga the internal temperature has not even increased by 10 K. After this time, e decreases to its current value and the interior cools. Therefore there is no runaway within such a ‘Cold’ Ganymede. This is more similar to Profile B in Figure 5.2.
- 3) ‘Just Right’ Ganymede. In what is very much a case of ‘Goldilocks Syndrome’, there are scenarios whereby the temperatures within Ganymede do allow runaways to occur. An intermediate starting temperature of 183 K allows Q/k_2 to be large enough for the eccentricity to increase to large values, but small enough for the dissipation caused by the eccentricity to warm up the satellite. Initially, the evolution looks like that of ‘Cold’ Ganymede, with e

increasing to 0.02 by about 1 Ga. However, over this time the Q/k_2 has also been decreasing slowly, but in this scenario it is large enough to ‘go critical’ - the warming accelerates and a runaway then occurs. The temperature rises rapidly (over a few times 10^7 years) and passes 251 K to form a water layer hundreds of km deep. Q/k_2 then decreases dramatically by two orders of magnitude, and the eccentricity also decreases suddenly. This particular run was done within the $\nu = 2$ LLR - the system remains there until 2.6 Ga when it is disrupted by the increase in Q^*/Q^*_J , which shows that the $\nu = 2$ LLR is stable against large decreases in Q^* (as are also the $\nu = 3/2$ and $\nu = 1/2$ LLRs). The minimum ice I shell thickness just before the LLR was disrupted in this particular scenario was found to be 80 km.

For large runaways to occur, the internal temperature before entry into the LLR must be between about 180 K and 200 K. This is only possible if there is no radiogenic heating that is keeping the inside of the satellite warm - however, in practice it is more realistic to assume that there will be ongoing radiogenic heating, assuming that Ganymede accreted from a carbonaceous chondrite composition. Showman *et al.* (1997b) have found that for most radionuclide distributions within Ganymede, the radiogenic heating will be more than sufficient to keep the mantle temperature above 200 K. In other words, the large runaways described in the ‘Just Right’ scenario appear to be impossible in these ‘realistic’ scenarios. There are a couple of ways around this that are largely dependent on how they evaluate the Q of the ice.

Despite this, their model does still allow for *small* runaways, triggered at higher temperatures. These smaller runaways are allowed to occur between 180 K and 251 K, and result in smaller temperature increases of +10 K to +30 K. The largest runaways, at about 190 K, cause a temperature increase of about +70 K, and also occur over the shortest time interval. Either way, it seems that whatever the size of runaway, a water layer is not necessarily a required result - a 'warm, frozen' Ganymede is an equally viable product. Runaways may be even larger if Q_I is smaller (and vice versa).

Showman *et al.* (1997b) observe that the sharp, linear edges of the 'Bright Terrain' (BT) suggests that they formed in a satellite-spanning system of graben. A popular explanation for the existence of BT is that it formed as a result of global expansion as a result of phase changes in Ganymede's interior (e.g. Squyres 1980). Showman *et al.* (1997b) also support the 'global expansion' concept but, like McKinnon (1981), suggest that since complete differentiation occurred very early in the history of Ganymede any expansion and lithospheric fracture accompanying that differentiation must have been unrelated to the formation of the BT later on. In fact, it would probably be very difficult to see today. **However, passage through a Laplace-Like Resonance can potentially result in heating, global expansion, and subsequent surface fracturing.** This is investigated next.

5.2.2 Global expansion due to ice melting

Showman et al. (1997b) model a small thermal runaway in Ganymede's ice shell, with initial temperatures of about 240 - 250 K. The volume change as a result of conversion of the various ice phases to liquid is calculated by treating the ice layers as shells and integrating the volume change over the whole shell thickness. The sequence of ice phases in a frozen interior of Ganymede consists of ice I at the surface, then 'high pressure' ice III, V, and VI phases, and the silicate mantle. As described in the 'Warm Ganymede' Section, 5.1.2, heating starts at the ice I-III boundary because the melting point of any of the ice phases is the lowest there (251 K), so a liquid water layer will begin to form there. Melting of the high pressure ice phases causes global expansion of Ganymede, since they are denser than water, but melting of ice I would cause contraction since it is less dense than water. Thus, for expansion to result, the melting high pressure ice phases must produce a greater volume increase than the volume decrease caused by ice I melting at the top of the water layer. It should be noted that the exact thickness of the ice layers is not given, but the authors state that the ice I thickness specifies the water layer depth and the other ice layer thicknesses, for a given rock core size, which itself is determined by the core density.

There is evidence that the room-pressure regime of negative thermal expansivity (α) at 0° to 4°C exists at higher pressures as well. This is the range of temperature in which water increases in density as it warms. Such a region would exist at the top of a water layer (possibly the top 10² metres for sufficient heat flux), and would be stable against convection, acting as a thermal boundary layer and increasing the interior temperatures for a given surface temperature. If this exists, the volume of high-pressure ice melted would be greater for a given volume of ice I melting than if α were positive everywhere. If that is the case, then more expansion results.

5.2.2.2 Discussion

Unfortunately, after this point in the Showman *et al.* (1997b) paper things become a little confused because of how the authors set up their reference frames. Their initial reference state is a fully differentiated but frozen Ganymede at 240 - 250 K. This has ice I, ice III, ice V, and ice VI (in that order from the surface downwards) over a silicate core. The internal structure of the satellite for a given core density is determined solely by the initial thickness of the outermost ice I shell in their model, which is reasonable considering that one must have different low-density shell thicknesses for different core sizes and densities to produce the same bulk density of the satellite. However, the core density is used as a direct equivalent to the core radius - a 3500 kg/m³ core is identified as being a small core, and a 2500 kg/m³ core is identified as a large one. Additionally, no numbers for the radius of the ice layers are actually given, so all one has to go by is the ice I thickness. This means that it is not possible for the reader to determine the stage during ice I melting at which ice V starts to melt, for example. The thicknesses of the individual high-pressure ice layers are not given either, which would have been useful. This is further compounded by the fact that the deep interior densities provided by Anderson *et al.* (1996) based on Galileo gravity data - 5000 to 8000 kg m⁻³ for a metallic core, with a 3300 kg m⁻³ silicate layer on top of that - are nowhere near as small as the ones given by Showman *et al.* (1997b), but Anderson *et al.* do provide radii for their layers. It may be possible to put the 'realistic' core models of Anderson into the Showman *et al.* model - if the combined radius and bulk density of the silicate mantle and metallic core are known, one can deduce how much ice must make up the rest of the satellite. It should also be possible to determine the (or at least, *a*) distribution of ice phases up to the surface using the phase diagram for ice shown in Figure 5.1. From that, it should be possible to determine reference states that have explicitly defined high-pressure ice thicknesses and core sizes. This is explored in greater detail in Chapter 6 and 7.

As a result, the graphs given by Showman *et al.* (1997b) are of limited use. They show the total fractional expansion of Ganymede due to internal melting, with increasing core density (decreasing core size) of 3500, 3000 and 2500 kg m⁻³, plotted against ice I thickness. This expansion is given relative to a reference state where the ice I thickness is 160 km thick - it is not clear what effect changing this initial ice I thickness (and therefore the rest of the internal structure) would have on the expansion. In addition, the x-axes of the graphs represent the amount of that ice layer melted in a runaway. The graphs go all the way up to 0 km ice I thickness, which represents complete melting of the ice I layer up to the surface. Taking the melting to the surface appears even more irrelevant when their stated initial reference state is that of a ‘warm frozen’ Ganymede at 240 - 250 K, which is only capable of small ‘runaway’ of a mere +10K over a period of $\sim 10^8$ years! Also, because only the ice I thickness is shown, one cannot immediately determine when (or which of) the high-pressure ices have started to melt.

Some information can be gleaned directly from their graphs, however:

- The global expansion is not linear as the ice I layer melts. There is an upwards kink after about 70 km of the ice I layer has been melted, which means that whatever high-pressure (henceforth referred to as **HP**) ice is now starting to be melted provides a greater expansion. This may imply that the higher density ice V or VI is starting to melt.

- If a negative α region is assumed to exist as the upper layer of the water layer, there is already 0.6% expansion before the ice I layer begins to melt. This is because all of the ice III (and some of the ice V) has melted by this time as a result of the increased interior temperatures caused by the negative α thermal boundary layer. While there is more expansion if the more realistic negative α layer is assumed to exist, there is at the same time more potential for the HP ices to have completely melted at a given point in the ice I melting, which would lead to contraction if melting continues and thus reduce the *total* expansion of the satellite.

However, it is unlikely for this to happen in a real icy Galilean satellite, since the water is very likely to contain dissolved salts. Water that is sufficiently saline ($> 3\%$ by mass saline) lacks this thermal expansivity phase - it increases uniformly in density until it freezes (Melosh *et al.*, 2002).

- For 3500 kg m^{-3} (i.e. smaller, in this model) cores, there is always an excess of HP (III, V, VI) ices after the ice I layer is completely melted. Given that a greater volume of HP ice melts for a given quantity of ice I, this implies that there must be more than $\sim 200 \text{ km}$ of HP ice at the start of the melting. For positive α , expansion when all the available ice I has melted is 1.8% - for negative α , it peaks at 2.2%.

- For 3000 kg m^{-3} cores and a more realistic negative α region at the upper layer of the water layer, the HP ices are completely melted after 130 km of ice I is melted - continued ice I melting results in contraction, the peak expansion being $\sim 2\%$. At the time the HP ices have completely melted, the surface of Ganymede is a shell of ice I some 30 km thick, overlying a deep water layer that is probably at least 200 km deep if the thickness of the melted ice III, V, and VI layers is included. Note that for positive α , the HP Ices do not completely melt before the ice I layer does - by the time the ice I layer completely melts, the total global expansion is $\sim 1.8\%$.
- For 2500 kg m^{-3} (i.e. larger, in this model) cores, the HP layers are thinner than in the other models. This means that all the HP ice has completely melted by the time only about half the ice I has, which means the expansion peaks at $\sim 1\%$ (for $-\alpha$) or $\sim 0.6\%$ for $+\alpha$ and declines with continued ice I melting.

In summary, while the basic model seems to be generally sensible, there are problems in the interpretation of the results of Showman *et al.* (1997b) - also, the values for core densities may not be entirely realistic, so I shall now put more accurate values into their model and examine the results.

5.2.2.3 Extrapolation

Using the model presented in Showman *et al.* (1997b) and discussed in the previous section, I start with a ‘warm, frozen’ pre-LLR Ganymede with an ice temperature of 245 K, which is exactly what Showman *et al.* (1997b) use as their ‘frozen reference state’. In fact, this is around the high end of the frozen models: if it was only about six degrees warmer Ganymede would enter the LLR with a water layer already, which as we have already seen does not allow the satellite to expand at all. Q/k_2 should be large enough ($\sim 10^3$) to pump up the eccentricity while being low enough to allow that eccentricity increase to generate some internal heating (I am assuming that Q/k_2 will stay at the same high level anywhere between 183 K and 250 K, and is only low ($\sim 10^1$) if a water layer is present as in the case of the ‘Too Warm’ Ganymede model).

In such a scenario, the orbital evolution model of Showman *et al.* suggests that the eccentricity would be pumped up to a smaller value than for the ‘Just Right’ Ganymede model described earlier that resulted in a large runaway. As before, Q/k_2 starts to decrease, the dissipation increases, which causes more warming, etc. The warming accelerates, Q/k_2 decreases dramatically (which in itself releases energy and generates more heating), and a thermal runaway occurs. However, for such a warm mantle, the internal temperature can only rise by about +10 K at most over the span of $\sim 10^8$ years. Even so, this still forms a water layer at a similar temperature to the ‘Just Right’ model (about 260 K) assuming reasonable values for a convective parameter of ice (required in equation (5) of Showman *et al.*, 1997b). After this, the internal evolution would probably follow the ‘Just Right’ model; if the LLR were disrupted at 2.6 Ga and the Laplace resonance entered soon thereafter, tidal heating would cease and the water layer would freeze again a billion years later.

Would the water layer be as extensive as in the ‘Just Right’ model, which resulted in a water layer hundreds of kilometres deep after a large +65 K runaway? If all that matters is that the internal temperature is above the melting point (251 K) rather than how much hotter it is then there is probably nothing to worry about and the water layer can be arbitrarily deep, and my previously stated misgivings will have been allayed - the ice will be melted regardless of the temperature excess, so long as it that excess is maintained. This is the case while the tidal heating is ongoing during the LLR, but not after it has been disrupted. After that, it takes about 1 Ga for the latent heat of the water layer to be overcome and the temperature to drop below the water layer’s freezing point at 251 K. The exact duration of this ‘latent heat buffering’ will depend on the water layer thickness, however.

The next problem is evaluating how much of the ice melts. From the model given here, this just seems to depend on how long the heating continues (again, not on the magnitude of the temperature excess) - in other words, on how long the LLR lasts. If the LLR were disrupted before 2.6 Ga, presumably the water layer would be thinner. Conversely, if the LLR was disrupted after 2.6 Ga the satellite would have been heated for longer, and the water layer would be deeper, and possibly still in existence today.

I may be oversimplifying things drastically here, however. Since the exact timing of the disruption of the LLR is essentially arbitrary - the authors state that they can break the LLR at any time during the LLR (after the eccentricity has been pumped) simply by changing the initial temperature, and for a given initial temperature they can alter the time the system enters the LLR by changing z_1 and z_2 (the system currently enters the LLR in all the models mentioned above

after $\sim 10^8$ years, since the initial z_1 and z_2 values are near the $u = 2$ LLR and heading towards capture into it). Of course, it takes time for z_1 and z_2 to reach appropriate ($u = 3/2$ or 2 LLR) initial values anyway, so the times given here should not be construed to mean ‘time since satellite formation’ - rather, they effectively mean ‘time since start of LLR’.

The implication is that the thickness of the water layer (and the duration of the Laplace-like resonance and the timing of its disruption) can be completely arbitrary using this model on its own - this would have to be limited by observation and analysis of the current surface geology of Ganymede, and by correlation with the phase diagram of water.

Showman *et al.* (1997b) then go on to calculate the lithospheric stress induced by satellite expansion during a runaway. They assume that the current surface temperature of Ganymede is 130 K (however, the actual temperature ranges from 90 - 150 K (John Spencer, *pers. comm.*)), and the upper 10 km or so of the crust is considered. Assuming a thermal gradient of $\sim 5 \text{ K km}^{-1}$, the temperatures we are interested in are no greater than 200 K (actually about 180 K) over that depth. They plot the hydrostatic pressure as a function of depth and the calculated lithospheric stress (in the case they give, for a 2% expansion) on a depth/pressure graph. The intersection of the lines shows the maximum depth of open fracture for zero-strength ice (though actually the tensile strength for ice may be 1 - 3 MPa, which probably decreases the maximum depth). Two other factors that can be constrained are involved - the expansion time-scale and the surface temperature. For a realistic evolution from a ‘warm, frozen’ Ganymede at 245 K that I described earlier, the expansion time-scale (taken here to be how long the runaway lasts, which is roughly how long it takes for the water layer to form) should be about 10^8 years. For a

2% expansion, this corresponds to a maximum fracture depth (for zero-strength ice) of < 1 km for a surface temperature of 130 K, ~ 1 km for a surface temperature of 110 K, and ~ 3 km for a surface temperature of 90 K.

If BT formation took place recently, as is likely given recent crater-count data (Zahnle *et al.* 1998), then the surface temperature was probably similar at its formation to what it is now (while the luminosity of the sun is known to be increasing over the history of the Solar System, it would not have been significantly less luminous so recently in the past than today). Realistically, the expansion would have to be nearer 1% to keep Galileo Regio intact (McKinnon, 1981). If the 245 K ‘warm, frozen’ Ganymede and the 10^8 year runaway/expansion that I am assuming are realistic, this means that the BT boundaries are actually graben, and cannot be very deep - probably only on the order of ~ 200 m to 500 m. Whether this is realistic or not is uncertain - again, it can be confirmed or denied by observation.

But, after all this, is expansion even *required* to form the BT? Showman *et al.* offer one suggestion as to how this may be possible - that tidal flexing over the course of the LLR for a warm Ganymede model such as the one I have described above could result in a tidal strain amplitude of $\sim 10^{-5}$ over the whole LLR. This amplitude is apparently enough to ‘pump’ liquid or warm ice to the surface through the cracks and fractures that resulted from a runaway at the start of the LLR - similar models of ‘tidal pumping’ have been proposed to explain the lineaments seen on Europa by Tufts *et al.* (2000). Showman *et al.* propose this as an *alternative* model that does not require a runaway to occur. Given that their runaway model, while theoretically possible, may not actually produce significant expansion in practice, this alternative may actually

be more likely to hold for Ganymede. However, I have repeated the calculations (qualitatively at least) with more realistic parameters and I am able to produce at least *some* expansion with their model, given my admittedly hard-to-test assumptions.

The alternative model of Showman *et al.* (1997b) requires that Ganymede has a pure ice mantle. This allows the ice grains to anneal and thus the ice layers to become more viscous. The high viscosity would grow rapidly after satellite formation to prevent solid-state convection, so conductive heat loss would be low and the interior would heat up. Ganymede would then enter the LLR in a warm, molten state, with a water layer like the ‘Warm’ Ganymede model described earlier. However, the higher viscous dissipation would raise the Q of Ganymede to $\sim 10^2$ (instead of $< 10^1$ for the normal pre-LLR water layer scenario). This means that the eccentricity could be pumped up to ~ 0.01 for reasonable values of Q_J . This would therefore provide the strain amplitudes needed for the ‘water pumping’ to cause resurfacing. So we might not need a runaway to resurface Ganymede after all! What is more, in this scenario the water layer may still exist and could be detectable with an orbiting satellite (the tidal bulge could be up to 16 m high).

I end this discussion with an interesting possibility. Showman *et al.* disrupted the LLRs in their (1997b) paper by increasing Q^*_I/Q^*_J as shown in Showman and Malhotra (1997a). This was done by increasing the Q of Io by a factor of 6, as discussed at the end of Section 5.2. However, Showman and Malhotra (1997a) showed that **decreasing** Q^*_2/Q^*_J - in other words, the Q of Europa - by two orders of magnitude also disrupts the LLR and pushes the whole system into the Laplace Resonance. We have already seen in Ganymede a way to do just that -

a ‘cold, frozen’ Ganymede has a Q/k_2 of $\sim 10^3$, while one with a water layer has a Q/k_2 of around 10^1 - a decrease of two orders of magnitude. In other words, creating a water layer in an icy outer shell in Europa may have precisely the effect needed to disrupt the LLR, and may be physically reasonable.

A new scenario would be that the system would enter the LLR as normal. It would progress for a couple of billion years, Ganymede would have its runaway near the start, and for some reason Europa would not, perhaps because it started off colder. Then, 1 Ga ago, Europa would start to “wake up” and its Q/k_2 would start to decrease such that its eccentricity would provide some heating, which would lead to a Ganymede-style runaway, and a water layer would form under the european crust. Q_{europa} would now have plummeted two orders of magnitude, so the LLR would be disrupted, and the system would subsequently evolve into the Laplace Resonance.

However, the above scenario may not be entirely correct - the eccentricity of Europa would have to decrease more than shown in Showman and Malhotra (1997a) after entry into the Laplace Resonance. Furthermore, while it is certainly possible that Europa could have undergone thermal runaways (in the ice) similar to what has been proposed for Ganymede, Europa's effective Q/k_2 cannot change as much as Ganymede's because a much smaller fraction of Europa's mass is ice (i.e. its effective Q/k_2 is much more dominated by its rocky core). Also, decoupling of Europa's ice shell probably will not increase k_2 by much (Ross and Schubert 1987). It is therefore more likely that Q_I^*/Q_J^* can increase by a factor of 3 - 6 than that Q_2^*/Q_J^* will decrease by a factor of 100.

The real test of these orbital evolution scenarios would be to create realistic models of the interiors of the Galilean satellites, based on the most recent data available. With these in hand, it will be possible to bring the pieces of the puzzle together and construct a scenario that incorporates the orbital and thermal evolution described here and the current state of the interiors of the satellites. Fortunately, Galileo has provided us with a wealth of gravity data on its various flybys of the satellites that can be used to constrain their interior structures. In the next two chapters, I shall examine and extend the interior structure models published by Anderson *et al.* (1996a, 1996b, 1998b, 2001).

Chapter 6 The interior structures of the Galilean satellites

6.1 Introduction

Prior to the Galileo mission, models for the interiors of the Galilean satellites were poorly constrained. The earliest attempts at modelling the interiors of the icy Galilean satellites, published by Reynolds and Cassen (1979), concluded that the icy Galileans - Europa, Ganymede and Callisto - consisted of a completely frozen ice shell, possibly above a rocky core. They calculated that thermal convection could cool down the body sufficiently to freeze out any liquid water layer early in the satellite's history. Parmentier and Head (1979) agreed, and proposed another method of heat loss that could hasten the freezing of a liquid layer - ice diapirism. Later models (e.g. Schubert *et al.*, 1981; Kirk and Stevenson, 1987; Mueller and McKinnon, 1988) proposed various internal structures, but because the heat flow through the satellites in question is largely unconstrained there was no consensus on what we should expect there.

Recently however, Galileo has provided very useful gravitational data from close satellite flybys that provide several important constraints to their possible internal structures. The internal models of the Galilean satellites proposed by Anderson *et al.* (1996a, 1996b, 1998a, 1998b, 2001) are based on these recently acquired data, and are therefore the logical ones to examine given that they contain fewer ambiguities. The models for each satellite are presented in turn, summarised, discussed, and expanded in this chapter.

6.2 The ONIONSKIN moment of inertia model

Alongside the previously published models, I also present my own models for the interior structures of the satellites. This modelling is carried out on an expanded version of a spreadsheet developed by Richard Ghail at Imperial University in London - I have called this model 'ONIONSKIN' because it calculates moment of inertia of a satellite based on many thin concentric shells, not unlike the skin of an onion. I take the observed values of radius, mass, density, and moment of inertia factor C/MR^2 , and construct a satellite made of layers of different types of (appropriate) material, such as ice I, ice III, rock, iron and/or iron sulphide (N.B. 'layer' refers to a distinct type of material - 'shell' refers to a radius increment used to calculate moment-of-inertia). I also attempt to account for self-compression of this material due to the mass of the overlying material. The size of the layers is determined by the percentage mass of the satellite which they represent and their uncompressed density - both of which can be changed dynamically - although whereas the percentage mass of a layer is very flexible, the uncompressed density of a material is fixed once the material is chosen. However, mixtures of different material (e.g. a rock/ice mixture) can have a wide range of densities so this becomes an important variable in these cases.

The moment of inertia factor C/MR^2 is determined by dividing the satellite into 10,000 equally spaced shells from core to surface. The moment of inertia of each of these shells is calculated using:

$$I = \frac{2}{3} m r^2 \quad (6.1)$$

which is used to calculate the moment of inertia of a single shell of radius r and mass m . This is expanded to:

$$I = \frac{8}{3} \rho \cdot \Delta r \cdot [r_i^4 \rho_i] \quad (6.2)$$

where Δr is the thickness of a shell, r_i is the radius of the shell, and ρ_i is the density of the shell at that depth within the satellite. This is the same as equation (6.1), but converts the mass of the shell into volume and density using $m = (4/3)\rho r^3$.

The total moment of inertia of these shells is then summed to produce the moment of inertia for the whole satellite in the model. By manipulating the percentage mass and type of material comprising each physical layer, it is possible to construct a model - or a range of models - that have values that lie within the derived error-bars for the satellite's radius, mass, density, and moment of inertia factor and thus are realistic. The process used in this model is shown in Flowcharts 5.1 and 5.2.

Figure 6.1: ONIONSKIN Model Flowchart

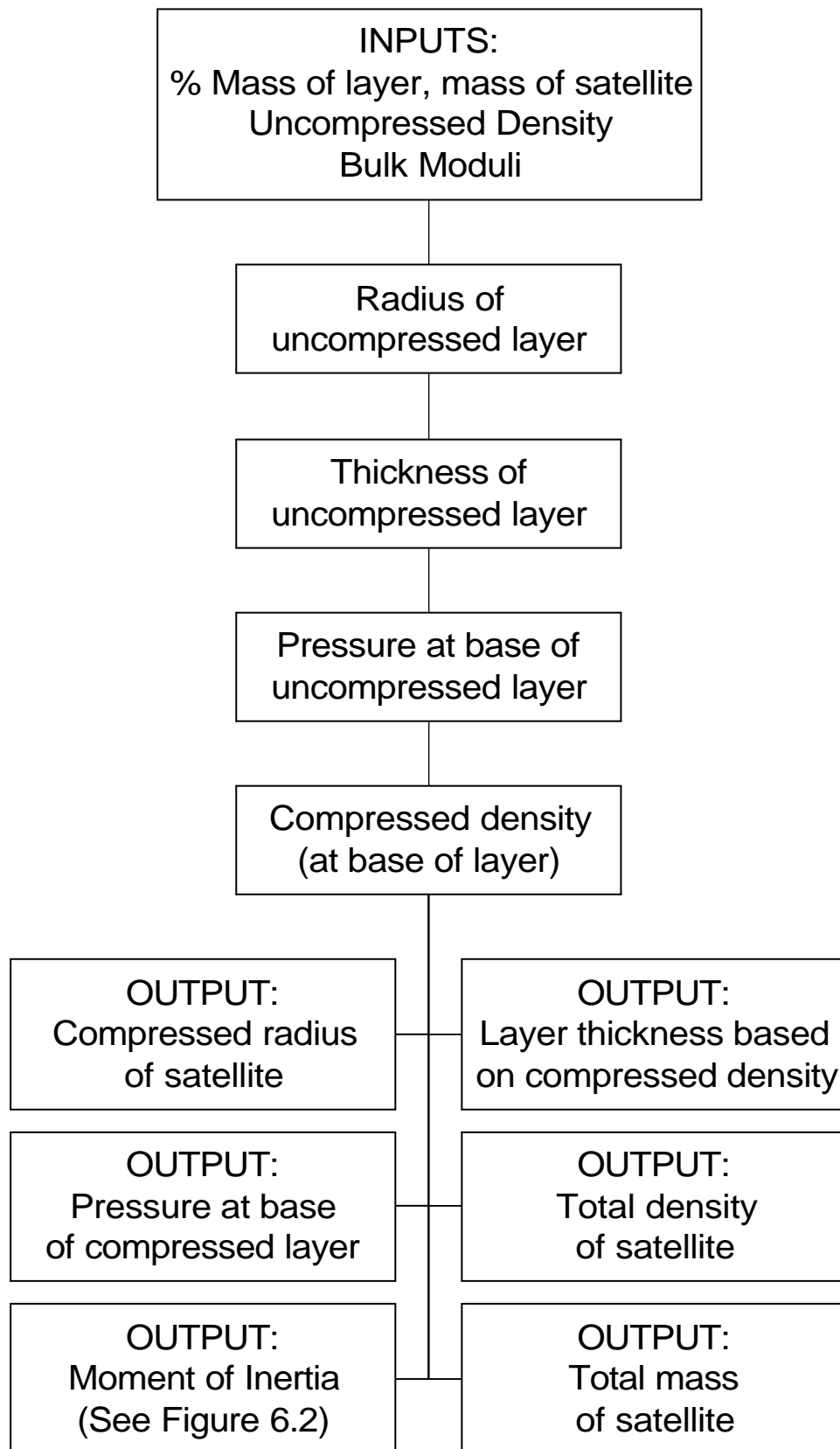
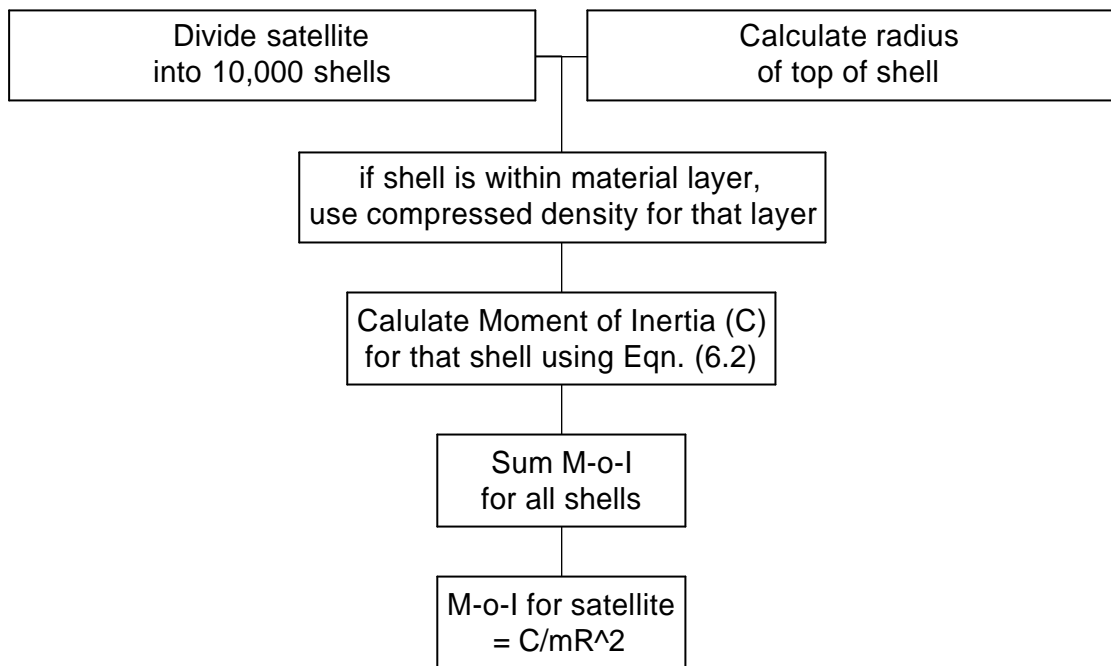


Figure 6.2: Determining Moment of Inertia in ONIONSKIN



There are three important *caveats* to be aware of with the ONIONSKIN model: first, the compressed density at the base of a layer is used to determine the moments of inertia of *all* the appropriate shells within that layer - no attempt is made to model the density range across the shells between the top and base of the layer. (This is corrected in Chapter 7, but can be a source of inaccuracy in the ONIONSKIN models and should be borne in mind here).

Second, the ONIONSKIN model is a purely physical model constrained primarily by moment of inertia, radius, density and mass - no chemical or thermal modelling is carried out as part of the model verification. However, care is taken to assume reasonable densities for materials comprising the layers and to find appropriate physical parameters (e.g. bulk moduli to determine self-compressibility), and obviously certain results requiring layer densities that are too high or low to be realistic are ruled out straight away.

Third, ONIONSKIN is currently an empirical model - that is, appropriate values must be entered manually into the model and manipulated by hand to converge on the target values. This necessarily limits the investigation of the model's possible 'phase space' to those values that are obvious to the user. It is clear that the results that the model produces are not unique - various combinations and types of materials can produce models that fit within the acceptable 1σ error range. I later developed an automated process to work through the phase space and pick out those models that conform to the target values - this program is called SATMOD, and is described more fully in Chapter 7 - as such, the ONIONSKIN results are presented here as preliminary findings from the time of its development.

Despite these limitations however, ONIONSKIN generally produces results that broadly agree with those published and referred to here, which bodes well for its validation. Furthermore, tests on a uniform sphere, which should have a moment of inertia of exactly 0.4 produce a moment of inertia of 0.4000 ± 0.0001 (probably due to rounding errors in Excel), well within acceptable margins of error.

6.3 The internal structure of Io

6.3.1 Published models

Anderson *et al.* (1996a) propose that Io is differentiated into at least two layers depending on the type of core it possesses: one model requires a large Fe-FeS core occupying 45% - 58% of the interior by radius (13 - 28% of the satellite's mass), surrounded by a silicate mantle/crust. Alternatively, if the core consists of pure iron, it occupies 31% - 40% of Io's interior (7% - 15% by mass). This may be surprising given that Io's C/MR^2 value is near the undifferentiated value of 0.4, but it should be recalled that Io does not possess a thick shell of low density material (such as ice) to increase the density contrast with the interior. Differentiation into a crust is probable though this has not been explicitly modelled by Anderson *et al.* (1996a).

In Anderson *et al.* (2001), this model was refined into a three-layer model that includes a low density crust. This crust could be either thin and low density (< 50 km thick, $< 2600 \text{ kg m}^{-3}$) overlying a dense mantle and metallic core, or could be much thicker and denser (100 - 200 km thick, $3000 - 3200 \text{ kg m}^{-3}$) if it included a melt-rich aesthenosphere (and a smaller core). The actual density of the crust is unclear, however, as it depend on how much crustal recycling has occurred on Io - a very recycled crust would be thin, low density, would melt more easily and have eruption temperatures much lower than the high temperature eruptions seen today (McEwen *et al.*, 1998). A solution to this would be that Io's crust has not been recycled often, which implies that Io has been tidally heated for only a small fraction of the

lifetime of the solar system - i.e. that Io has entered the orbital resonances with Europa and Ganymede comparatively recently. I have shown in Chapter 4 that this could be a possibility. This would allow the crust to be denser, allowing high temperature magma to rise to the surface more easily. Therefore, I shall assume that the crust density is $\sim 3000 \text{ kg m}^{-3}$.

Assuming the mean value of C_{22} ($(55.37 \pm 1.2) \times 10^{-5}$) derived from the gravity data (Anderson *et al.*, 2001), possible internal structures for Io derived by Anderson *et al.* are shown in Table 6.1 (for a Fe-FeS eutectic core, $\rho = 5150 \text{ kg m}^{-3}$) and Table 6.2 (assuming a Fe core, $\rho = 8000 \text{ kg m}^{-3}$). While these core compositions could potentially be refined, the chemistry of the Galilean satellites is currently very poorly constrained. The Fe and Fe-FeS compositions represent two likely core materials and are common assumptions in planetary science, used by Anderson *et al.* in all their papers.

It should be noted that Anderson *et al.* (2001) use a different value for Io's radius ($1821.6 \pm 0.5 \text{ km}$) from the currently accepted and more accurate value derived from photometric analysis and limb fitting of satellite images ($1818.1 \pm 0.12 \text{ km}$, from Davies *et al.*, 1998), but this does not affect the calculation significantly. I use the Davies *et al.* (1998) value for my own models, but use the Anderson *et al.* (2001) value for the summary of their model presented in Tables 6.1 and 6.2:

Table 6.1: Io Internal Structure according to Anderson *et al.* (2001), assuming Fe-FeS eutectic core (5150 kg m⁻³) and crust density 3000 kg m⁻³.

Io	Fe-FeS core (5150 kg m⁻³)	Fe-FeS core (5150 kg m⁻³)
Io total radius	1821.6 km	1821.6 km
Io total volume	2.53 x 10 ¹⁹ m ³	2.53 x 10 ¹⁹ m ³
Io total mass	8.93199 x 10 ²² kg	8.93199 x 10 ²² kg
Io total density	3548.05 kg m ⁻³	3548.05 kg m ⁻³
Crust thickness	40 km (2%)	350 km (19%)
Mantle thickness	652 km (36%)	962 km (53%)
Core thickness	1129 km (62%)	510 km (28%)
Crust density	3000 kg m ⁻³	3000 kg m ⁻³
Mantle density	3320 kg m ⁻³	3800 kg m ⁻³
Core density	5150 kg m ⁻³	5150 kg m ⁻³

Table 6.2: Io Internal Structure according to Anderson *et al.* (2001), assuming Fe core (8000 kg m⁻³) and crust density 3000 kg m⁻³.

Io	Fe core (8000 kg m⁻³)	Fe core (8000 kg m⁻³)
Io total radius	1821.6 km	1821.6 km
Io total volume	2.53 x 10 ¹⁹ m ³	2.53 x 10 ¹⁹ m ³
Io total mass	8.93199 x 10 ²² kg	8.93199 x 10 ²² kg
Io total density	3548.05 kg m ⁻³	3548.05 kg m ⁻³
Crust thickness	40 km (2%)	300 km (16%)
Mantle thickness	1144 km (63%)	1175 km (65%)
Core thickness	638 km (35%)	346 km (19%)
Crust density	3000 kg m ⁻³	3000 kg m ⁻³
Mantle density	3360 kg m ⁻³	3800 kg m ⁻³
Core density	5150 kg m ⁻³	5150 kg m ⁻³

6.3.2 Io ONIONSKIN Models

Tables 6.3 and 6.4 show possible ONIONSKIN models for the internal structure of Io assuming an Fe-FeS core with uncompressed density of 5150 kg m^{-3} . Table 6.5 and 6.6 show possible ONIONSKIN models for the internal structure of Io assuming an Fe core with uncompressed density of 8000 kg m^{-3} .

The Fe-FeS ONIONSKIN model represents one viable internal structure that lies between the two extremes shown in Table 6.1. This model has a small core that is 31.5% of Io's radius, a deep mantle, and a thick crust with a density of 3000 kg m^{-3} .

The Fe ONIONSKIN model is slightly different from the Anderson *et al.* (2001) models shown in Table 6.2 - the crust is a little thicker, the core is larger, and the mantle density is lower than their “small core” model on the right-hand column of Table 6.2. Nevertheless, the parameters remain well within their acceptable error ranges so my Fe core ONIONSKIN model is viable.

Figure 6.3 shows a cutaway view of Io, illustrating the Fe-FeS eutectic core Ionian internal structure model described in Table 6.3.

Table 6.3: ONIONSKIN model of the internal structure of Io with an Fe-FeS eutectic core (density: 5150 kg m⁻³).

Layer	Percent Mass	Uncompressed Density (kg m ⁻³)	Layer Mass (kg)	P/T Density (kg m ⁻³)	Model Radius (km)	Thickness of Layer (km)	Base Pressure (GPa)
Rock Crust	30.00	3000	2.67960 x 10 ²²	3026	1818.10	244.61	1.3346
Rock Mantle	65.00	3561	5.80579 x 10 ²²	3739	1573.49	999.81	7.6339
Fe-FeS Core	5.00	5150	4.46600 x 10 ²¹	5647	573.68	573.68	10.5673
Total:	100.00		8.93199 x 10²²			1818.10	

Percent mass represents the mass fraction of the satellite that is taken up by the material layer, **Uncompressed Density** is the density of the uncompressed material, **Layer Mass** is the mass of the layer, **P/T Density** is the density of the material at the base of the layer given self-compression, **Model Radius** is the radius of the top of the material layer, **Thickness of Layer** is the difference between the top and bottom of the layer, and **Base Pressure** is the pressure at the base of the layer.

Table 6.4: Io Fe-FeS core ONIONSKIN model results compared with target values for radius, mass, C/MR², and density

	Target Values	1σ error range		Model Results	Error
Radius	1818.1	± 0.12 km		1818.10	± 0.00 km
Mass	8.93199 x 10 ²²	± 0.00114 x 10 ²² kg		8.93199 x 10 ²² kg	-
C/MR²	0.376995	± 0.0075		0.380922	+ 0.003927
Density	3548.05	± 0.61 kg m ⁻³		3548.17	+ 0.12 kg m ⁻³

Table 6.5: ONIONSKIN model of the internal structure of Io with an Fe core (density: 8000 kg m⁻³).

Layer	Percent Mass	Uncompressed Density (kg m ⁻³)	Layer Mass (kg)	P/T Density (kg m ⁻³)	Model Radius (km)	Thickness of Layer (km)	Base Pressure (GPa)
Rock Crust	39.00	3000	3.48348 x 10 ²²	3036	1818.07	333.81	1.8270
Rock Mantle	56.00	3600	5.00191 x 10 ²²	3791	1484.26	991.23	8.0278
Fe Core	5.00	8000	4.46600 x 10 ²¹	8896	493.03	493.03	13.4049
Total:	100.00		8.93199 x 10²²			1818.07	

(Table key as for Table 6.3)

Table 6.6: Io Fe core ONIONSKIN model results compared with target values for radius, mass, C/MR², and density

	Target Values	1s error range		Model Results	Error
Radius	1818.1	± 0.12 km		1818.07	- 0.03 km
Mass	8.93199 x 10 ²²	± 0.00114 x 10 ²² kg		8.93199 x 10 ²² kg	-
C/MR²	0.376995	± 0.0075		0.373993	- 0.003002
Density	3548.05	± 0.61 kg m ⁻³		3548.34	+ 0.29 kg m ⁻³



Figure 6.3: The internal structure of Io. The cutaway view of Io shown here illustrates the three-layer ONIONSKIN internal structure (Fe-FeS eutectic core) model described in Table 6.3. The solid orange shell represents the thick crust/aesthenosphere, the mottled orange layer represents the partially molten mantle, the red layer represents the molten metallic core. Io is shown to scale with the other Galilean satellite cutaways shown in Figures 6.4, 6.5, and 6.6. Image by Constantine Thomas, rendered using POV-Ray 3.02.

6.4 The internal structure of Europa

6.4.1 Published models

Anderson *et al.* (1998b) suggest that Europa can best be described by a three-layer model consisting of a metallic core, a silicate mantle/crust, and a water layer/ice shell. They rule out two-layer models of an undifferentiated silicate/metal ‘core’ surrounded by an ice shell on the grounds that the bulk density of the ‘core’ component would be unrealistically large, implying enrichment in dense metallic phases relative to Io. The amount of radiogenic material within such a configuration would provide extra heating to melt the satellite and differentiate it into a metallic core and silicate mantle, so the presence of a metallic core seems inescapable.

The Anderson *et al.* (1998b) models are shown in Table 6.7. Assuming a reasonable outer ice shell density of 1050 kg m^{-3} , a geologically reasonable silicate component density of 3300 kg m^{-3} (similar to that of Io), and a Fe-FeS eutectic core, Anderson *et al.* (1998b) propose that the European ice shell should be approximately 120 km thick, and the core should be approximately 0.46 Europa radii in size. This translates to a metallic core radius of 720 km, a silicate mantle thickness of 725 km (total: 1445 km), and an ice shell thickness of 120 km (total: 1565 km).

Alternatively, if a pure Fe core is assumed (with the same silicate and ice shell densities), Europa has a similar thickness of ice (~ 120 km) and a core radius of ~ 0.33 Europa radii. This is equivalent to a metallic core radius of 516 km, a silicate mantle thickness of 929 km (total: 1445 km), and an ice shell thickness of 120 km (total: 1565 km). Anderson *et al.* (1998b) use older, larger values for the radius of Europa but again these should not make a significant difference to the model.

Table 6.7: Europa Internal Structure according to Anderson *et al.* (1998b)

Europa	Fe core (8000 kg m^{-3})	Fe-FeS eutectic core (5150 kg m^{-3})
Ice shell thickness	120 km	120 km
Silicate crust/mantle thickness	929 km	725 km
Metallic core radius	516 km	720 km
Total radius	1565 km	1565 km

Higher silicate densities (up to a maximum of 3800 kg m^{-3}) yield thicker ice shells (up to 170 km or so in both cases) and smaller cores (down to a minimum of no metallic core at all). Lower silicate densities (down to a minimum of 3000 kg m^{-3}) yield thinner ice shells (down to 80 km thick on both cases) and larger cores (~ 595 km for Fe only, 814 km for Fe-FeS).

6.4.2 Europa ONIONSKIN models

Schenk (2002) determines an observationally derived constraint on the thickness of the ice shell, by examining the shapes of the few impact craters on Europa, Ganymede, and Callisto. He finds two anomalous transitions in the depth-diameter ratios of fresh craters on these satellites - these transitions are not found on rocky bodies such as the Moon. In addition, these transitions occur at different depths on Europa from those on Ganymede and Callisto. He interprets this change as being indicative of a change in the structure of the ice shells - the first transition is interpreted to represent a change in rheology with depth (e.g. a brittle-ductile transition), and the second - being rather abrupt - is interpreted as representing the boundary between ice and liquid water. Schenk (2002) uses these data and the crater scaling relationship of McKinnon and Schenk (1995) to determine the distance to these transition layers, and suggests that the ice-water transition layer on Europa is between 19 and 25 km below the surface. Being based on direct observation, this provides a more rigid constraint than the gravity constraints of Anderson *et al.* (1998b) alone - I shall therefore assume that these are valid thicknesses for the Ice I shell.

My interpretation of the magnetic data discussed in Section 3.2.2.1 suggests that a pure Fe core is unlikely in Europa. The lack of intrinsic magnetic field implies that a solid or non-conductive molten core is present, most likely composed of FeS or a eutectic mix of Fe-FeS - I shall assume that a solid eutectic core is present in the ONIONSKIN model presented here.

Tables 6.8 and 6.9 show a possible ONIONSKIN model for the internal structure of Europa assuming an Fe-FeS eutectic core with uncompressed density of 5150 kg m^{-3} . The model incorporates a deep layer of liquid saltwater, required in order to account for the presence of an induced magnetic field at Europa, as discussed in Section 3.3.2. This water is assumed to be kept liquid largely as a result of tidal dissipation and some radiogenic heating from the silicate body below, and is assumed to have an uncompressed density of 1050 kg m^{-3} - 5% saline, which is more saline than terrestrial seawater ($\sim 3.5\%$ saline). This lies between the two extremes given by current models of European ocean chemistry that range from $\sim 30\%$ (Kargel *et al.*, 2000) to $\sim 3\%$ (similar to Earth's oceans) (Zolotov *et al.*, 2001).

The ONIONSKIN model presented here is a very close fit to the radius, density and moment of inertia parameters determined by Anderson et al (1998b). It should be noted that core occupies 50.4% of the radius of the European rocky body (i.e. core + mantle) - indeed, the core is 47.1% of the radius of Europa *including* the ice and water layers. For comparison, the rocky terrestrial planets are generally understood to have metallic cores occupying between 40% and 50% of their radii, so such a large core is at the upper limit of this range. This is, however, no reason to consider such a model unlikely.

The mantle density (3100 kg m^{-3}) is consistent with that of low-density hydrated silicate material, and lies near the lower bound stated by Anderson *et al.* (1998b) of 3000 kg m^{-3} . Below this lower bound, it becomes more likely that the hydrated silicates would be baked by heat and pressure at the great depths possible within such a large mantle and release their water, thus increasing in density. It also becomes less likely for Europa to retain a large hydrated mantle having differentiated such a large metallic core. According to the ONIONSKIN model, however, there appear to be no insurmountable physical problems that could preclude a relatively deep water layer lying under a thin ice shell on Europa today.

Figure 6.4 shows a cutaway view of Europa illustrating the model described in Tables 6.8 and 6.9.

Table 6.8: ONIONSKIN model of the internal structure of Europa with an Fe-FeS core (density: 5150 kg m⁻³).

Layer	Percent Mass	Uncompressed Density (kg m ⁻³)	Layer Mass (kg)	P/T Density (kg m ⁻³)	Model Radius (km)	Thickness of Layer (km)	Base Pressure (GPa)
Ice I	1.24	921	5.99980 x 10 ²⁰	924	1560.66	21.52	0.0261
Salt water	5.25	1050	2.51992 x 10 ²¹	1097	1539.14	81.38	0.1453
Rock Mantle	74.55	3100	3.57828 x 10 ²²	3163	1457.77	722.65	3.3664
Fe-FeS Core	18.95	5150	9.09570 x 10 ²¹	5466	735.11	735.11	7.8793
Total:	100.00		4.79984 x 10²²			1560.66	

(Table key as for Table 6.3)

Table 6.9: Europa Fe-FeS core ONIONSKIN model results compared with target values for radius, mass, C/MR², and density

	Target Values	1s error range		Model Results	Error
Radius	1560.67	± 0.65 km		1560.66	- 0.01 km
Mass	4.79984 x 10 ²²	± 0.00062 x 10 ²² kg		4.79984 x 10 ²²	-
C/MR²	0.347504	± 0.005		0.346073	- 0.001431
Density	3014.45	± 2.2 kg m ⁻³		3014.46	+ 0.01 kg m ⁻³

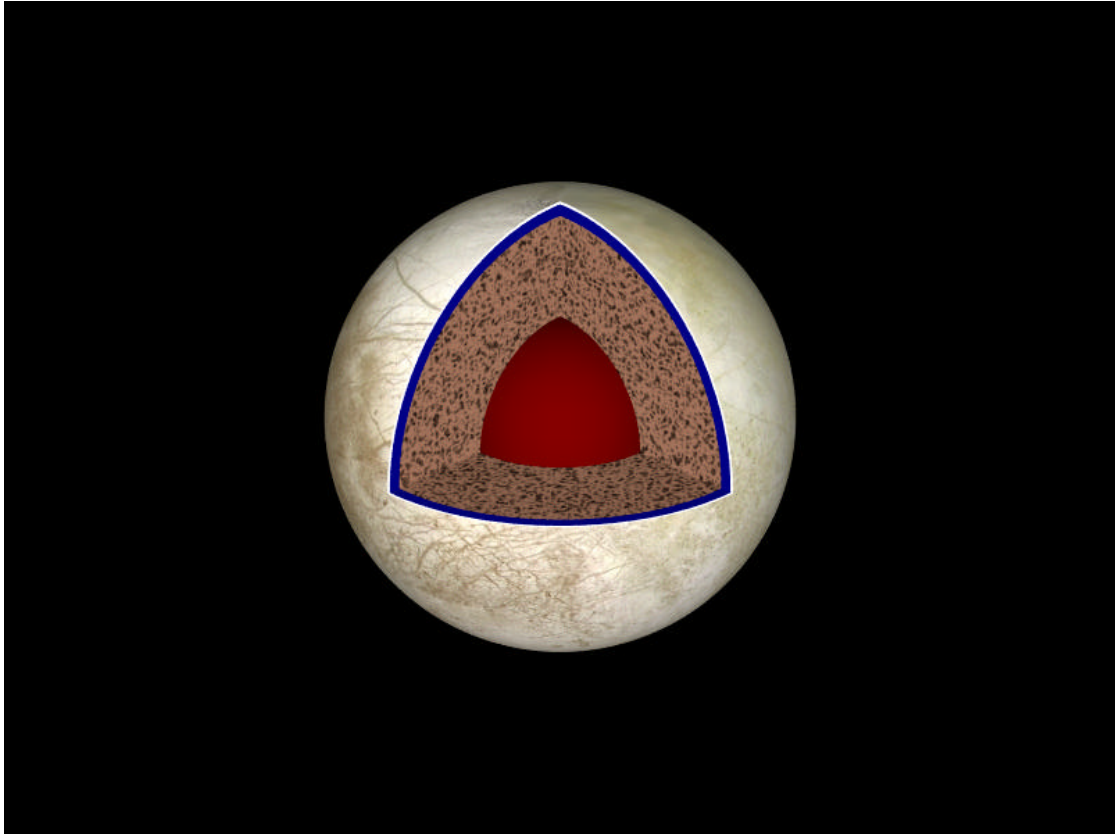


Figure 6.4: The internal structure of Europa. The cutaway view of Europa shown here illustrates the four-layer ‘thin ice, thick water layer’ ONIONSKIN internal structure (Fe-FeS eutectic core) model described in Table 6.8. The white layer represents the ice I shell at the surface, the blue layer represents the water layer, the mottled brown layer represents the silicate mantle, and the dark red layer represents the (solid?) metallic core. Europa is shown to scale with the other Galilean satellite cutaways shown in Figures 6.3, 6.5, and 6.6. Image by Constantine Thomas, rendered using POV-Ray 3.02.

6.5 The internal structure of Ganymede

6.5.1 Published Models

Gravity data indicate that Ganymede is strongly differentiated, since it has a very small value of C/MR^2 (~ 0.311) - the smallest value known for any solid body in the Solar System. The models of Anderson *et al.* (1996b) suggest that it has differentiated into a metallic core, a silicate mantle/crust, and a thick ice shell. The specifics of their three-layer model assume a silicate density of 3300 kg m^{-3} , and a core density of either 5150 kg m^{-3} for a Fe-FeS eutectic core or 8000 kg m^{-3} for a pure Fe core. Depending on the model, the core and mantle together vary in size between the extremes of 1415 km (largest Fe core) and 1933 km (smallest Fe-FeS core) in radius with corresponding ice shell thicknesses of between 699 km and 362 km. The core ranges from between 19.2% and 74.3% of the silicate/metal body radius for an Fe core, or between 27.2% and 85% of the silicate/metal body radius for an Fe-FeS core. The higher values may be unreasonable, as they imply a very large metallic core relative to the silicate mantle. A similar situation is known to exist at Mercury, but may be unique to that planet. The other terrestrial planets (and indeed, the other Galilean satellites) are believed to have metallic cores occupying between 30% and 50% of their radii, so these values are assumed here to be more geophysically reasonable for Ganymede.

Models with a thick layer of ice but with a low implied ice density (near that of ice I) are unrealistic since over the thicknesses given the ice will transform to denser phases that will increase the bulk density of the ice shell. It is therefore likely that models with an Fe core of

$< 0.2 R_G$ or Fe-FeS core models of $0.2 R_G$ are unrealistic, since they have an ice shell ~700 km thick with a density barely greater than that of ice I.

The values in Tables 6.10 and 6.11 are calculated by direct analysis of the graphs in Anderson *et al.* (1996b). I take round values (easily readable from the graphs) for the metallic core radii (0.2 - 0.5 radii, where applicable), assumed density values (8000 or 5150 kg m^{-3} depending on core composition, and 3300 for mantle composition). Knowing the fractional radii, I can determine the radius and therefore the thicknesses of the layers - from those I can calculate their volumes. I know the densities of the core and silicate mantle, and now also the volumes, so I can calculate the masses of those shells. The remaining ice shell mass is the total Ganymede mass minus the mass of the iron/rock shells - from that (and knowing the bulk density of Ganymede) I can then calculate the density of the ice shell.

For the purposes of this thesis, I am assuming that realistic Ganymede models will be those where the iron core takes up between 30% and 50% of the total (core + mantle) radius, which is a similar proportion to that of the terrestrial planets (the core/mantle ratios are shown for each model in Tables 6.10 and 6.11) - these 'realistic' values are marked in **bold** in the tables below. This could be a misguided assumption - it could be argued that I should consider a more lunar-like internal structure (i.e. small core, thick mantle). However, since the Moon is a planetary oddity because of the way it formed (very volatile-poor, born of planetary impact etc.), comparison to the Moon is probably not valid.

With these assumptions in mind, reasonable parameters for Ganymede's interior are shown in bold type in Tables 6.10 and 6.11.

Table 6.10: Ganymede Fe core (8000 kg m⁻³) model according to Anderson *et al.* (1996b).

	Layer Type	Fractional Radius	Radius of Layer (km)	Thickness of Layer (km)	Volume of Layer (m ³)*	Mass of Layer (kg)	Bulk Density of Layer (kg m ⁻³)*
MODEL 1	Ice shell	1.000	2634.1	703.3047	4.64064 x 10 ¹⁹	4.76611 x 10 ²²	1027
	Rock mantle	0.733	1930.7953	1559.3872	2.99361 x 10 ¹⁹	9.87891 x 10 ²²	3300
	Iron Core	0.141	371.4081	371.4081	2.14606 x 10 ¹⁷	1.71685 x 10 ²¹	8000
	Totals	mantle/core thickness: 19.2%		2634.1	7.65571 x 10 ¹⁹	1.48167 x 10 ²³	1935.38
MODEL 2	Ice Shell	1.000	2634.1	763.889	4.91565 x 10 ¹⁹	5.48664 x 10 ²²	1116
	Rock Mantle	0.710	1870.211	1343.391	2.67882 x 10 ¹⁹	8.84009 x 10 ²²	3300
	Iron Core	0.200	526.82	526.82	6.12457 x 10 ¹⁷	4.89965 x 10 ²¹	8000
	Totals	mantle/core thickness: 28.2%		2634.1	7.65571 x 10 ¹⁹	1.48167 x 10 ²³	1935.38
MODEL 3	Ice Shell	1.000	2634.1	966.7147	5.71394 x 10 ¹⁹	7.43737 x 10 ²²	1302
	Rock Mantle	0.633	1667.3853	877.1553	1.73506 x 10 ¹⁹	5.7257 x 10 ²²	3300
	Iron Core	0.300	790.23	790.23	2.06704 x 10 ¹⁸	1.65363 x 10 ²²	8000
	Totals	mantle/core thickness: 47.4%		2634.1	7.65571 x 10 ¹⁹	1.48167 x 10 ²³	1935.38
MODEL 4	Ice Shell	1.000	2634.1	1216.9542	6.46355 x 10 ¹⁹	8.57976 x 10 ²²	1327
	Rock Mantle	0.538	1417.1458	363.5058	7.02188 x 10 ¹⁸	2.31722 x 10 ²²	3300
	Iron Core	0.400	1053.64	1053.64	4.89965 x 10 ¹⁸	3.91972 x 10 ²²	8000
	Totals	mantle/core thickness: 74.3%		2633.04	7.65571 x 10 ¹⁹	1.48167 x 10 ²³	1935.38

*: Volume and density are calculated assuming a spherical (not ellipsoidal) Ganymede with radius 2634.1 km.

Table 6.11: Ganymede Fe-FeS eutectic core (5150 kg m⁻³) model according to Anderson *et al.* (1996b).

	Layer Type	Fractional Radius	Radius of Layer (km)	Thickness of Layer (km)	Volume of Layer (m ³)*	Mass of Layer (kg)	Bulk Density of Layer (kg m ⁻³)*
MODEL 1	Ice	1.000	2634.1	700.6706	4.62828 x 10 ¹⁹	4.71289 x 10 ²²	1018.281
	Rock	0.734	1933.4294	1406.6094	2.96618 x 10 ¹⁹	9.7884 x 10 ²²	3300
	Iron	0.200	526.82	526.82	6.12457 x 10 ¹⁷	3.15415 x 10 ²¹	5150
	Totals	mantle/core thickness: 27.2%		2634.1	7.65571 x 10 ¹⁹	1.48167 x 10 ²³	1935.38
MODEL 2	Ice	1.000	2634.1	774.4254	4.9617 x 10¹⁹	5.54406 x 10²²	1117.373
	Rock	0.706	1859.6746	1069.4446	2.48731 x 10¹⁹	8.20812 x 10²²	3300
	Iron	0.300	790.23	790.23	2.06704 x 10¹⁸	1.06453 x 10²²	5150
	Totals	mantle/core thickness: 42.5%		2634.1	7.65571 x 10¹⁹	1.48167 x 10²³	1935.38
MODEL 3	Ice	1.000	2634.1	903.4963	5.4846 x 10 ¹⁹	6.74561 x 10 ²²	1229.919
	Rock	0.657	1730.6037	676.9637	1.68114 x 10 ¹⁹	5.54777 x 10 ²²	3300
	Iron	0.400	1053.64	1053.64	4.89965 x 10 ¹⁸	2.52332 x 10 ²²	5150
	Totals	mantle/core thickness: 60.9%		2634.1	7.65571 x 10 ¹⁹	1.48167 x 10 ²³	1935.38
MODEL 4	Ice	1.000	2634.1	1085.2492	6.09932 x 10 ¹⁹	7.91025 x 10 ²²	1296.906
	Rock	0.588	1548.8508	231.8008	5.99423 x 10 ¹⁸	1.97809 x 10 ²²	3300
	Iron	0.500	1317.05	1317.05	9.56964 x 10 ¹⁸	4.92836 x 10 ²²	5150
	Totals	mantle/core thickness: 85.0%		2634.1	7.65571 x 10 ¹⁹	1.48167 x 10 ²³	1935.38

*: Volume and density are calculated assuming a spherical (not ellipsoidal) Ganymede with radius 2634.1 km.

Concurrently with Anderson *et al.* (1996b), Schubert *et al.* (1996) produced another model of Ganymede's interior. Their model was based more on thermal constraints than physical - they assume a value of 0.010 W m^{-2} for the heat flux at the rock-ice interface, that this interface lies at a depth of $\sim 70\%$ of Ganymede's radius ($\sim 1840 \text{ km}$), and a silicate heat density (the amount of power generated per unit volume of silicate material due to the radiogenic material within it) of $1.8 \times 10^{-8} \text{ W m}^{-3}$. While no justification is given for assuming these numbers, the Schubert *et al.* (1996) models do not seem geophysically unreasonable, if their estimate for the silicate heat density is correct. The implications for Ganymede's internal structure are shown in Tables 6.12 and 6.13.

Table 6.12: Ganymede Fe core models according to Schubert *et al.* (1996)

Layer Type	Fractional Radius	Radius of Layer (km)	Thickness of Layer (km)	Volume of Layer (m ³)	Mass of Layer (kg)	Bulk Density of Layer (kg m ⁻³)
Ice Shell	1.000	2634.1	790.23	5.0298×10^{19}	5.74135×10^{22}	1141.467
Rock Mantle	0.700	1843.87	1251.1975	2.5387×10^{19}	8.37773×10^{22}	3300
Iron Core	0.225	592.6725	592.6725	8.72033×10^{17}	6.97626×10^{21}	8000
Totals	mantle/core thickness: 32.1%	2634.1	2634.1	7.65571×10^{19}	1.48167×10^{23}	1935.38

Table 6.13: Ganymede Fe-FeS core models according to Schubert *et al.* (1996)

Layer Type	Fractional Radius	Radius of Layer (km)	Thickness of Layer (km)	Volume of Layer (m ³)	Mass of Layer (kg)	Bulk Density of Layer (kg m ⁻³)
Ice Shell	1.000	2634.1	790.23	5.0298×10^{19}	5.70430×10^{22}	1134.101
Rock Mantle	0.700	1843.87	1011.4944	2.38434×10^{19}	7.86831×10^{22}	3300
Iron Core	0.316	832.3756	832.3756	2.41572×10^{18}	1.2441×10^{22}	5150
Totals	mantle/core thickness: 45.1%	2634.1	2634.1	7.65571×10^{19}	1.48167×10^{23}	1935.38

These models produce a pure Fe core of 22.5% of Ganymede's radius (R_G) with a silicate mantle of 47.5% R_G , or a Fe-FeS core of 31.6% of Ganymede's radius with a silicate mantle of 38.4% R_G . This results in a total heat flow of 4.7×10^{11} W (calculated from the silicate volume multiplied by the assumed silicate heat density), and a *surface* heat flux (at the top of the ice shell) of 0.005 W m^{-2} . The lithosphere thickness H of 77.5 km is calculated using:

$$H = 567 \frac{\ln(T_b/T_s)}{q} \quad (6.3)$$

which is rearranged from McKinnon and Parmentier (1986), with T_b (temperature at base of lithosphere) = 218 K (the assumed temperature at the base of a brittle icy lithosphere within the ice shell), T_s (temperature at surface) = 110 K, q (heat flow through lithosphere) = 0.005 W m^{-2} . The assumed and calculated values are shown in Table 6.14.

Table 6.14: Heat flow parameters for Ganymede
($q = 0.010 \text{ W m}^{-2}$ at rock-ice interface) according to Schubert *et al.* (1996).

Parameter	Value
<i>Assumed values:</i>	
Silicate heat density (W m^{-3})	1.8×10^{-8}
Heat flow at rock-ice interface (W m^{-2})	0.010
<i>Calculated values:</i>	
Total heat production (W)	$4.29 - 4.56 \times 10^{11}$
Heat flow at surface (W m^{-2})	0.005
Lithosphere thickness (km)	77.5

The total planet-wide heat flow at the rock/ice boundary is $4.29 - 4.56 \times 10^{11}$ W for the Fe and Fe-FeS models respectively, calculated by multiplying the volume of the rock layers from Table 6.12 and 6.13 by the silicate heat density. Note that this assumes that all the radioisotopes are located in the silicate mantle, and that the iron core and ice shell are not providing any heat.

Reynolds & Cassen (1979) assume that the surface heat flow of Ganymede lies between 0.035 and 0.155 W m^{-2} , given that solid state convection occurs in the ice I. They determine that their maximum heat flow of 0.155 W m^{-2} is reached when $(T_b - T_s) = 93 \text{ K}$, and their minimum value of 0.035 W m^{-2} is reached when $(T_b - T_s)$ becomes so small that a ‘stagnant lid’ regime (i.e. purely conductive, with no convective heat transfer) takes over. These values and scaled values from the Earth and Moon are adopted for the following calculations. Again, it is assumed that all of Ganymede’s radioisotopes are contained within the rocky part of the satellite, and that the ice contains no heat-generating elements.

The Reynolds & Cassen values of $0.035 - 0.115 \text{ W m}^{-2}$ enclose the range of values determined by McKinnon and Parmentier (1986) from lithosphere thicknesses, derived from Passey (1982). However, they represent heat flows at the *surface* of the ice shell, not at the rock-ice interface. Obviously, the exact value at that location will vary depending on the radius of the silicate body. I have incorporated these rock/ice interface (R/I) heat fluxes into the Anderson *et al.* (1996b) physical models, and the results are shown in Table 6.15.

A heat flow of 0.035 W m^{-2} at the surface implies a total heat production of $[0.035 \times \text{ice shell surface area} =] 3.0 \times 10^{12} \text{ W}$, and a surface heat flow of 0.115 W m^{-2} implies a total heat production of $1.00 \times 10^{13} \text{ W}$. Using these values, the heat flow at the rock-ice interface can be calculated by dividing the total heat production by the surface area of the rock shell. Similarly, the silicate heat density can be calculate by dividing the total heat production by the volume of the rock shell. The columns in bold type in Table 6.15 indicate the more likely internal configurations of Ganymede, based on the more reasonable ratios of the metal core:silicate mantle radius. Note that for this model I have again assumed that only the silicate mantle contains heat-generating elements.

Table 6.15: Heat flow of Ganymede (0.035 & 0.115 W m⁻²) using Reynolds & Cassen (1979) heat flow models.

		Fe core (0.2 R_G)	Fe core (0.3 R_G)	FeS core (0.3 R_G)	FeS core (0.4 R_G)
Core:Mantle%	-	28.2%	47.4%	42.5%	60.9%
Rock Radius (m)	2634100	1870211	1667385.3	1859674.6	1730603.7
Rock Surface Area (m²)	8.71915 x 10 ¹³	4.39533 x 10 ¹³	3.49367 x 10¹³	4.34594 x 10¹³	3.76361 x 10 ¹³
Rock Volume (m³)	7.65571 x 10 ¹⁹	2.67882 x 10 ¹⁹	1.73506 x 10¹⁹	2.48731 x 10¹⁹	1.68114 x 10 ¹⁹
--- MODEL 1 ---					
Total Heat Flow (W)	3.0517 x 10 ¹²	3.0517 x 10 ¹²	3.0517 x 10¹²	3.0517 x 10¹²	3.0517 x 10 ¹²
Heat Flow at Surface (W m⁻²)	0.035	0.035	0.035	0.035	0.035
Heat Flow at R/I depth (W m⁻²)	-	0.069	0.087	0.070	0.081
Silicate Heat Density (W m⁻³)	-	1.13920 x 10 ⁻⁷	1.75885 x 10⁻⁷	1.22691 x 10⁻⁷	1.81526 x 10 ⁻⁷
--- MODEL 2 ---					
Total Heat Flow (W)	1.0027 x 10 ¹³	1.0027 x 10 ¹³	1.0027 x 10¹³	1.0027 x 10¹³	1.0027 x 10 ¹³
Heat Flow at Surface (W m⁻²)	0.115	0.115	0.115	0.115	0.115
Heat Flow at R/I depth (W m⁻²)	-	0.228	0.287	0.231	0.266
Silicate Heat Density (W m⁻³)	-	3.74308 x 10 ⁻⁷	5.77907 x 10⁻⁷	4.03128 x 10⁻⁷	5.96441 x 10 ⁻⁷
--- MODEL 3 ---					
Total Heat Flow (W)	4.35958 x 10 ¹¹	4.35958 x 10 ¹¹	4.35958 x 10¹¹	4.35958 x 10¹¹	4.35958 x 10 ¹¹
Heat Flow at Surface (W m⁻²)	0.005	0.005	0.005	0.005	0.005
Heat Flow at R/I depth (W m⁻²)	-	0.010	0.012	0.010	0.012
Silicate Heat Density (W m⁻³)	-	1.62743 x 10 ⁻⁸	2.51264 x 10⁻⁸	1.75273 x 10⁻⁸	2.59322 x 10 ⁻⁸

Models 1 and 2 in Table 6.15 show the Anderson *et al.* (1996a) physical models, using the Reynolds and Cassen (1979) surface heat flow bounds of 0.035 W m^{-2} and 0.115 W m^{-2} . Model 3 shows the same physical models with the 0.005 W m^{-2} surface heat flows taken from the Schubert *et al.* (1996) model. The derived heat flow at the rock-ice interface is also derived for each of the models shown. For Model 3, the internal structure is less constrained (and probably more realistic) since Schubert *et al.*'s $0.7 R_G$ rock-ice interface radius is ignored, and the calculated silicate heat density is slightly different from the assumed value from the original model shown in Table 6.13 ($1.63 - 2.51 \times 10^{-8} \text{ W m}^{-3}$, rather than $1.8 \times 10^{-8} \text{ W m}^{-3}$).

Comparing the different models, it is clear that while the Schubert *et al.* (1996) model is physically realistic, the assumed value for the silicate heat density assumed is about an order of magnitude smaller than the value calculated using the $0.035 - 0.115 \text{ W m}^{-2}$ surface heat flows. Is it possible to determine which model is more 'thermally realistic'?

Assuming that the total heat flow of Ganymede is generated entirely by radiogenic heating within its silicate body, the silicate heat density according to the $0.035 - 0.115 \text{ W m}^{-2}$ models lies between 1.1×10^{-7} and $6.0 \times 10^{-7} \text{ W m}^{-3}$. By comparison, the volume of Earth's silicate mantle (and crust) is $9.1055 \times 10^{20} \text{ m}^3$, and its total global heat flow is $4.1 \times 10^{13} \text{ W}$ (Davies, 1980) so the Earth's current silicate heat density is $4.5028 \times 10^{-8} \text{ W m}^{-3}$. The volume of the lunar mantle and crust (assuming a combined thickness of 1388 km) is $2.1811 \times 10^{19} \text{ m}^3$, and the Moon's total global heat flow is $1.1388 \times 10^{12} \text{ W}$, so the current lunar silicate heat density is $5.2210 \times 10^{-8} \text{ W m}^{-3}$ (these figures are reproduced in Table 6.17). Thus, the Reynolds and Cassen (1979) values for Ganymede's silicate heat density are

between two and twelve times greater than that of the Earth and Moon, while Ganymede's total global heat flow lies between that of the Earth and Moon.

If the silicate heat density in a chondritic-type body should be $\sim 3 \times 10^{-8} \text{ W m}^{-3}$, and if Ganymede formed from such a body, then it is clear that the Reynolds & Cassen (1979) values for Ganymede's silicate heat density are much too high to be physically reasonable.

However, it should be remembered that we are assuming that the 'silicate heat density' represents only the heat generated by radioactive decay - but there are other methods of generating heat in a planetary interior and we could broaden the definition to include any kind of heat generation per unit volume, such as tidal heating. The Reynolds & Cassen (1979) values may therefore be more applicable if we consider them to be representative of a combination of radiogenic heating and tidal heating rather than radiogenic heating alone.

The Schubert *et al.* model provides a silicate heat density for Ganymede of $(2.04 \pm 0.44) \times 10^{-8} \text{ W m}^{-3}$ - about two-fifths that of the Earth and Moon today. This could be valid if the silicate material around Jupiter from which the Galilean satellites formed is less rich in radioactive isotopes than the material in the inner solar system from which the Earth accreted. However, it is unclear whether this is a valid assumption or not.

An interesting - and possibly more realistic - model would be one that uses earth-like values for heat production in Ganymede. This is done by multiplying the silicate heat density of the Earth by the rock volume of the Ganymede models. This would yield the total global heat flow of a Ganymede with earth-like (radiogenic) composition. We can then calculate heat flow values at the rock/ice interface and the ice shell surface for a Ganymede with earth-like radiogenic composition in the silicate mantle, shown in Table 6.16. Heat flow parameters for the Earth and Moon are shown for comparison in Table 6.17.

Table 6.16: Internal Structure and corresponding Heat Flow of Ganymede with Earth-like radiogenics

		Fe core (0.2 R_G)	Fe core (0.3 R_G)	FeS core (0.3 R_G)	FeS core (0.4 R_G)
Core:Mantle radius %	-	28.2%	47.4%	42.5%	60.9%
Rock Radius (m)	2634100	1870211	1667385.3	1859674.6	1730603.7
Rock Surface Area (m²)	8.71915 x 10 ¹³	4.39533 x 10 ¹³	3.49367 x 10¹³	4.34594 x 10¹³	3.76361 x 10 ¹³
Rock Volume (m³)	7.65571 x 10 ¹⁹	2.67882 x 10 ¹⁹	1.73506 x 10¹⁹	2.48731 x 10¹⁹	1.68114 x 10 ¹⁹
Total Heat Flow (W)	-	1.20622 x 10 ¹²	7.81263 x 10¹¹	1.11998 x 10¹²	7.56985 x 10 ¹¹
Heat Flow at Surface (W m⁻²)	-	0.014	0.009	0.013	0.009
Heat Flow at R/I depth (W m⁻²)	-	0.027	0.022	0.026	0.020
Silicate Heat Density (W m⁻³)	-	4.5028 x 10 ⁻⁸	4.5028 x 10 ⁻⁸	4.5028 x 10 ⁻⁸	4.5028 x 10 ⁻⁸

Table 6.17: Heat Flow parameters for the Earth and Moon

	Earth	Moon
Core:Mantle radius %	54.5%	17%
Radius (m)	6378000	1738000
Surface Area (m²)	5.11186 x 10 ¹⁴	3.79585 x 10 ¹³
Mantle/Crust Volume (m³)	9.10552 x 10 ²⁰	2.1811 x 10 ¹⁹
Total Heat Flow (W)	4.10003 x 10 ¹³	1.13875 x 10 ¹²
Heat Flow at Surface (W m⁻²)	0.080	0.030
Silicate Heat Density (W m⁻³)	4.5028 x 10 ⁻⁸	5.22100 x 10 ⁻⁸

6.5.2 Ganymede ONIONSKIN Model

The Ganymede interior structure models presented in the previous section are all physically reasonable, depending on the assumptions made regarding heat production assumed within the satellite. However, all lack a liquid water layer, the presence of which has been implied by the detection of an induced magnetic field along with an intrinsic dynamo field (see Chapter 3). Also, they are based on assumptions that the silicate and metal layers have fixed densities (3300 and 5150 to 8000 kg m⁻³ respectively), which is somewhat restrictive and possibly unrealistic.

One possible (six-layer) ONIONSKIN model for Ganymede is presented in Tables 6.18 and 6.19. A major feature of interest is the very deep (~ 590 km) salt water layer that occupies most of the Ganymede's radius beyond the silicate surface. Also of note is the ~ 380 km thick ice VI layer at the base of the water layer. The ice I crust is therefore completely decoupled from the silicate surface in this model, and the water layer has many implications for the surface geology and evolution of Ganymede. It should be noted that the silicate body radius is larger than that of Europa.

The model also contains a molten Fe-FeS core with an uncompressed density of 5965 kg m⁻³. I showed in Chapter 3 that it was likely that convection due to a condensing inner core creates Ganymede's intrinsic magnetic field - this is modelled here. The resulting model fits the observed radius, density, and moment of inertia parameters derived by Anderson *et al.* (1996) very well.

Figure 6.5 illustrates the internal structure of Ganymede shown in Table 6.18.

Table 6.18: ONIONSKIN model of the internal structure of Ganymede.

Layer	Percent Mass	Uncompressed Density (kg m ⁻³)	Layer Mass (kg)	P/T Density (kg m ⁻³)	Model Radius (km)	Thickness of Layer (km)	Base Pressure (GPa)
Ice I	4.50	921	6.66837 x 10 ²¹	931	2632.89	84.94	0.1128
Salt Water	34.50	1050	5.11242 x 10 ²²	1353	2547.95	588.71	1.2714
Ice VI	15.00	1322	2.22279 x 10 ²²	1473	1959.24	382.53	2.1574
Rock Mantle	36.00	3600	5.33470 x 10 ²²	3738	1576.71	776.10	7.4657
Molten Fe-FeS core	7.00	5965	1.03730 x 10 ²²	6348	800.61	303.24	10.4349
Solid Fe Core	3.00	8000	4.44558 x 10 ²¹	6921	497.37	497.37	15.5792
Totals:	100.00		1.48186 x 10²³			2632.89	

(Table key as for Table 6.3)

Table 6.19: Ganymede FeS core ONIONSKIN model results compared with target values for radius, mass, C/MR², and density

	Target Values	1s error range		Model Results	Error
Radius	2632.89	± 0.27 km		2632.89	± 0.00 km
Mass	1.48186 x 10 ²³	± 0.00019 x 10 ²³ kg		1.48186 x 10 ²³	-
C/MR²	0.311185	± 0.0028		0.309404	- 0.000790
Density	1938.30	± 0.42 kg m ⁻³		1938.30	± 0.00 kg m ⁻³

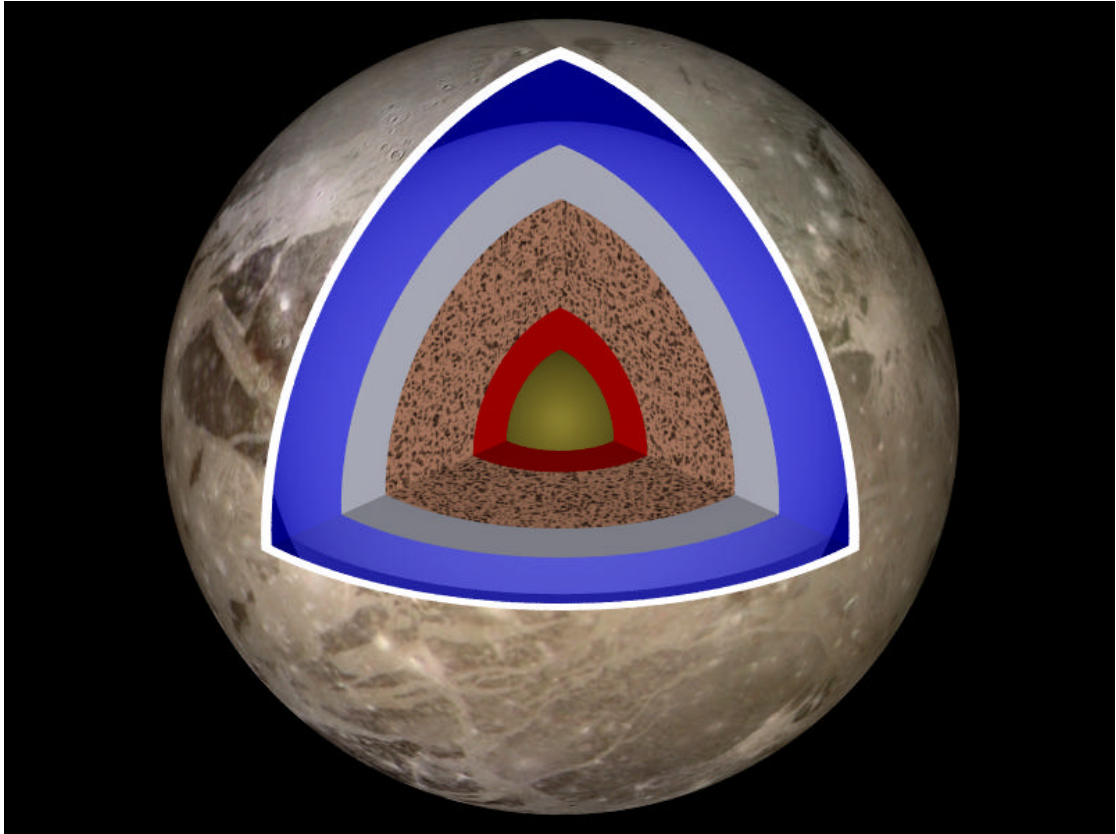


Figure 6.5: The internal structure of Ganymede. The cutaway view of Ganymede shown here illustrates the six-layer ONIONSKIN internal structure model described in Table 6.18. The white layer at the surface is the ice I layer, the blue layer represents the water layer, the grey layer represents ice VI, the mottled brown layer represents the silicate mantle, the red layer represents the molten Fe-FeS outer core, and the brassy layer represents the solid Fe core. Ganymede is shown to scale with the other Galilean satellite cutaways shown in Figures 6.3, 6.4, and 6.6. Image by Constantine Thomas, rendered using POV-Ray 3.02.

6.6 The internal structure of Callisto

6.6.1 Published models

Callisto is an enigma. Its surface is tectonically inert, but Galileo detected the signature of a magnetic field on one of its flybys of the satellite (Khurana *et al.* 1998). This could only be explained if a liquid salty water layer existed a few hundred kilometres below Callisto's surface, and a magnetic field was being induced by the jovian field (Kivelson *et al.* 1999).

Anderson *et al.* (1998a) explored some models of Callisto's interior, but unfortunately this was prior to the discovery of the water layer. It is therefore difficult to incorporate such a layer into their models, which made no provision for such a situation. They proposed that Callisto, with a moment of inertia factor of 0.358 ± 0.004 (determined from the C10 flyby), consists of a rock/metal core taking up 25% of the satellite's radius, a mixed rock-ice mantle, and a pure ice crust. This is described in Table 6.20.

Table 6.20: Callisto Internal Structure according to Anderson *et al.* (1998a).

Callisto	Radius
Ice shell thickness	350 km
Rock-ice mantle thickness	1457 km
Silicate core radius	602 km
Total radius	2409 km

Anderson *et al.* (2001) more recently presented a more accurate report on the interior structure and physical parameters of Callisto. Callisto's moment of inertia C/MR^2 is refined to 0.3549 ± 0.0042 - too small for Callisto to be completely undifferentiated, but too large for it to have separated completely into a rock core, water mantle, and ice crust. They present a range of two- and three-layer models for Callisto's interior - their three-layer models consist of an ice layer nearest the surface with a density range between 900 and 1500 kg m⁻³, a rock/ice middle layer with density between 2300 and 3500 kg m⁻³, and a rock or metal core of density 3550, 5150 or 8000 kg m⁻³. Their rock core models yield the most realistic results, but they still do not account for the existence of a water layer within the satellite, as determined by magnetometer measurements (Kivelson *et al.*, 1999). As such their models remain incomplete.

6.6.2 Callisto ONIONSKIN Models

Here I present a possible ONIONSKIN model of Callisto's interior that does account for the water layer. Kivelson *et al.* (1999) propose that such a water layer must be tens of kilometres thick, but also that it must be a tens of kilometres below the surface in order for the detected magneto-convective field to have the correct magnitude. As yet, a mechanism that would form a water layer so close to the surface is not understood. The main problem is that the water layer would be placed entirely within the ice I layer, with no apparent mechanism to allow it to exist there. This problem remains insurmountable at the time of writing. Instead, I continue to focus on physically plausible density and temperature models and disregard this problem. The resulting model is presented in Table 6.21 and 6.22.

Table 6.21: ONIONSKIN model of the internal structure of Callisto with a silicate core (density: 3500 kg m⁻³).

Layer	Percent Mass	Uncompressed Density (kg m ⁻³)	Layer Mass (kg)	P/T Density (kg m ⁻³)	Model Radius (km)	Thickness of Layer (km)	Base Pressure (GPa)
Ice I	6.30	921	6.77844 x 10 ²¹	932	2409.21	104.10	0.1200
salt water	7.50	1050	8.06957 x 10 ²¹	1136	2305.10	111.70	0.2671
Ice III	3.50	1138	3.76580 x 10 ²¹	1182	2193.40	54.01	0.3415
Ice/Rock Mantle	72.70	1938	7.82210 x 10 ²²	2054	2139.39	1250.96	3.6745
Rock Core	10.00	3500	1.07594 x 10 ²²	3663	888.43	888.43	6.6341
Totals:	100.00		1.07594 x 10²³			2409.21	

(Table key as for Table 6.3)

Table 6.22: Callisto silicate core ONIONSKIN model results compared with target values for radius, mass, C/MR², and density

	Target Values	1s error range		Model Results	Error
Radius	2409.33	± 0.29 km		2409.20	- 0.14 km
Mass	1.07594 x 10 ²³	± 0.00014 x 10 ²³ kg		1.07594 x 10 ²³	-
C/MR²	0.353676	± 0.0042		0.352195	- 0.001481
Density	1836.57	± 0.45 kg m ⁻³		1836.87	- 0.30 kg m ⁻³

It should be noted that this model actually represents a lower bound, since most of the derived model results lie near the lowest error bounds of the target values proposed in Anderson *et al.* (2001). It is possible to reach slightly more “accurate” results (lying nearer the centre of these error bounds), but it becomes progressively harder to achieve these results. There are several reasons for this. First, the density constraint is very tight and very sensitive to change - increasing the ice/rock mantle or rock core mass by anything more than approximately 1% produces densities that are unacceptably high or low. The radius constraint is similarly tightly restricted. There is also a potential base pressure constraint at the base of the ice III layer if ice V is also present (it is not present in this particular model, however). In effect, this acts to severely limit the range of proportions of the material above and including the ice III layer - the pressure at the base of the ice III *must* be 346 MPa in order to allow it to change phase to ice V. However, this constraint is not considered here, as it is assumed that the top of the ice/rock mantle lies above the ice III/V phase boundary. This means that the ice III transforms to ice V within the ice/rock mantle (and indeed, the ice V transforms to ice VI, and ice VII towards the rock core), but these phase changes are subsumed into the density of the ice/rock mix.

The ice/rock mantle is assumed to be a layer of constant density (excluding the effects of self-compression), consisting of a uniformly mixed 71:29 mixture of ice (with a density of 1300 kg m^{-3}) and rock (with a density of 3500 kg m^{-3} , identical to the core). Such uniform mixing across a large ice/rock mantle is however rather unlikely, since the rock is more likely to be concentrated towards the core. If this happens, the density of the ice/rock mantle should increase with depth - however, attempts to model this layer by dividing it into three layers whose density increases with depth give rise to severe problems in keeping the model constrained to the target radius, density and moment of inertia targets. This problem can potentially be solved using a more complex program that can explore the full parameter space of the model, and this has led to the development of the more advanced SATMOD program described in Chapter 7.

Figure 6.6 shows a cutaway view of Callisto that illustrates the internal structure of the satellite, as described in Table 6.21.

Figure 6.7 shows ‘slices’ through each of the Galilean satellites, illustrating the relative sizes of the bodies and of their core and mantle layers. Image by Constantine Thomas, rendered using POV-Ray 3.02.

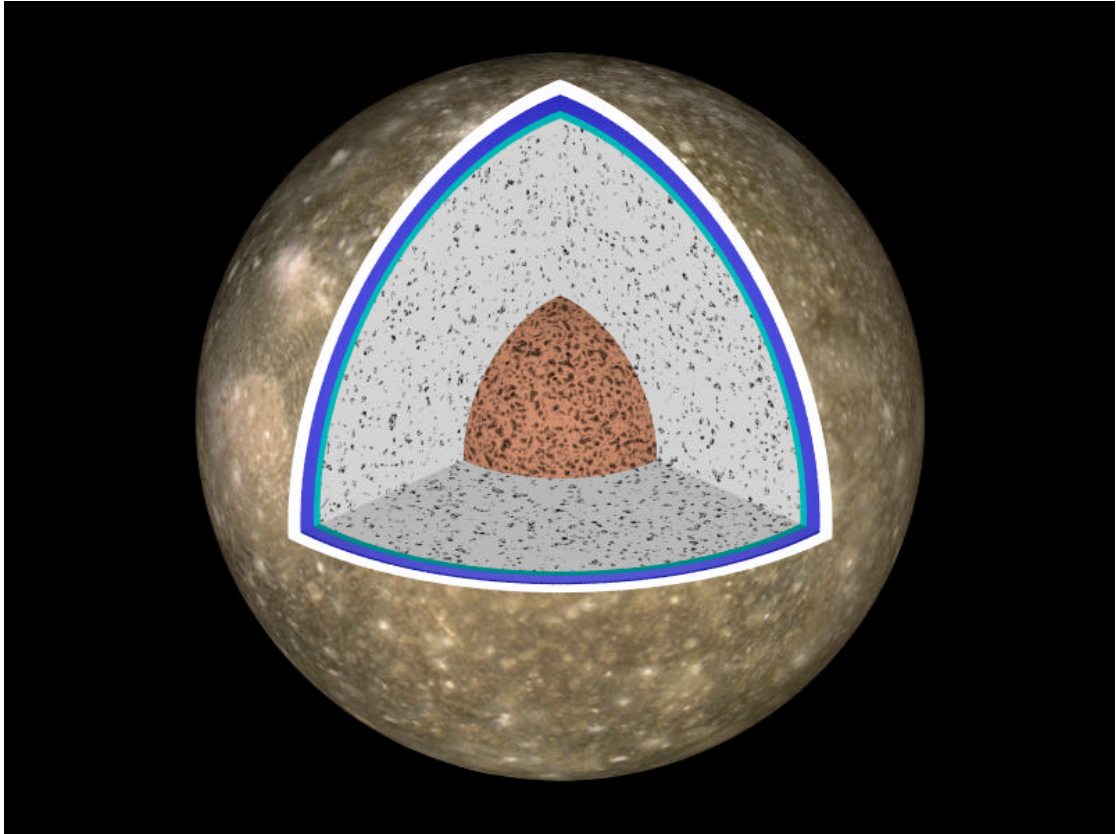


Figure 6.6: The internal structure of Callisto. The cutaway view of Callisto shown here illustrates the five-layer ONIONSKIN internal structure (silicate core) model described in Table 6.20. The white layer at the surface is the ice I layer, the blue layer represents the water layer, the cyan layer represents ice III, the speckled white layer represents the ice/rock mantle, and the mottled brown layer represents the silicate core. Callisto is shown to scale with the other Galilean satellite cutaways shown in Figures 6.3, 6.4, and 6.5. Image by Constantine Thomas, rendered using POVRay 3.02.

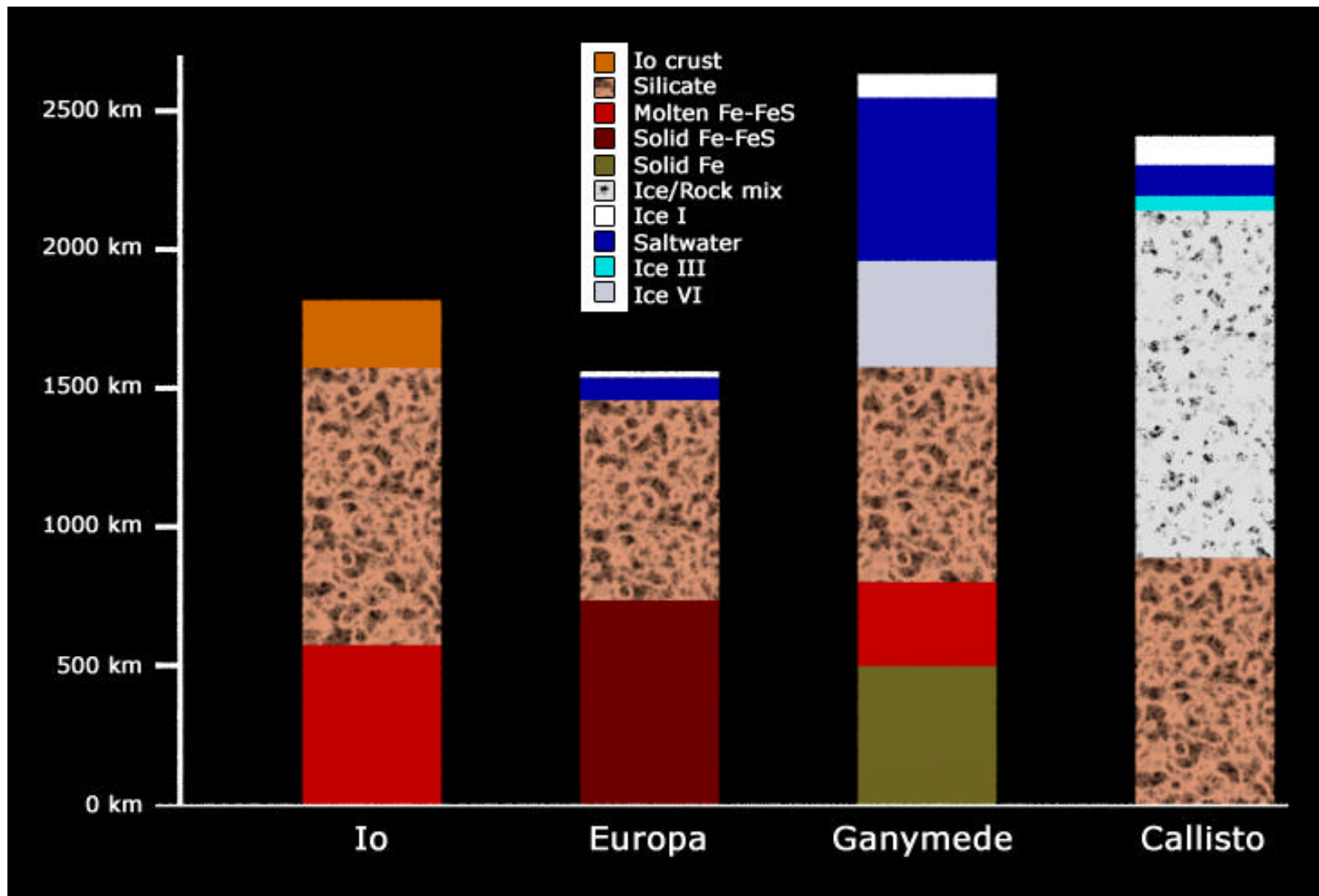


Figure 6.7: A comparison of the internal structures of the Galilean Satellites produced by my ONIONSKIN model.

6.7 The next stage

Although the ONIONSKIN model yields better constrained models than current work by other authors (e.g. Anderson *et al.*), it became clear that many refinements were required in order to produce more realistic models. In order to do this, I developed a FORTRAN program called SATMOD, which extends ONIONSKIN and allows us to explore the full parameter space of each model. SATMOD is described in the next chapter, and the program is applied to Callisto in order to provide a more accurate model of the interior.

Chapter 7 SATMOD: The next step in satellite modelling.

7.1 Introduction

The SATMOD (SATellite MODeller) FORTRAN program is a more advanced and fully developed version of the original ONIONSKIN spreadsheet presented in Chapter 6. I designed it in order to construct more accurate models of the interior structure of satellites and to more fully explore the range of possible models. It can also potentially be used to construct similar models for any spherical planetary body for which the relevant basic physical parameters are known.

The observed values of radius, mass, density, and moment of inertia factor C/MR^2 (and 1σ error bars) are first entered into SATMOD. Appropriate layer materials are then entered (e.g. ice I, ice III, ice/rock mixtures, silicate, iron and/or iron sulphide), along with the uncompressed density and bulk modulus for each material, and the percentage of the mass of the satellite that each layer represents. Like ONIONSKIN, SATMOD then constructs a range of possible models by calculating the radius, mass, bulk density and C/MR^2 of the satellite given the properties of the layers entered into the program - however, SATMOD also accounts for self-compression of layers due to the mass of overlying material (i.e. increasing density with depth) and the variation in gravitational acceleration with depth in the body. These modifications allow SATMOD to produce much more realistic results than ONIONSKIN.

SATMOD is designed to adopt a “brute force” strategy - it constructs a range of models by multiplying each of the layer mass percentages by factors that range in various increments between 0.5 and 1.5 (the total mass still adds up to 100%). The resulting physical parameters of the model satellite are then compared with the values derived from Galileo Orbiter observations (published in various papers by Anderson *et al.*). The density of individual layers can also be varied over a user-defined range if appropriate (e.g. ice/rock mixtures), which means that the models are recalculated for all layer densities as well as for every permutation of layer mass. If the calculated values of the predicted parameters fall within the error bounds of the observed values, the resulting model is output to a text file; if the calculated values fall beyond the error bounds of the observed values, the model is discarded. Thus, SATMOD only produces physically valid models that agree with the parameters observed by the Galileo Orbiter. Other methods are also used to discard unrealistic models, such as those that result in high density material overlying low density material, or that produce pressures at the base of layers that are too high for a material to be stable (e.g. the various ice phases).

This means that the full parameter space can be explored, covering every possible model given a range of input parameters - a marked improvement over ONIONSKIN, which can only determine viable models by manual trial and error. However, ONIONSKIN still has its uses - when more than six layers are involved, all with varying densities, a working model can be put together by trial and error much more quickly in ONIONSKIN than the time in which it takes SATMOD to calculate it. This allows us to use ONIONSKIN to find values in the right ‘ballpark’ to insert into SATMOD, and saves wasting time guessing the input parameters.

There are some important caveats to be aware of regarding SATMOD. The program produces physical models constrained solely by moment of inertia, radius, density and mass. No chemical or thermal modelling is carried out as part of the model verification - though obviously this can be carried out on the results afterwards. However, care is taken to assume reasonable densities for materials comprising the layers and to use appropriate physical parameters. It should also be noted that SATMOD does not account for any variation in the bulk modulus of the material with pressure and temperature.

More often than not, many hundreds or even thousands of valid models are produced. By taking a wide range of factors and increments and (where appropriate) layer densities, it is possible to identify peaks in the distribution of valid models and to select promising models from them that fit the observed parameters.

Since SATMOD only uses physical rather than chemical or thermal constraints, it is difficult to pick out one single model to highlight. All the output models agree with observed parameters and are therefore potentially valid. Thus, I present one possible model picked from the distribution peak, selected as a representative sample. Even with these caveats, SATMOD produces results that are more realistic than those produced by ONIONSKIN.

Here, I shall illustrate the use of SATMOD to produce a more accurate model of Callisto's internal structure. I shall also attempt to determine the thermal structure of the satellite based on the results of this modelling.

7.2 Callisto SATMOD model

The original ONIONSKIN model (see Section 6.6.2) consisted of five layers - ice I, saltwater, ice III, a deep ice-rock mixture, and a rock core. These materials were selected since they were proposed in the models of Anderson *et al.* (2001). I noted that the ice-rock layer produced by ONIONSKIN had a uniform density throughout, but occupied over half the radius of Callisto. I also realised that this is not realistic - some gravitational settling of the rock through the ice should be expected, resulting in a density gradient that increases toward the silicate core. I therefore use SATMOD to produce a more detailed model of Callisto.

The SATMOD program allows me to incorporate this density gradient through the ice-rock mantle by treating it as three separate ice-rock layers that increase in density toward the centre of the satellite. It is possible to include more layers, but the processing time required to run SATMOD increases drastically with each new layer. Each of the three ice-rock layers in the SATMOD model has a recalculated bulk modulus to account for the changing percentage of ice and rock - I assume a silicate component density of 3500 kg m^{-3} and ice component density of 1300 kg m^{-3} . I also assume that the bulk modulus of the ice in the ice-rock mix is 15 GPa, irrespective of the actual type of ice present. The ice V and VI bulk moduli and densities are similar but not identical to these assumed values, so this is a possible source of error in the model. The SATMOD input parameters are shown in Table 7.1 and were refined from the original ONIONSKIN model - the numbers in parentheses in the table are the increments by which the associated parameters are varied within the range.

Table 7.1: Input SATMOD Parameters to Callisto model

Mass: 1.07594×10^{23}			
Radius: 2409.3 km		Radius Error: ± 0.29 km	
Bulk Density: $1836.57 \text{ kg m}^{-3}$		Density Error: $\pm 0.45 \text{ kg m}^{-3}$	
C/MR ² : 0.353676		C/MR ² Error: ± 0.0042	
Layer	Mass%	Density (kg m^{-3})	K (GPa)
Ice I	7.5	921	9.2
Water	3.125	1050	3.0
Ice III	6.0	1138	8.5
Ice-Rock1	33.0	1600 - 2300 (25)	variable
Ice-Rock2	33.0	1800 - 2600 (25)	variable
Ice-Rock3	11.625	2100 - 2900 (25)	variable
Rock Core	5.75	3500	148

Layer Mass% Multiplication Factor: 0.5 - 1.5 (0.25)

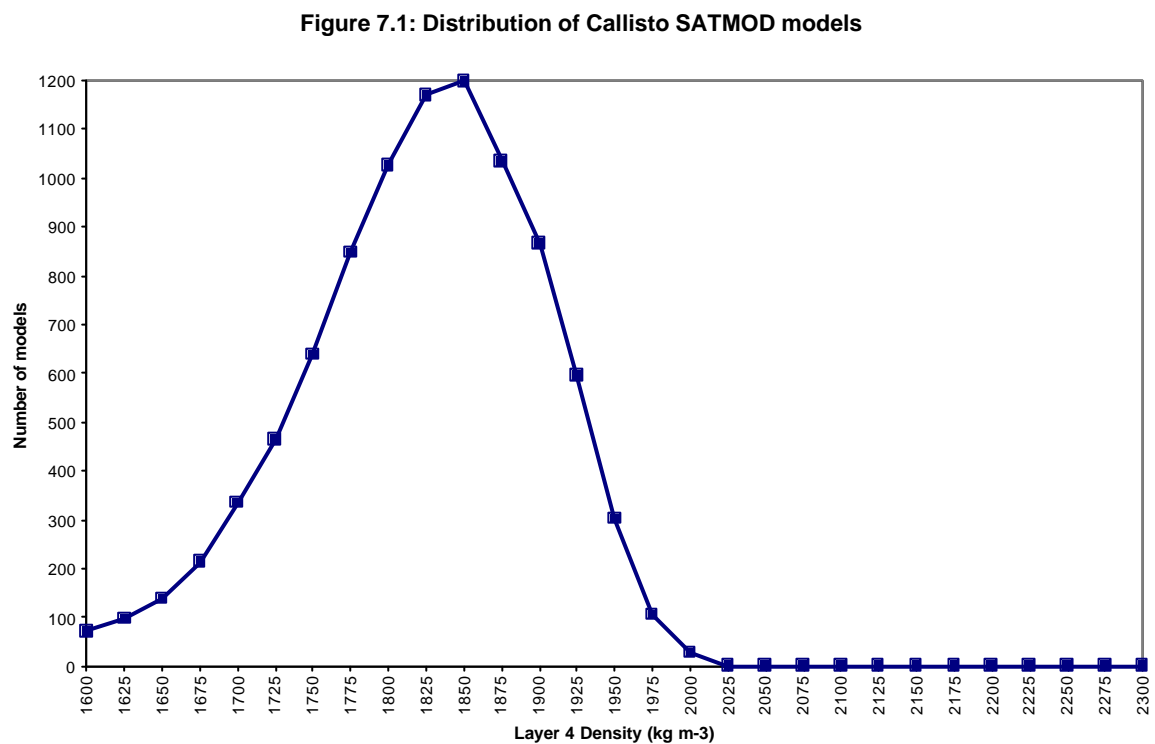
Two additional constraints are set - the program rejects any models where the pressure at the base of the ice I layer is greater than 207 MPa, or where the pressure at the base of the ice III layer is greater than 346 MPa. If the base pressure were that large, the ice would change into a higher density phase which would have to be explicitly modelled. Since we are assuming that these higher density phases do not exist outside the ice/rock mix layers, we can reject models that produce them. These constraints explain why the distribution curve in Figure 7.1 is skewed slightly toward the lower densities - as the Layer 4 density increased, more models were generated where the pressure at the base of the ice III was greater than 346 MPa, and were therefore rejected.

As with the ONIONSKIN models, the ice is assumed to be pure, and the water is assumed to be 5% saline by mass. No salt layers are modelled here, though they may exist - unfortunately there is presently no way to estimate what a realistic thickness could be for these, and their interaction with the ice layers would complicate the modelling considerably. This is therefore left for future work.

It should be noted that the saltwater layer may be more - or less - saline, but the salinity cannot be constrained without complex chemical modelling of Callisto, again beyond the scope of this thesis. It is also difficult to state qualitatively the effects of a different salinity in this model. A denser saltwater layer near the surface would increase Callisto's moment of inertia, but this could be countered in several ways - by changing the densities of the ice/rock mixtures, or of the core itself, or the thicknesses of any of the other layers in the satellite. Callisto models with denser (i.e. more saline) oceans are almost certainly viable, but this merely adds yet another dimension to the parameter space and makes it even more difficult for us to choose a single model to focus on - if a way is found to determine the salinity via chemical modelling, this could be used to remove this extra dimension. For the purposes of this thesis, however, I shall assume the salinity of the water is 5% by mass.

The program generated a total of 9132 models that satisfied all the constraints of radius, mass, moment of inertia, and bulk density for the input parameters shown in shown in Table 7.1.

Figure 7.1 shows the distribution of the output models that were produced, binned according to uppermost ice-rock layer ('Layer 4') density: after several model runs, it became clear that this layer is the most important in determining the density structure below it. There is an obvious peak in the distribution of models with Layer 4 densities at 1850 kg m^{-3} .



7.3 Discussion

7.3.1 Initial results

A single model was selected from the distribution peak to discuss here - this is tabulated in Table 7.2, and illustrated in Figure 7.2.

Table 7.2: Callisto SATMOD output model

Layer	uncompressed density	Bulk Modulus	ice%
4	1850.00 kg m ⁻³	48.25 GPa	75.00
5	2220.00 kg m ⁻³	69.41 GPa	59.09
6	2525.00 kg m ⁻³	89.06 GPa	44.32

Layer	Mass %	Compressed Density (kg m ⁻³)	Layer Thickness (km)	Base Pressure (GPa)
Ice I	6.300	932.86	104.05	0.1200
Saltwater	5.625	1127.76	83.35	0.2390
Ice III	3.500	1179.16	52.73	0.3187
Ice-Rock1	46.50	1915.39	585.74	1.7663
Ice-Rock2	23.25	2289.85	475.05	2.9522
Ice-Rock3	11.70	2636.32	503.31	4.1017
Rock Core	3.125	3624.31	605.04	5.4455

	Target Values	1σ error range	Model Results	Error
Radius	2409.33	± 0.29 km	2409.27	- 0.06 km
Mass	1.07594 x 10 ²³	± 0.00014 x 10 ²³ kg	1.07594 x 10 ²³	-
C/MR ²	0.353676	± 0.0042	0.350907	- 0.002679
Density	1836.57	± 0.45 kg m ⁻³	1836.73	+ 0.16 kg m ⁻³

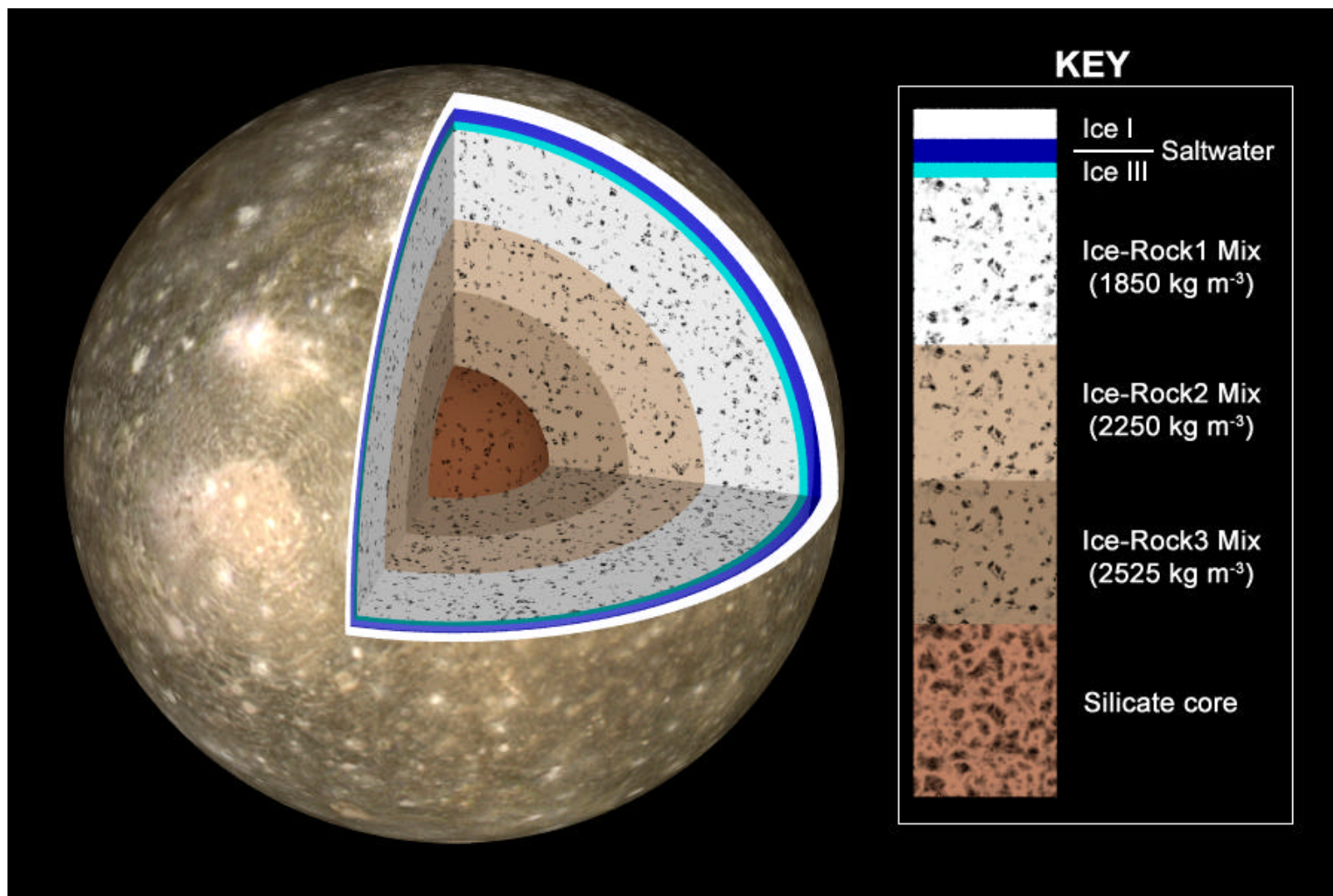


Figure 7.2 Cutaway through SATMOD Callisto model

The model presented here was selected as a potentially realistic candidate out of 1198 possible candidates from the distribution peak, since it consists of an ice I shell at least 100 km thick (agreeing with geological observations), a saltwater layer several tens of kilometres thick (required to explain the magnetic field), ice-rock layers with uniformly increasing thickness and density toward the centre of the satellite, and a sizeable silicate core.

This model has an ice-rock layer that ranges in density from 1850 kg m^{-3} (75% ice) at its top to 2525 kg m^{-3} (44% ice) at its base. The transition to the rock core remains rather discrete, but is more acceptable here than the transition from 71% ice to 100% rock in the Callisto ONIONSKIN model presented in Section 6.6.2. It should be noted that the three ice-rock layer boundaries do not reflect the location of different higher-pressure ice phases in the mixture - the layers are instead defined by the proportion of rock within them, and the density of the silicate component is assumed to swamp the ice component.

The saltwater layer is located between a thick ice I layer above and a thin ice III layer below it, totalling just over 240 km in depth. As expected, the base pressure of the ice III layer is less than the ice III-ice V phase transition at 346 MPa. This means that the uppermost part of the ice-rock mixture is actually a mix of ice III and silicate material, which then becomes a mix of ice V and silicate when the pressure reaches 346 MPa. The rest of the upper portion of the Ice/Rock1 layer consists of ice V + rock. As the pressure increases, the middle/lower part of the Ice/Rock1 layer becomes ice VI + rock, and transforms into ice VII + rock about a third of the way into the Ice/Rock2 layer, remaining as such until the silicate core boundary is reached.

One possible explanation for the thickness and location of the water layer is that it is the last vestige of a more extensive layer that existed earlier in Callisto's history (Williams *et al.*, 2001). The water layer would have cooled monotonically with time and become almost completely frozen today, since Callisto lacks any major alternative heat source (such as tidal heating) to augment its radiogenic heat flow. However, if there were a larger water layer in the past, the 'pure' high pressure ice layers should be deeper, since the rock component would have separated out from the ice component to a much greater extent - but attempts to generate more fully differentiated models with the layer compositions used here always result in C/MR^2 values that are too low to fit observed values. The implication is that if the model/class of models presented here are correct - which does appear to be the case given the moment of inertia constraints - then the water layer has never been more than ~ 200 km thick, and the rocky material has only sunk through nearly 70 km of ice III over the 4.6 billion year history of the Solar System. Clearly, the internal structure and evolution of Callisto is much more complicated than previously envisaged, but further investigation of this problem is left for future work.

As noted earlier, SATMOD does not account for any thermal or chemical evolution - it only fits a physical model to observed values. A model of Callisto determined by chemical and thermal differentiation of a primordial chondritic composition (that also remains within the error bounds of the values observed by the Galileo orbiter) may yield other possible configurations that are more realistic - a small iron sulphide core may be present, the rock component may be more fully separated from the ice component if different silicate densities are assumed, and/or extremely thick salt deposits or denser brine oceans may exist. These alternatives remain to be investigated, but could provide further insights into the question of the origin of the water layer.

For now however, I have a working model of Callisto based on purely physical constraints - mass, radius, density, and moment of inertia. I shall now attempt to investigate the thermal profile through this model in order to see whether or not it is “thermally realistic”.

7.3.2 The temperature problem

The first stage in producing a “thermal profile” through the upper layers of the SATMOD Callisto model generated in the previous section is to note the base pressures of the ice I, saltwater, and ice III layer. These pressures can then be cross-referenced with the phase diagram of water, to determine the temperatures that must exist at the base of the layers - the base pressure determines where the thermal profile crosses the water/ice(I or III) phase boundary on the P-T diagram.

There is an empirical relation between the melting curves of the various forms of ice, reproduced here from the review by Fortes (1999):

$$P = P_o + a \left[\left(\frac{T}{T_o} \right)^c - 1 \right] \quad (7.1)$$

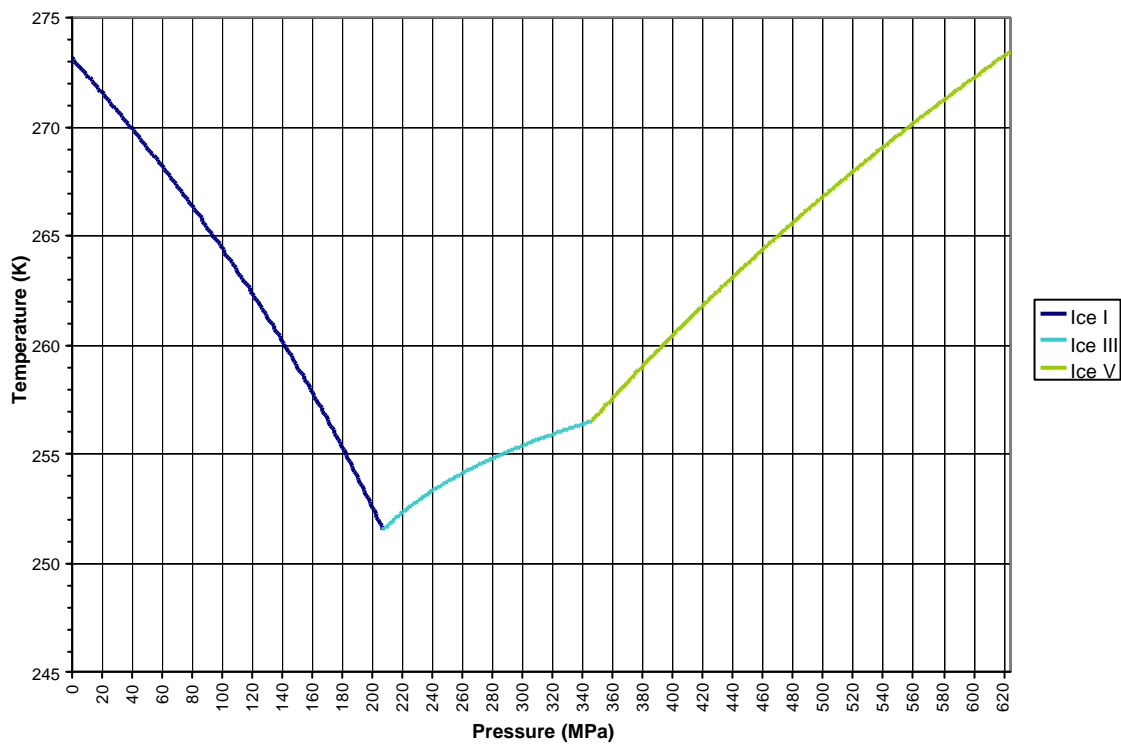
where P_o , T_o , a , and c are defined in Table 7.3.

Table 7.3: Parameters for ice melting curve equation

	P_0 (MPa)	T_0 (K)	a (MPa)	c
Ice I	0	273.16	-395.2	9
Ice III	207	251.15	62	60
Ice V	346	256.15	410	8.1
Ice VI	625	273.31	707	4.46
Ice VII	2210	355	534.2	5.22

The melting curves for ice I, ice III, and ice V are plotted on Figure 7.3:

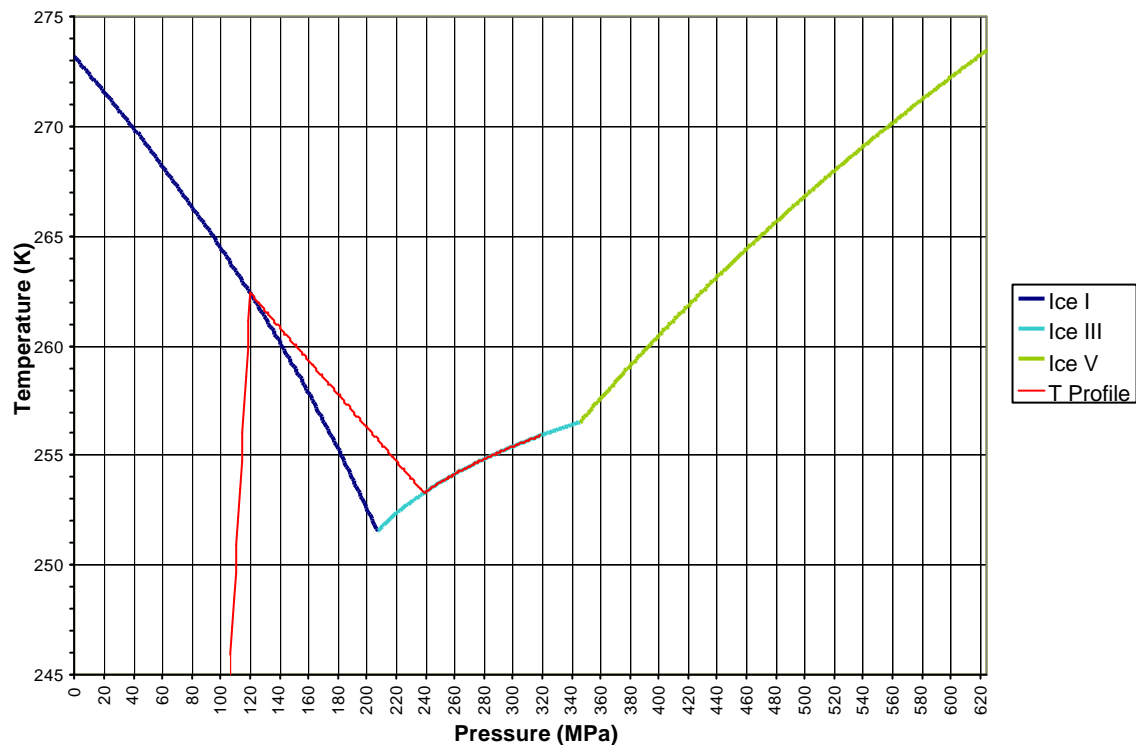
Figure 7.3: Melting curves for ice I, ice III, and ice V



Only the boundaries between the ice phases and liquid water are shown in Figure 7.3 - ice I lies below the blue line, ice III lies below the cyan line, and ice V lies below the green line, and liquid water lies above all the lines.

I can now plot the temperature profile implied by the base pressures generated in the SATMOD Callisto model I presented in Section 7.3 - this is shown as the red line in Figure 7.4 (this profile stops at ~ 320 MPa because this is the base of the ice III layer shown in Table 7.2):

Figure 7.4: Temperature profile through SATMOD Callisto model



The temperature profile intersects the y-axis at 110 K, the surface temperature of Callisto. However, we can instantly see a major problem - the temperature drops by nearly 10 K between the top and bottom of the water layer. This is only possible if the top of the water layer is being heated, but there is no known mechanism by which this can happen on Callisto.

Furthermore, the temperature of the water should actually increase with depth because of adiabatic compression. This is determined using equation (7.2):

$$\frac{dT}{dr} = \frac{\alpha g T}{C_p} \quad (7.2)$$

where α is the thermal expansion coefficient of water ($\sim 5 \times 10^{-5}$), g is the acceleration due to gravity on Callisto, T is the temperature, and C_p is the specific heat of water ($4200 \text{ J kg}^{-1} \text{ K}^{-1}$). The value of g at the base of the ice shell is calculated as 1.266 m s^{-2} . Assuming a temperature of 260 K (the temperature at the base of the ice I), the adiabatic temperature gradient in Callisto's water layer is 0.0039 K/km. For the 83.35 km thick water layer presented in this model, the temperature at the ocean floor should therefore be 0.33 K warmer than that at the top of the water layer.

This temperature gradient reveals a major flaw in the current SATMOD model - the water layer should be much thicker, and there should be ice V at its base, not ice III. Is it possible to produce a model with SATMOD that incorporates these extra constraints? This is explored in the next section.

7.3.3 The salt problem

It should be noted that equation (7.1) calculates the freezing curves for pure water - it does not account for the effects of salt contamination. The electrolytic salts are required to create an induced magnetic field in Callisto - Zimmer *et al.* (2000) suggest that the electrical conductivity of Callisto's ocean should exceed 0.02 S m^{-1} if it begins at a depth of 300 km below the surface. If the ocean is buried at a shallower depth, this minimum required conductivity should be smaller, and vice versa if the ocean is buried deeper. This conductivity corresponds to a salinity of less than 1 % by mass in the water - smaller than the 3.5% salinity of Earth's oceans - so Callisto's ocean is certainly conductive enough to generate the magnetic field if its salinity is > 10 % as has been discussed in the models presented in this chapter.

While it is well known that the presence of dissolved salts in water depresses its freezing point at low pressures, the effect of salts on the formation of the high pressure ice phases is not known at all. If the temperatures of all of the melting curves are lowered by the same amount, then the effect on the temperatures at the interfaces between the layers will be straightforward. However, the gradients of the various high-pressure ice melting curves in salty water are unknown, and it is possible that they would change by different amounts to that of ice I, resulting in unpredictable temperatures at the base of the layers. As a result, the applying the pure water melting curves to Callisto is somewhat flawed.

It should also be noted that the ice layers are assumed to be ‘pure’ due to fractional crystallisation. This is generally a valid assumption, since ice does not incorporate salts from its source water unless it is frozen very rapidly. If the freezing occurs slowly (as it probably would when an ice shell slowly freezes and thickens) then the salts will not be incorporated into the ice structure. Thus, we would expect that the saltwater ocean would be increasing in salinity with time, as the ice layers thickened above and below it. However, this does assume that no salt is precipitating from the water, and also that high pressure ices do not incorporate salt when they form.

However, it is still possible to speculate on some of the effects of salt contamination on Callisto’s ocean. The composition of Callisto’s ocean is likely to be dominated by magnesium sulphate salts, assuming that Callisto formed from similar material as Europa, where chemical modelling by Kargel *et al.* (2000) and surface measurements from the Galileo NIMS instrument (McCord *et al.*, 1998) indicate that MgSO_4 salts are a likely major contaminant of the water.

Figure 7.5 shows the phase diagram for the H_2O - MgSO_4 system at 0.1 MPa pressure.

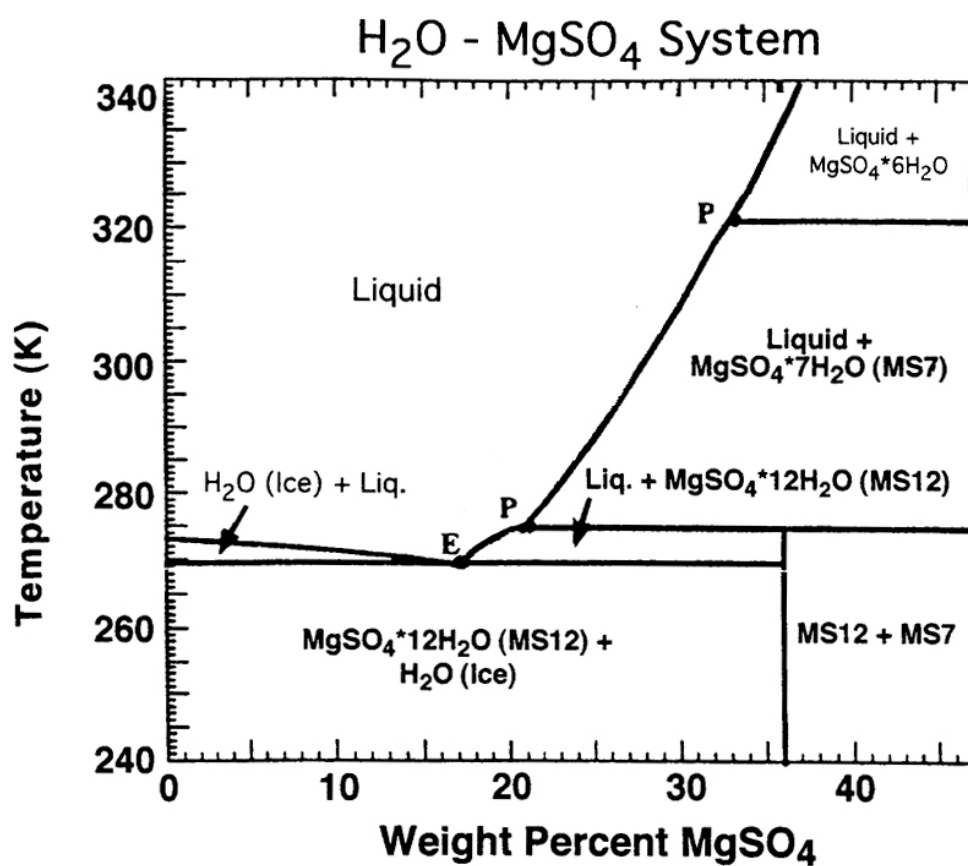


Figure 7.5: Temperature-composition diagram of the H_2O - MgSO_4 system at 0.1 MPa pressure (from Spaun and Head, 2001). E is the Eutectic Point, P are Peritectic Points.

Can the presence of salts in the ocean correct the inverse temperature gradient problem illustrated in Figure 7.4? Assuming a concentration of $\sim 5\%$ MgSO_4 (with an uncompressed density $\sim 1050 \text{ kg m}^{-3}$, as required in Table 7.1), the phase diagram Figure 7.5 indicates that the temperature at which the saltwater would start to freeze is only depressed by $\sim 1 \text{ K}$. The eutectic point is depressed by a few Kelvin at pressures of $\sim 200 \text{ MPa}$ and the sequence of crystallisation remains unchanged (Spaun and Head, 2001) so it is unlikely that the total decrease in the freezing point is greater by more than $\sim 5 \text{ K}$. This alone would not be sufficient to level the temperature profile through the water shown in Figure 7.4 - the temperature at the top of the water layer (262 K) would need to drop to or below the temperature indicated at the top of the ice III (253 K) to become realistic. On one hand, such a ‘flattening’ of the ice I melting curve, would force the thickness of the ice I shell to decrease slightly since the temperature profile would cross the new ice I melting curve at a different depth (which would contradict the physical model). On the other hand, the temperature at the base of the ice I shell would have to be very tightly constrained to between 251 and 253 K , which would be near the base of any modified or unmodified ice I melting curve. The resulting ocean in this case would be very thin, which would further contradict the physical model produced by SATMOD. Furthermore, the effect of the salts on the melting curves of the other ice phases is unknown, so it is unclear what (if any) effect this will have on the thermal modelling. It thus appears to be impossible given current knowledge to produce a realistic (increasing with depth) thermal gradient through the ice and water in this model, even when incorporating the effects of salts into the melting curve.

One other possibility is that the ocean contains more than just MgSO_4 salt - NaCl in particular can strongly depress the freezing point of water. However, the geochemical analyses of Zolotov and Scott (2001) and Kargel *et al.* (2000) indicate that NaCl cannot be present in sufficient concentrations to reduce the freezing point of the water significantly.

7.4 A thermally realistic Callisto model?

In order to create a thermally realistic Callisto model, I modified the SATMOD program so that it could (a) vary the mass % of the various layers by different amounts (including not varying them at all) and (b) vary the density of the saltwater layer to allow for different water salinities, which may produce working models where none were available using the default 1050 kg m^{-3} uncompressed density.

These modifications allowed me to incorporate the temperature constraints into the model by fixing the mass (and therefore the thickness and base pressure) of the ice I, water, and high pressure ice layers. This means that models can be produced where the temperature of the water has to be warmer at the bottom than at the top. The mass of each of these layers is determined by trial and error, while referencing the water phase diagram in order to produce a positive gradient in the water layer.

It rapidly became apparent that it was impossible to produce a model using the input parameters shown in Table 7.1 that could produce a positive thermal gradient in the water. This is obvious when one examines the phase diagram in Figure 7.4 - if the pressure at the base of the ice is less than $\sim 170 \text{ MPa}$, the temperature has to decrease through the water layer to reach the ice III melting curve.

It is worthwhile at this stage to list the Callisto model constraints:

- radius error bar (± 0.29 km)
- bulk density error bar (± 0.45 kg m⁻³)
- moment of inertia error bar (± 0.0042)
- mass error bar ($\pm 0.00014 \times 10^{23}$ kg)
- Ice I crust ~ 100 km thick (from Kivelson *et al.* papers and Schenk (2002))
- A saltwater layer must lie below ice I shell (Kivelson *et al.*)
- Temperature at base of saltwater layer must be greater than at the top of the water layer.

There are other constraints based on SATMOD:

- ice/rock layers must increase in density towards the centre of Callisto
- Pressure at base of ice I layer must be ≤ 207 MPa
- Pressure at base of water layer must be < 346 MPa for there to be ice III at its base, or < 625 MPa for there to be ice V below the water.
- Density of salt water layer must be $<$ density of high pressure ice layer below it.
- A uniform spread of ice/rock layer densities is preferred, but not required.

These constraints conspire to limit the possible parameter space of the models produced by SATMOD, and require some more direct user intervention in the program (e.g. the aforementioned fixing of upper ice layer thicknesses so that the temperature increases with depth through the water layer).

Despite the modifications and attempts to include the effects of salts on the melting curves, it appears to be impossible to generate even a single model that has an ice III layer that is also consistent with all the constraints listed above, despite my many attempts to do so. Given the very small temperature range covered by the positive gradient of the ice III melting curve, it is also very unlikely that there could actually be ice III at the bottom of the water layer.

The alternative is a model that contains an ice I shell with a base pressure of ~ 130 MPa, a thick water layer with a base pressure of ~ 430 MPa and an ice V layer at the base of the ocean. This would require a positive temperature gradient through the water, and thus at least be realistic in that sense.

However, after several attempts, it became apparent that it was also not possible to generate a model with an ice V layer that fit within the observed error bounds for radius, bulk density and moment of inertia. Having run out of alternative options, I therefore decided to expand the moment of inertia error bar in order to locate the closest possible model to these constraints. No working models were found within an error range of 2σ (± 0.0084) - however, some working models were located within an error range of 3σ (± 0.0126) - the model presented hereafter represents one such 'near miss' model.

7.4.2 A working model

The input parameters for the ice V model are shown in table 7.4:

Table 7.4: Ice V SATMOD parameters input

Mass: 1.07594×10^{23}			
Radius: 2409.3 km		Radius Error: ± 0.29 km	
Bulk Density: $1836.57 \text{ kg m}^{-3}$		Density Error: $\pm 0.45 \text{ kg m}^{-3}$	
C/MR^2 : 0.353676		C/MR^2 Error: $\pm 0.0126 (3\sigma)$	
Layer	Mass%	Density (kg m^{-3})	K (GPa)
Ice I	6.50	921	9.2
Water	14.0	1050 - 1150 (25)	3.0
Ice V	7.0	1235	13.2
Ice-Rock1	22.5	1400 - 2200 (25)	variable
Ice-Rock2	20.0	1600 - 2400 (25)	variable
Ice-Rock3	20.0	2000 - 2800 (25)	variable
Rock Core	10.0	3500	148

Ice-Rock layers mass% multiplication factor: 0.5 - 1.5 (0.25)
(mass% of top three layers are fixed)

These input parameters generated a total of two models when the uncompressed saltwater layer density was 1075 kg m^{-3} , eight models when the saltwater density was 1100 kg m^{-3} , and 30 models when the saltwater density was 1125 kg m^{-3} . One model was selected from the group of models with the 1125 kg m^{-3} water layer and is shown in Table 7.5:

Table 7.5: Ice V SATMOD Callisto output model

Layer	uncompressed density	Bulk Modulus	ice%
2	1125.00 kg m ⁻³	3.0 GPa	-
4	2050.00 kg m ⁻³	60.34 GPa	65.91
5	2275.00 kg m ⁻³	73.94 GPa	55.68
6	2800.00 kg m ⁻³	105.68 GPa	31.82

Layer	Mass %	Compressed Density (kg m ⁻³)	Layer Thickness (km)	Base Pressure (GPa)
Ice I	6.500	933.25	107.46	0.1240
Saltwater	14.00	1269.29	194.22	0.4362
Ice V	7.000	1290.39	110.24	0.6190
Ice-Rock1	33.75	2109.39	428.89	1.7992
Ice-Rock2	25.00	2369.35	521.30	3.1957
Ice-Rock3	10.00	2908.48	404.70	4.2551
Rock Core	3.750	3631.60	642.52	5.7766

	Target Values	1s error range	Model Results	Error
Radius	2409.33	± 0.29 km	2409.33	± 0.00 km
Mass	1.07594 x 10 ²³	± 0.00014 x 10 ²³ kg	1.07594 x 10 ²³	-
C/MR²	0.353676	± 0.0126	0.342168	- 0.011508
Density	1836.57	± 0.45 kg m ⁻³	1836.59	+ 0.02 kg m ⁻³

This results in a model of Callisto that is 33.15% rock and 66.85% ice. The ice I and V layers are assumed to be pure, and the saltwater layer is ~ 12.5% saline. Almost all the ice in the ice-rock1 layer and in the upper 30% or so of the ice-rock2 layer is ice VI, and the ice in the lower 70% of the ice-rock2 layer and the entire ice-rock3 layer is ice VII.

Figure 7.6: Temperature profile through ice V SATMOD Callisto model

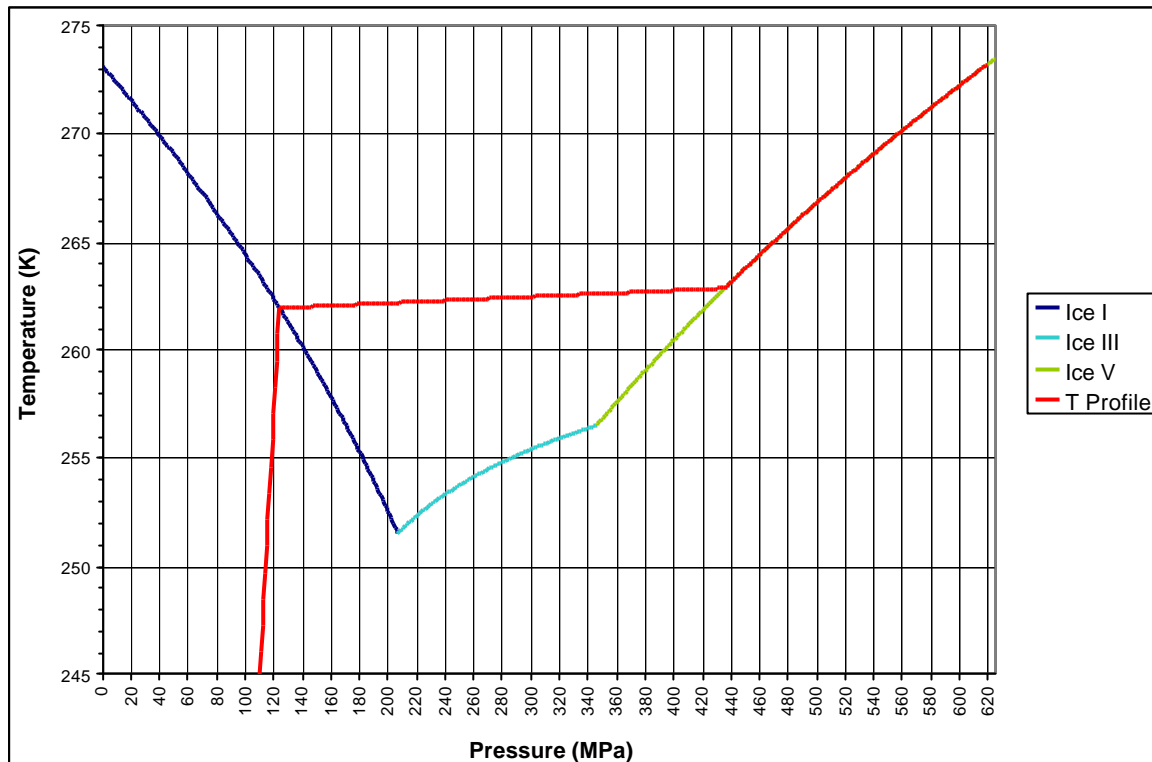


Figure 7.6 shows that the temperature profile through the water layer is positive with depth, which is physically realistic. The actual temperature difference is + 0.92 K, whereas the temperature difference calculated using equation (7.2) should be value of +0.42 K - this could be explained if the thermal gradient through the water is slightly superadiabatic.

A saltwater density of 1125 kg m^{-3} corresponds to an MgSO_4 concentration of approximately 10 %. Referring to the $\text{H}_2\text{O}-\text{MgSO}_4$ phase diagram (Figure 7.5), this concentration decreases the freezing point of the saltwater by $\sim 2 \text{ K}$, and further depression due to increased pressure would act to steepen the temperature gradient with depth through the water. The presence of salts would therefore make the thermal gradient slightly more superadiabatic.

What of Callisto's deeper interior? Table 7.6 shows the expected geothermal gradients in each of the layers, assuming that the heat is being transported through the planet by conduction, and the silicate heat density (see section 6.5.1) is such that the geothermal gradient through the ice I layer is 162 K. This is the difference in temperature between the surface at 110 K and the base of the ice I layer at 262 K - the required silicate heat density for this to be the case is $\sim 2.13 \times 10^{-8} \text{ W m}^{-3}$ - approximately half that of the Earth.

Table 7.6: Conductive geothermal gradients through Callisto

	Geotherm (K/km)	Average thermal conductivity of layer
Ice I	1.415	3.00
Saltwater	7.749	0.60
Ice V	4.583	1.21
Ice-Rock1	2.761	2.24
Ice-Rock2	2.192	2.72
Ice-Rock3	1.785	3.15
Rock Core	1.240	3.68

The average thermal conductivity of each layer is calculated from the percentages of rock and ice in the layer, and using ice thermal conductivity values from Fortes (1999).

However, whereas the ice I layer probably acts as a conductive “stagnant lid” (Ruiz, 2001), the conductive temperature gradients through the deeper layers are so high that the ice V would certainly be completely molten within a few kilometres of the top of the layer, causing the rock to sink through the molten ice and form a much larger solid core.

We have already seen that the temperature gradient through the saltwater must be much shallower (by a factor of $\sim 10^3$) than the conductive gradient because the heat would be transported through the water by *convection*, not conduction. Given the thicknesses of the layers, it is very likely that the other layers would also be convecting, which decreases the temperature gradients by a factor of 10^2 to 10^3 - even the thick ice-rock layer would only be ~ 2 or 3 K warmer at its base than at its top if this were the case. It also implies that the convection in these layers is vigorous enough to carry the rock along with the ice, which is possible if the rock units are small (if they were large and therefore massive they would be more likely to sink through the ice rather than convect with it).

Table 7.7: Convective (realistic) geothermal gradients through Callisto

	% Mass of layer	Mass of layer (kg)	Cumulative mass of layers (kg)	Gravity at top of layers (m s^{-2})	Convective Geotherms (K/km)
Ice I	6.50	6.99361×10^{21}	1.07594×10^{23}	1.237	1.4147*
Saltwater	14.00	1.50632×10^{22}	1.00600×10^{23}	1.267	0.0040
Ice V	7.00	7.53158×10^{21}	8.55372×10^{22}	1.285	0.0239
Ice-rock1	33.75	3.63130×10^{22}	7.80057×10^{22}	1.305	0.0239
Ice-rock2	25.00	2.68985×10^{22}	4.16927×10^{22}	1.131	0.0215
Ice-rock3	10.00	1.07594×10^{22}	1.47942×10^{22}	0.900	0.0177
Rock core	3.75	4.03478×10^{21}	4.03478×10^{21}	0.652	0.0098
TOTALS		1.07594×10^{23}	1.07594×10^{23}		

Table 7.7 shows the more realistic convective geothermal gradients through Callisto (as well as the conductive gradient through the outer ice I shell, marked by an asterisk). With these gradients, the temperatures throughout the ice V and ice-rock layers lie well below the melting curves of ice VI and VII, and the temperature at the centre of Callisto is $\sim 300\text{K}$. Although these values are probably not completely accurate, it is nevertheless likely that convective heat transport in Callisto's interior can produce a shallow temperature gradient that does not significantly raise the temperature of the interior and melt the ice deep within the satellite.

The temperatures within Callisto calculated using the values from Table 7.7 are shown in Figure 7.7, and the new ice V model of Callisto is illustrated in Figure 7.8.

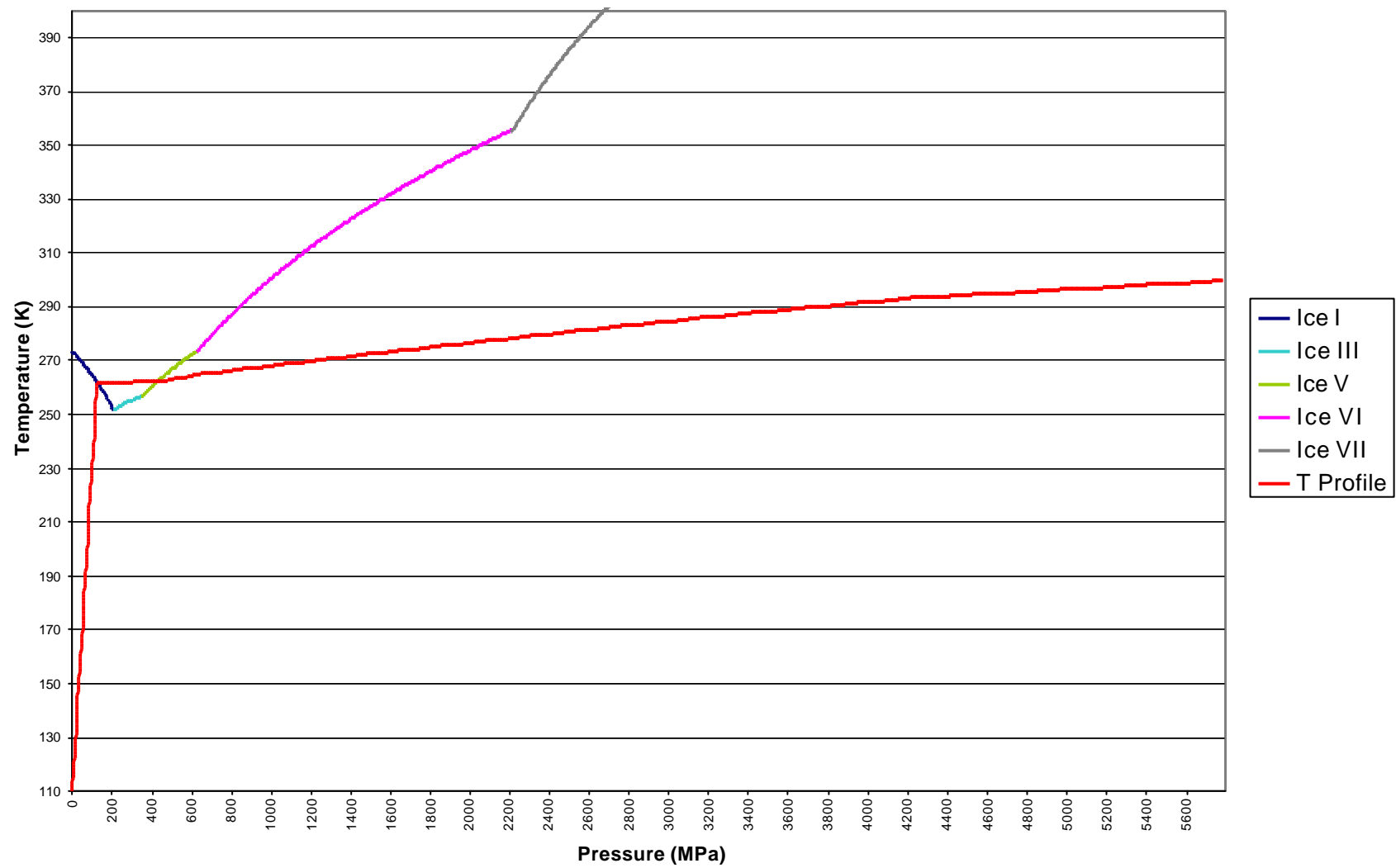


Figure 7.7: Convective temperature profile through Callisto.

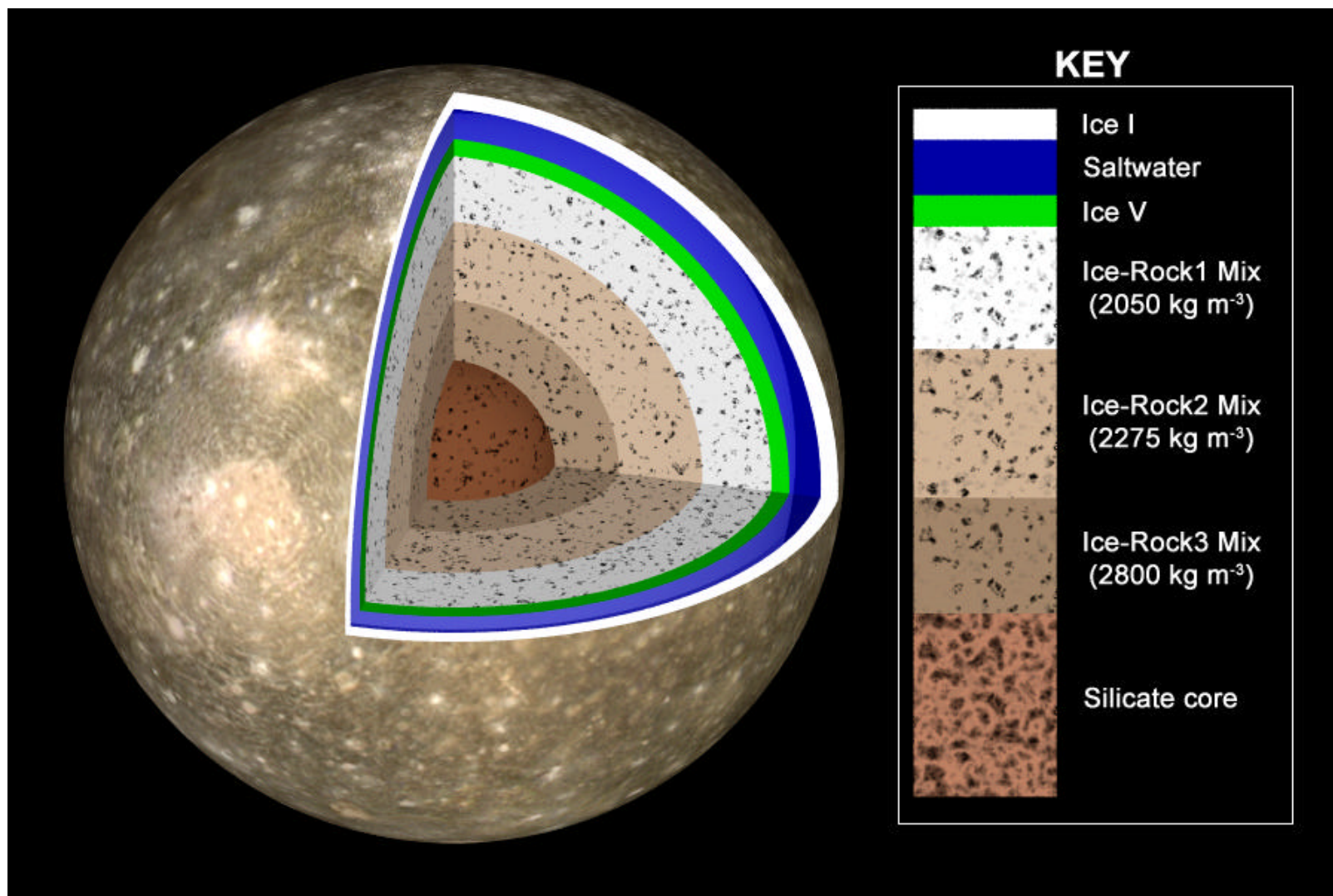


Figure 7.8: Cutaway through final Ice V SATMOD Callisto model

7.5 Conclusion

In this chapter I have presented my improved SATMOD program that produces more accurate models of the internal structure of satellites and planets than ONIONSKIN, and demonstrated its utility by determining more realistic models of Callisto's interior that agree with the observations of Anderson *et al.* (2001).

I have also attempted to account for temperature and geothermal gradients in the satellite interior in the new model, and demonstrated that it is very difficult to reconcile the temperatures with the physical constraints - indeed, the only working models appear to have moments of inertia that are between 2σ and 3σ lower than that indicated by the constraints of Anderson *et al.* (2001). There are two possible explanations for this: either the calculated moment-of-inertia values for Callisto or the observed parameters on which they are based - e.g. the gravitational parameter C_{22} - are inaccurate, or the input parameters for the SATMOD model are not sufficiently refined to locate models that lie within the 1σ error bar of the observed parameters. This latter option does highlight a practical flaw in SATMOD's operation - while it explores a greater parameter space than the ONIONSKIN model presented in Chapter 6, it is still dependant on input parameters that are essentially refined by trial and error. As with any model, it becomes harder to produce results that fit the required parameters as more constraints are added. It is possible that there are ice III or ice V models that do lie within the observed parameters, but if they do exist they require much more processing time and more refining of the model to arrive at.

Nevertheless, I suggest that the model I have proposed here is otherwise realistic enough to be a valid possibility for the internal structure of Callisto.

Chapter 8 Conclusion

In this thesis I have discussed the geology, magnetic fields, orbital evolution, and internal structures of the Galilean satellites. In this chapter I construct a coherent picture of each of the satellites that incorporates these data.

8.1 The structural and orbital evolution of Io

The surface of Io is volcanically active, and the global heat flow is too great to be explained by radiogenic heating alone. Some extra heat source must be driving this activity, and this source was identified by Peale *et al.* (1979) and Malhotra (1991) as the tidal dissipation caused by Io's orbital evolution into the Laplace resonance. The lack of magnetic field could also be explained by the high degree of heating - particularly if it is concentrated in the mantle - as this would inhibit magnetoconvection in the core and prevent a fixed dipole field from forming. Kivelson *et al.* (2001) have recently suggested that a weak induced field, no larger than the background Jovian field at Io, might explain the Galileo magnetometer data. However, the presence of a magnetic field at Io remains ambiguous.

Is it possible to elaborate more on the state of the Ionian interior? Peale *et al.* (1979) first proposed the idea that, although they are similar in size, the central region of Io has suffered much more total heating (mostly due to tidal dissipation) than the Moon, and suggested that Io may have suffered ten times as much heating. This would melt much of Io's interior into a magma ocean, and would drive the volcanism and resurfacing of the crust. Although this idea later fell out of favour because convection

would cool Io too rapidly to allow such a magma ocean to exist, (e.g. Nash *et al.* 1986), Keszthelyi *et al.* (1999) have resurrected this scenario to explain the high heat flow found by the Galileo orbiter (higher than previously estimated from Voyager), high temperature volcanism, and lack of a magnetic field at Io. Their model suggests that a thick ‘mushy’ mantle of convecting molten rock and suspended solid crystals lies between a solid silicate crust and a metallic core. The slurry would convect enough to thoroughly mix the interior but would not cool rapidly enough to solidify completely. This would explain the presence of high temperature lavas observed on the surface (McEwen *et al.*, 1998), since they could originate from such a high degree of partial melting.

In summary, Io probably formed as a largely rocky body in an orbit around Jupiter closer than the current one. Tidal forces then pushed the satellite away from Jupiter until it entered a Laplace-like resonance with Europa and Ganymede. The resulting tidal dissipation melted much of Io’s interior and initiated massive surface volcanism and degassing that continues to the present, even after the LLR is disrupted and the Laplace resonance is entered. Today, Io possesses a molten metallic core, overlaid by a partially molten silicate mantle and a thick crust/aesthenosphere.

8.2 The structural and orbital evolution of Europa

The surface geology of Europa - and that of the other icy Galilean satellites - is problematic because it does not necessarily provide clues as to the evolution of the interior of the satellite. The appearance of the European surface largely reflects processes that occur within the ice and water layers above the silicate surface, although it is possible that if any processes such as silicate volcanism are still occurring on the silicate surface then they could be indirectly responsible for some of the features visible on the ice surface.

Evidence for a global salt water layer beneath Europa's icy surface today rests largely on the presence of the induced magnetic field and is not in doubt. Evidence for non-synchronous rotation of the ice shell (e.g. Hoppa *et al.*, 1999; Hoppa *et al.*, 2001) due to decoupling of the ice crust from the silicate surface is further evidence for the continuing existence of a water layer. However, debate continues as to whether this water layer is close to the surface or under a great thickness of ice, and whether it can directly affect and create the features observed on the surface (Greenberg *et al.*, 1999; Thomson and Delaney 2001) or if the surface geology is the results of solid-state diapirism of warm ice (Pappalardo *et al.*, 1998). Much of this debate has been based on geophysical arguments, with little physical evidence to back up the arguments. Current interior structure models (including my ONIONSKIN model) cannot differentiate between the models and do not rule out either model, and thus cannot help to resolve the debate at present. However, Schenk (2002) presents a strong case that the European ice shell thickness is currently between 19 and 25 km, based on analysis of crater shapes - this provides a much more solid foundation from which to

work, though this result cannot be verified until more detailed seismic or radar surveys of Europa take place.

While the European surface is clearly very young because of the very small numbers of impact craters, the age of the water layer is by no means clear. It is possible that the water layer is similar in age to the surface, but it is also possible that it has existed for longer and that resurfacing has occurred to continuously alter the geology. Pappalardo *et al.* (1998) suggest that mottled terrain, which consists largely of Chaos, formed as a result of global compressional stresses which inhibited the formation of ridged plains units. However, they find that the longitudes in which these stresses should be concentrated are located 50° away from the current longitudes of the mottled terrain (which is concentrated in two large areas centred at longitudes 120°W and 300°W). The implication is that the mottled terrain forms at the compressive foci, and the ice shell as a whole rotates around the satellite. As the shell moves away from the compressional zones, plains units are allowed to form again and may overprint Chaos terrain. This would imply that some evolution of the surface has taken place while the water layer has been in existence (the past ten million years or so at the very minimum).

The origin of the water layer is probably tidal dissipation within Europa due to its orbital evolution. The tidal heating that would have occurred as a result of passage through Laplace-like resonances is insufficient to melt the interior of Europa, implying that the satellite must have differentiated fully soon after its formation, before entry into the LLR. This implies that the silicate body of Europa must contain sufficient radioisotopes for radiogenic (and possibly accretional) heating to

have differentiated the satellite before any tidal dissipation occurred. However, it is certainly possible for tidal heating to melt much of Europa's ice shell and maintain a water layer, particularly as the dissipation would be concentrated in the outer layers of the satellite.

As noted at the end of Chapter 5, melting a thin (relative to the rest of the body) solid ice shell above the silicate body of Europa is not likely to decrease Q^*_2/Q^*_J enough to disrupt a Laplace-like resonance. The required dramatic decrease in Q^*_2/Q^*_J could only be possible if a significant fraction of the silicate/metal portion of Europa melted at the end of the LLR. Interpretation of magnetometer data implies that the metallic core is not producing an intrinsic fixed dipole field today, and is therefore not convecting. If it were molten, it is likely that intrinsic dynamo action would be continuing and generating a dipole field today. Otherwise, such a scenario would be similar to that in Io and tidal heating is not sufficient to *melt* Europa's silicate mantle, although it may heat it to some extent. However, I also discussed more realistic possible mechanisms that would allow disruption of the LLR and entry into the Laplace resonance, so it appears that contriving a significant decrease in Q^*_2/Q^*_J is no longer required.

It is likely that Europa entered the Laplace resonance fully differentiated - perhaps even with a molten core and intrinsic magnetic field. Whether a water layer existed at the time is not clear; Showman *et al.* (1997b) suggest that if Ganymede entered the LLR with a water layer, its eccentricity would not be pumped to large values. Unfortunately this was not specifically modelled for Europa by Showman *et al.* (1997b) so this question remains unresolved.

If the situation is like the one at Ganymede, Europa may have entered the LLR with a warm ice shell, and a thermal runaway may have occurred to generate the water layer as a result of passage through the resonance. Present tidal heating may be sufficient to keep some of the water layer molten, but it is likely that the ice I shell is cooling and thickening with time and the water layer is therefore thinner than it was during the LLR. The water layer itself may therefore be much older than the features currently seen on the surface of Europa.

8.3 The structural and orbital evolution of Ganymede

The interior structure of Ganymede is perhaps the most interesting of the Galilean satellites. It is the most strongly differentiated terrestrial body in the Solar System, possibly comprised of a solid inner metallic core, a convecting, molten outer metallic core generating an magnetic (internal dipole) field, a silicate mantle, an ice VI shell, a deep water layer, and an ice I shell at the surface. The interior and surface of Ganymede are very different from those of its sister satellite Callisto, which is similar in size and bulk density - this dichotomy is one of the most enduring mysteries of the Galilean satellites.

Unlike Io and Europa, Ganymede has not been subjected to complete resurfacing - old cratered terrain still exists as polygonal blocks of 'Dark Terrain'. However, unlike Callisto, *some* tectonic activity and resurfacing has occurred, and this is concentrated in bands and belts of 'Bright Terrain' over the satellite. Since the one key difference between Ganymede and Callisto is the fact that the former has been involved in strong orbital resonances with the inner Galilean satellites and latter has not, it is reasonable to conclude that the Ganymede-Callisto dichotomy may be due to this different orbital evolution.

Was tidal dissipation during a Laplace-like resonance sufficient to *completely* differentiate Ganymede? No. Showman *et al.* (1997b) have shown that Ganymede must have been differentiated before it entered the LLRs. While tidal dissipation due to its increased eccentricity during the LLR would heat Ganymede, it is insufficient to cause further rock/metal differentiation. However, it would certainly be sufficient to at least affect the ice shell around the silicate body.

My ONIONSKIN model shows that it is possible that a very deep water layer - possibly hundreds of kilometres deep - may still exist under Ganymede's ice I surface today, which would explain the induced magnetic field also detected around the satellite. It is likely that Ganymede entered the LLR with a water layer since it would have had a molten core and higher global heat flow earlier in its evolution. According to the Showman *et al.* (1997b) model, this is a 'warm Ganymede' in which the water layer remains liquid until the present - this is anticipated by the authors if a more realistic scenario is considered where Ganymede contains (at least) chondritic levels of radioisotopes in the silicate body and core. This also means that significant global expansion would not have occurred as a result of entry into the LLR, since the water layer already existed - however, heating as a result of passage through the LLR may prolong the existence of the water layer. It is possible that a small amount ($< 1\%$) of global expansion could still result, and this may be sufficient to generate crustal stress fields along which 'Bright Terrain' could form. Thus, my ONIONSKIN model is consistent with the Showman *et al.* (1997b) 'warm Ganymede' model.

8.4 The structural and orbital evolution of Callisto

Even after the Voyager flybys in 1979, Callisto was usually considered the least interesting of the Galilean satellites - its heavily cratered appearance and lack of tectonic activity led many authors to focus their attention on more ‘interesting’ bodies. One author was even prompted to use “[t]he geology of Callisto is not boring” (Schenk, 1995) as the opening words to a scientific paper in an attempt to draw attention to the neglected satellite!

The Galileo orbiter has revealed that Callisto is indeed a very interesting body worthy of study. The existence of an induced magnetic field - and by implication a layer of liquid salty water near the surface (Kivelson *et al.*, 1999) - came as a complete surprise. Reconciling this water layer with new models of the internal structure (Anderson *et al.*, 2001) is a challenge I have taken up in this thesis.

My Callisto SATMOD model shows that it is physically possible for a thin water layer to be present in Callisto, sandwiched between a thick Ice I shell and a thin, clean Ice V shell below it, which becomes contaminated with rocky material as depth increases. This ice/rock mix spans over half of Callisto’s radius, and contains Ice V near the top, and Ice VI and VIII towards the middle and bottom. An undifferentiated rock/metal core occupying approximately one-quarter of Callisto’s radius lies at the centre of the satellite.

SATMOD is a purely physical model, so I also considered the heat flow and geotherm required to maintain the water layer. I concluded that the Ice V layer at the base of the ocean was the most realistic scenario, even though the physical model did not fully agree with the observed parameters (the moment of inertia is too low). It is possible that refinement of the model may yield a Callisto that does agree with the observed parameters, but this is left for future work.

Since Callisto has apparently not been involved in any significant orbital resonances of the kind that have shaped the other three Galilean satellites, the heat source maintaining this water layer must be radiogenic in origin. The implication is that either there are more radioisotopes generating heat within Callisto's interior than previously considered, or there is some mechanism preventing efficient heat loss and cooling from the satellite, so that the water layer can continue to exist.

Ruiz (2001) proposes that the reason for the water layer's continued existence is that it would be kept liquid by the rheological properties of the ice I above it: he suggests that the ice I crust would consist of large ice grains, so that dislocation creep becomes much more important than grain boundary sliding which is usually favoured at small near-surface stresses. Larger ice grains could form if the ice was warm (as it would have been in Callisto's past). This would inhibit convection and prevent heat from being efficiently carried out from Callisto's interior and thus keep the water layer molten, and also relieves the condition that an 'antifreeze' contaminant may be present or that some other special conditions are required.

Recent evidence suggests that the ocean may be very old - work by Williams *et al.* (2001) indicates that an ocean was present when the ancient Valhalla impact basin was formed, since no shocked and disrupted terrain is evident on the antipode of the impact - the shock waves would not have been able to propagate efficiently through an ocean if one existed at the time.

As discussed in previous sections, the other Galilean satellites differentiated early in their histories, probably not long after accretion. Since this process was unrelated to orbital evolution, an explanation is required for why Callisto has not fully differentiated. Stevenson (2001) proposes that Callisto may have formed very slowly - over perhaps a million years or more - near the end of the period of Jovian accretion. Accretion was slow because of the lack of available material at this late stage of formation, compounded by the location of proto-Callisto near the edge of the proto-jovian nebula. This means that accretional heating was insufficient at Callisto to separate the icy components from rocky components, whereas the accretion of the other Galilean satellites was more rapid and did allow differentiation to occur and run to completion. Thus, Callisto may still be in the process of differentiating today, as the rock component slowly separates out from the ice component and becomes more concentrated towards the centre of the satellite.

8.5 Future work

In this work I have presented a synthesis of the ‘post-Galileo’ data regarding the internal structure and orbital evolution of the Galilean satellites that is available at the time of submission (December 2001). However, the Galileo mission is still ongoing and is scheduled to end in 2003 when the orbiter plunges into the Jovian atmosphere and is destroyed. Eventually, therefore, the work contained herein will have to be refined to include the new data which should be collected.

There is clearly much work to be done in order to refine the general SATMOD internal structure model - not least by including thermal considerations. It should be possible to adapt the model to calculate the level of radiogenic heating at a given time in the satellite’s history, given the proportions of rocky material (assuming various chondritic compositions) and distribution of that material within the body. Global heat flow levels can then be calculated along with the geothermal gradient, which would help to further constrain the location of the water layers in the icy Galilean satellites and would also indicate how they may have evolved with time. For now though, these parameters must be examined ‘by hand’, as I have done in Chapter 7.

The coupled orbital and thermal evolution models of Showman *et al.* (1997) also require further expansion, to cover Io and Europa in similar depth. If this is done, we shall have a much more complete understanding of how orbital evolution and the tidal dissipation that results can affect the interiors of these bodies, and how that in turn affects the orbital and thermal evolution of the other satellites involved in the resonances.

‘Planetary Oceanography’ - the study of water layers on other worlds - is a very new field, and much remains to be done to build the foundations of this subject. In all cases, the ‘oceans’ of the Galilean satellites dwarf those of the Earth, and pressures at the ‘seafloors’ are at least an order of magnitude greater than under the deepest oceans of Earth. The Galilean oceans are not exposed to a free surface and are not affected by the wind as oceans are on Earth, so the processes that drive ocean circulation may be very different there. We still have little understanding of the subtleties of the circulation and chemical composition of these water layers, and how they evolve with time. For example, is there a salt cycle within the Galilean ‘oceans’ that continuously recycles the salt and keeps the salinity constant, or is salinity building up with time? Is material still being introduced to the oceans? Is there activity at the ‘seafloor’ - on the silicate - or high pressure ice - surface that affects the water layer? What effect does the higher pressure at the silicate surface have on any volcanic or tectonic activity there? Most controversially, is there a possibility that life of some form may exist in the water? There is much potential for interdisciplinary crossover between terrestrial oceanography, volcanology, and planetary science here.

The discoveries that have been made based on the data returned by the Galileo orbiter, coupled with the older Voyager data, have revolutionised our view of the evolution of the Galilean satellites and turned them into fully-fledged worlds with their own distinctive 'character'. They still hold many mysteries, and much work remains to be done to resolve them, and future missions and dedicated orbiters will undoubtedly provide the answers while revealing more questions for us to ask.

References

- Anderson J. D., Sjogren W. L., and G. Schubert 1996a. Galileo Gravity Results and the Internal Structure of Io. *Science*, **272**, 709-712.
- Anderson J. D., Lau E. L., Sjogren W. L., Schubert G., and W. B. Moore 1996b. Gravitational constraints on the internal structure of Ganymede. *Nature*, **384**, 541-543.
- Anderson J. D., Schubert G., Jacobson R. A., Lau E. L., Moore W. B., and W. L. Sjogren 1998a. Distribution of Rock, Metals and Ices in Callisto. *Science*, **280**, 1573-1576.
- Anderson J. D., Schubert G., Jacobson R. A., Lau E. L., Moore W. B., and W. L. Sjogren 1998b. Europa's Differentiated Internal Structure: Inferences from Four Galileo Encounters. *Science*, **281**, 2019-2022.
- Anderson J. D., Jacobson R. A., McElrath T. P., Moore W. B., Schubert G., and P. C. Thomas 2001. Shape, Mean Radius, Gravity Field, and Interior Structure of Callisto. *Icarus*, **153**, 157-161.
- Burns J. A. 1977. Orbital Evolution. In *Planetary Satellites*, Univ. Arizona Press, Tuscon, 113-155.
- Burns J. A. 1986. The Evolution of Satellite Orbits. In *Satellites*, Univ. Arizona Press, Tuscon, 117-158.
- Carlson P. M., Johnson R. E., and M. S. Anderson 1999. Sulfuric acid on Europa and the radiolytic sulphur cycle. *Science*, **286**, 97-99.
- Carlson R., Smythe W., Baines K., Barbinis E., Becker K., Burns R., Calcutt S., Calvin W., Clark R., Danielson G., Davies A., Drossart P., Encrenaz T., Fanale F., Granahan J., Hansen G., Herrera P., Hibbits C., Hui J., Irwin P., Johnson T., Kamp

- L., Kieffer H., Leader F., Lellouch E., Lopes-Gautier R., Matson D., McCord T., Melhlam R., Ocampo A., Orton G., Roos-Serote M., Segura M., Shirley J., Soderblom L., Stevenson A., Taylor F., Torson J., Weir A., and P. Weissman 1996. Near-Infrared Spectroscopy and Spectral Mapping of Jupiter and the Galilean Satellites: Results from Galileo's Initial Orbit. *Science*, **274**, 385-388.
- Carlson R. W., Weissman P. R., Smythe W. D., Mahoney J. C., and the NIMS Science and Engineering Teams 1992. Near-Infrared Mapping Spectrometer Experiment on Galileo, *Space Science Reviews*, **60**, 457-502.
 - Carr M. H., Belton J. S., Chapman C. R., Davies M. E., Geissler P., Greenberg R., McEwen A. S., Tufts B. R., Greeley R., Sullivan R., Head J. W., Pappalardo R. T., Klaasen K. P., Johnson T. V., Kaufman J., Senske D., Moore J., Neukum G., Schubert G., Burns J. A., Thomas P., and J. Veverka 1998. Evidence for a subsurface ocean on Europa, *Nature*, **391**, 363-365.
 - Cassen P. M., Peale S., and Reynolds R. T. 1982. Structure and Thermal Evolution of the Galilean Satellites. In *The Satellites of Jupiter*, Univ. Arizona Press, Tuscon, 93-128.
 - Chapman C. R., Merline W. J., Bierhaus B., Keller J., Brooks S., McEwen A., Tufts B. R., Moore J., Carr M., Greeley R., Bender K. C., Sullivan R., Head J., Pappalardo R., Belton M. J. S., Neukum G., Wagner R., Pilcher C., and the Galileo SSI Team 1997. Populations Of Small Craters On Europa, Ganymede, And Callisto: Initial Galileo Imaging Results. *LPSC XXVII*, #1221.
 - Connerney J. E. P. 1993. Magnetic Fields of the Outer Planets. *Journal of Geophysical Research - Planets*, **98**, E10, 18659-18679.
 - Crary F. J. and F. Bagenal 1998. Remanent magnetism and the interior structure of Ganymede. *Journal of Geophysical Research - Planets*, **103**, E11, 25757-25773.

- Davies G. F. 1980. Review of Oceanic and Global Heat Flow Estimates. *Reviews of Geophysics and Space Physics*, **18**, 718-722.
- Davies M. E., Colvin T. R., Oberst J., Zeitler W., Schuster P., Neukum G., McEwen A. S., Phillips C. B., Thomas P. C., Veverka J., Belton M. J. S., and G. Schubert 1998. The Control Networks of the Galilean Satellites and Implications for Global Shape. *Icarus*, **135**, 372-376.
- Dermott S. F. 1979. Tidal Dissipation in the Solid Cores of the Major Planets. *Icarus*, **37**, 310-321.
- Fortes A. D. 1999. The Glacial Mantles of the Icy Planets, at:
<http://www.es.ucl.ac.uk/edu/students/planet/student/work/ices.htm>
- P. Goldreich 1965. An Explanation of the Frequent Occurrence of Commensurable Mean Motions in the Solar System. *Monthly Notices Roy. Astron. Soc.*, **130**, 159 - 181.
- Goldreich P. 1963. On the Eccentricity of Satellite Orbits in the Solar System. *Monthly Notices Roy. Astron. Soc.*, **126**, 258-268.
- Goldreich P. 1966. Final Spin States of Planets and Satellites. *The Astronomical Journal*, **71**, 1-7.
- Goldreich P., and S. Soter 1966. Q in the Solar System. *Icarus*, **5**, 375-389.
- Goldreich P. and S. Peale 1966. Spin-Orbit Coupling in the Solar System. *The Astronomical Journal*, **71**, 1-7. 425-438.
- Gomes R. S. 1998. Orbital Evolution in Resonance Lock. II. Two Mutually Perturbing Bodies. *Astron. Journal*, **116**, 997-1005.
- R. Greenberg 1977. Orbit-orbit Resonances among Natural Satellites. In *Satellites*, in *Planetary Satellites*, Univ. Arizona Press, Tuscon, 157-168.

- R. Greenberg 1987. Galilean Satellites: Evolutionary Paths In Deep Resonance. *Icarus*, **70**, 334-347.
- Greenberg R., Hoppa G. V., Tufts B. R., Geissler P., Riley J., and S. Kadel 1999. Chaos on Europa. *Icarus*, **141**, 263-286.
- W. K. Hartmann 1993. Moons and Planets (3rd Ed.). Wadsworth Publishing, pp 472.
- Head J. W., Pappalardo R. T., Collins G. C., Greeley R., and the Galileo SSI Team 1997. Tectonic resurfacing on Ganymede and its role in the formation of Grooved Terrain. *LPSC XXVIII*, #1110.
- Hoppa G. V., Tufts B. R., Greenberg R., Hurford T. A., O'Brien D. P., and P. E. Geissler 2001. Europa's rate of rotation derived from the tectonic sequence in the Astypalaea region. *Icarus*, **153** (1), 208-213.
- Hoppa G. V., Greenberg R., Geissler P., Tufts B. R., Plassmann J., and D. D. Durda 1999. Rotation of Europa: Constraints from terminator and limb positions. *Icarus*, **137**, 341-347.
- Hurford T. A. and R. Greenberg 2001. Tidal Amplitude for a self-gravitating, compressible sphere. *LPSC XXXII*, #1741.
- Kaula W. M. 1964. Tidal Dissipation by solid Friction and the Resulting Orbital Evolution. *Reviews of Geophysics*, **2**, 661-685.
- Kargel J. S., Kaye J. Z., Head J. W., Marion G. M., Sassen R., Crowley J. K., Ballesteros O. P., Grant S. A., and D. L. Hogenboom 2000. Europa's Crust and Ocean: Origin, Composition, and the Prospects for Life. *Icarus*, **148**, 226-265.
- Khurana K. K., Kivelson M. G., Stevenson D. J., Schubert G., Russell C. T., Walker R. J., and C. Polanskey 1998. Induced magnetic fields as evidence for subsurface oceans in Europa and Callisto. *Nature*, **395**, 777-780.

- Kirk R. L. and Stevenson D. J. 1987. Thermal evolution of a differentiated Ganymede and implications for surface features. *Icarus*, **69**, 91-134.
- Kivelson M. G., Khurana K. K., Walker R. J., Russell C. T., Linker J. A., Southwood D. J., and C. Polanskey 1996a. A Magnetic Signature at Io: Initial Report from the Galileo Magnetometer. *Science*, **273**, 337-340.
- Kivelson M. G., Khurana K. K., Russell C. T., Walker R. J., Warnecke J., Coroniti F. V., Polanskey C., Southwood D. J., and G. Schubert 1996b. Discovery of Ganymede's magnetic field by the Galileo spacecraft. *Nature*, **384**, 537-541.
- Kivelson M. G., Khurana K. K., Stevenson D. J., Bennett L., Joy S., Russell C. T., Walker R. J., Zimmer C., and C. Polanskey 1999. Europa and Callisto: Induced or intrinsic fields in a periodically varying plasma environment. *Journal of Geophysical Research - Space Science*, **104**, A3, 4609-4625.
- Kivelson M. G., Schubert G., Khurana K. K., Volwerk M. Magnetic Evidence for the Internal Structure and Thermal Evolution of Ganymede. Submitted to *Science*, March 2001(b).
- Kivelson M. G., Khurana K. K., Russell C. T., Joy S. P., Volwerk M., Walker R. J., Zimmer C., and J. A. Linker 2001a. Magnetized or unmagnetized: Ambiguity persists following Galileo's encounters with Io in 1999 and 2000. *Journal Of Geophysical Research - Space Physics*, **106**, A11, 26121-26135.
- Kivelson M. G., Khurana K. K., Russell C. T., and R. J. Walker 2001b. Magnetic Signature of a Polar Pass over Io, *Eos Trans. AGU*, 82(47), Fall Meeting Supplement, Abstract P11A-01, F684. (see also: <http://www.jpl.nasa.gov/galileo/news/release/press011210.html>)
- Kivelson M. G., Khurana K. K., and M. Volwerk. The Permanent and Inductive Magnetic Moments of Ganymede 2002. *Icarus*, **157**, 507-522.

- Kuskov O. L., and V. A. Kronrod. 2001. Core Sizes and Internal Structure of Earth's and Jupiter's Satellites. *Icarus*, **151**, 204-227.
- Malhotra R. 1991. Tidal Origin of the Laplace Resonance and the Resurfacing of Ganymede. *Icarus*, **94**, 399-412.
- McCord T. B., Hansen G. B., Fanale F. P., Carlson R. W., Matson D. L., Johnson T. V., Smythe W. D., Crowley J. K., Martin P. D., Ocampo A., Hibbitts C. A., Granahan J. C. and the Galileo NIMS Team 1998. Salts on Europa's Surface Detected by Galileo's Near Infrared Mapping Spectrometer. *Science*, **280**, 1242-1245.
- McEwen A. S., Keszthelyi L., Spencer J. R., Schubert G., Matson D. L., Lopes-Gautier R., Klaasen K. P., Johnson T. V., Head J. W., Geissler P., Fagents S., Davies A. G., Carr M. H., Breneman H. H., and M. J. S. Belton 1998. High-Temperature Silicate Volcanism on Jupiter's Moon Io. *Science*, **281**, 87-90.
- McKinnon W. B. 1981. Tectonic deformation of Galileo Regio and limits to the planetary expansion of Ganymede. *Proc. Lunar Planet. Sci.*, **12B**, 1585-1597.
- McKinnon W. B. and E. M. Parmentier 1986. Ganymede and Callisto. In *Satellites*, Univ. Arizona Press, Tuscon, 718-763.
- McKinnon W. B. and P. M. Schenk 1995. Estimates of comet fragment masses from impact crater chains on Callisto and Ganymede. *Geophysical Research Letters*, **22**, 1829-1832.
- McKinnon W. B. 1999. Convective instability in Europa's floating ice shell. *Geophysical Research Letters*, **26**, 951-954.
- Melosh H. J. 1982. A Simple Mechanical Model of Valhalla Basin, Callisto. *Journal of Geophysical Research*, **87**, 1180-1890.

- Melosh H. J., Ekholm A. G., Showman A. P., and R. D. Lorenz 2002. Is Europa's subsurface water ocean warm? *LPSC XXXIII*, #1824.
- Moore J. M., Asphaug E., Morrison D., Bender K. C., Sullivan R. J., Greeley R., Geissler P. E., Chapman C. R., Pilcher C. B., and the Galileo SSI Team 1997. Landform degradation and mass wasting on the icy Galilean satellites. *LPSC XXVIII*, #1407.
- Morabito L. A., Synott S. P., Kupferman P. N., and S. A. Collins 1979. Discovery of Currently Active Extraterrestrial Volcanism. *Science*, **204**, 972.
- Mueller S. and W. B. McKinnon 1988. Three-layered models of Ganymede and Callisto: Compositions, structures, and aspects of evolution. *Icarus*, **76**, 437-464.
- Murray C. D. and S. F. Dermott 1999. *Solar System Dynamics*. Cambridge University Press.
- Nash D. B., Carr M. H., Gradie J., Hunten D. M., C. F. Yoder 1986. Io. In *Satellites*, Univ. Arizona Press, Tuscon, pp 629-688.
- Ojakangas G. W., and D. J. Stevenson 1987. Episodic Volcanism of Tidally Heated Satellites with Application to Io. *Icarus*, **66**, 341-358.
- Pappalardo R. T., Head J. W., Greeley R., Sullivan R. J., Pilcher C., Schubert G., Moore W. B., Carr M. H., Moore J. M., Belton M. J. S., and D. L. Goldsby 1998a. Geological evidence for solid-state convection in Europa's ice shell. *Nature*, **391**, 365-367.
- Pappalardo R. T., Sherman N. D., Head J. W., Collins G. C., Greeley R., Klemaszewski J., Sullivan R., Phillips C., and the Galileo SSI Team 1998b. Distribution of Mottled Terrain on Europa: A Possible Link to Nonsynchronous Rotation Stresses. *LPSC XXIX*, #1923.

- Parmentier E. M. and J. W. Head 1979. Internal processes affecting surfaces of low-density satellites: Ganymede and Callisto. *Journal of Geophysical Research*, **84**, 6263-6276.
- Parmentier E. M., Squyres S. W., Head J. W., and M. L. Allison 1982. The tectonics of Ganymede. *Nature*, **295**, 290-293.
- Peale S. J., Cassen P., and R. T. Reynolds 1979. Melting of Io by Tidal Dissipation. *Science*, **203**, 892-894.
- Pollack J. B. and R. T. Reynolds 1974. Implications of Jupiter's Early Contractional History for the Composition of the Galilean Satellites. *Icarus*, **21**, 248-253.
- Reynolds R. T. and P. M. Cassen 1979. On the Internal Structure of the Major Satellites of the Outer Planets. *Geophysical Research Letters*, **6**, 121-124
- Ruiz J. 2001. The stability against freezing of an internal liquid-water ocean in Callisto. *Nature*, **412**, 409-411.
- Sarson G. R., Jones C. A., Zhang K., and G. Schubert 1997. Magnetoconvection dynamos and the Magnetic Fields of Io and Ganymede. *Science*, **276**, 1106-1108.
- Sarson G. R., Jones C. A., and K. Zhang 1999. Dynamo action in a uniform ambient field. *Physics of the Earth and Planetary Interiors*, **111**, 47-68.
- Schenk P. M. 1995. The geology of Callisto. *Journal of Geophysical Research*, **100**, 19023-19040.
- Schenk P. M., McKinnon W. B., Gwynn D., and J. M. Moore 2001. Flooding of Ganymede's bright terrains by low-viscosity water-ice lavas. *Nature*, **410**, 57-60.
- Schenk P. M. 2002. Thickness constraints on the icy shells of the galilean satellites from a comparison of crater shapes. *Nature*, **417**, 419-421.

- Schubert G., Stevenson D. J., and K. Ellsworth 1981. Internal structures of the Galilean satellites. *Icarus*, **47**, 46-59.
- Schubert G., Zhang K., Kivelson M. G., and J. D. Anderson 1996. The magnetic field and internal structure of Ganymede. *Nature*, **384**, 544-545.
- Shoemaker E. M., Lucchitta B. K., Wilhelms D. E., Plescia J. B., and S. W. Squyres 1982. The Geology of Ganymede. In *Satellites of Jupiter*, Univ. Arizona Press, Tuscon, 435-520.
- Showman A. P. and R. Malhotra 1997a. Tidal Evolution into the Laplace Resonance and the Resurfacing of Ganymede. *Icarus*, **127**, 93-111.
- Showman A. P., Stevenson D. J., and R. Malhotra 1997b. Coupled Orbital and Thermal Evolution of Ganymede. *Icarus*, **129**, 367-383.
- Smith B. A., Soderblom L. A., Johnson T. V., Ingersoll A. P., Collins S. A., Shoemaker E. M., Hunt G. E., Masursky H., Carr M. H., Davies M. E., Cook II A. F., Boyce J., Danielson G. E., Owen T., Sagan C., Beebe R. F., Veverka J., Strom R. G., McCauley J. F., Morrison D., Briggs G. A., and V. E. Suomi 1979. The Jupiter System Through the Eyes of Voyager 1. *Science*, **204**, 951-972.
- Spaun N. A., Head J. W., Collins G. C., Prockter L. M., and R. T. Pappalardo 1998. Conamara Chaos Region, Europa: Reconstruction of mobile polygonal ice blocks. *Geophysical Research Letters*, **25**, 4277-4280.
- Spaun N. A., Head J. W., R. T. Pappalardo and the Galileo SSI Team 1999a. Chaos and Lenticulae on Europa: Structure, Morphology and Comparative Analysis. *LPSC XXX*, #1276.
- Spaun, N. A., L. M. Prockter, R. T. Pappalardo, J. W. Head, G. C. Collins, A. Antman, R. Greeley, and the Galileo SSI Team 1999b. Spatial distribution of lenticulae and chaos on Europa, *LPSC XXX*, #1847.

- Spencer J. R. 1987. Thermal Segregation of Water Ice on the Galilean Satellites. *Icarus*, **69**, 297-313.
- Spencer J. R., Prockter L., Pappalardo R. T., Head J. W., and the Galileo SSI Team 1998, Local Volatile Migration on Ganymede: Galileo SSI Images, PPR Radiometry, and Theoretical Considerations. *LPSC XXIX*, #1149.
- Squyres S. W. 1980. Volume changes in Ganymede and Callisto and the origin of Grooved Terrain. *Geophysical Research Letters*, **7**, 593-596.
- Stevenson D. J. 1983. Planetary Magnetic Fields. *Rep. Prog. Phys.*, **46**, 555-620.
- Stevenson D. J. 2001. Jupiter and its moons. *Science*, **294**, 71-72.
- Strom R. G., Woronow A., and M. Gurnis 1981. Crater Populations on Ganymede and Callisto. *Journal of Geophysical Research*, **86**, 8659-8647.
- Thomas C. and Wilson L. 2000. Photoclinometric Analysis of Resurfaced Regions on Europa. *LPSC XXXI*, #1328.
- Thomson R. E., and J. R. Delaney 2001. Evidence for a weakly stratified European ocean sustained by seafloor heat flux. *Journal of Geophysical Research - Planets*, **106**, E6, 12355-12365.
- Tufts B. R., Greenberg R., Hoppa G., and P. Geissler 2000. Lithospheric dilation on Europa. *Icarus*, **146**, 75-97.
- Williams D. A., Klemaszewski J. E., Chuang F. C., and R. Greeley 2001. Galileo Imaging Observations of the Valhalla Antipode: Support for a Subsurface Ocean on Callisto? *DPS 2001*, #35.06
- Wilson L. 1998. Io writes its history in hot metal. *Nature*, **394**, 520-521.
- Yoder C. F. 1979. How tidal heating in Io drives the Galilean orbital resonance locks. *Nature*, **279**, 767-770.
- Yoder C. F. and S. J. Peale 1981. The Tides of Io. *Icarus*, **47**, 1-35.

- Zahnle K., Dones L, and H. F. Levison 1998. Cratering Rates on the Galilean Satellites. *Icarus*, **136**, 202-222.
- Zimmer C., Khurana K. K., and M. G. Kivelson 2000. Subsurface Oceans on Europa and Callisto: Constraints from Galileo Magnetometer Observations. *Icarus*, **147**, 329-347.
- Zolotov M. Y. and E. L. Shock 2001. Composition and stability of salts on the surface of Europa and their oceanic origin. *Journal of Geophysical Research - Planets*, **106**, E12, 32815-32827.

Appendix 1 Bulk and Orbital Properties of the Galilean Satellites

Tables A.1, A.2, and A.3 summarise the bulk properties of the Galilean satellites as calculated from Galileo data:

Table A.1: Galilean satellite triaxial ellipsoid radii

	mean R (m)	A axis (m)	B axis (m)	C axis (m)
Io	1818133	1826500	1815700	1812200
Europa	1560667	1562400	1560200	1559400
Ganymede	2632890	2633845	2632589	2632136
Callisto	2409338	2409559	2409275	2409180

Table A.2: Bulk properties of the Galilean satellites and Jupiter

	mean R (m)	Volume (10^{19} m^3)	Mass (10^{23} kg)	Bulk density (kg m^{-3})	<i>b</i> (m)	bulk q_r
Io	1818133	2.51744	0.893199	3548.05	1821092	1.7121×10^{-3}
Europa	1560667	1.59228	0.479984	3014.45	1561300	4.9833×10^{-4}
Ganymede	2632890	7.64516	1.48186	1938.30	2633267	1.9079×10^{-4}
Callisto	2409338	5.85844	1.07594	1836.57	2409417	3.6991×10^{-5}
JUPITER	71398000		18986.1			

mean R and ABC axes: Io, Europa from Davies *et al.* (1998); Jupiter from Anderson *et al.* (1996a); Ganymede, Callisto from Colvin (pers.comm., 1999).

Volume is calculated using $V = (4/3) \pi A B C$ where **A**, **B**, **C** are the length of the ellipsoid axes (Davies *et al.* (1998)).

Mass is from Anderson *et al.* (1996a - Io, Jupiter; 1998b - Europa; 1996a - Ganymede; 2001 - Callisto).

Bulk density is calculated using M/V .

b is the **Mean Equatorial Radius** $= \sqrt{AB}$.

Bulk q_r is the ratio of the centrifugal to gravitational acceleration at the satellite's equator, calculated using:

$$q_r = \left(\frac{b}{a} \right)^3 \left(\frac{M_J}{M_s} \right) \quad (\text{Davies } et al., 1998)$$

where a is the semimajor axis of the satellite orbit, M_J is the mass of Jupiter, and M_s is the mass of the satellite.

Table A.3: Tidal and gravitational parameters of the Galilean satellites.

	C_{22}	a	C/MR^2	g
Io	553.7×10^{-6}	0.43120	0.376995	1.80297
Europa	131.5×10^{-6}	0.35184	0.347504	1.31492
Ganymede	38.18×10^{-6}	0.26683	0.311185	1.42638
Callisto	10.2×10^{-6}	0.36765	0.353676	1.23676

C_{22} is the C_{22} gravitational coefficient, calculated in the various papers by Anderson *et al.* using observations by the Galileo spacecraft.

a is the (dimensionless) response coefficient (depends on density distribution with depth ($\alpha = 0.5$ for uniform density)):

$$a = \frac{4C_{22}}{3q_r} \quad (\text{Anderson } et al., 1996a)$$

C/MR^2 is the moment of inertia factor, calculated using:

$$\frac{C}{MR^2} = \frac{2}{3} \left[1 - \frac{2}{5} \sqrt{\left(\frac{4-3\mathbf{a}}{1+3\mathbf{a}} \right)} \right] \quad (\text{Anderson } et al., 1996a)$$

\mathbf{g} is the surface gravity in m s^{-2} , calculated using:

$$g = \frac{GM}{R^2}$$

k_2 Love number is calculated using:

$$k_2 = 3\mathbf{a} = \frac{4C_{22}}{q_r} = \frac{(3/2)}{1 + \tilde{\mathbf{m}}} \quad \text{where} \quad \tilde{\mathbf{m}} = \frac{19\mathbf{m}}{2\mathbf{r}gR}$$

In **Table A.4**: \mathbf{a} , \mathbf{m} , \mathbf{r} , $\mathbf{q_r}$, \mathbf{g} and \mathbf{a} calculated previously in this appendix; \mathbf{m} is bulk rigidity of satellite (Murray and Dermott, 1999); \mathbf{C}_{22} from Anderson *et al.*; \mathbf{r} = semimajor axis (m) (Davies *et al.*, 1998); \mathbf{e} = free (forced in **bold**) eccentricity (Malhotra, 1991); \mathbf{I} = orbital inclination w.r.t. Jupiter equator (Hartmann, 1993); \mathbf{P} = satellite orbital period, \mathbf{n} = orbital mean motion ($^\circ \text{ d}^{-1}$) (Murray & Dermott, 1999);

Table A.5 shows the errors in the key values shown in **Table A.4**.

Table A.4: Some useful orbital and physical parameters of Jupiter and the Galilean satellites

Quantity	Jupiter	Io	Europa	Ganymede	Callisto
mean radius (r)	7.1398×10^7 m	1.8181×10^6 m	1.5607×10^6 m	2.6329×10^6 m	2.4093×10^6 m
bulk rigidity (μ)	N/A	5×10^{10} N m ⁻²	5×10^{10} N m ⁻²	1×10^{10} N m ⁻²	1×10^{10} N m ⁻²
mass (m)	1.89861×10^{27} kg	8.93199×10^{22} kg	4.79984×10^{22} kg	1.48186×10^{23} kg	1.07594×10^{23} kg
bulk density (ρ)	1326 kg m ⁻³	3548.05 kg m ⁻³	3014.45 kg m ⁻³	1938.30 kg m ⁻³	1836.57 kg m ⁻³
surface gravity (g)	24.866 m s ⁻²	1.8030 m s ⁻²	1.3149 m s ⁻²	1.4264 m s ⁻²	1.2368 m s ⁻²
C ₂₂ gravitational coefficient	-	553.7×10^{-6}	131.5×10^{-6}	38.18×10^{-6}	10.2×10^{-6}
bulk q_r	-	1.7121×10^{-3}	4.9833×10^{-4}	1.9079×10^{-4}	3.6991×10^{-5}
moment of inertia factor	0.254	0.376995	0.347504	0.311185	0.353676
rotational period	9.92425 hrs	42.456 hrs	85.224 hrs	171.72 hrs	400.536 hrs
semi-major axis (a) in m	N/A	4.21680×10^8	6.70990×10^8	1.07034×10^9	1.88261×10^9
orbital eccentricity (e)*	-	0.0041 (0.00001)	0.0101 (0.0001)	0.0006 (0.0015)	0.007
orbital inclination (I)	-	0.03	0.46	0.18	0.25
orbital period (P in days)	-	1.769	3.551	7.155	16.689
mean motion (n in ° d ⁻¹)	-	203.49	101.37	50.32	21.57

*: **bold** values are forced eccentricities, values in parentheses (or not bold) are free eccentricities.

Table A.5: Known errors in the important physical parameters of the Galilean satellites

Quantity	Jupiter	Io	Europa	Ganymede	Callisto
mean radius (r)		± 120 m	± 650 m	± 270 m	± 290 m
mass (m)	0.00024×10^{27} kg	$\pm 0.00114 \times 10^{22}$ kg	$\pm 0.00062 \times 10^{22}$ kg	$\pm 0.00189 \times 10^{22}$ kg	$\pm 0.00137 \times 10^{22}$ kg
bulk density (ρ)	-	± 0.61 kg m ⁻³	± 2.21 kg m ⁻³	± 0.42 kg m ⁻³	± 0.45 kg m ⁻³
C ₂₂ gravitational coefficient	-	$\pm 1.2 \times 10^{-6}$	$\pm 2.5 \times 10^{-6}$	$\pm 0.87 \times 10^{-6}$	$\pm 0.3 \times 10^{-6}$
bulk q _r	-	$\pm 4.731 \times 10^{-7}$	$\pm 6.292 \times 10^{-7}$	$\pm 6.816 \times 10^{-8}$	$\pm 1.493 \times 10^{-8}$
C/MR ²		± 0.00035	± 0.0005	± 0.0028	± 0.0042

Radius errors from Davies *et al.* (1998), other errors derived from calculated values from Anderson *et al.* papers.

Appendix 2 LPSC Abstracts

Over the course of my PhD studies, I presented several abstracts at the annual Lunar and Planetary Science Conference (LPSC) in Houston, Texas. While these abstracts have been interesting short-term projects, most do not fit into the topic of this thesis. Nevertheless, they represent interesting avenues of research that could be investigated in future work, and are presented in this appendix:

- Thomas C., Ghail R. C., & Wilson L. 2002. The Internal Structure of Callisto., *Lun. Plan. Sci. XXXIII*, #1196.
- Ghail R. C. & Thomas C. 2001. Unravelling the kinematics of Marius Regio, Ganymede., *Lun. Plan. Sci. XXXII*, #1554.
- Thomas C. 2001. A morphological examination of Lugalmeslam crater, Ganymede., *Lun. Plan. Sci. XXXII*, #1412
- Thomas C. & Ghail R. C. 2001. Using elliptical craters as strain markers in Marius Regio, Ganymede., *Lun. Plan. Sci. XXXII*, #1399.
- Thomas C. & Wilson L. 2000. Photoclinometric Analysis of Resurfaced Regions on Europa., *Lun. Plan. Sci. XXXI*, #1328.
- Thomas C. 1999. Is Global Expansion of Ganymede Still Required Given New Thermal Evidence from Callisto?, *Lun. Plan. Sci. XXX*, #1635.
- Thomas C., Head J. W., and the Galileo SSI Team 1998. Morphology of Byblus Sulcus, Ganymede from Galileo SSI Data., *Lun. Plan. Sci. XXIX*, #1897.
- Thomas, C. 1997. Is Tyre Macula an Ice Cauldron?, *Lun. Plan. Sci. XXVIII*, #1005.

THE INTERNAL STRUCTURE OF CALLISTO. C. Thomas¹ and R. C. Ghail². ¹: Planetary Science Research Group, Planetary Science Research Group, Environmental Science Dept., Institute of Environmental and Natural Sciences, Lancaster University, Lancaster LA1 4YQ, England. ²: T. H. Huxley School, Imperial College, London SW7 2BP, England. E-mail: constantine.thomas@lancaster.ac.uk

Introduction: Recently, the Galileo orbiter has provided very useful gravitational data from close flybys of Io, Europa, Ganymede and Callisto that provide several important constraints to their possible internal structures. We present a new model for the internal structure of Callisto based on gravity data.

Existing models: Callisto is an enigma. Its surface is tectonically inert, but Galileo detected the signature of a magnetic field on one of its flybys of the satellite [1]. This could only be explained if a liquid salty water layer existed a few hundred kilometres below Callisto's surface, and a magnetic field was being induced by the jovian field.

Anderson *et al.* (1998a) explored some models of Callisto's interior [3], but unfortunately this was prior to the discovery of the water layer. It is therefore difficult to incorporate such a layer into their models, which made no provision for such a situation. They proposed that Callisto, with a moment of inertia factor of 0.358 ± 0.004 (determined from the C10 flyby), consists of a rock/metal core taking up 25% of the satellite's radius, a 1450 km thick mixed rock-ice mantle, and a 350 km thick pure ice crust.

A more accurate report on the interior structure and physical parameters of Callisto has recently been presented by Anderson *et al.* (2001) [4]. Callisto's moment of inertia C/MR^2 is refined to 0.3549 ± 0.0042 - too small for Callisto to be completely undifferentiated, but too large for it to have separated completely into a rock core, water mantle, and ice crust. They present a range of two- and three-layer models for Callisto's interior - their three-layer models consist of an ice layer nearest the surface with a density range between 900 and 1500 kg m⁻³, a rock/ice middle layer with density between 2300 and 3500 kg m⁻³, and a rock or metal core of density 3550, 5150 or 8000 kg m⁻³. Their rock core models yield the most realistic results, and are similar to those presented in [3]. but they still do not account for the existence of a water layer within the satellite, as determined by magnetometer measurements [2]. As such their models remain incomplete.

The ONIONSKIN moment of inertia model: We have constructed our own model for the interior structures of Callisto. This model is called 'ONIONSKIN' because it calculates moment of inertia of a satellite based on many thin concentric shells, not unlike the skin of an onion. We take the observed values of radius, mass, density, and moment of inertia factor C/MR^2 , and construct a satellite made of layers of different types of (appropriate)

material, such as ice I, ice III, rock, iron and/or iron sulphide (N.B. 'layer' refers to a distinct type of material - 'shell' refers to a radius increment used to calculate moment-of-inertia). We also attempt to account for self-compression of this material due to the mass of the overlying material. The size of the layers is determined by the percentage mass of the satellite which they represent and their uncompressed density - both of which can be changed dynamically - although whereas the percentage mass of a layer is very flexible, the uncompressed density of a material is fixed once the material is chosen. However, mixtures of different material (e.g. a rock/ice mixture) can have a wide range of densities so this becomes an important variable in these cases.

The moment of inertia factor C/MR^2 is determined by dividing the satellite into 10000 equally spaced shells from core to surface. The moment of inertia of each of these shells is calculated and then summed to determine the moment of inertia for the whole satellite in the model. By manipulating the percentage mass and type of material comprising each physical layer, it is possible to construct a model - or a range of models - that have values that lie within the derived error-bars for the satellite's radius, mass, density, and moment of inertia factor and thus are realistic.

There are three important *caveats* to be aware of with the ONIONSKIN model: first, the compressed density at the base of a layer is used to determine the moments of inertia of *all* the appropriate shells within that layer - no attempt is made to model the density range across the shells between the top and base of the layer.

Second, the ONIONSKIN model is a purely physical model constrained primarily by moment of inertia, radius, density and mass - no chemical or thermal modelling is carried out as part of the model verification. However, care is taken to assume reasonable densities for materials comprising the layers and to find appropriate physical parameters (e.g. bulk moduli to determine self-compressibility), and obviously certain results requiring layer densities that are too high or low to be realistic are ruled out straight away.

Third, ONIONSKIN is currently an empirical model - that is, appropriate values must be entered manually into the model and manipulated by hand to converge on the target values. This necessarily limits the investigation of the model's possible 'phase space' to those values that are obvious to the user. It is clear that the results that the model produces are not unique - various combinations and types of materials can produce models that fit within the acceptable 1 σ error range. An automated process to work through the phase space and pick out those models

that conform to the target values is planned but has not been developed yet, and would be extremely useful in determining the possible internal structures of the satellites.

These problems will be refined in future work, but can be a source of inaccuracy in the current models and should be borne in mind here. Despite these limitations however, ONIONSKIN generally produces results that broadly agree with published models [3, 4], which bodes well for its validity.

Callisto ONIONSKIN model results: Here we present a possible ONIONSKIN model of Callisto’s interior that also incorporates a salty water layer. Kivelson *et al.* (1999) propose that such a water layer must be tens of kilometres thick, but also that it must be a tens of kilometres below the surface in order for the detected magneto-convective field to have the correct magnitude. As yet, a mechanism that would form a water layer so close to the surface is not understood. The main problem is that the water layer would be placed entirely within the ice I layer, with no apparent mechanism to allow it to exist there. This problem remains insurmountable at the time of writing. Instead, we continue to focus on physically plausible density and temperature models and disregard this problem. The resulting model is presented in Tables 1 and 2.

It should be noted that this model actually represents a lower bound, since most of the derived model results lie near the lowest error bounds of the target values proposed in [4]. It is possible to reach slightly more “accurate” results (lying more within these error bounds), but it becomes progressively harder to achieve these results. There are several reasons for this. First, the density constraint is very tight and very sensitive to change - increasing the ice/rock mantle or rock core mass by anything more than approximately 1% produces densities that are unacceptably high or low. The radius constraint is similarly tightly restricted. There is also a potential base pressure constraint at the base of the ice III layer if ice V is also present (it is not present in this particular model, however). In effect, this acts to severely limit the range of proportions of the material above and including the ice III layer - the pressure at the base of the ice III *must* be 346 MPa in order to allow it to change phase to ice V. However, this constraint is not considered here, as we assume that the top of the ice/rock mantle lies above the ice III/V phase boundary. This means that the ice III transforms to ice V within the ice/rock mantle (and indeed, the ice V transforms to ice VI, and ice VII towards the rock core), but these phase changes are subsumed into the density of the ice/rock mix.

The ice/rock mantle is assumed to be a layer of constant density (excluding the effects of self compression), consisting of a uniformly mixed 71:29 mixture of ice (with a density of 1300 kg m⁻³) and rock (with a density of 3500 kg m⁻³, identical to the core). Such uniform mixing across a large ice/rock mantle is however rather un-

likely, since the rock is more likely to be concentrated towards the core. If this happens, the density of the ice/rock mantle should increase with depth - however, attempts to model this layer by dividing it into three layers whose density increases with depth give rise to severe problems in keeping the model constrained to the target radius, density and moment of inertia targets. At this stage, this problem is insurmountable, and is left for future work to rectify.

Table 1: ONIONSKIN model of the internal structure of Callisto with a silicate core (density: 3500 kg m⁻³).

Layer	% Mass	P/T density (kg m ⁻³)	Model radius (km)	Layer Thickness (km)
Ice I	8.05	936	2408.85	133.79
salt water	5.00	1169	2275.06	72.83
Ice III	4.25	1182	2202.23	65.16
Ice/Rock Mantle	72.70	2054	2137.07	1249.62
Rock Core	10.00	3662	887.45	887.45
Totals:	100			2408.85

Table 2: Callisto silicate core ONIONSKIN model compared with target values for radius, mass, C/MR², and density

	Target Values	1σ error range
Radius	2410.3	± 1.50 km
Mass	1.07214 x 10 ²³	± 0.00062 x 10 ²³ kg
C/MR ²	0.353608	± 0.0042
Density	1834.37	± 3.4 kg m ⁻³
	Model Results	Error
Radius	2408.85	- 1.45 km
Mass	1.07214 x 10 ²³	-
C/MR ²	0.351551	- 0.002057
Density	1831.18	- 3.19 kg m ⁻³

References: [1] K. K. Khurana *et al.* (1998). *Nature*, **395**, 777-780. [2] M. G. Kivelson *et al.* (1999). *Journal of Geophysical Research - Space Science*, **104**, A3, 4609-4625. [3] J. D. Anderson *et al.* (1998a), *Science*, **280**, 1573-1576. [4] J. D. Anderson *et al.* (2001), *Icarus*, **153**, 157-161.

Unravelling the Kinematics of Marius Regio, Ganymede. Richard Ghail¹ and Constantine Thomas²¹T.H. Huxley School, Imperial College, London, SW7 2BP, UK. *R.Ghail@ic.ac.uk*²Environmental Science Department, Lancaster University, Lancaster, LA1 4YQ, UK. *Constantine.Thomas@lancaster.ac.uk*

Context: Marius Regio is located at 40°N, 200°W, in the mid-latitudes near the antijovian point. It was imaged at 940 m pixel⁻¹ during orbit G8 of the Galileo mission (Fig. 1). The dark region in the south-west of the image is northern Marius Regio; the complex region of bright terrain in the north-east is Ur Sulcus. Dividing the two terrains is Nippur Sulcus. The region of ridged bright terrain in the NW corner of the imaged part of Marius Regio is the easternmost extent of Philus Sulcus, and to the east is the southernmost extent of Elam Sulci. Akitu Sulcus is the east-west feature crossing the centre of Marius Regio, and orthogonal of it to the west is Byblus Sulcus.

Mapping Method: Galileo image c0394517800 was rectified to a Ganymede spheroid and Mercator projection (preserving angular relationships), photometrically corrected and interpolated to 500 m pixel⁻¹ (from 940 m pixel⁻¹). Three low-phase, high-resolution (86 m pixel⁻¹) Galileo G2 images were similarly projected and merged in a 3:1 ratio with the G8 scene, effecting topographic shading on the G2 images. These three images were also processed at 100 m pixel⁻¹ resolution for detailed mapping. Global context for the G8 scene was provided by the Galileo/Voyager global 2 km pixel⁻¹ global mosaics.

Mapping proceeded by dividing the scene into several morphological units (*e.g.*, dark cratered terrain) that provide a context for the structural geology. In structurally simple areas, the youngest features were mapped first, followed by progressively older structures until the stratigraphic sequence was complete. More complex areas were first broken down into smaller regions in which the stratigraphic sequence is preserved before that process was applied.

Interpretation: Though apparently complex, the structural history of Marius Regio and adjacent sulci consists of a sequence of block rotations of semi-rigid plates 100 to 500 km across, resulting in shear and accommodation structures. Planks and smooth bright terrain are inferred to result from transtensional extension, while ridged bright terrain correspond to transpressional shortening. The superposition of multiple scales and phases of deformation results in the observed complexity. Though deformation is concentrated at plate margins, considerable internal deformation is apparent within plates. In-plate shortening is accommodated by widely spaced parallel ridges; sub-parallel fracturing results from stretching within the plate; and *en-echelon* fractures indicate

internal shearing. Elliptical craters provide useful in-plate strain markers [1] within blocks of dark terrain.

Various forms of plate tectonics have been proposed [2, 3] to explain the distribution of light and dark terrain on Ganymede. We find no evidence of the large rigid plates bounded by spreading ridges, subduction zones and transform faults that characterise terrestrial plate tectonics. Zones of extension and compression on the surface are a passive response to the openings and closures generated by block rotations, rather than an active process driving the tectonic movements. Plate tectonics on Ganymede is characterised by a number of usually small semi-rigid plates suffering both internal and plate-margin deformation. This is perhaps not surprising, given the positive buoyancy and low yield strength of ice. The small plate size indicates a thin convecting layer (~500 km thick), perhaps a convecting mantle of ice or water above a rocky interior, and a thin lithosphere (~50 km). This probably varies considerably across Ganymede, since large regions of dark terrain (*e.g.*, Galileo Regio) are evidently stable. Variable plate size is consistent with the observed multiple scales of deformation; larger plates generate larger openings or closures at their margins as they rotate.

Speculation: Marius Regio has a long tectonic history of relatively simple block rotations with transtensional and transpressional adjustments.

One possibility is that prior to entry into its current orbital resonance, Ganymede closely resembled Callisto. During an extended laplacian resonance entry period [4, 5], tidal stirring and heating caused Ganymede's convecting ice mantle or water ocean to drive the breakup of its lithosphere, perhaps by eddy currents on sublithospheric topography. This activity probably ceased in the recent past (<1 Ga, [6]) when the resonance established itself and the forced orbital eccentricity decayed.

Nonetheless, it is not possible to rule out that several structures within the interior of Marius Regio are relics of earlier sulci and ridges, rather than manifestations of more recent internal deformation. In that case, Ganymede's tectonic history is not monotonic but more complex, with several phases of deformation, or indeed a long period of quasi-uniformitarian tectonic activity.

References: [1] Thomas, C. & Ghail, R.C., 2001 *LPSC XXXII*, this issue. [2] Murchie, S.L., & Head, J.W., 1988, *JGR* 93, 8795-8824. [3] Prockter, L.M., *et*

MARIUS REGIO KINEMATICS. R. C. Ghail & C. Thomas

al., 2000, *JGR* 105, 22519-22540. [4] Showman, A., & Malhotra, R., 1997, *Icarus* 127, 93-111. [5] Showman,

A. *et al.*, 1997, *Icarus* 129, 367-383. [6] Zahnle, K., & Dones, L., 1998, *Icarus* 136, 202-222.

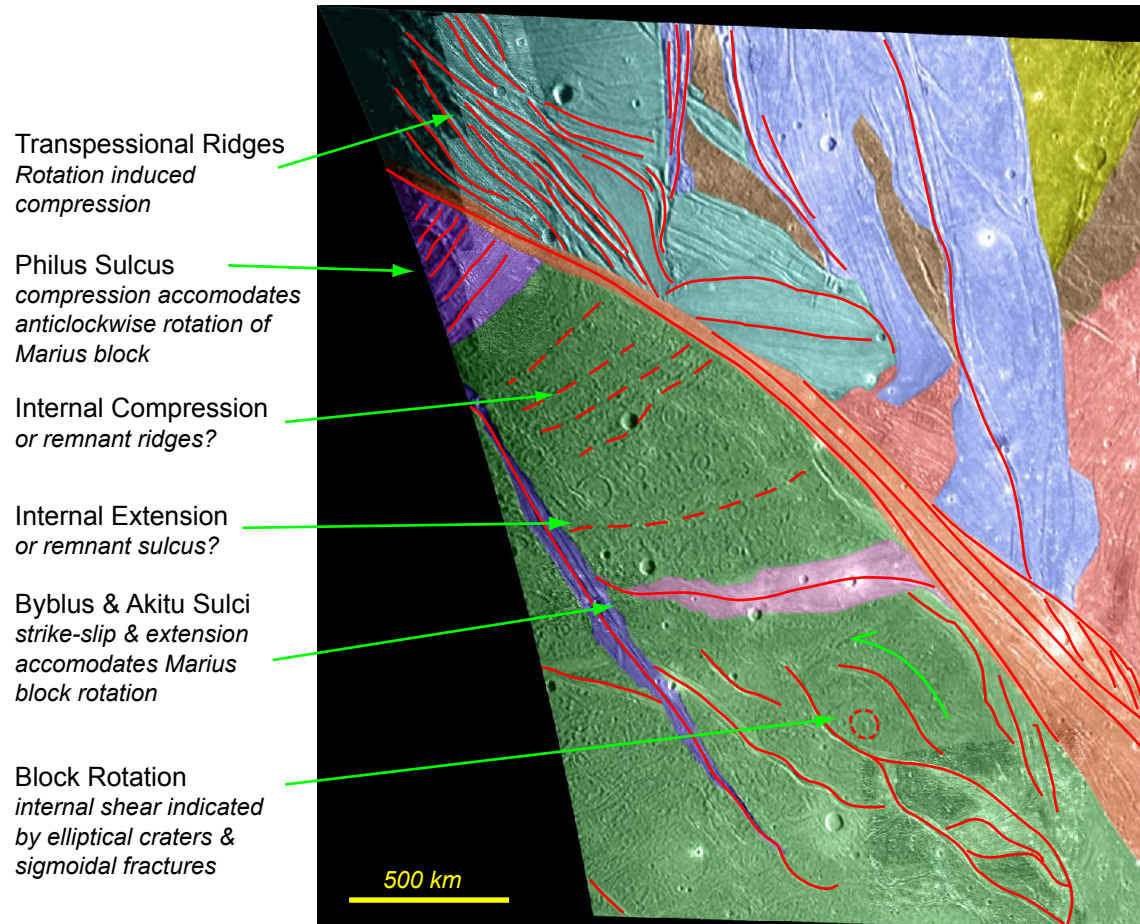


Figure 1. Major Tectonic Features of northern Marius Regio.

A MORPHOLOGICAL EXAMINATION OF LUGALMESLAM CRATER, GANYMEDE. C. Thomas.

Planetary Science Research Group, Environmental Science Department, Lancaster University, Lancaster LA1 4YQ, United Kingdom. (constantine.thomas@lancaster.ac.uk).

Overview: Lugalmeslam is an impact crater approximately 60 km in diameter on Ganymede, located at 24°N 194°W on the southern border of Mashu Sulcus, which geographically separates Northern from Central Marius Regio. It has an unusual elliptical rim where it overlaps the bright terrain of Mashu Sulcus and it was hypothesised that extension in this terrain may have directly affected the rim (R. Pappalardo, *Pers. Comm.*). A detailed analysis of the crater's morphology is presented here which provides new insights into the processes affecting Lugalmeslam.

Datasets: Lugalmeslam was first imaged during the 1979 Voyager 2 flyby of Ganymede and was specifically targeted during the Galileo G8 flyby in May 1997. Three datasets are available for this area: a Voyager 2 low-resolution (2.5 km/pxl) colour set consisting of orange, blue, and violet filter images, a medium-resolution (1.3 km/pxl) clear filter Voyager 2 image acquired when the spacecraft was closer to Ganymede during its flyby, and a high-resolution (0.149 km/pxl) Galileo image obtained during the G8 orbit. These images were calibrated and geometrically reprojected to glean the greatest possible amount of information from them. The colour filters were combined to make a single OBV colour image with orange in the red channel, blue in the green channel, and violet in the blue channel. Finally, the colour (OBV) image, the Clear filter (CLR) image, and the G8 image were superimposed over each other as separate image layers.

Solar illumination and Albedo variation: The Galileo image was acquired at a high solar incidence angle (~ 73°), with the sun low on the eastern horizon. The Voyager images were acquired at a low incidence angle (~ 27°), with the sun high in the southern sky. Brightness variations caused by topography are therefore enhanced in the Galileo image, whereas intrinsic albedo variations in the surface are enhanced by the low incidence angle of the Voyager images. When compared with the Voyager OBV and CLR images, large-scale albedo variations in the G8 image are very hard to see - the boundary between 'Dark Terrain' and 'Bright Terrain' that is visible in the Voyager 2 images cannot be distinguished at all in the Galileo image even with extreme image manipulation.

Crater Floor Morphology: The Voyager images clearly show a dark arc just inside the western rim of the crater - if this were any kind of shadow, it would have to be cast by higher ground to its south. However, the viewing geometry is completely inappropriate for this arc to be a shadow of the rim. Furthermore, true shadow would be seen as completely black areas in the OBV colour image, and the arc is clearly a darker shade of brown than the surrounding Dark Terrain. This dark region must therefore be caused by albedo variations in the crater floor in this region. Indeed, because the sun is high in the sky and no shadows are visible in the Voyager images, only very steep slopes - steeper than 63° from horizontal - can cast shadows. It should be noted that this represents the maximum possible slope in the imaged region, and the actual slopes may not necessarily be this steep. Despite the high incidence angle however, it is possible to see small-scale albedo variations in the Galileo image. Although hard to distinguish, the darkest areas correspond to topographic lows, and also represent the smoothest terrain at this 149 m/pxl resolution. Local topographic highs and the rims of most small craters within and around Lugalmeslam are brighter than surrounding terrain. This is in agreement with the relationship between topography and surface brightness noted by [1]. As implied by the VGR images, the crater floor in the arc just within the western part of the crater rim appears to be slightly darker than the rest of the crater floor. Examination of the image indicates that this area

contains less of the small (< 1 km across, probably a few hundred metres high) bright-topped hills that give the surrounding terrain a characteristic texture. This provides a partial explanation as to why this area appears darker than the rest of the crater floor - areas in the G8 image where the density of these small bright features is lower are also darker at the lower VGR resolutions. The intrinsic photometric properties (colour, reflectivity etc.) of the material may also vary, but such small-scale variations across the floor of Lugalmeslam are impossible to determine in the single filter Galileo image. Parts of the rim wall are locally quite bright, and the floor near the southeastern wall of crater is more rugged (exposing more bright ridge tops) than the rest of the crater. The north and northeastern part of the crater contain many medium-sized craters with bright rims, so the average brightness of this region at kilometre-scale is higher than in the rest of Lugalmeslam. The central part of the crater is occupied by a convoluted ring of hummocky terrain, which apparently outlines a small arc of darker material to the east of the actual centre. The inner edge of this arc appears to be a ridge/scarp that represents the highest part of this area. This arc outlines what is generally lower ground (and darker albedo material), though the exact centre of the crater is marked by a small bright central peak structure approximately 3.5 km across that appears to approach a similar level to that of the ridge arc around it.

Rim Morphology: For ease of reference, the rim morphology will be described here in terms of a clock face, with the 12:00 position oriented towards the north. The western rim of Lugalmeslam is very obvious, and a 410 pixel (61.09 km) diameter circle - the 'ideal circle' - can be used to approximate the shape of this portion of the rim. The rim follows this ideal circle very closely going anti-clockwise between the 12:00 and 6:00 positions. The eastern rim is much more irregular than the west, and significantly deviates from the ideal circle - in fact, the entire eastern half of the rim lies outside the ideal circle. It was traced by following inward-facing scarps of similar character and appearance, and also by using photoclinometrically derived perspective views as a rough guide. The most clearly delineated portion of the rim lies between the 10:00 and 6:00 positions. Between 10:00 and 9:00 the horizontal distance between the rim top and crater floor is between three or four kilometres. The rim wall steepens considerably between 8:00 and 6:00, where it rises from crater floor to rim top over a distance of the order of 500 metres. The rim deteriorates significantly and very suddenly beyond this point - between 6:00 and 4:00 it is a much wider, shallower slope spread over a distance of between nine and ten kilometres. A flatter area - a lower terrace - along the crater wall is evident in this area, intermediate in height between the rim top to the east and the crater floor. The 4:00 position marks a sudden downward break in slope that can be followed from the base of the crater wall out to the southeast of the crater itself. The northeastern portion of the rim between the 11:00 and 4:00 positions appears very heavily degraded. The rim appears to bifurcate at the 4:00 break - one rim follows a higher path than the other. The 'high rim' is more discontinuous and is made of long, smoothly-curved arcuate ridges - this is interpreted here to be the 'true rim' of the crater. The 'low rim' lies nearer the crater floor and has a more strongly crenulated appearance, with distinct scarps casting shadows on the terrain below. Near the 1:00 position, these scarps stop abruptly and cannot be seen elsewhere along the rim. Between 12:00 and 2:00 (particularly nearer 12:00) the rim is extremely difficult to trace and in some places disappears almost completely. The slope towards the centre of the crater appears to be the shallowest in this region, though the terrain between the wall and crater centre contains many small (one to five kilometre diameter) craters. The rim appears to rise between the 11:00 and 1:00 positions, until it becomes clearly defined again near 10:00.

The BT/DT boundary: Lugalmeslam itself lies astride the border between the Dark Terrain of Central Marius Regio to its southwest and the Bright Terrain of Mashu Sulcus to its northeast - 22.7% of the crater's area lies within Mashu Sulcus, while 77.3% lies in the Dark Terrain. The rim of the crater is easy to follow in the Dark Terrain but considerably harder to distinguish in the Bright Terrain, where it blends in more with the background topography - photoclinometry was used to help locate the rim here. There is no sharply defined boundary visible in the Galileo image between the Bright Terrain and Dark Terrain - no obvious fault lines or other such features separate the two terrain types. Instead, the Bright Terrain merely seems to emerge directly from the Dark Terrain. It is interesting to note that there is little discernable difference in the Galileo image between the fine (< 1 km) textures of the actual surface of the Bright Terrain and Dark Terrain. Bright and Dark Terrain are peppered by hundreds of small craters up to 1 km in diameter, and there are only 25 larger craters up to 5 km in diameter. No craters larger than 5 km in diameter are present in the G8 image apart from Lugalmeslam itself. Crater densities on both sides of the boundary (as defined by Voyager images) are very similar - the crater density in the Bright Terrain is 0.030 craters per km², whereas the crater density in the Dark Terrain is slightly less at 0.025 craters per km². This difference is too small to be statistically significant and reveals nothing about the relative ages of the two terrains. The Bright Terrain area also contains linear, though discontinuous, ridges that cross the G8 image at a bearing (measured clockwise from north) of 120° to 130°. The axes of these ridges are separated by a distance of 16 +/- 3 km - this spacing is generally fairly regular in the imaged area. Smaller ridges (a few hundred metres in height) can be found between these major ridges, but these are much less well-defined. The major ridges are between 2 and 5 km wide from base to base across the ridge axis, though some appear less distinct than others. A major ridge in the northeastern corner of the G8 mosaic is particularly triangular in cross section, and also the base of its northeastern flank is mantled by a particularly obvious patch of smooth dark material that is visible in the CLR image. Indeed, most of these major ridges have dark material associated with their bases, again supporting the hypothesis that dark material is being deposited in topographic lows from higher ground. The width of the crater within the BT area is ~ 17 km, which is approximately the same as the wavelength of the major ridges. One ridge appears to run roughly at a tangent to the northeastern rim (intersecting at the 1:00 position). Another small ridge approaches the outside rim near the 3:00 position but does not appear to penetrate the rim. The next ridge (which marks where the Bright Terrain stops encroaching into the Dark Terrain at Voyager resolutions) does cut into the crater and extends approximately 10 km into the crater floor from the southeast (at exactly the 4:00 position), but this ridge cannot be seen to continue on the opposite side. The spacing between the first pair of ridges is ~ 21 km, while the second pair are ~ 11 km apart. No further ridges can be seen further south in the Dark Terrain. There are also at least two sets of small ridge-like lineaments that comprise a fabric oriented roughly perpendicular to the ridges that cross both the Dark and Bright Terrain areas. These are not visible in the Voyager images - the topography across them is very low. This fabric appears to be older than the BT ridges as it can be seen to be deformed by them as it crosses them. The spacing between the individual ridges of this linear fabric is 1 - 1.5 km. Just beyond the south-eastern crater rim, these lineaments are oriented tangential to the rim and one of these small ridge sets appears to intersect the rim between the 4:00 and 5:00 positions. The lineaments are not present within the crater or very close to the outside of the rim. The lineaments continue past the crater rim into the BT area where they can be seen to follow the topography of the major ridges therein, though they do curve northwards beyond the crater.

Interpretation: The origin of Mashu Sulcus has previously been interpreted by [2] as "tectonic blocks of dark materials, downdropped and resurfaced by light smooth material, and subsequently fractured pervasively by narrow grabens, tension fractures, or both. Sinusoidal groove cross sections due in part to mass wasting." Lugalmeslam itself

is mapped as a "partly degraded crater of intermediate age", while the northeastern portion of it is mapped as "Smooth [Light] Material" interpreted as "extrusive or pyroclastic deposits of brine". Examination of the higher resolution Galileo image requires extensive modification of this interpretation. There is no evidence for cryovolcanic activity of any kind in this area and nothing to suggest that the northeastern portion of Lugalmeslam is compositionally different to its surroundings. The small-scale textural similarity between the terrain seen in Mashu Sulcus and Central Marius Regio seen in the Galileo image suggests that the only difference between the so-called Bright and Dark Terrain in this area is that the former contains large ridges and the latter does not - in other words, the only reason that Mashu Sulcus is brighter at Voyager resolution is due to averaging out of sub-pixel albedo variations brought about by the presence of the ridges and not because of any intrinsic compositional differences. It would appear that the southeastern rim of Lugalmeslam has failed along planes of weakness denoted by the small NE-SW trending lineaments and rotated downwards towards the crater floor. Debris has filled in the base of the inner rim wall and spread inwards towards the centre of the crater, thus resulting in a more gradual slope here to the surviving rim - it may be no coincidence that the crater rim between the 4:00 and 5:00 positions is straight and oriented at the same angle as the small lineaments that intersect it. The northeastern quarter of the rim that overlaps Mashu Sulcus is the most heavily disrupted segment. It is interesting to note that the crater rim in this area is roughly parallel to the fabric of the NW-SE ridges in Mashu Sulcus. The fact that one of these major ridges actually intersects the rim in the northeastern quadrant of the crater may not be a coincidence - it is likely that the process that created the ridges disrupted the rim.

Further Work: It is obvious that some tectonic process has affected the Dark Terrain of Central Marius Regio to turn it into the 'Bright Terrain' of Mashu Sulcus - the two terrains seem identical apart from the presence of the ridges in Mashu Sulcus. It is also apparent that tectonism has affected the shape of Lugalmeslam by disrupting its rim - however, there is no evidence to support the hypothesis that Lugalmeslam has been actively extended along an axis by tectonic movement in Mashu Sulcus. The exact nature of the tectonic processes occurring in the Sulcus is unclear - however, the lack of features commonly associated with extension in this region (such as cracks and fracture belts) that are so prevalent in other areas of Ganymede (e.g. Nicholson Regio, Byblus Sulcus) hint that perhaps the ridges may not be extensional in nature. Compressional and strike-slip tectonism have been identified elsewhere on Ganymede by other authors [3, 4, 5, 6] and this form of activity may be applicable here.

The chronology of events in this area is very ambiguous. It is most likely that the Mashu Sulcus ridges and the NE-SW lineaments formed more recently than Lugalmeslam in order to disrupt the crater rim - however, the lack of lineaments in the crater floor requires explanation if this is the case. Furthermore, the lack of ejecta or secondary impacts around the crater implies that it is old and has suffered much thermal, gravitational, or micrometeorite erosion. Clearly there is more to investigate in order to determine the chronology of events in this area, and further analysis will be attempted in order to clarify the exact nature of the processes affecting Lugalmeslam.

References: [1] Spencer J., (1987) *Icarus* 69, 297-313. [2] Murchie and Head (1989), USGS Map JG-4. [3] Thomas C. *et al.* (1998) *LPSC XXIX* #1897. [4] Ghail R. C. and Thomas C. (2001) *LPSC XXXII*, this issue. [5] Murchie S. L. and Head J. W. (1988) *JGR*, **93**, 8795-8824. [6] Prockter L. M. *et al.* (2000) *JGR*, **105**, 22519-22540.

USING ELLIPTICAL CRATERS AS STRAIN MARKERS IN MARIUS REGIO, GANYMEDE. Constantine Thomas¹ and Richard Ghail², ¹Environmental Science Department, Lancaster University, Lancaster, LA1 4YQ, United Kingdom. constantine.thomas@lancaster.ac.uk ²T.H. Huxley School, Imperial College, London, SW7 2BP, United Kingdom. R.Ghail@ic.ac.uk.

Introduction: Marius Regio is located at 40°N, 200°W, in the mid-latitudes near the antijovian point. It was imaged at 940 m pixel⁻¹ during orbit G8 of the Galileo mission. It consists of large blocks of older dark terrain, separated by swathes of younger bright material. Ghail and Thomas [1] suggest that the dark terrain has undergone tectonic deformation which is recorded in the non-circularity of some dark-terrain craters. Accordingly, elliptical dark-terrain craters can be restored to circularity by removing inferred tectonic movements to provide a quantitative measure of the strain.

Technique: To test this hypothesis, we chose a prominent elliptical crater within a strike-slip rotational block (Fig 1) in the area mapped by [1], immediately south of Akitu Sulcus. Rotation is implied by the curvature of the bounding en-echelon fractures, but cannot be recovered directly from the crater deformation. Wrench movement along the strike-slip faults was reversed by skewing a rectangular block bounded by the faults (Fig 2). A range of values were tested and the best fit found. However, restoring the wrench movement did not recover a circular crater. A further uniform shortening parallel to the strike-slip

faults was required to restore circularity. Again, a range of values were tested and the best fit determined.

Results: A 5.75° skew together with 5% shortening was required to circularise the crater completely. We can therefore infer transtensional strike-slip movement of the original block, consistent with the interpretation of [1]. The deformation observed in the crater implies 13 km of sinistral strike-slip movement along 180-km long wrench faults, plus 10 km uniform extension. Strike-slip deformation dominates over extension, again consistent with a transtensional interpretation. The block-bounding faults intersecting the wrench faults can be confidently interpreted as *en-echelon* fractures caused by transtension.

Conclusions: Despite ignoring rotation for model simplicity, the quantitative degree of strain from transtensional movement along paired wrench faults can be successfully recovered by restoring the circularity of elliptical craters. We intend to apply this method to other craters on Ganymede and extend it to include craters deformed by extension, compression and transpression.

References: [1] Ghail, R. C., & Thomas, C., (2001) *LPSC XXXII*, this issue.

Fig 1. Strike-Slip Block and Deformed Crater

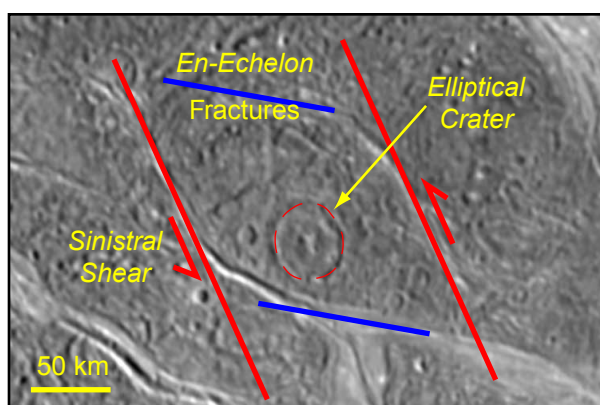
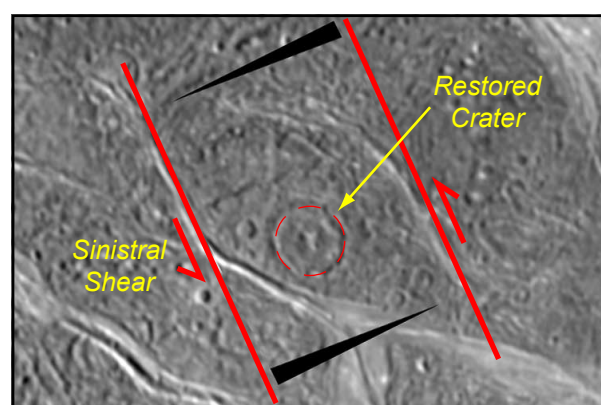


Fig 2. Restored Block and Crater



PHOTOCLINOMETRIC ANALYSIS OF RESURFACED REGIONS ON EUROPA. C. Thomas & L. Wilson. Planetary Science Research Group, Environmental Science Dept., Institute of Environmental and Natural Sciences, Lancaster University, Lancaster LA1 4YQ, England. constantine.thomas@lancaster.ac.uk.

Introduction: The Galileo Solid State Imaging (SSI) camera imaged a region of Europa centred at 5.73°N 326.54°W at a resolution of 25.3 metres per pixel (50.6 metres per line pair) during the E4 flyby through the Jovian system as part of the E4ESDRKMAT02 observation. The imaged area (c0374685452r.img) is located on the subjovian hemisphere in a region previously observed only at very low (< 5 km) resolution by Voyager and at 330 metre resolution in other E4 Galileo images.

The imaged region is characterised by complex sets of criss-crossing fractures, multiple and doublet ridges in various orientations characterised as 'washboard plains' [1]. The surface on which these ridges are located is broken up in many places around this area, and there is evidence for lateral movement of 'rafts' of surface material similar to that interpreted in the Chaos terrains imaged on other orbits [1] elsewhere in the E4ESDRKMAT02 observation.

There are at least three examples in c0374685452r.img of terrain that is locally smoother than its surroundings, and these are interpreted here as the result of resurfacing events that have covered underlying material [1]. These areas are irregular in shape and closely follow ridge boundaries.

One particular area - a roughly elliptical feature referred to henceforth as the 'pond' given its appearance [2] (shown in Figure 1) - is the subject of analysis in this abstract. Since ridges to the north and south of the pond are submerged by it, it is possible to determine the depth of the pond if the height of the submerged ridges is known. To this end, topographic profiles of the area within and around the pond were derived using photogrammetry. The pond morphology (also derived partly from photogrammetry) and the resulting implications for the rheology and nature of the erupted fluid are described.

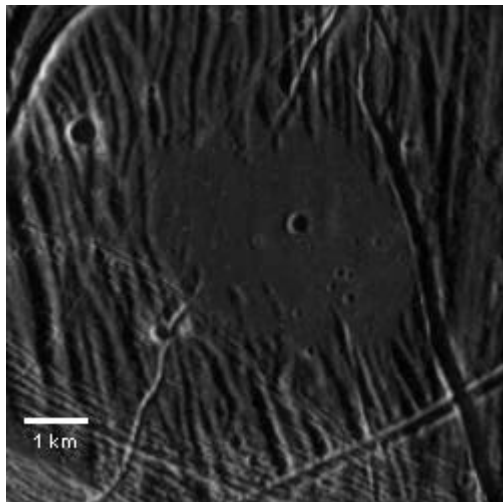


Figure 1: Pond-like feature imaged by Galileo.

Morphology: The smooth pond covers an area of approximately $6.5 \times 10^6 \text{ m}^2$; it can be roughly approximated by a 3700 m x 1240 m ellipse. Its albedo is low and similar to that of surrounding terrain which is comprised of dense interleaving N-S trending sinuous ridges and troughs. The relief of these features is low, though some high-standing ridges are present to the south of the pond.

The pond itself appears regionally smooth, though this conclusion is reinforced by the presence of large (8x8) pixel image compression artifacts that serve to average out the DNs in the region. Small impact craters between 50 and 125 m in diameter are present in the pond's southeastern quadrant, and a relatively large circular crater with a diameter of 250 m is located (coincidentally?) near the centre of the

pond. The only other structures visible in the pond are what appear to be the tops of broad ridges that enter it from the north and south.

The smooth, flat appearance of the area covered by the pond contrasts with the obvious topographic variation of the ridged terrain surrounding it, indicating that the pond material was rapidly emplaced as a fluid that submerged pre-existing topography to varying degrees. This suggests a high effusion rate from an as-yet unidentified source probably hidden beneath the pond material.

The pond material covers low-lying regions between the ridges impinging on it, mainly on the northern and southern edges where the ridges are perpendicular to the pond margin. Ridges disappear towards the centre of the pond, indicating that it is deepest there. However, since ridge traces are still visible in this central region, the maximum depth of the pond cannot be that much greater than the maximum height of the ridges it covers; these heights are derived in the photogrammetric analysis below so that a minimum volume of the pond can be calculated. The eastern and western margins of the feature are more nearly parallel to (and therefore follow) the ridged surface texture.

The eastern border of the pond is marked by a 200 m wide fracture that braids to the north, the western rim of which has a 'fuzzy' appearance interpreted here as pond overflow into the fracture when the pond material was erupted. A 100 m wide NE-SW fracture traverses (but disappears into) the pond. The pond is stratigraphically the youngest unit in the imaged region since it floods or embays all the fractures and ridges that impinge on it.

There are neither obvious flow fronts within the pond nor any levees along its margins visible at the resolution of the image. This sets the maximum height of any levees that do exist to no greater than a few metres, limiting the maximum yield strength of the pond material (if it was indeed erupted as a non-Newtonian fluid) to $< 10 \text{ Pa}$.

Image Preparation: To prepare the image for photogrammetric analysis, it was first calibrated and then reprojected (using the USGS ISIS software package) to a sinusoidal reprojection centred on the central crater in the pond. The image was then output from ISIS as a raw image with the DN range determined by the DSK2DSK program, which determines the full range of DNs contained in the image.

The reprojection process always rotates the raw image so that north is directly 'up' in the reprojected image, so the reprojected image should be further rotated such that the solar illumination is coming directly from the right of the image in order to maximise the accuracy of the profiles. All illumination and orientation information is acquired from the image labels, and it is necessary to assume that it is completely accurate - given the current lack of accurate SPICE pointing data for Europa this may not be the case. Furthermore, it should be noted that rotating the image may introduce resampling errors (attributing slightly different DNs to pixels from those that they possess in the original calibrated image), though the reprojection process itself is likely to introduce errors as it reprojects and rotates the original calibrated image. Furthermore, image compression blocks in the image are (ironically) concentrated in the smooth areas such as the pond and may cause errors since the actual terrain pixels are subsumed into the compression artifact. However, while these errors may affect the outcome of the photogrammetry process it is unlikely that they are very significant and they will certainly not affect the broad shape of the profile.

Photogrammetric analysis: The aim of the photogrammetric analysis of the pond area performed here is to determine the maximum height of the ridges that are submerged by the pond in order to estimate a lower bound for its depth and volume.

As there is no evidence in large-scale mosaics of this area to suggest a regional east-west slope across this locality [1], a regionally flat 'background' surface for the area can be assumed here. Each profile was derived using a range of possible pixel DN values that could potentially correspond to locally flat surfaces in the analysed row

PHOTOCLINOMETRIC ANALYSIS OF RESURFACED REGIONS ON EUROPA: C. Thomas & L. Wilson.

of the image. The topographic slope between adjacent pixels is derived by taking the ratio of the DN of each pixel to a DN value that corresponds to a flat surface appropriate to that terrain type (the latter is known as the Flat Surface DN, or FSDN). By interpreting this ratio in terms of a chosen photoclinometric function using techniques similar to those described in [3], the slope corresponding to the brightness difference can be calculated across a horizontal distance equal to the image resolution (25.3 m/pxl in this case) - the higher the ratio, the steeper the slope.

It is assumed that the pond surface is itself an approximately flat and level plane. Thus profiles that are generated across the pond surface that are not flat and level must not use an appropriate assumed FSDN. If an assumed FSDN across a row is too high, the sun-facing slopes are shallower than expected while those facing away from the sun are steeper, resulting in skewed topography and an artificial sun-facing regional slope across the profile. Since the incident illumination in the image is from the right of the image, this means that the terrain on the left edge of the pond would appear much lower than the terrain on the right edge of the pond - the inverse applies if the chosen FSDN is too low. Those FSDN values that yielded such unreasonable slopes could be and were discarded, leaving a much smaller range of more reasonable FSDN values that could be used in the analysis. The most appropriate FSDN was then picked out from this reduced range using the image as a guide and used to generate the final profile for that row.

This FSDN was then used in a second profile-generating program where the FSDN could be varied across the profile. This could be used to 'fine-tune' the profile in various ways and could also be used to more accurately determine the absolute albedoes of the features in the profile since the FSDN is directly proportional to the albedo. Craters are assumed to have opposite rims at the same height, so if they appeared at different heights in the profile the FSDN across the crater could be tweaked until they were the same - this would then yield an optimum estimate for the FSDN of the crater. Symmetrical-looking ridges on the pond are another feature than can be adjusted in this way - if the ridge FSDN were too high or low it would result in an asymmetrical ridge on the profile and a height difference in the pond on either side of the ridge. The FSDN of the ridge can be adjusted so that the ridge becomes symmetrical in profile and the pond becomes level, and the albedo of the ridge can then be determined.

Several assumptions are made about the topography of features in the pond region - that craters (most of those found in the image appear to be bowl-shaped) have rims that are the same height, that any ridges are symmetrical in profile along their axes relative to the surface that they are on (e.g. a 'double ridge' is assumed to consist of two symmetrical side-by-side ridges with triangular cross-section). While these assumptions may not be strictly realistic they appear to be generally supported by visual interpretation of the image and so serve as a good starting point for this analysis.

Preliminary topographic profiles were derived in this way across the pond and the ridges to its north and south, using visual interpretation as an aid. In addition, albedo effects can significantly alter derived slope values by artificially increasing or decreasing the DN values expected from topography alone - however, these are generally noticeable in the profiles as isolated examples of anomalously steep slopes (such as those found on the bright sun-facing walls of some ridges and troughs).

The shapes of the profiles are determined by the photometric function used. Obviously, this has to match that of the surface if the profiles are to be completely accurate. The most detailed and accurate photometric function is the Hapke function but this is extremely complicated, containing many terms (e.g. pore size between grains of material on the surface) that can only be guessed at, and it is computationally very difficult to incorporate into a profile-generating program such as the one used here. There is one function - the Lommel-Seeliger function - that is essentially a 'distillation' of the Hapke function that does not contain the more complicated terms. The Lommel-Seeliger function relies on the incidence and emergence angles alone, and since it is directly related to the Hapke function it is the one used here. There are other functions - the Lambert (incidence angle dependence only) and the Minnaert, but these functions are not simply related to the Hapke and are therefore less likely to be appropriate. The Lambert and Lommel-Seeliger functions represent end-members on a

scale that ranges from an 'icy-type' surface (Lambert) to a 'lunar-type' surface (Lommel-Seeliger). It should be noted that any phase-angle dependence of these functions is not relevant when generating topographic profiles, since the phase angle within a single image is effectively the same anywhere within the image area. Further development of the program used to derive these profiles is anticipated to allow the use of more accurate photometric functions.

Results: Since the pond itself is interpreted as being flat and with no regional slope, the FSDN across that region can be assumed to be the same as the average DN over the entire area covered. At least two such appropriate initial FSDNs were derived; one for pond material (FSDN 35), the other for the ridges to the north and south (FSDN 40). However, it was found to be difficult to constrain the FSDN to a single value along the profiles - in some cases up to ten different values were used along a profile, though within the pond these rarely varied by ± 3 DN at most. For example, the crater at the centre of the pond was found to require a higher FSDN (40) than the surrounding pond material in order to keep the opposite rims at the same height, although this may be more due to the fact that most of the crater diameter is occupied by shadow. As expected, the pond material FSDN value was found to be lower than that of the surrounding ridges.

The observed morphology of the northern and southern pond margins results from low relief ridges gradually sloping downwards towards the centre of the pond; those ridges that are locally taller are more likely to stand out above the pond surface closer to the centre, and small-scale variations in the angle of slope beneath the pond could also result in lower relief ridges protruding from the surface nearer the centre.

The heights of ridges to the north and south of the pond are consistently found using the photoclinometric techniques described here to lie between 10 and 30 metres above the surrounding terrain - all of these are eventually completely submerged within the pond itself. Work in ongoing to verify these results with more profiles across the area.

Since it is possible to see traces of ridges continuing through the pond at least part of the way across the feature, the pond is unlikely to be greater than 50 metres deep at most, and is most likely to be roughly parabolic in cross-section so that the ridge tops can remain close to the surface for their traces to be visible. Using this depth, the maximum volume of material erupted to form the pond is therefore approximately 0.35 km^3 .

References: [1] J. W. Head et al. (1998) In LPSC XXIX, Abstract #1412, LPI, Houston. [2] J. W. Head et al. (1998) In LPSC XXIX, Abstract #1491, LPI, Houston. [3] Mougini-Mark, P.J. & Wilson, L. (1981) MERC: a FORTRAN IV program for the production of topographic data for the planet Mercury. *Comp. Geosci.* **7**, 35-45.

IS GLOBAL EXPANSION OF GANYMEDE STILL REQUIRED GIVEN NEW THERMAL EVIDENCE FROM CALLISTO? C. Thomas, Planetary Science Research Group, Environmental Science Dept., I.E.N.S., Lancaster University, Lancaster LA1 4YQ, U.K. Email: constantine.thomas@lancaster.ac.uk

Summary: Showman et al. [1, 2] have recently provided a detailed model of the internal evolution of Ganymede that takes into account the highly differentiated nature of the satellite and the presence of a dense core [3] and intrinsic magnetic field [4], and couples this with the orbital evolution of the Galilean satellites as modelled by [5]. However, the more recent discovery of an induced magnetic field around Callisto [6] may have significant implications for the evolution of the crust of Ganymede and explanations for its current configuration.

Magnetic Field Observations: Callisto was observed on the C3 and C9 fly-bys of the Galileo orbiter at opposite phases of the variation of the background (Jovian) magnetic field. Intrinsic ferromagnetic dipolar field models, in which the magnetic field is generated by convection within a convecting metallic core, were found not to agree with the perturbations that were observed. Instead, it was found that they could best be modelled as being generated by a dipolar magnetic field induced in a conducting sub-surface layer beneath Callisto's crust. Further evidence that the field was induced was the fact that the dipole moments detected were anti-parallel on opposite sides of Jupiter. This layer was interpreted to be a globally extensive, electrically conducting ocean of salty water at least 10 km in depth, assuming a salinity similar to that of the oceans of Earth [6]. However, to correlate with the apparently geologically quiescent surface of Callisto, the uppermost part of an 'ocean' would have to be located deep below the surface, most likely probably several tens of kilometres.

An sub-surface ocean was confirmed for Europa later in the Galileo mission when an induced magnetic field was observed there during the E4 and E14 fly-bys [6]. Although the exact depth of such a liquid layer has not yet been determined, it is likely that it does lie close to the surface based on geological evidence.

Unlike both the other satellites described here, a magnetic field with the signature of an intrinsic (internally generated) dipole was unambiguously detected at Ganymede by Galileo [4, 7]. This field must be generated by an internal 'dynamo' in a convecting, conducting (i.e. molten metallic) core.

Ganymede Orbital Evolution: Ganymede is part of a complex orbital resonance peculiar to the Jovian system. In this resonance, the ratios of the mean motions (i.e. the mean orbital angular velocities) of the Ganymede-Europa and Europa-Io pairs are both almost exactly 2:1; in other words, when Ganymede completes one orbit around Jupiter, Europa completes two, and Io completes four. In addition, the conjunctions between the satellites within each pair drift, and there is a 1:1 relation between the rates of motion of the Io-Europa and Europa-Ganymede conjunctions - this is known as the Laplace Resonance. This orbital configuration allows the secular transfer of energy and angular momentum from Io to Europa to Ganymede, and the tidal dissipation within these bodies that results significantly affects the surface and interiors of these satellites [1]. Indeed, it is the tidal dissipation within Io that results in the extensive volcanic activity observed on its surface today [8] and it has been suggested [9] that this also provides the heat source for the ocean beneath Europa's surface.

Showman et al. [1, 2] propose that the Io-Europa-Ganymede system passed through one or more Laplace-Like Resonances (LLRs) before settling into the current one; these served to pump the eccentricity of Ganymede, potentially resulting in extensive and rapid tidal heating that mostly affecting its outer icy layers. In their models, Ganymede is captured into an LLR very soon after its formation and complete differentiation into a metallic core, rocky mantle, and icy crust consisting of Ice I at and below the surface, underlain by high pressure (HP) ice phases such as Ice III, Ice V, and Ice VI.

Showman et al. [2] predict that global thermal runaways would occur if the internal thermal profile was within a particular temperature range when Ganymede entered the LLR - if the interior

was too hot or cold, runaways would not occur at all. Large runaways cause an increase in internal temperature of between 50 and 100 K which results in the melting of most of the Ice I layer and more importantly of the HP ices deeper below the surface. As the dense HP ices melt, they expand more than the melting Ice I contracts and cause a net 'global expansion'. Such an expansion was first proposed by [10] to explain the formation of the Bright Terrain that covers ~ 50 % of Ganymede's surface. Such a scenario is presented as an alternative to previous hypotheses proposing that the global expansion occurred due to the volume change that resulted in the freezing to Ice I of a water ocean within Ganymede [11].

However, Showman et al. admit that there are problems with this scenario, the most important of which being that if there is even the normal carbonaceous chondrite abundance of radioisotopes in the rocky interior of Ganymede then the internal temperature would be too high to allow such large runaways to occur in the first place. Instead, Ganymede comes into the LLR with a warm interior and already possesses a thick ocean of liquid water between a thin Ice I surface crust and possibly a remnant Ice VI layer overlying the rocky mantle. In this case, presence of the ocean means that the eccentricity is not pumped to a high enough value within the LLR to generate sufficient tidal dissipation to have a significant effect on the satellite other than to stabilise the temperature to a level warm enough to maintain the ocean. The ocean therefore remains until the LLR is disrupted, whereupon it cools and eventually freezes ~ 1 Ga later.

It therefore appears that large runaways may be impossible given a realistic radionuclide distribution within Ganymede. There are uncertainties, particularly in the determination of Q (the tidal dissipation factor) and the assumed properties of the ice, that may allow large runaways to occur within this model, however. If they do occur, some degree of global expansion is likely which could satisfy the requirement that the Bright Terrain on the surface of Ganymede formed as a result of such an event.

It could be argued that the formation of an ocean before entry into the LLR would result in global expansion through the melting of HP ices at the base of the primordial ice crust. However, the high heat flow caused by accretional and radioisotope heating at such an early stage in Ganymede's history may well preclude the freezing of any liquid water to form the HP ices at the base of the ocean in the first place. Even if it were possible, the resulting expansion and fracturing caused by the melting of any HP ice would not be recorded in the crust visible today because that would not have formed. The boundaries of the Bright Terrain belts on Ganymede are sharp, and Bright Terrain is much less cratered and cuts through more ancient, heavily cratered Dark Terrain blocks [12]. It is therefore apparent that the Bright Terrain cannot be associated with the early differentiation of the satellite and so must have formed later in Ganymede's history. Dissipation resulting from passage through a Laplace-Like Resonance is a viable candidate for a phenomenon that could result in the generation of Bright Terrain, although the reasoning shown below throws doubt on the possibility that the Bright Terrain could have resulted from global expansion.

Callisto's Ocean: The recent discovery of an ocean layer within Callisto may create severe problems for any global expansion hypotheses for Ganymede. Callisto has never been involved in any orbital resonances throughout its entire history. Callisto's heavily cratered, primordial surface shows very little (if any) sign of tectonic activity even in high resolution Galileo images, indicating that it has not suffered any tidal heating pulses that could have created changes in its interior that would affect its surface, such as those proposed for Ganymede [e.g. 13]. However, a conducting liquid layer - most likely a salty H₂O ocean - still exists deep within the satellite's interior today. The existence of this ocean is troublesome indeed, since it must be maintained

by some hitherto unrecognised heat source.

The internal structure model for Callisto of Anderson et al. [14] proposed that a clean ice layer would extend from the surface to a depth of ~ 350 km in a partially-differentiated three-layer model of the satellite which at the time seemed reasonable. However, Anderson et al. [14] admit that the amount of ice-rock separation they calculate may be a lower limit. If Callisto actually has a strong elastic lithosphere and is not in hydrostatic equilibrium (a fact that remains ambiguous and may be confirmed or denied in the close Callisto fly-bys scheduled later in GEM), the calculated moment of inertia (0.359) would be an overestimate and Callisto would therefore be more strongly differentiated. Such a deviation from hydrostatic equilibrium could arise from a tidal bulge caused by an internal water layer, although the satellite's distance from Jupiter and the depth of the ocean within it may result in too small a tidal bulge to cause such a significant enough deviation. Nevertheless, since the data from which Anderson et al.'s internal structure model [14] are derived is based on only one reliable dataset (the C10 fly-by), it would be prudent to remember that the equilibrium treatment is still an assumption at this stage, and that the possibility remains that Callisto may actually be more differentiated than currently appreciated.

Given this possibility, coupled with the recent confirmation of an ocean layer on Callisto [6], it is possible that the model of Anderson et al. [14] now requires extensive modification. The presence of the ocean would imply that there is no intimate mixture of rock and ice between a rock/metal core and ice crust as proposed by [14]. Instead, there would be sufficient radiogenic heating to allow more complete ice-rock separation early in Callisto's history. Assuming the radioisotopes are concentrated in the silicate component of the satellite, this ocean would most likely be located at the base of the ice crust nearest the heat source that created it.

However, there is still the question as to why the ocean remains in a liquid form within Callisto today. As mentioned earlier, tidal heating cannot have sustained the ocean's existence, since Callisto has not been involved in any orbital resonances with the other satellites. Accretional heating and heating from short-lived radioisotopes would only keep an ocean in a liquid state early in Callisto's history and then would cease to be effective. The presence of a large amount of long-lived radio-isotopes (and a correspondingly smaller amount of other heavy elements) in Callisto's silicate component could actively maintain an ocean today, although this is admittedly unlikely unless there was a significantly higher proportion of such isotopes concentrated within the proto-Jovian nebula from which the satellites formed and if this is the case, then there are significant implications for the thermal evolution of the other Galilean satellites. Another possibility is that the ocean is no longer being actively heated (and hence is ancient), but rather is simply not being cooled efficiently, possibly because of highly inefficient heat loss mechanisms within the interior of Callisto.

Clearly, much investigation remains to be done into this topic but the evidence suggests that an ocean has to exist today deep below Callisto's surface. This can only be maintained if there is some previously unrecognised internal heat source within the satellite.

Synthesis and Implications for Ganymede: Ganymede and Callisto have often been considered as 'sister worlds' - they have similar sizes, and bulk compositions and densities - yet they have evolved on very divergent paths: Ganymede's surface is divided into pseudocircular blocks of ancient, heavily cratered Dark Terrain and bands of Bright Terrain with pervasive linear ridges and troughs throughout that obviously formed as a result of some kind of prolonged tectonic activity. In contrast, Callisto's surface shows no indication of any tectonic activity whatsoever, instead bearing the scars of impacts apparently dating back to its formation.

Given the similarities in the size and densities of these satellites, it is likely that Ganymede and Callisto were very similar worlds very early in their histories and that something happened that caused them to evolve on separate paths. The obvious difference is that Ganymede became involved in the Laplace-Like Resonances proposed by Showman et al. [1, 2] and that the tidal dissipation caused by this created the Bright Terrain. Callisto did not become involved in any orbital resonances due to its remoteness from the inner Jovian system and thus it was not subjected to the extensive resurfacing that Gany-

mede suffered.

Since the two worlds are similar, and assuming the reasoning presented here is valid, it does not seem unreasonable to assume that Ganymede possesses the same mysterious internal heat source that maintains the ocean within Callisto today. If this heat source was active from the formation of both satellites, an ocean would certainly have had to be present within Ganymede before it entered the Laplace-Like Resonance. This extra heat source would most likely completely rule out the possibility of any kind of thermal runaway within Ganymede, and what is more it would act to keep the ocean liquid until today. Thus, not only is the possibility of a global expansion through the melting of high pressure ice phases removed (since they most likely would never have had a chance to form in the first place), but the continued internal heating later in Ganymede's history would offset the cooling and freezing of the ocean (and prevent the global expansion that would result from this) after the satellite leaves the LLR and enters the Laplace Resonance observed today.

It is therefore possible, given the realistic orbital and thermal evolution models of [1, 2, 5] and the reasoning presented here, that global expansion of Ganymede's crust is no longer necessary to explain the Bright Terrain/Dark Terrain dichotomy. Preliminary examination of Galileo images of Ganymede also indicates that the prime reason for invoking global expansion in the first place - the apparent lack of compressional features on Ganymede's surface - may no longer be valid. Evidence for possible compressional features has been observed in the Northern Marius Regio area of Ganymede, imaged during the G8 fly-by (Galileo image c0394517800) and is noted by [15]. Within this area, compression may have occurred to form the axial ridges within Byblus Sulcus, and may also have formed some of the arcuate ridges within Nippur Sulcus in the northern part of the image.

Conclusions: The existence of a liquid ocean within Callisto maintained by a previously unrecognised heat source may have important implications for the internal and surface evolution of Ganymede and the other Galilean satellites. This additional heat source may also be present in Io and Europa unless it is somehow only associated with larger accumulations of ice such as those found in the two outer Galileans. Most significantly though, the similarity of the bulk properties of Callisto and Ganymede makes it likely that the heat source maintaining the ocean in a liquid state in Callisto is also present within Ganymede. If this is so, mechanisms for global expansion of Ganymede proposed to explain the formation of Bright Terrain may no longer be valid since the formation of high pressure ice phases and/or the melting of Ice I would be precluded by the higher heat flow that would instead result in the formation and maintenance of an ocean within Ganymede. It may be possible for Galileo to detect Ganymede's ocean if an induced magnetic field signature can be separated from that of the internal dynamo.

Initial examination of Galileo images of Ganymede reveals possible compressional features within the Bright Terrain, throwing doubt on the validity of one of the cornerstone arguments for global expansion; that of the apparently complete lack of such features on the surface. If this element of doubt exists, it would be prudent to re-examine the surface of Ganymede in case other compressional features have been mis-identified. Furthermore, mechanisms for the formation of Bright Terrain would have to be re-evaluated if global expansion is no longer an option.

References: [1] Showman & Malhotra (1997) *Icarus* **127**, 93-111; [2] Showman et al. (1997) *Icarus* **129**, 367-383; [3] Anderson et al. (1996) *Nature* **384**, 541-543; [4] Kivelson et al. (1996) *Nature* **384**, 537-541; [5] Malhotra (1991) *Icarus* **94**, 399-412; [6] Khurana et al. (1998) *Nature* **395**, 777-780; [7] Kivelson et al. (1998) *JGR-Planets* **103**, E9, 19963-19972; [8] Peale et al. (1979) *Science* **203**, 892-894; [9] Ross & Schubert (1987) *Nature* **325**, 133-134; [10] Squyres (1980) *GRL* **7**, 593-596; [11] Shoemaker & Passey (1979) *EOS* **60**, 869; [12] Shoemaker et al. (1982) in *Satellites of Jupiter*, U.of Ariz. press, 435-520; [13] Kirk & Stevenson (1987) *Icarus* **69**, 91-134; [14] Anderson et al. (1998) *Science* **280**, 1573-1576; [15] Thomas et al. (1998) *LPSC XIX poster*, available at <http://www.es.lancs.ac.uk/es/research/psrg/posters/1998/ct-post.htm>

MORPHOLOGY OF BYBLUS SULCUS, GANYMEDE FROM GALILEO SSI DATA. C. Thomas^{1,2}, J. W. Head¹, and the Galileo SSI team. ¹ Dept. of Geological Sciences, Box 1846, Brown University, Providence, RI 02912, USA; ² also at Lancaster University, Lancaster LA1 4YQ, England (c.thomas1@lancaster.ac.uk).

Introduction: Byblus Sulcus is a bright groove lane identified in Voyager 2 images, located at 39°N 201°W in northern Marius Regio on Ganymede. It was imaged at high resolution (86 m/pxl) and high sun angle on September 6th 1996, during the G2 orbit of the Galileo Orbiter. This region was targeted in order to provide high resolution images of an impact feature named Nergal with a distinctive dark/bright ejecta blanket - also in the imaged region is a roughly east-west trending groove lane named Akitu Sulcus. Another (near-terminator) image of north Marius Regio containing this area was taken at a 940 m/pxl resolution during the later G8 orbit to provide regional context for the G2 image; this also provides useful topographic information. This region was mapped previously by Murchie and Head [1] on a 1:5,000,000 scale using Voyager images as a base. They defined three geological units in this area - dark furrowed terrain (df) containing eastward-trending furrows, light grooved material (lg) consisting of high albedo sets of conspicuous grooves, and bright or partly degraded craters (c1,c2) [1]. A preliminary analysis of this area based only on G2 Galileo data presented by Head et al. [2] is expanded here.

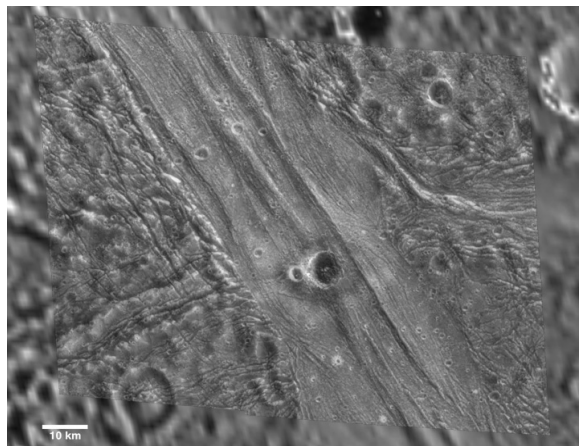


Figure 1: 'Merged' G2 (high sun)/G8 (low sun) Galileo SSI mosaic of the Byblus Sulcus region on Ganymede.

Data: For this analysis the G2 images were mosaicked, projected onto the G8 context image and reprojected as a Lambert equal area projection centred at 39°N 201°W. Layering both images over each other (see Figure 1) proved to be a very powerful yet simple aid to image interpretation - by rendering the G2 image partially transparent over the G8 image, it was possible to directly correlate albedo features in the high sun G2 image with topography observed in G8.

G8 Morphology: The overall shape of Byblus Sulcus is lenticular, thinning to the north and south and widest (~ 30 km across) in the area imaged at high resolution during G2. The southern apex of the sulcus ends in a deep crack that shallows and curves eastwards at its termination, and its albedo at this resolution is higher than that of the surrounding dark terrain. Ridges and scarps run parallel to but are not centred along the axis of the sulcus - these have a wavelength of approximately 10 km that can be readily observed in both G2 and G8 images using Fourier transform analysis [3]. This topography is especially visible in the northern half of Byblus (which includes the G2 image) - in the southern half the topography is more subdued, consisting of multiple shorter wavelength parallel ridges with comparatively lower relief. Nergal crater is distinctly visible in G8, but due to the low-sun imaging geometry no albedo differences between its environs and more distant bright terrain can be distinguished.

Two other small groove lanes trending roughly E-W and NE-SW are cut by Byblus Sulcus. Preliminary analysis suggests that they may be displaced by a 60 km sinistral shear across Byblus, supporting an observation noted by Murchie & Head [4]. Several other lineaments (e.g. furrows) along its length also appear displaced in this manner. These features are readily identifiable on either side of Byblus by their similar (and in the case of the groove lanes, unique) morphologies. This observation is investigated further in this study.

G2 Morphology: The G2 mosaic is divided here into three main areas based on the Voyager images - highly tectonised dark terrain in the west, the morphologically distinct Byblus Sulcus (trending N145E) in the central third of the image, and a second region of dark terrain in the east that contains the westernmost portion of Akitu Sulcus.

Western Dark Terrain (WDT): This region is characterised by a low albedo background surface interspersed with bright rounded higher-albedo hills several kilometres across, and two orthogonal sets of dark lineaments (fractures and troughs) that divide the terrain into polygonal units a few kilometres across. One set of these lineaments trends roughly parallel to the groove lane (N145-135E) and cross-cuts the other trend (N65E), which is itself sharply cut by Byblus Sulcus. Although the NW trend continues all the way along the image, the lineaments appear to be more densely packed in the northern half of the image nearer the sulcus, and some of the major lineaments curve in towards it near the centre of the image.

The N65E trend is centred around three large sub-parallel ridges separated by two troughs, with smaller scale sinuous dark and bright lineaments run roughly parallel and through them. The topographic relief is difficult to discern using the G2 image alone, and was distinguished using the G8 low-sun image. While these features can be separated at high resolution, at lower resolution they can be grouped as a single feature and were classed as such by Murchie et al. [5], who interpreted them as a single System I furrow.

Byblus Sulcus (BS): The central N145E band in the G2 image is comprised of sets of parallel or subparallel densely packed flat-topped and 'knobbly' ridges approximately 1-3 km wide and one kilometre high. Individual ridges frequently widen out or thin along their length, to the point of becoming wide plateaux up to 5 km across or small linear knobs a kilometre or so across. Like other groove lanes on Ganymede, at lower (i.e. G8, Voyager) resolutions Byblus is distinguishable from the surrounding dark terrain by its higher relative brightness. At G2 resolution however, a significant contributor to the brightness of the sulcus appears to be local features such as the bright ejecta blankets of small craters, high-albedo material on sunward facing slopes and ridges, and small-scale surface texture rather than the actual base albedo of the sulcus material itself which instead appears not too dissimilar to that of the dark terrain.

The overall trend of the ridges within Byblus is unidirectional, parallel to the axis of the sulcus; however, closer examination reveals that ridges are oriented along smaller curvilinear/arcuate sub-trends that lie concordant to the main trend between extremes of N5-130E, with most lying between N145-150E. Of particular note is a lenticular region on the northeastern border of the sulcus in which ridges bend around a straight central axis that runs through its length and is parallel to the nearby Byblus/Eastern Dark Terrain boundary. The borders of several of these sub-trends frequently correspond to major topographic changes (usually west-facing scarps) running along the axis of the sulcus. In addition, these small-scale ridges are clearly superimposed on both the flat regions and the slopes of the large-scale G8 topography. Of particular note are two distinct broad high-relief ridges approximately ten kilometres apart that run along the strike of Byblus just east of its axis, that stand out visually only in the G8 image.

Eastern Dark Terrain (EDT): Tectonism is more complex in this part of the dark terrain - the 'furrow' visible in the Western Dark Terrain does not appear to correspond to any features visible in the east. A densely-packed set of dark lineaments (fractures) and bright lineaments (ridges) abuts against the northeastern border of Byblus near the lenticular region described previously. The orientation of these lineaments rotates from N145E (parallel to the Byblus trend) to N90E, and the area covered by them widens towards the central eastern part of the image; terrain is highly disrupted in this zone and some large craters near the Byblus are heavily tectonised. This region corresponds to Akitu Sulcus. To the north of this sulcus, a set of arcuate fractures defines a semicircular region that is comparatively fracture-free at G2 resolution.

Dark Terrain impact features: Craters in the dark terrain range in size from ~500 m to 12 km in diameter and can be found in varying states of degradation. The north-facing rims are generally the brightest parts of these craters (even though solar illumination is from the southeast with the sun 37° above the horizon), and ejecta are not generally obvious due to low albedo contrast. Dark terrain craters

range from those with a morphologically fresh appearance and sharply defined bright rims to degraded craters with poorly defined circumferences and shallow bowl-shaped interiors (often with more recent craters superposed) and heavily tectonised craters modified by fracturing.

Bright Terrain impact features: The craters in Byblus Sulcus range from ~300 m to 8 km in diameter. All the visible craters are fresh, with sharp rims; there are no degraded or partially destroyed (and by implication 'old') craters visible in this area at all. The morphology of these small fresh craters strongly resemble those in the Dark Terrain - in both instances the crater outlines are generally asymmetrical with most having a pronounced triangular or square plan. Bright ejecta is also visible around some of the craters here.

The main features of note in Byblus Sulcus are the two craters in the centre of the G2 image surrounded by dark lobate structures and an irregular bright ejecta blanket beyond. No secondary craters have been unambiguously identified; either they never formed, are below the limit of resolution, or they have been removed or covered by some unrecognised process.

The larger crater (Nergal) is ~8 km in diameter with a polygonal rim, dark floor, and a broad cruciform central peak structure. The eastern rim is highly modified and appears to follow the trend of impinging lineaments in Byblus - it appears that it has collapsed eastwards into the sulcus and formed a wide (albeit short in radial extent - just over a kilometre in length) debris fan. Lineaments can also be seen continuing through the crater, modifying the eastern crater floor and central peak structure; these are not as apparent in the western part of the crater.

The smaller (unnamed) crater to its west is ~3 km in diameter with a circular bowl-shaped appearance (though it does have a small central peak). It is not modified in any way by the lineament structure in Byblus; indeed, a pronounced bright lineament stops at the outer boundary of the southeastern wall of this crater.

These craters are both surrounded by thick dark lobate structures that are in places outlined by what appears to be a brighter levee-like structure, probably emplaced as a consequence of the impacts; close examination suggests there may be multiple lobe sets, though it is not unambiguous which ones are associated with which crater.

Both craters are in turn surrounded by an asymmetric bright deposit that appears confined to the Bright Terrain only - the eastern border appears to follow the Byblus/EDT boundary. The outline of the deposit is highly irregular and does not correspond to that of the dark lobes immediately surrounding the craters - indeed, there is a thin triangular extension of this deposit extending northwards along one of the major G8 ridges in the eastern portion of Byblus. A small crater to the NW of Nergal may contribute in part to this ejecta blanket.

The lineaments in the underlying sulcus appear to continue through Nergal itself (and its lobate ejecta) but not through the unnamed smaller crater - however, the smaller crater is located in a smoother, comparatively lineament-free area that continues approximately 40 km either way along the strike of Byblus. Either the ridges in this area have been subdued somehow (perhaps by cryovolcanism) or they never formed here.

Fracture trends: Dark lineament (fracture) trends were measured in both the Western and Eastern Dark Terrains in the G2 image (these were not visible at the G8 resolution). The trends in each region are shown in Figure 2 below, with fractures binned at five-degree intervals and orientations measured clockwise (eastwards) from north.

The histograms suggest a marked difference in the orientation of fractures on either side of Byblus Sulcus. The WDT contains two distinctly separable sets of lineaments; one between N41-100E associated with the System I furrow and the other between N110-165E corresponding to the fractures parallel to Byblus. The EDT shows a different, more dispersed set of orientations that are not clearly divisible into two separate groups; however, both Dark Terrains appear to contain a preponderance of fractures oriented between N131-140E.

Conclusions and further work: The dissimilarity in dark lineament orientation trends, surface morphologies and textural character on either side of Byblus Sulcus can most easily be explained if one assumes that features on either side are not directly correlative as they stand. Furthermore, the similarity between the orientations and morphologies of surface features displaced along Byblus suggests that the present configuration of the terrains may not be the original. Preliminary work suggests that this area may have been subject to shear; the appearance of this region today can be most simply explained by a 60 km displacement along a sinistral shear fault running approximately along the axis of Byblus.

There is still much work to be done to investigate this hypothesis fully - for example, the presence of shear accommodation zones in other parts of north Marius Regio has yet to be confirmed, although an area of interlinking lenticular features and sinuous groove lanes in the dark terrain to the southeast of Byblus (also imaged by Galileo at 188m/pxl resolution) has been tentatively identified as a potential candidate area and is currently being investigated. It is also not yet clear how the shear could be accommodated within Byblus Sulcus itself, although the curvilinear and lenticular sub-trends of the ridges within it may represent shear structures. Despite these reservations, the shear hypothesis most readily explains the apparent misalignment of several features on a regional (G8) scale and the disparity in lineament orientations and surface morphologies in the dark terrain on a local (G2) scale.

References: [1] S. L. Murchie & J. W. Head (1989), Geological map of the Philus Sulcus quadrangle of Ganymede, USGS Misc. Geol. Investigation, Map I-1966; [2] J. W. Head *et al.* (1997) LPSC 28, 539-540; [3] J. G. Patel *et al.*, Wavelengths of Ganymede Grooved Terrain determined from Fourier Analysis of Galileo Images, LPSC 29, 1998; [4] S. L. Murchie & J. W. Head (1988), JGR 93: pp. 8795-8824; [5] S. L. Murchie *et al.* (1990), JGR 95: pp. 10743-10768.

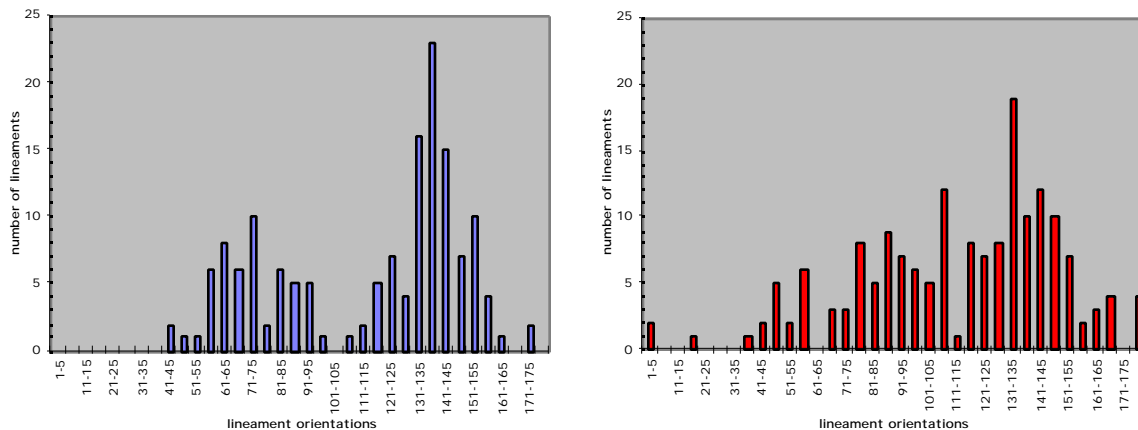


Figure 2: Dark Lineament Orientations in the Western (left) and Eastern (Right) Dark Terrains.

Is Tyre Macula an Ice Cauldron?; Constantine Thomas, Environmental Science Division, I.E.B.S., Lancaster University, Lancaster LA1 4YQ, England, c.thomas1@lancaster.ac.uk

Tyre Macula is a large, dark circular feature on Europa, classified first by Lucchita and Soderblom [1] as a “Class 2” impact feature similar in nature to the crater palimpsests on Ganymede. It lies near the junction of several dark lineaments, and exhibits several features that throw doubt on an impact origin. Here I propose that Tyre Macula is actually a large Ice Cauldron - a feature created by local ice subsidence as a result of subsurface geothermal heating on Europa.

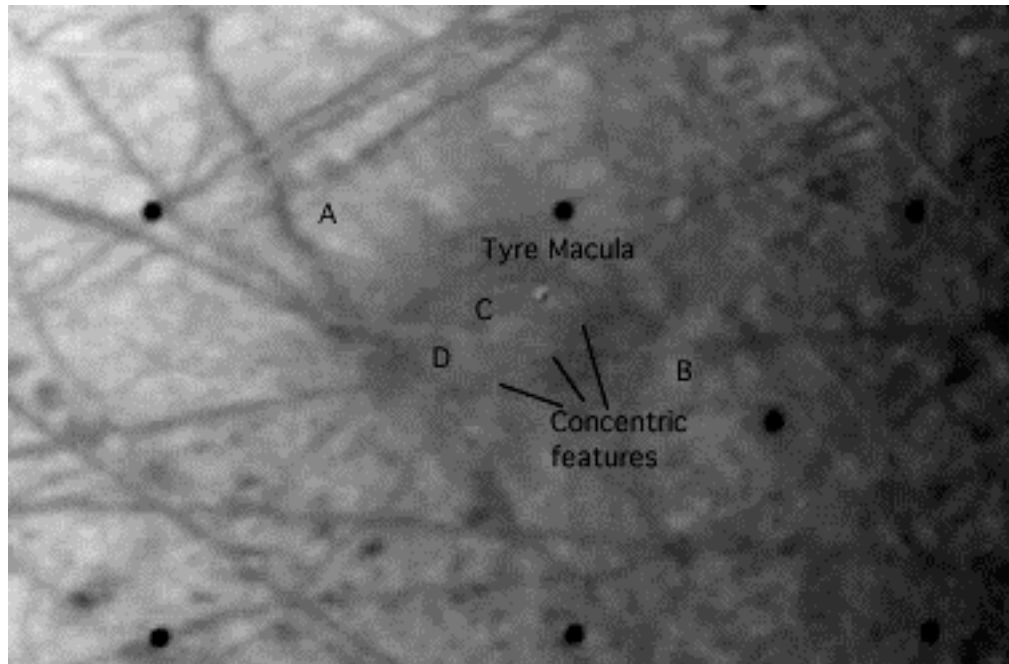


Figure 1: Tyre Macula (Voyager image c2064910, Magnification x2, Histogram Stretch)

Tyre Macula is the dark circular feature shown in Figure 1 and is approximately 120 km in diameter. It is cut by a wide dark ridge (A) striking north-south and appears to overlie another dark lineament (B) that strikes from east to west. A circular structure (C) is visible in the centre that appears (based on brightness variations within it) to be a bowl-shaped depression approximately 20 km in diameter - the small circular ‘feature’ to the north-east of this is actually an imaging artefact and not a geological structure. A small bright lineament (D) crosses Tyre Macula from west to east, and may be related in origin to lineament B. The time sequence to be interpreted is therefore that Tyre is intermediate in age between Ridge A and Lineaments B and D. Lucchita and Soderblom [1] also identified concentric structures within Tyre Macula that are visible and labelled in Figure 1. There appear to be three main regions comprising the feature - a slightly brighter central region 60 km in diameter is surrounded by a sharply defined darker ring that describes the accepted external circumference of Tyre up to a diameter of 120 km, and a tenuous fuzzy halo that extends beyond this to a diameter of 190 km.

The morphology of Tyre Macula is distinctly unlike that of the Ganymedian palimpsests to which it is compared by Lucchita and Soderblom - those palimpsests do

not possess central bowls, there is more internal structure visible in Tyre, and the feature itself is much more sharply defined. These differences lead me to the conclusion that Tyre Macula is not a palimpsest, while the features described above imply that it was formed by some hitherto unrecognised endogenic process.

The appearance of Tyre Macula is similar to that of **Ice Cauldrons** found in terrestrial domains that are both volcanic and ice-covered, except on a much larger scale. On Earth, Ice Cauldrons such as those located in Iceland vary in size from several hundred metres to a few (< 10) km across and are up to 200 metres deep. While no definite correlations between diameter, depth and thickness of ice sheet have been noted so far, the larger ones do appear to be deeper and are situated on thicker glaciers.

Ice Cauldrons are large circular features found on some glaciers that overlie volcanic terrain. They vary in appearance, but most consist of a central unfractured depression surrounded by an extensive ring of concentric and eccentric fractures, the separation of which increases radially with distance from the centre [2]. At least some Ice Cauldrons on Earth are temporary features, disappearing as a result of ice creep and snow cover.

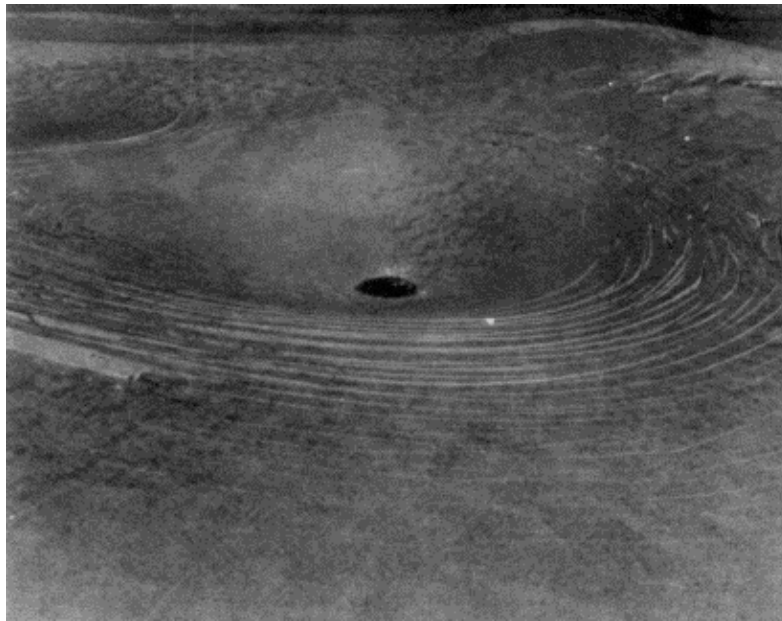


Figure 2: An Ice Cauldron in Iceland (C.A. Wood, 1980 [2])

On Earth, Ice Cauldrons such as the one shown in Figure 2 form through subsidence caused by subglacial heating. Ice is melted by localised geothermal heating to form a dome-shaped reservoir of water at the base of the glacier. Eventually, the water pressure exceeds the ice overburden pressure and the water bursts forth from under the glacier, causing a glacial flood. The glacier then sags rapidly into the void left by the water, creating concentric fractures in the ice through sudden brittle deformation [2]. No examples have been noted on Earth where the water has been extruded via the fractures - it always escapes from elsewhere along the base of the glacier - though in Figure 2 a small lake is visible in the centre of the structure which formed as the sinking glacier intersected the water table.

Europa is believed to have suffered extensive tidal heating as a result of the orbital evolution of the Galilean satellites. Most current (pre-Galileo) models assume the presence of a thick ice layer on the surface overlying a silicate crust, with the possibility of a transient or local liquid water ocean maintained at the boundary by tidal heating. Here however, I assume that no subglacial ocean was present at the time Tyre Macula formed, so that the ice and silicates would be in direct contact in this region.

I propose that heating from igneous intrusions or a volcanic eruption beneath the ice could have led to the formation of an Ice Cauldron at Tyre Macula by the mechanisms described earlier. Since there is no lateral edge to the planet-wide ice sheet, I suggest that a fracture was created in the ice above the pressurised reservoir of meltwater that allowed the water to escape at the surface in the centre of what would become Tyre Macula; as the water escaped from the ice/silicate interface, the overlying ice collapsed to form an Ice Cauldron. The darker albedo of Tyre Macula would therefore be the result of 'dirty water' escaping to the surface and covering the area.

The sequence of events would occur in this scenario as described here: A meltwater reservoir was created at the base of the ice layer by geothermal heating in the silicate crust. When the fluid pressure exceeded the ice overburden pressure, a fracture propagated upwards to form a vent above the reservoir and allowed the water to break through to the surface. Water flowed radially outwards from the vent until the supply was exhausted, whereupon the diameter covered by the flow was approximately 120 km. Assuming a flow thickness of about 30 m, this requires a volume $\sim 340 \text{ km}^3$ of erupted water, corresponding to a minimum reservoir radius (assuming a hemispherical reservoir) of just under 5.5 km. The central region then rapidly collapsed to create the central bowl. The reservoir is similar in scale to the observed radius of what I interpret to be the central bowl-shaped depression; transmission of the stresses through a thick ice sheet could explain the difference in size between the reservoir and the bowl. However, I suggest that the attendant wreath of fractures only extends to the edge of the bright central region at a radius of 30 km, since fracturing would expose brighter ice below the 'dirty water' veneer and thus increase the local albedo. Finally, the water froze as it flowed over the surface, and the resulting ice frost settled around the exterior to form the fuzzy halo around the entire structure.

Acknowledgements: I would like to thank Prof. Lionel Wilson for his comments on this work and Prof. Charles Wood who kindly granted permission for use of the Ice Cauldron photograph from his 1980 paper.

References: [1] Lucchita B. K. & Soderblom L.A., *Satellites of Jupiter*, 521, 1982. [2] Wood C.A., Ice Cauldrons and Basins in Iceland and on Callisto, *Conference on Multi-Ring Basins (Formation and Evolution)*, 118-120, 1980.

APPENDIX 3: Commensurability Charts for orbital evolution determined in Chapter 4.

Table C.1: Chart showing commensurabilities for $R_I = 2.5 R_J$

t (100 Ma)	Ratio	Io/Europa	Ratio	Io/Ganymede	Ratio	Io/Callisto	Ratio	Europa/Ganymede	Ratio	Europa/Callisto	Ratio	Ganymede/Callisto
4600	2:1 --->	0.498191	4:1 --->	0.247299		0.106008	2:1 --->	0.496395		0.212786	7:3 -->	0.428664
4500	2:1 --->	0.496	4:1 --->	0.246	10:1 --->	0.105	2:1 --->	0.496		0.213	7:3 -->	0.429
4400		0.493	4:1 --->	0.245	10:1 --->	0.105	2:1 --->	0.496		0.213	7:3 -->	0.429
4300		0.491		0.244	10:1 --->	0.104	2:1 --->	0.496		0.213	7:3 -->	0.429
4200		0.488		0.242	10:1 --->	0.104	2:1 --->	0.496		0.213	7:3 -->	0.429
4100		0.486		0.241	10:1 --->	0.103	2:1 --->	0.496		0.213	7:3 -->	0.429
4000		0.483		0.240	10:1 --->	0.103	2:1 --->	0.496		0.213	7:3 -->	0.429
3900		0.480		0.238	10:1 --->	0.102	2:1 --->	0.496		0.213	7:3 -->	0.429
3800		0.477		0.237	10:1 --->	0.101	2:1 --->	0.496		0.213	7:3 -->	0.429
3700		0.474		0.235	10:1 --->	0.101	2:1 --->	0.496		0.213	7:3 -->	0.429
3600		0.472		0.234	10:1 --->	0.100	2:1 --->	0.496		0.213	7:3 -->	0.429
3500		0.469		0.232	10:1 --->	0.100	2:1 --->	0.496		0.212	7:3 -->	0.429
3400		0.465		0.231	10:1 --->	0.099	2:1 --->	0.496		0.212	7:3 -->	0.429
3300		0.462		0.229	10:1 --->	0.098	2:1 --->	0.496		0.212	7:3 -->	0.429
3200		0.459		0.228	10:1 --->	0.098	2:1 --->	0.496		0.212	7:3 -->	0.429
3100		0.456		0.226	10:1 --->	0.097	2:1 --->	0.496		0.212	7:3 -->	0.429
3000		0.453		0.224	10:1 --->	0.096	2:1 --->	0.496		0.212	7:3 -->	0.429
2900		0.449		0.223	10:1 --->	0.095	2:1 --->	0.495		0.212	7:3 -->	0.429
2800		0.446		0.221	10:1 --->	0.095	2:1 --->	0.495		0.212	7:3 -->	0.429
2700		0.442		0.219		0.094	2:1 --->	0.495		0.212	7:3 -->	0.429
2600		0.438		0.217		0.093	2:1 --->	0.495		0.212	7:3 -->	0.428
2500		0.434		0.215		0.092	2:1 --->	0.495		0.212	7:3 -->	0.428
2400		0.430		0.213		0.091	2:1 --->	0.495		0.212	7:3 -->	0.428
2300		0.426		0.211		0.090	2:1 --->	0.495		0.212	7:3 -->	0.428
2200		0.422		0.209		0.090	2:1 --->	0.495		0.212	7:3 -->	0.428

2100		0.418		0.207		0.089	2:1 --->	0.495		0.212	7:3 -->	0.428
2000		0.413	5:1 --->	0.204		0.088	2:1 --->	0.495		0.212	7:3 -->	0.428
1900		0.408	5:1 --->	0.202		0.087	2:1 --->	0.495		0.212	7:3 -->	0.428
1800		0.403	5:1 --->	0.200		0.085	2:1 --->	0.495		0.212	7:3 -->	0.428
1700		0.398	5:1 --->	0.197		0.084	2:1 --->	0.495		0.212	7:3 -->	0.428
1600		0.393		0.194		0.083	2:1 --->	0.495		0.212	7:3 -->	0.428
1500		0.387		0.191		0.082	2:1 --->	0.495		0.212	7:3 -->	0.428
1400		0.381		0.188		0.081	2:1 --->	0.495		0.212	7:3 -->	0.428
1300		0.375		0.185		0.079	2:1 --->	0.495		0.212	7:3 -->	0.428
1200		0.368		0.182		0.078		0.494		0.212	7:3 -->	0.428
1100		0.361		0.178		0.076		0.494		0.212	7:3 -->	0.428
1000		0.353		0.175		0.075		0.494		0.212	7:3 -->	0.428
900		0.345		0.170		0.073		0.494		0.212	7:3 -->	0.428
800	3:1 --->	0.336		0.166		0.071		0.494		0.212	7:3 -->	0.428
700		0.326		0.161		0.069		0.494		0.212	7:3 -->	0.428
600		0.315		0.156		0.067		0.494		0.212	7:3 -->	0.428
500		0.302		0.149		0.064		0.494		0.212	7:3 -->	0.428
400		0.288		0.142		0.061		0.494		0.212	7:3 -->	0.428
300		0.270		0.133		0.057		0.494		0.212	7:3 -->	0.428
200		0.248		0.122		0.052		0.494		0.212	7:3 -->	0.428
100		0.215		0.106		0.045		0.494		0.212	7:3 -->	0.428
0		0.138		0.068		0.029		0.494		0.211	7:3 -->	0.428

Table C.2: Chart showing commensurabilities for $R_i = 3.85 R_J$

t (100 Ma)	Ratio	Io/Europa	Ratio	Io/Ganymede	Ratio	Io/Callisto	Ratio	Europa/Ganymede	Ratio	Europa/Callisto	Ratio	Ganymede/Callisto
4600	2:1 --->	0.498191	4:1 --->	0.247299		0.106008	2:1 --->	0.496395		0.212786	7:3 -->	0.428664
4500	2:1 --->	0.496	4:1 --->	0.246		0.106	2:1 --->	0.496		0.213	7:3 -->	0.429
4400		0.494	4:1 --->	0.245	10:1 --->	0.105	2:1 --->	0.496		0.213	7:3 -->	0.429
4300		0.491		0.244	10:1 --->	0.104	2:1 --->	0.496		0.213	7:3 -->	0.429
4200		0.489		0.243	10:1 --->	0.104	2:1 --->	0.496		0.213	7:3 -->	0.429
4100		0.486		0.241	10:1 --->	0.103	2:1 --->	0.496		0.213	7:3 -->	0.429
4000		0.484		0.240	10:1 --->	0.103	2:1 --->	0.496		0.213	7:3 -->	0.429
3900		0.481		0.239	10:1 --->	0.102	2:1 --->	0.496		0.213	7:3 -->	0.429
3800		0.479		0.237	10:1 --->	0.102	2:1 --->	0.496		0.213	7:3 -->	0.429
3700		0.476		0.236	10:1 --->	0.101	2:1 --->	0.496		0.213	7:3 -->	0.429
3600		0.473		0.235	10:1 --->	0.101	2:1 --->	0.496		0.213	7:3 -->	0.429
3500		0.470		0.233	10:1 --->	0.100	2:1 --->	0.496		0.212	7:3 -->	0.429
3400		0.468		0.232	10:1 --->	0.099	2:1 --->	0.496		0.212	7:3 -->	0.429
3300		0.465		0.230	10:1 --->	0.099	2:1 --->	0.496		0.212	7:3 -->	0.429
3200		0.462		0.229	10:1 --->	0.098	2:1 --->	0.496		0.212	7:3 -->	0.429
3100		0.459		0.227	10:1 --->	0.097	2:1 --->	0.496		0.212	7:3 -->	0.429
3000		0.456		0.226	10:1 --->	0.097	2:1 --->	0.496		0.212	7:3 -->	0.429
2900		0.453		0.224	10:1 --->	0.096	2:1 --->	0.496		0.212	7:3 -->	0.429
2800		0.449		0.223	10:1 --->	0.095	2:1 --->	0.495		0.212	7:3 -->	0.429
2700		0.446		0.221	10:1 --->	0.095	2:1 --->	0.495		0.212	7:3 -->	0.429
2600		0.443		0.219		0.094	2:1 --->	0.495		0.212	7:3 -->	0.429
2500		0.439		0.217		0.093	2:1 --->	0.495		0.212	7:3 -->	0.429
2400		0.435		0.216		0.092	2:1 --->	0.495		0.212	7:3 -->	0.428
2300		0.432		0.214		0.092	2:1 --->	0.495		0.212	7:3 -->	0.428
2200		0.428		0.212		0.091	2:1 --->	0.495		0.212	7:3 -->	0.428
2100		0.424		0.210		0.090	2:1 --->	0.495		0.212	7:3 -->	0.428
2000		0.420		0.208		0.089	2:1 --->	0.495		0.212	7:3 -->	0.428

1900		0.416		0.206		0.088	2:1 --->	0.495		0.212	7:3 -->	0.428
1800		0.411	5:1 --->	0.204		0.087	2:1 --->	0.495		0.212	7:3 -->	0.428
1700		0.407	5:1 --->	0.201		0.086	2:1 --->	0.495		0.212	7:3 -->	0.428
1600		0.402	5:1 --->	0.199		0.085	2:1 --->	0.495		0.212	7:3 -->	0.428
1500		0.397	5:1 --->	0.196		0.084	2:1 --->	0.495		0.212	7:3 -->	0.428
1400		0.392		0.194		0.083	2:1 --->	0.495		0.212	7:3 -->	0.428
1300		0.387		0.191		0.082	2:1 --->	0.495		0.212	7:3 -->	0.428
1200		0.381		0.188		0.081	2:1 --->	0.495		0.212	7:3 -->	0.428
1100		0.375		0.185		0.079	2:1 --->	0.495		0.212	7:3 -->	0.428
1000		0.369		0.182		0.078		0.494		0.212	7:3 -->	0.428
900		0.362		0.179		0.077		0.494		0.212	7:3 -->	0.428
800		0.355		0.175		0.075		0.494		0.212	7:3 -->	0.428
700		0.347		0.172		0.074		0.494		0.212	7:3 -->	0.428
600		0.339		0.168		0.072		0.494		0.212	7:3 -->	0.428
500	3:1 --->	0.330		0.163		0.070		0.494		0.212	7:3 -->	0.428
400		0.320		0.158		0.068		0.494		0.212	7:3 -->	0.428
300		0.309		0.153		0.065		0.494		0.212	7:3 -->	0.428
200		0.296		0.146		0.063		0.494		0.212	7:3 -->	0.428
100		0.282		0.139		0.060		0.494		0.212	7:3 -->	0.428
0		0.264		0.130		0.056		0.494		0.212	7:3 -->	0.428

Table C.3: Chart showing commensurabilities for $R_i = 5 R_J$

t (100 Ma)	Ratio	Io/Europa	Ratio	Io/Ganymede	Ratio	Io/Callisto	Ratio	Europa/Ganymede	Ratio	Europa/Callisto	Ratio	Ganymede/Callisto
4600	2:1 --->	0.498191	4:1 --->	0.247299		0.106008	2:1 --->	0.496395		0.212786	7:3 -->	0.428664
4500	2:1 --->	0.497	4:1 --->	0.246		0.106	2:1 --->	0.496		0.213	7:3 -->	0.429
4400	2:1 --->	0.495	4:1 --->	0.246	10:1 --->	0.105	2:1 --->	0.496		0.213	7:3 -->	0.429
4300		0.493	4:1 --->	0.245	10:1 --->	0.105	2:1 --->	0.496		0.213	7:3 -->	0.429
4200		0.492		0.244	10:1 --->	0.105	2:1 --->	0.496		0.213	7:3 -->	0.429
4100		0.490		0.243	10:1 --->	0.104	2:1 --->	0.496		0.213	7:3 -->	0.429
4000		0.488		0.242	10:1 --->	0.104	2:1 --->	0.496		0.213	7:3 -->	0.429
3900		0.486		0.241	10:1 --->	0.103	2:1 --->	0.496		0.213	7:3 -->	0.429
3800		0.485		0.240	10:1 --->	0.103	2:1 --->	0.496		0.213	7:3 -->	0.429
3700		0.483		0.240	10:1 --->	0.103	2:1 --->	0.496		0.213	7:3 -->	0.429
3600		0.481		0.239	10:1 --->	0.102	2:1 --->	0.496		0.213	7:3 -->	0.429
3500		0.479		0.238	10:1 --->	0.102	2:1 --->	0.496		0.213	7:3 -->	0.429
3400		0.477		0.237	10:1 --->	0.101	2:1 --->	0.496		0.213	7:3 -->	0.429
3300		0.476		0.236	10:1 --->	0.101	2:1 --->	0.496		0.213	7:3 -->	0.429
3200		0.474		0.235	10:1 --->	0.101	2:1 --->	0.496		0.213	7:3 -->	0.429
3100		0.472		0.234	10:1 --->	0.100	2:1 --->	0.496		0.213	7:3 -->	0.429
3000		0.470		0.233	10:1 --->	0.100	2:1 --->	0.496		0.212	7:3 -->	0.429
2900		0.468		0.232	10:1 --->	0.099	2:1 --->	0.496		0.212	7:3 -->	0.429
2800		0.466		0.231	10:1 --->	0.099	2:1 --->	0.496		0.212	7:3 -->	0.429
2700		0.464		0.230	10:1 --->	0.098	2:1 --->	0.496		0.212	7:3 -->	0.429
2600		0.462		0.229	10:1 --->	0.098	2:1 --->	0.496		0.212	7:3 -->	0.429
2500		0.459		0.228	10:1 --->	0.098	2:1 --->	0.496		0.212	7:3 -->	0.429
2400		0.457		0.227	10:1 --->	0.097	2:1 --->	0.496		0.212	7:3 -->	0.429
2300		0.455		0.225	10:1 --->	0.097	2:1 --->	0.496		0.212	7:3 -->	0.429
2200		0.453		0.224	10:1 --->	0.096	2:1 --->	0.496		0.212	7:3 -->	0.429
2100		0.451		0.223	10:1 --->	0.096	2:1 --->	0.495		0.212	7:3 -->	0.429
2000		0.448		0.222	10:1 --->	0.095	2:1 --->	0.495		0.212	7:3 -->	0.429

1900		0.446		0.221	<i>10:1 ---></i>	<i>0.095</i>	<i>2:1 ---></i>	0.495		0.212	<i>7:3 --></i>	0.429
1800		0.443		0.220		0.094	<i>2:1 ---></i>	0.495		0.212	<i>7:3 --></i>	0.429
1700		0.441		0.218		0.094	<i>2:1 ---></i>	0.495		0.212	<i>7:3 --></i>	0.429
1600		0.439		0.217		0.093	<i>2:1 ---></i>	0.495		0.212	<i>7:3 --></i>	0.429
1500		0.436		0.216		0.093	<i>2:1 ---></i>	0.495		0.212	<i>7:3 --></i>	0.428
1400		0.433		0.215		0.092	<i>2:1 ---></i>	0.495		0.212	<i>7:3 --></i>	0.428
1300		0.431		0.213		0.091	<i>2:1 ---></i>	0.495		0.212	<i>7:3 --></i>	0.428
1200		0.428		0.212		0.091	<i>2:1 ---></i>	0.495		0.212	<i>7:3 --></i>	0.428
1100		0.425		0.211		0.090	<i>2:1 ---></i>	0.495		0.212	<i>7:3 --></i>	0.428
1000		0.422		0.209		0.090	<i>2:1 ---></i>	0.495		0.212	<i>7:3 --></i>	0.428
900		0.420		0.208		0.089	<i>2:1 ---></i>	0.495		0.212	<i>7:3 --></i>	0.428
800		0.417		0.206		0.088	<i>2:1 ---></i>	0.495		0.212	<i>7:3 --></i>	0.428
700		0.413	<i>5:1 ---></i>	0.205		0.088	<i>2:1 ---></i>	0.495		0.212	<i>7:3 --></i>	0.428
600		0.410	<i>5:1 ---></i>	0.203		0.087	<i>2:1 ---></i>	0.495		0.212	<i>7:3 --></i>	0.428
500		0.407	<i>5:1 ---></i>	0.201		0.086	<i>2:1 ---></i>	0.495		0.212	<i>7:3 --></i>	0.428
400	<i>5:2 --></i>	<i>0.404</i>	<i>5:1 ---></i>	0.200		0.086	<i>2:1 ---></i>	0.495		0.212	<i>7:3 --></i>	0.428
300	<i>5:2 --></i>	<i>0.400</i>	<i>5:1 ---></i>	0.198		0.085	<i>2:1 ---></i>	0.495		0.212	<i>7:3 --></i>	0.428
200	<i>5:2 --></i>	<i>0.397</i>	<i>5:1 ---></i>	0.196		0.084	<i>2:1 ---></i>	0.495		0.212	<i>7:3 --></i>	0.428
100		0.393	<i>5:1 ---></i>	0.195		0.083	<i>2:1 ---></i>	0.495		0.212	<i>7:3 --></i>	0.428
0		0.390		0.193		0.083	<i>2:1 ---></i>	0.495		0.212	<i>7:3 --></i>	0.428